

Potential and Challenges of ORC driven Heat Pumps Based on Gas Bearing Supported Turbomachinery

THÈSE N° 8567 (2018)

PRÉSENTÉE LE 1^{ER} JUIN 2018

À LA FACULTÉ DES SCIENCES ET TECHNIQUES DE L'INGÉNIEUR
LABORATOIRE DE CONCEPTION MÉCANIQUE APPLIQUÉE
PROGRAMME DOCTORAL EN ENERGIE

ÉCOLE POLYTECHNIQUE FÉDÉRALE DE LAUSANNE

POUR L'OBTENTION DU GRADE DE DOCTEUR ÈS SCIENCES

PAR

Violette MOUNIER

acceptée sur proposition du jury:

Prof. F. Maréchal, président du jury
Prof. J. A. Schiffmann, directeur de thèse
Prof. P. Colonna, rapporteur
Prof. V. Lemort, rapporteur
Dr P. Ott, rapporteur



ÉCOLE POLYTECHNIQUE
FÉDÉRALE DE LAUSANNE

Suisse
2018

Abstract

Nowadays, domestic space heating accounts for more than 16% of the worldwide primary energy consumption. Electrically Driven Heat Pumps (EDHPs) have been identified as a key technology to provide energy savings in this sector. However, since EDHPs require electrical power, issues related to network overload at peak-time and high operating costs occur more and more. Furthermore, depending on the local energy mix, EDHPs may have a high electricity carbon intensity, particularly when the electricity is generated from fossil fuels. A promising alternative to address these shortcomings is the use of Thermally Driven Heat Pumps (TDHPs), which are powered by a heat source instead of electricity. TDHPs offer the possibility of running with numerous types of heat sources, even renewable ones. Typical TDHP systems are absorption heat pumps, ejectors, and gas engine driven heat pumps. An alternative technical option is to combine a bottoming vapor compression Heat Pump cycle (HP) with a topping Organic Rankine Cycle (ORC) in which the ORC turbine drives directly the HP compressor. This system configuration is named ORC driven Heat Pump (HP-ORC). This technology provides flexibility regarding the selection of the thermal energy source while offering the possibility of producing electricity (cogeneration). Furthermore, when combined with gas bearing supported turbomachinery, the HP-ORC technology offers a compact, oil-free, and efficient heating solution.

The first concept of a HP-ORC system based on gas bearing supported turbomachinery has been investigated in previous work and results were very promising regarding the experimental performance achieved by the proof of concept. The goal of this thesis is to identify the potential of this technology and the challenges that need to be addressed. Since HP-ORC systems are complex, an integrated design and optimization procedure has been applied with the aim of providing the best system design while satisfying competitive objectives such as performance, investment cost, and feasibility.

While integrated design procedures are attractive, they are complex and time consuming due to the high number of design variables and a large number of iterations required to achieve satisfactory convergence. Accurate reduced order models for the various system components are, therefore, highly beneficial for improving the automated design process. However, these models are currently missing for small-scale turbomachinery. Hence, updated reduced order models for small-scale radial inflow turbines and centrifugal compressors are developed in a first step. These pre-design models are more than three orders of magnitude faster than mean-line analysis models while predicting isentropic efficiencies within a 4% deviation band.

Abstract

Furthermore, these new reduced order models provide updated design guidelines for radial turbomachinery operating with refrigerant, offer insights into the underlying phenomena that shape the efficiency contours, and identify the turbomachinery dimensions that have a significant impact on the design process.

In a second step, the updated turbomachinery models have been used for the integrated optimization of the Compressor Turbine Unit (CTU), yielding CTU efficiencies in excess of 60%, which represents a 20-pt efficiency gain compared to the proof of concept. The optimization results suggest that the performance trade-off is governed mainly by the turbomachinery components. In addition, the design robustness of the CTU is investigated, showing the importance of mitigating manufacturing errors in the bearing design while having fluid leakage and turbomachinery tip clearances as small as possible.

In a third step, the integrated design optimization of the thermodynamic cycle with respect to a thermo-economic trade-off is developed. For domestic heat pump applications (floor heating at 35°C with a ground source at 7°C), the optimum working fluid and heat exchanger design are retrieved. Using a hot source at 180°C, exergetic efficiencies in excess of 50% and COPs above 1.8 are achieved, showing a 30% increase compared to the performance of the proof of concept. In addition, two configurations are compared, one where the ORC expander and HP compressor are coupled through the same shaft, and a second one where the ORC and the HP cycle are connected electrically, i.e., mechanically uncoupled. Although the uncoupled HP-ORC offers more design and operational flexibility, it presents inferior thermo-economic trade-offs compared to the coupled configuration (14% less efficient and 16% more expensive on average). Finally, the HP-ORC is compared to typical sorption systems, suggesting that single effect absorption heat pumps are competitive at low heat source temperatures (<120°C), whereas HP-ORC systems perform better if the heat source temperature is higher than 150°C.

In a final step, the optimization tools described in this thesis are applied to three case studies for which the HP-ORC offers competitive advantages over alternative technologies (1) in terms of performance and CO₂ emissions (domestic and greenhouse heating applications), and (2) in terms of engine performance and size (air conditioning in helicopters using the engine exhaust heat).

Keywords: Thermally driven heat pumps, gas bearings, organic Rankine cycle, ORC driven heat pumps, radial turbomachinery, optimization, thermo-economic, robustness

Résumé

De nos jours, le chauffage domestique est responsable de 16% de la consommation totale d'énergie primaire dans le monde. L'usage des Pompes à Chaleur entraînées électriquement (PACe) est une des solutions permettant une réduction drastique de cette consommation. Cependant, les PACe sont totalement dépendantes d'une source d'électricité, ce qui peut entraîner des surcharges du réseau pendant les périodes de pointe, ainsi que des coûts d'opération élevés, l'électricité étant l'une des énergies primaires les plus chères. En outre, selon le mix énergétique local, les PACe peuvent présenter une empreinte carbone importante, particulièrement lorsque l'électricité est produite à partir de ressources fossiles. Afin de pallier aux inconvénients des PACe, les PAC entraînées thermiquement (PACth) sont une technologie alternative prometteuse. En effet, puisque les PACth ne sont pas entraînées par une source d'électricité mais par une source de chaleur, elles peuvent utiliser plusieurs types d'énergie primaire, qu'elle soit d'origine fossile (fioul, gaz) ou renouvelable (biomasse, solaire). Les PACth les plus répandues sont les pompes à chaleur à absorption, les systèmes à éjecteur et les pompes à chaleur entraînées par gaz. Une autre technologie prometteuse de PACth est un système PAC entraîné par un cycle de Rankine organique (ORC), alors appelé PAC-ORC. Ce système est constitué d'un cycle PAC classique directement entraîné par la turbine d'un cycle ORC. Ce système offre une grande flexibilité dans le choix de la source de chaleur (par exemple renouvelable et à basse température), et permet de produire de l'électricité via l'arbre reliant la PAC et l'ORC (cogénération). De plus, si la technologie PAC-ORC est associée à des turbomachines montées sur paliers à gaz, une solution de chauffage compacte, sans huile et performante est proposée.

Le premier concept d'un système PAC-ORC opérant avec des turbomachines montées sur paliers à gaz a été étudié lors de travaux précédents, présentant des résultats hautement prometteurs. Le but de cette thèse est d'explorer plus en détail le potentiel et les défis de la technologie PAC-ORC. Les systèmes PAC-ORC étant complexes, une procédure d'optimisation intégrée est alors mise en place afin de trouver le design satisfaisant au mieux des objectifs d'efficacité, de coût et de faisabilité.

Les procédures d'optimisation intégrée sont très intéressantes pour la conception automatisée de systèmes complexes. En revanche, en raison du nombre important de variables de conception et d'itérations requises pour obtenir une convergence satisfaisante, ces méthodes sont complexes et chronophages. L'accès à des modèles d'ordre réduit précis sont alors hautement bénéfiques pour accélérer les procédures de conception automatisée. De tels modèles ne

Résumé

sont cependant pas disponibles pour les turbomachines de petite taille. Pour cette raison, des modèles estimant l'efficacité d'un compresseur centrifuge et d'une turbine radiale sont dans un premier temps développés. Ces modèles sont 1500 fois plus rapides que les modèles 1D, alors qu'ils prédisent la même efficacité avec une erreur inférieure à 4%. De plus, ces modèles apportent des recommandations nouvelles de conception pour les turbomachines de petite taille.

En utilisant ces nouveaux modèles, l'optimisation intégrée de l'unité compresseur turbine montée sur paliers à gaz est réalisée dans un second temps. Des efficacités supérieures à 60% sont prédites, ce qui correspond à une augmentation de 20 points par rapport aux premiers tests expérimentaux réalisés. L'étude suggère que la performance du système est majoritairement influencée par les turbomachines. Enfin, la robustesse du design optimum a été étudiée, démontrant la nécessité d'éviter au maximum les erreurs de fabrication des paliers à gaz, tout en contrôlant au mieux les jeux au niveau des volutes, des turbomachines et des joints.

L'optimisation du cycle thermodynamique a ensuite été réalisée, en considérant un objectif de performance maximum tout en minimisant le coût d'investissement de la machine. Pour une application de chauffage domestique (chauffage au sol à 35°C avec une source géothermique à 7°C), les dimensions idéales des échangeurs de chaleur et le réfrigérant optimum sont identifiés. Avec une source de chaleur disponible de 180°C, des efficacités exergétiques supérieures à 50% et des COP autour de 1.8 sont obtenus. Dans un second temps, deux configurations de PAC-ORC ont été comparées, l'une avec les cycles ORC et PAC couplés directement et mécaniquement par un arbre, et une seconde configuration où l'ORC et la PAC sont connectés électriquement. Bien que la configuration découplée offre plus de flexibilité, elle présente un compromis performance-coût beaucoup moins intéressant (14% moins efficace pour un coût 16% plus élevé en moyenne). Enfin, le cycle PAC-ORC a été comparé avec une technologie typique de pompe à chaleur à absorption. Bien que ces dernières soient compétitives pour des sources de chaleur inférieures à 120°C, les cycles PAC-ORC obtiennent de bien meilleures performances au-delà de 150°C.

Pour conclure cette thèse, les outils d'optimisation développés précédemment ont été appliqués à trois études de cas pour lesquelles la technologie PAC-ORC offre des avantages compétitifs en terme de (1) performance et réduction des émissions de CO₂ (chauffage domestique et de serres agricoles) et (2) en terme de performance et taille du moteur (climatisation d'une cabine d'hélicoptère en utilisant la chaleur des gaz d'échappement).

Mots clés: Pompes à chaleur entraînées thermiquement, paliers à gaz, cycle de Rankine organique, pompes à chaleur entraînées par ORC, turbomachines radiales, optimisation, robustesse

Acknowledgments

Throughout this Ph.D., I had the unique opportunity to work on a complex, intense, and multidisciplinary project. I learned a lot of technical skills but also about myself. And this would have been not possible without all the people that were by my side during this rewarding experience.

First, I want to express my gratitude to my thesis supervisor Prof. Jürg Schiffmann, who gave me the opportunity to carry out this Ph.D. work at LAMD. I highly appreciated his expertise, thoughtful advice, his encouragements, and for helping me develop my technical and personal skills. I would like to extend my gratitude to François Maréchal, Peter Ott, Piero Colonna, and Vincent Lemort for having accepted to be part of my thesis jury and for their helpful comments. I am also thanking you Cécile for your great help with the doctoral process.

I would also like to thank the HEIG-VD, especially Jean Baptiste Carré and Roger Roethlisberger, for their commitment and immense help with the experimental work. I am also addressing my thanks to Jonathan Demierre for answering my questions about the ORC-ORC project and for helping us on the experimental part. A special thank-you note to the EPFL workshops (ATME, ATPR, and Microcity) for their time and everything they have taught me.

I am also very grateful to all the people I met during this Ph.D. First, I would like to say thank you to all the LAMD team and particularly to Julie. Beyond all the fantastic help you provide me with the administration, you always have encouraged me in the difficult moments. Many thanks for organizing most of the LAMD events in which we had a lot of fun! I would also like to thank my colleagues and friends for the great time I had in Neuchâtel. Karim and Chaimaa, for all the thoughtful discussions and awesome moments we have shared (now I love Egyptian food!). Ceyhun, for our all the activities we have made together (Istanbul trip, yoga, concerts, and many more!) and for being such a good listener. Eric, Patrick, Lili, Laura, and Yuanhao for our many dinners, soup parties (true story!), bouldering, and lake swimming where we always had a good time. Christophe for your unlimited patience when I was asking you tips about mechanical design (CATIA is almost my friend), for your humor and optimism in general. Cyril, Elliott, and Antonio for your help, enthusiasm, contagious fun, and for sharing coffee-breaks (and Swiss knowledge!) with me. Kévin for all the cheering up moments, for your help regarding turbines and ORCs, and for bringing another French touch in the lab. Finally, thank you to all my colleagues who have all helped me with this thesis work, either on technical questions, paper/thesis proof-reading, experimental work, and in all the fun

Acknowledgements

moments: Kossi, Adeel, Rukshan, Luis, Ansgar, Christoph, Markus, Thierry, Nicolas, Philipp, Suresh, and Matthias. I am also grateful to all the students who have contributed to this thesis work: Elliott (the same as above), Yann, Laurent, Aziz, Joep, Katie, Albina, Sylwia, Farid, Solange, and Jaime.

I am also thanking all the friends I met in Switzerland. First to Caroline (zouz!), for your support ever since we met in Baden and for cheering me up by Skype in times of considerable doubt. To Andyn and Agnieszka, for our several dinners in Zürich and all the laughter we have shared. To my Toastmaster club and its incredible members, who have encouraged me and made me more confident in my public speaking skills. Finally, a big thank you to the plop team! Alise and Geoffroy, for our many weekends around a fondue or some French crêpes. Sophie and Nicolas, for our crazy (and non-engineering!) conversations. Nathou, for encouraging me ever since we met. Jeremy and Pierre, for helping me while crossing the Ph.D. valley of doom, especially in the writing phase. And finally to Paul, Marjorie, Blanche, Lucie, and Charlène for all the fun and support all these years.

I want to extend my gratitude to my family, especially my mother, my stepfather, and my three sisters, Salomé, Justine, and Anaïs, for their encouragements and our memorable adventures in the past four years (Indochine concert, London trip, U.S. trip, etc...). Thanks a lot also to Pascal and Isabelle, who have cheered me up on many occasions and always have given me great advise. Finally, I want to dedicate this work to my father, who had passed away few months before I started this Ph.D. I know he was attached to the problem of energy, and I am sure he would have been proud to see me trying to contribute to a more environmentally friendly world.

Last but not least, there is no word strong enough to say how I am grateful to you Thibaut. Firstly, you helped me a lot with this thesis by answering at any time of the day to my silly questions about computers, and by helping me with Inkscape drawings, Matlab problems, blue screens of death, and git-related nightmares when I was overwhelmed. I think you made me become a geek, but that is OK (at least we can laugh together at programmer jokes now). But beyond this, you always have been there, supporting my moods and helping me putting less pressure on myself. In the most challenging moments, you were the reason I could go on and never give up. If I write these lines today, it is thanks to you.

Neuchâtel, 8 Février 2018

Violette.

Contents

Abstract	i
Résumé	iii
Acknowledgments	v
List of Figures	xi
List of Tables	xvii
Nomenclature	xix
List of Publications	xxvii
1 Introduction	1
1.1 Motivation	1
1.2 State of the art on Thermally Driven Heat Pumps (TDHPs)	4
1.2.1 Sorption technologies	6
1.2.2 Ejectors	7
1.2.3 Gas Engine driven Heat Pumps	9
1.2.4 ORC driven Heat Pumps	10
1.2.5 Summary	12
1.3 HP-ORC based on gas bearing supported turbomachinery	13
1.3.1 External sources	13
1.3.2 Heat exchangers	13
1.3.3 Compressor Turbine Unit	13
1.3.4 Pump	15
1.4 Experimental proof of concept	16
1.5 Optimization and design of complex energy systems	18
1.6 Objectives and structure of the thesis	19
2 Pre-design models for small-scale radial turbomachinery	23
2.1 Introduction	24
2.2 Small-scale turbomachinery: Terminology	24
2.3 Classic design steps for turbomachinery	25

Contents

2.4	Generation of the turbomachinery pre-design models	27
2.5	Radial inflow turbine	28
2.5.1	Generation of the reduced order model	28
2.5.2	Influence of the pressure ratio	32
2.5.3	Influence of the working fluid	35
2.5.4	Influence of the turbine loss mechanisms on the efficiency contours . .	36
2.5.5	Sensitivity Analysis	46
2.5.6	Pre-design model validation	51
2.5.7	Limitations of the turbine pre-design model	54
2.6	Centrifugal compressor	55
2.6.1	Generation of the reduced order model	55
2.6.2	Reduced order model in the Ns-Ds design space	57
2.6.3	Influence of the compressor loss mechanisms on the efficiency contours	60
2.6.4	Sensitivity analysis	70
2.6.5	Comparison with literature	73
2.6.6	Influence of the working fluid	75
2.6.7	Pre-design model validation	79
2.6.8	Limitations of the compressor pre-design model	82
2.7	Summary and conclusions	83
3	Integrated design optimization of the Compressor Turbine Unit	85
3.1	Introduction	85
3.2	CTU modeling	86
3.2.1	Shaft model	88
3.2.2	Radial bearing model	88
3.2.3	CTU axial load and axial bearing models	89
3.2.4	Turbomachinery models	94
3.3	Multi-objective optimization	95
3.4	Results and discussion	101
3.4.1	Pareto optimum curves for the operating point OP3	101
3.4.2	Shaft and bearing design variables	103
3.4.3	Turbomachinery design variables	107
3.5	Robustness analysis	112
3.5.1	Influence of the design point	114
3.5.2	Influence of the tip clearance	117
3.5.3	Influence of the fluid leakage	119
3.5.4	Influence of manufacturing errors	122
3.5.5	Tolerance ranges	127
3.6	Limitations of the integrated optimization procedure	128
3.7	Summary and conclusions	129

4	Integrated design optimization of the HP-ORC cycle	131
4.1	Introduction	131
4.2	HP-ORC description	133
4.3	Components modeling	135
4.3.1	Cycle model	135
4.3.2	CTU model	139
4.3.3	Heat exchanger model	140
4.4	Economic model	143
4.5	Multi-objective optimization	144
4.6	Results and discussion	146
4.6.1	HP-ORC working fluid screening	146
4.6.2	Stage 1: Design selection based on the heat exchanger cost	147
4.6.3	Stage 2: Influence of the component costs	154
4.6.4	Stage 3: Influence of the HP-ORC configuration	157
4.7	Comparison to a Single Effect Absorption Heat Pump (SEAHP)	162
4.7.1	SEAHP description	162
4.7.2	SEAHP modeling	162
4.7.3	Results and discussion	165
4.8	Improvement of the prototype performance	168
4.9	Limitations of the integrated optimization procedure	171
4.10	Summary and conclusions	172
5	Application examples	175
5.1	Introduction	175
5.2	Definition of the case studies	176
5.2.1	Modeling	176
5.2.2	Case study A: Domestic space heating	177
5.2.3	Case study B: Heating of agricultural greenhouses	177
5.2.4	Case study C: Cabin air conditioning in helicopters	178
5.3	Multi-objective optimization	179
5.4	Results and discussion	181
5.4.1	Case study A	181
5.4.2	Case study B	183
5.4.3	Case study C	185
5.4.4	Discussion	188
5.5	Summary and conclusions	188
6	Conclusions and future work	191
A	Turbomachinery pre-design models	197
B	Plate Heat Exchanger design	199
C	Heat and mass transfer correlations	203

Contents

Bibliography	215
Curriculum Vitae	217

List of Figures

1.1	Comparison of conventional heating systems with TDHP technologies	3
1.2	Working principle of a EDHP (a) and a TDHP (b)	4
1.3	Schematic layout of an Absorption Heat Pump (AHP) and its main components	6
1.4	Schematic layout of an Ejector Refrigeration System (ERS) and its main components	8
1.5	Schematic layout of a Gas Engine driven Heat Pump (GEHP) and its main components	9
1.6	Schematic layout of a HP-ORC and its main components in its (a) coupled and (b) uncoupled configuration	10
1.7	Schematic of the HP-ORC CTU	14
1.8	Picture of the CTU including the centrifugal compressor (left), the shaft and bearings (center), and the radial turbine (right)	16
1.9	Picture of the HP-ORC prototype as tested by Demierre et al.	16
1.10	Pareto front of a two-objective optimization	18
1.11	Graphical summary of the thesis structure and objectives	21
2.1	Main steps of the turbomachinery design process	25
2.2	Procedure for generating the turbomachinery pre-design models	28
2.3	1D layout of a radial inflow turbine	29
2.4	Predicted and measured turbine isentropic efficiency for different turbine pressure ratios as obtained by Demierre et al.	29
2.5	Iso-efficiency contours in the Ns-Ds diagram generated at fixed pressure ratios (colored lines) and for a varying pressure ratio (black line) for R134a working fluid	32
2.6	Goodness of fit of the $\eta_{is,0D} = f(Ns, Ds, PR)$ model for R134a working fluid	33
2.7	Iso-efficiency contours in the Ns-Ds diagram generated at fixed pressure ratios superimposed by the theoretical curve NsDs=2 for R134a working fluid	34
2.8	Iso-efficiency contours in the Ns-Ds diagram for various pressure ratios and for four organic working fluids suggesting only limited influence of the working fluid on the efficiency contours	35
2.9	Evolution of the turbine nozzle loss ratio (a) and interspace loss ratio (b) at different pressure ratios	37
2.10	Velocity triangle at the turbine rotor inlet and evolution of the relative speed W_4 at optimal, high Ns-Ds, and low Ns-Ds conditions	38

List of Figures

2.11 Evolution of the turbine incidence loss ratio at different pressure ratios	39
2.12 Evolution of the (a) relative and (b) absolute Mach numbers at the turbine rotor inlet at different pressure ratios	40
2.13 Evolution of the turbine tip clearance loss ratio at different pressure ratios . . .	41
2.14 Evolution of the passage loss ratio (a) and relative Mach number at the turbine rotor outlet (b) at different pressure ratios	43
2.15 Velocity triangle at the turbine rotor outlet and evolution of the relative speed W_6 at low and high pressure ratio	44
2.16 Evolution of the turbine trailing edge loss ratio at different pressure ratios . . .	44
2.17 Underlying phenomena imposing the shape of the turbine efficiency contours	45
2.18 Ns-Ds contours when performed at different blade height to tip radius ratios $\zeta = \frac{b_4}{r_4}$ for isentropic efficiencies of 0.8 and 0.7 and for PR=4	46
2.19 Ns-Ds contours when performed at different clearance ratios CR for isentropic efficiencies of 0.8 and 0.7 and for PR=4	47
2.20 Ns-Ds contours when performed at different shroud to tip radius ratios $\epsilon = \frac{r_{6s}}{r_4}$ for isentropic efficiencies of 0.8 and 0.7 and for PR=4	48
2.21 Goodness of fit of the $\eta_{is,0D} = f(Ns, Ds, PR, \epsilon)$ model	49
2.22 Comparison of the new performance map with the original map of Balje	50
2.23 Example of a convex hull generated from a random set of variables x_1 and x_2 . .	52
2.24 Comparison of the optimum rotational speeds and efficiencies between the 0D (constrained and unconstrained) and the 1D model with (a) fixed ORC heat input at 22 kW and (b) varied ORC heat input	53
2.25 1D layout of a centrifugal compressor	55
2.26 Repartition of the compressor and turbine feasible points in a Ns-Ds diagram for R134a working fluid	57
2.27 77% iso-efficiency contours in the compressor Ns- ζ diagram generated at different pressure ratios for R134a working fluid	58
2.28 Goodness of fit: (a) $\eta_{is,0D} = f(Ns, Ds, PR, \zeta)$ model (b) $\eta_{is,0D} = f(Ns, PR, \zeta)$ and $Ds_{0D} = f(Ns, PR, \zeta)$ models	59
2.29 Velocity triangle at the compressor impeller inlet assuming a zero-swirl at optimal and low Ns conditions	60
2.30 Evolution of the compressor incidence loss ratio in the Ns- ζ diagram at different pressure ratios	61
2.31 Evolution of the relative Mach number at the compressor impeller inlet in the Ns- ζ diagram at different pressure ratios	62
2.32 Evolution of the compressor skin friction loss ratio in the Ns- ζ diagram at different pressure ratios	63
2.33 Evolution of the relative Mach number at the compressor impeller outlet in the Ns- ζ diagram at different pressure ratios	64
2.34 Velocity triangle at the compressor impeller outlet assuming a fixed impeller outlet angle β_4 at optimal, high Ns-low ζ , and low Ns-high ζ conditions	64

2.35 Evolution of the compressor tip clearance loss ratio in the Ns- ζ diagram at different pressure ratios	65
2.36 Evolution of the compressor blade loading loss ratio in the Ns- ζ diagram at different pressure ratios	66
2.37 Evolution of the compressor disc friction loss ratio in the Ns- ζ diagram at different pressure ratios	67
2.38 Evolution of the compressor recirculation loss ratio in the Ns- ζ diagram at different pressure ratios	68
2.39 Underlying phenomena shaping the efficiency contours of the compressor pre-design model in the Ns- ζ diagram	69
2.40 Influence of the tip clearance ratio CR on the compressor efficiency contours at PR=2.5	70
2.41 77% iso-efficiency contours in the compressor Ns- ζ diagram generated at PR=2.5 and varying $\epsilon = \frac{r_{2s}}{r_4}$	71
2.42 Goodness of fit of the $\eta_{is,0D} = f(Ns, PR, \zeta, \epsilon)$ and $Ds_{0D} = f(Ns, PR, \zeta, \epsilon)$ models	72
2.43 Comparison of the predicted optimum Ds with respect to the Cordier line (left) and of the predicted best efficiency with respect to Balje's prediction (right) . .	74
2.44 Optimum Ds, ζ , ϵ , and η_{is} for the best efficiency points along Ns for PR=2.5 . .	74
2.45 (a) Isentropic efficiencies and (b) specific diameters in the Ns- ζ domain at different working fluids and pressure ratios	76
2.46 (a) Goodness of fit of the $\eta_{is,0D} = f(Ns, PR, \zeta)$ model (based on a dataset built with a collection of the proposed fluid data) for different working fluids and (b) evolution of the compressor tip clearance loss ratio in the Ns- ζ diagram	77
2.47 Goodness of fit of the $\eta_{is,0D} = f(Ns, PR, \zeta, CR)$ model for different working fluids	78
2.48 Comparison of the optimum rotational speeds and efficiencies versus the pressure ratio between the 0D (constrained and unconstrained solutions) and the 1D model for a centrifugal compressor operating at a fixed HP evaporator power of 12 kW	80
2.49 Efficiency contours of $\eta_{is} = f(Ns, PR, \zeta)$ versus the the original dataset	81
2.50 Comparison of the optimum rotational speeds and efficiencies between the 0D and the 1D model for a centrifugal compressor operating at different HP evaporator powers	81
2.51 Comparison of optimum efficiencies predicted by the 0D and by the 1D model for a centrifugal compressor operating with different working fluids	82
3.1 CTU schematic with its main components and dimensions	86
3.2 Rigid-body model of the CTU rotor supported on two radial journal bearings .	87
3.3 Schematic of a Herringbone Grooved Journal Bearing (HGJB)	88
3.4 Axial force generation across the Compressor Turbine Unit	89
3.5 Pressure distribution profile on the turbomachinery front side for an operating condition tested by Demierre et al.	90

List of Figures

3.6	Pressure distribution profile on the turbomachinery backside for an operating condition tested by Demierre et al.	91
3.7	Axial forces applied to the turbomachinery for four different operating points (OP) performed by Demierre et al.	92
3.8	Total axial force applied to the CTU for four different operating points (OP) . . .	93
3.9	Schematic of a Spiral Groove Thrust Bearing (SGTB)	93
3.10	Summary of the different CTU optimization levels	96
3.11	Layout of the optimization levels (a) Opt1 and Opt2, (b) Opt3 and Opt4	97
3.12	Pareto optimum curves for different optimizations levels applied to the operating condition OP3 and compared to the Proof of Concept	101
3.13	Pareto optimum solutions of the radial bearing dimensions versus the CTU stability (levels Opt2 and Opt3.3 performed at OP3)	104
3.14	Pareto optimum solutions of the axial bearing dimensions versus the CTU stability (levels Opt2 and Opt3.3 performed at OP3)	105
3.15	Pareto optimum solutions of the shaft dimensions versus the CTU stability (levels Opt2 and Opt3.3 performed at OP3)	106
3.16	Evolution of the mechanical efficiency and turbomachinery isentropic efficiencies throughout the optimization levels for a stability target equal to the one of the proof of concept	107
3.17	Pareto optimum solutions of the 0D turbomachinery dimensions versus the CTU efficiency	109
3.18	Pareto optimum solutions of the 1D turbine dimensions versus the CTU efficiency	110
3.19	Pareto optimum solutions of the 1D compressor dimensions versus the CTU efficiency	111
3.20	Optimum turbomachinery designs for different optimization levels for a rotor-dynamic stability equal to the one of the proof of concept	111
3.21	Pareto optimum solution locations considered for the robustness analysis . . .	112
3.22	CTU off-design performance and stability when Pareto optimum designs for OP3 are selected	114
3.23	CTU off-design performance and stability when Pareto optimum designs obtained at different OPs are selected at a stability target of $\Gamma_{CTU} = 1$	115
3.24	Impact of the tip clearance e_{turbo} on the CTU efficiency and rotordynamic stability	117
3.25	Impact of the tip clearance e_{turbo} on the turbomachinery isentropic efficiencies and rotor speed	118
3.26	CTU fluid leakage pathways and pressure levels encountered in the experimental data performed by Demierre et al.	119
3.27	Schematic of a labyrinth seal	120
3.28	Impact of the seal clearance on the CTU performance	121
3.29	Effect of the radial bearing manufacturing errors on the CTU performance and stability	123
3.30	Effect of the axial bearing manufacturing errors on the CTU performance and SGTB load capacity	124

3.31 Effect of the turbomachinery diameters manufacturing errors on the CTU performance and stability	125
3.32 Effect on the CTU performance of the manufacturing errors occurring on the turbomachinery shroud diameters and blade heights	126
4.1 HP-ORC schematic diagram of the topping Organic Rankine Cycle and the bottoming single-stage vapor compression heat pump cycle where the HP compressor and ORC turbine are (a) mechanically coupled and (b) uncoupled	134
4.2 Simulation layout of the coupled HP-ORC	137
4.3 (a) T-s and (b) heat exchangers T-Q diagrams of the HP-ORC operating with R600a at $T_{hot,in}=180^{\circ}\text{C}$ for two cycle design solutions: subcritical and supercritical ORC evaporation process	138
4.4 Geometry parameters of a Plate Heat Exchanger	141
4.5 Pareto curves of the selected working fluids for two performances objectives (COP and η_{exe}) and two hot source temperatures	148
4.6 HX cost repartition along the dominant Pareto fronts	148
4.7 Pareto optimum solutions of the selected working fluids for two performances objectives (COP and η_{exe}) at $T_{hot,in}=120^{\circ}\text{C}$	149
4.8 Pareto optimum solutions of the selected working fluids for two performances objectives (COP and η_{exe}) at $T_{hot,in}=180^{\circ}\text{C}$	150
4.9 Overall HP-ORC Pareto fronts for two performances objectives (COP and η_{exe}) and two hot source temperatures	154
4.10 Pareto-dominant curves for two performances objectives (COP and η_{exe}) and two hot source temperatures including the cost of the heat exchangers, boiler, CTU, and GHX	155
4.11 Repartition of the component costs on the dominating Pareto fronts shown in Figure 4.10	156
4.12 Comparison of the HP-ORC Pareto-dominant fronts between the coupled and uncoupled configuration, based on the HX economic trade-off	157
4.13 Comparison of the HP-ORC Pareto-dominant fronts between the coupled and uncoupled configuration, based on the overall cycle economic trade-off (HX, GHX, CTU, and boiler)	158
4.14 Sankey diagram of the CTU power flows for the HP-ORC in its (a) coupled and (b) uncoupled configuration	160
4.15 Cost repartition comparison between the coupled and uncoupled HP-ORC configuration when maximizing the COP at $T_{hot,in}=180^{\circ}\text{C}$ (stage 2)	161
4.16 Schematic layout of the Single Effect Absorption Heat Pump (SEAHP)	163
4.17 COP versus the hot source temperature for the HP-ORC and the SEAHP	165
4.18 Thermo-economic comparison of the HP-ORC and the SEAHP cycles based on (a) HX cost only and (b) on all component costs	167
4.19 Thermo-economic comparison of the HP-ORC prototype towards the optimum Pareto fronts shown in Figure 4.5	169

List of Figures

5.1	Schematic layout of the optimization procedure	180
5.2	Pareto curve of the case study A compared to the base case optimization shown in chapter 4 (Figure 4.10)	181
5.3	Pareto curve of the case study B	183
5.4	Comparison of conventional heating systems with the HP-ORC technology for agricultural greenhouse heating	185
5.5	Pareto curve of the case study C	185
5.6	HP-ORC power consumption, component weight, and component volume as a function of the COP	186
B.1	Pressure drops occurring in the HP-ORC heat transfer units	201
B.2	Influence of the pressure drop on the HP-ORC performance when the COP is maximized at 180°C	201

List of Tables

1.1	Cost and CO ₂ emissions of various energy sources	2
1.2	ORC driven Heat Pump (HP-ORC) concepts in literature	11
1.3	Summary of the different TDHP concepts	12
2.1	1D turbine inputs for the reduced order generation based on the original Balje maps, small-scale ORC operating conditions, and geometrical design guidelines recommended by Baines	31
2.2	Boundary conditions for the turbine pre-design model validation	51
2.3	Description of the inputs of the centrifugal compressor 1D model indicating the ranges considered for the generation of the reduced order model	56
2.4	Boundary conditions for the compressor pre-design model validation	79
2.5	Summary of the proposed turbomachinery pre-design models	84
3.1	Shaft material properties	88
3.2	Boundary conditions of the CTU optimization	99
3.3	Design variables of the CTU optimization	100
3.4	Optimum design variables at four different locations on the Opt3.3 Pareto front	113
3.5	Optimum design variables of the CTU optimization achieved at $\Gamma_{CTU} = 1$ for different operating conditions	116
3.6	Sensitivity analysis boundaries on the labyrinth seal variables	120
3.7	Sensitivity analysis boundaries on the radial bearing variables	122
3.8	Sensitivity analysis boundaries on the axial bearing variables	124
3.9	Sensitivity analysis boundaries on the turbomachinery variables	125
3.10	Recommended tolerances for the manufacturing of the CTU radial and axial bearings	127
4.1	Boundary conditions of the HP-ORC	135
4.2	Geometry parameters of the CTU shaft and bearings	140
4.3	Heat transfer correlations for PHEs	142
4.4	Boiler investment cost as a function of the primary fuel and the power range . .	143
4.5	Design variables of the coupled HP-ORC optimization	145
4.6	Design variables of the uncoupled HP-ORC optimization	145
4.7	Working fluid selection	146

List of Tables

4.8	Working fluids thermodynamic features at $C_{Tot}=\$5'000$ when maximizing the COP at $T_{hot,in}=120^{\circ}\text{C}$	151
4.9	Working fluids thermodynamic features at $C_{Tot}=\$5'000$ when maximizing the η_{exe} at $T_{hot,in}=120^{\circ}\text{C}$	151
4.10	Working fluids thermodynamic features at $C_{Tot}=\$5'000$ when maximizing the COP at $T_{hot,in}=180^{\circ}\text{C}$	152
4.11	Working fluids thermodynamic features at $C_{Tot}=\$5'000$ when maximizing the η_{exe} at $T_{hot,in}=180^{\circ}\text{C}$	152
4.12	Turbomachinery and cycle features at $C_{Tot}=\$5'000$ when maximizing the η_{exe} at $T_{hot,in}=120^{\circ}\text{C}$	153
4.13	Turbomachinery and cycle features at $C_{Tot}=\$5'000$ when maximizing the COP at $T_{hot,in}=180^{\circ}\text{C}$	153
4.14	Optimum working fluid selection for the two HP-ORC configurations	158
4.15	Cycle and CTU parameters for the two HP-ORC configurations	159
4.16	Heat and mass transfer correlations for the SEAHP heat exchangers	164
4.17	Design variables of the SEAHP optimization	164
4.18	Experimental thermodynamic conditions of the HP-ORC proof of concept	168
4.19	Optimum design variables of the cycle optimization compared to the prototype	170
5.1	Heating, cooling, and temperature requirements for the three considered case studies	176
5.2	Boundary conditions common to each case study	177
5.3	Boundary conditions of the case study A	177
5.4	Boundary conditions of the case study B	178
5.5	Boundary conditions of the case study C	178
5.6	Design variables of the multi-objective optimization	180
5.7	Optimum design variables of the case study A for a COP target of 1.85	182
5.8	Optimum design variables of the case study B for a COP target of 2.4	184
5.9	Optimum design variables of the case study C for a COP target of 0.7	187
B.1	Geometry parameters of the Plate Heat Exchangers common to each transfer unit	199
B.2	Geometry parameters of the Plate Heat Exchangers specific to each transfer unit as designed by SWEP	199
C.1	Nusselt number correlations used for the different flow regimes/heat transfer processes occurring in the HP-ORC	203
C.2	Nusselt and Sherwood number correlations used for the different flow regimes/heat and mass transfer processes occurring in the SEAHP	204

Nomenclature

Roman Symbols

$[C]$	System damping matrix [-]
$[G]$	Gyroscopic effects matrix [-]
$[K]$	System stiffness matrix [-]
$[M]$	System inertia matrix [-]
$\dot{E}x$	Exergy [W]
\dot{E}	Mechanical power [W]
\dot{m}	Mass flow rate [$\text{kg}\cdot\text{s}^{-1}$]
\dot{Q}	Heating power [W]
\dot{V}	Volumetric flow rate [$\text{m}^3\cdot\text{s}^{-1}$]
\dot{W}	Electrical power [W]
A	Area [m^2]
a	Speed of sound [$\text{m}\cdot\text{s}^{-1}$]
B	Blockage coefficient [-]
b	Blade height [m] / PHE channel spacing [m]
C	Cost [\$] / Absolute velocity [$\text{m}\cdot\text{s}^{-1}$] / Clearance [m]
c	Concentration [-]
D, d	Diameter [m]
Ds	Specific diameter [-]
DT	Temperature difference [K]
DT_{min}	Minimum temperature difference (Pinch) [K]

Nomenclature

e	Clearance [m]
F	Force [N] / Fluid [-]
f	Excitation force [N] / Objective function [-] / Friction factor [-]
G	Fluid mass flux [$\text{kg}\cdot\text{m}^{-2}\cdot\text{s}^{-1}$] / Optimization variables [-]
g	Acceleration due to gravity [$\text{m}\cdot\text{s}^{-2}$]
H	Bearing normalized groove depth [-]
h	Specific enthalpy [$\text{J}\cdot\text{kg}^{-1}$] / Depth [m] / Heat transfer coefficient [$\text{W}\cdot\text{m}^{-2}\cdot\text{K}^{-1}$]
HR	Heat exchange rate [$\text{W}\cdot\text{m}^{-1}$]
k	Thermal conductivity [$\text{W}\cdot\text{m}^{-1}\cdot\text{K}^{-1}$]
L	Length [m]
M	Mach number [-]
N	Rotational speed [rpm]
N_{ch}	Number of plates [-]
Ns	Specific speed [-]
Nu	Nusselt number [-]
NY	Lifetime [year]
P	Pressure [Pa]
Pr	Prandtl number [-]
q''	Heat flux [$\text{W}\cdot\text{m}^{-2}$]
R	Gas constant $R=8.314$ [$\text{J}\cdot\text{K}^{-1}\cdot\text{mol}^{-1}$]
r	Radius [m]
Ra	Roughness [-]
Re	Reynolds Number [-]
s	Specific entropy [$\text{J}\cdot\text{kg}^{-1}\cdot\text{K}^{-1}$]
Sh	Sherwood number [-]
T	Temperature [K]
U	Tip velocity [$\text{m}\cdot\text{s}^{-1}$] / Overall heat transfer coefficient [$\text{W}\cdot\text{m}^{-2}\cdot\text{K}^{-1}$]

v	Fluid velocity [m.s^{-1}]
W	Relative velocity [m.s^{-1}] / Width [m]
x	Vapor quality [-]
Z	Number of blades [-]

Greek Symbols

α	Turbine nozzle angle [deg] / Bearing groove width ratio [-] / Fluid diffusivity [$\text{m}^2.\text{s}^{-1}$]
β	Turbomachinery angle [deg] / Bearing groove angle [deg] / PHE chevron angle [deg]
δ	PHE plate thickness [m]
ϵ	Shroud to tip radius ratio [-]
η	Efficiency [-]
Γ	Logarithmic decrement [-]
γ	HGJB groove length ratio [-] / Mass transfer coefficient [m.s^{-1}]
Λ	PHE wavelength of surface corrugation [m]
λ	Damping coefficient [-]
μ	Dynamic viscosity [Pa.s]
ω	Rotational speed [rad.s^{-1}]
ϕ	PHE enlargement factor [-]
ρ	Density [kg.m^{-3}]
σ	Surface tension [N.m^{-1}]
ξ	Turbine nozzle/interspace loss coefficient [-]
ζ	Blade height to tip radius ratio [-]

Subscripts

θ	Tangential
a	Ambient
abs	Absolute
ax, x	Axial
b	Bulk

Nomenclature

<i>bend</i>	Bending
<i>bl</i>	Blade Loading
<i>cl</i>	Clearance
<i>cold</i>	Cold source
<i>comp</i>	Compressor
<i>cond</i>	Condensation
<i>condh</i>	HP Condensation
<i>condo</i>	ORC Condensation
<i>cr</i>	Critical
<i>cs</i>	Cold side
<i>df</i>	Disc friction
<i>evap</i>	Evaporation
<i>evh</i>	HP evaporator
<i>evo</i>	ORC evaporator
<i>exe</i>	Exergetic
<i>f</i>	Friction
<i>h</i>	Hub / Hydraulic
<i>hot</i>	Hot source
<i>hs</i>	Hot side
<i>I</i>	Investment
<i>imp</i>	Impeller
<i>in</i>	Inlet
<i>inc</i>	Incidence
<i>is</i>	Isentropic
<i>l</i>	Liquid
<i>lat</i>	Latent
<i>m</i>	Meridional

<i>mech</i>	Mechanical
<i>noz</i>	Nozzle
<i>O</i>	Operational
<i>out</i>	Outlet
<i>pass</i>	Passage
<i>rad,r</i>	Radial
<i>rc</i>	Recirculation
<i>reg</i>	Regenerator
<i>rel</i>	Relative
<i>rms</i>	Root mean squared
<i>rot</i>	Rotor
<i>s</i>	Shroud / Solution
<i>sat</i>	Saturated state
<i>sc</i>	Sub-cooling
<i>sf</i>	Skin friction
<i>sh</i>	Super-heating
<i>sink</i>	Sink
<i>tot</i>	Total
<i>tp</i>	Tip
<i>ts</i>	Total-to-static
<i>tt</i>	Total-to-total
<i>turb</i>	Turbine
<i>v</i>	Vapor
<i>w</i>	Wall

Acronyms

AHP	Absorption Heat Pump
AMB	Active Magnetic Bearing

Nomenclature

CFD	Computational Fluid Dynamics
COP	Coefficient Of Performance
CR	Clearance Ratio
CTU	Compressor Turbine Unit
DEAHP	Double Effect Absorption Heat Pump
DTC	Double Tube Coil
EDHP	Electrically Driven Heat Pump
ERS	Ejector Refrigeration System
FFB	Fluid Film Bearing
GEHP	Gas Engine driven Heat Pump
GHX	Ground Heat Exchanger
GSHP	Ground Source Heat Pump
GWP	Global Warming Potential
HGJB	Herringbone Grooved Journal Bearing
HP	Heat Pump
HP-ORC	ORC driven Heat Pump
HX	Heat Exchanger
LMCD	Logarithmic Mean Concentration Difference
LMTD	Logarithmic Mean Temperature Difference
LR	Loss Ratio
MOO	Multi-Objective Optimization
NG	Natural Gas
ODP	Ozone Depletion Potential
OP	Operating Point
ORC	Organic Rankine Cycle
PAC	Pompe à Chaleur
PACe	Pompe à Chaleur entraînée électriquement

PACth Pompe à Chaleur entraînée thermiquement

PER Primary Energy Ratio

PHE Plate Heat Exchanger

PR Pressure Ratio

QMOO Queuing Multi-Objective Optimization

R^2 Coefficient of determination

REB Rolling Element Bearing

RMSE Root Mean Squared Error

SEAHP Single Effect Absorption Heat Pump

SGTB Spiral Grooved Thrust Bearing

SHX Solution Heat Exchanger

SV Solution Valve

TCO Total Cost of Ownership

TDHP Thermally Driven Heat Pump

WP Wood Pellet

List of Publications

Journal papers

1. Mounier V, Mendoza LC, Schiffmann J. *Thermo-economic Optimization of an ORC driven Heat Pump Based on Small Scale Turbomachinery and Comparison with Absorption Heat Pumps*. Int J Refrig 2017;81:96–110. doi:10.1016/j.ijrefrig.2017.05.021.
2. Mounier V, Olmedo LE, Schiffmann J. *Small Scale Radial Inflow Turbine Performance and Pre-design Maps for Organic Rankine Cycles*. Energy 2018;43:1072-1084. doi:10.1016/j.energy.2017.11.0021.
3. Mounier V, Schiffmann J. *Integrated Design Guidelines of a Gas Bearing Supported Compressor-Turbine-Unit for Domestic Heat Pumps driven by ORC. (In preparation)*
4. Olmedo LE, Mounier V, Schiffmann J. *Dimensionless Performance Prediction Maps of Scroll Expanders for Micro-Scale Organic Rankine Cycles*. Energy 2018; doi:10.1016/j.energy.2018.05.001.
5. Rosset K, Mounier V, Guenat E, Schiffmann J. *Comparative analysis of turbo-ORC systems for waste heat recovery on passenger car engines*. Energy (**Under review**)

Proceedings

1. Mounier V, Mendoza LC, Schiffmann J. *Performance Assessment and Comparison of Thermally driven Heat Pumps Systems*, 24th IIR International Congress of Refrigeration, 2015, doi: 10.18462/iir.icr.2015.0316.
2. Mounier V, Schiffmann J. *ORC Driven Heat Pump Running on Gas Bearings for Domestic Applications: Proof of Concept and Thermo-Economic Improvement Potential*. 12th IEA Heat Pump Conference, Rotterdam, 2017
3. Mounier V, Picard C, Schiffmann J. *Data-driven Updated Pre-design Tool for Small Scale Centrifugal Compressors In Refrigeration*. Turbo Expo: Power for Land, Sea, and Air, Oslo, 2018 (**Recommended for journal publication**)
4. Rosset K, Mounier V, Guenat E, Pajot O, Schiffmann J. *Potential of Small-Scale Turbomachinery for Waste Heat Recovery on Automotive Internal Combustion Engines*. 3rd Int. Semin. ORC Power Syst., Brussels: 2015

1 Introduction

1.1 Motivation

In the past fifty years, concerns about the shortage of fossil fuels and the rise of global warming have advocated for a more rational use of primary energy as well as a smarter mix between renewable energy sources and fossil fuels. Space heating accounts for more than 16% of the world total energy consumption [1]. Hence, finding more efficient and environmentally friendly technologies for space heating is now pivotal. A significant step has been made with Electrically Driven Heat Pumps (EDHPs), which enable to reduce significantly the energy consumption compared to conventional heating solutions. However, this technology is facing the emerging issue of increased electricity consumption, raising questions about the risk of network overload at peak-time. Particularly, Switzerland may face such issues since the country is planning to gradually phase out its nuclear power production after a popular vote that took place on the 21st of May 2017 ¹ to forbid the construction of new nuclear plants. Moreover, some countries produce most of their electricity through the combustion of fossil fuels (coal, oil, and natural gas), leading to heating solutions with a high electricity carbon intensity. Furthermore, from the power plant to the end users, the energy is converted twice with EDHPs, leading to a primary energy utilization from 25% (coal power plants) to 56% (modern combined gas power plants).

Therefore, heat pumps driven by heat instead of electricity are a promising alternative to EDHPs to provide space heating solutions that are more environmentally friendly. The main advantage of Thermally Driven Heat Pumps (TDHPs) is that they can run on numerous types of heat sources, especially renewable sources such as biomass, geothermal sources, and solar thermal. Moreover, since the system is driven by heat, overloading the electrical grid at peak-time is mitigated. TDHP operating costs are also lower since, in Europe, the cost of heating fuels (gas, oil, and wood) is generally lower than electricity costs ². In order to show the potential of TDHPs, the following study presents a brief comparison of the TDHP

¹<https://www.admin.ch/gov/fr/accueil/documentation/votations/20170521/Loi-sur-l-energie.html>

²<http://euanmearns.com/energy-prices-in-europe/>

Chapter 1. Introduction

technology towards conventional heating systems available on the market, such as oil boilers, gas boilers, wood pellets boilers, and EDHPs. They are compared regarding their Total Cost of Ownership (TCO) and the CO₂ emissions these heating systems produce over their lifetime. Those quantities are defined as follows:

The Total Cost of Ownership (TCO) evaluates the economic impact of a product along its lifetime. The TCO is defined in equation 1.1, where $C_{I,tot}$ represents the system total initial investment cost, $C_{O,y}$ the operational cost per year, NY the lifetime in years, and r_m the annual escalation rate. The operational costs cover the costs of the energy source (fuel or electricity) to drive the system and the maintenance costs, which are here not considered. The operational costs $C_{O,y}$ are therefore only dependent on the energy source costs, which are summarized in Table 1.1 in \$/kWh^{3 4 5}. These costs are based on what consumers pay at a domestic level. A nominal annual escalation rate r_m of 4% is considered, based on the predictions made by the world bank for crude oil and natural gas prices⁶. In this study, the conversion rates 1CHF=\$1 and 1€=\$1.17 were used.

$$TCO = C_{I,Tot} + \sum_{y=1}^{NY} C_{O,y}(1 + r_m)^y \quad (1.1)$$

The CO₂ emissions are calculated over the heating system lifetime. They are estimated using the values reported in Table 1.1^{7 8} in g/kWh. For fossil fuels and wood pellets, it includes the emissions from mining, processing, and transport. The emissions due to electricity include the grid losses and the emissions released by the primary energy source. Two countries with different energy mix have been considered for electricity generation: Switzerland (CH)⁹ (60% hydroelectric, 35% nuclear, and 4% thermal) and Germany (DE)¹⁰ (41% coal, 22% natural gas, 5% oil, 16% hydroelectric, and 12% nuclear).

Table 1.1 – Cost and CO₂ emissions of various energy sources

Energy source	Oil	Natural Gas (NG)	Wood Pellet (WP)	Electricity (CH)	Electricity (DE)
CO ₂ emissions [g/kWh]	330	270	20	130	588
Cost $C_{O,y}$ [\$/kWh]	0.07	0.09	0.08	0.2	0.3

The comparison is based on a 40 kW domestic heating system (residential building with ten dwellings of 120 m² each [2]). The lifetime is assumed to be 20 years. The heating consumption of each dwelling is assumed to 12'000 kWh/year, which corresponds to a total building heating consumption over 20 years of 2.4 MWh.

³<http://www.bfe.admin.ch>

⁴<http://www.agrola.ch/evolution-des-prix-110.html>

⁵<https://1-stromvergleich.com/power-price-germany-electricity/>

⁶<https://knoema.com/ncszerf/natural-gas-prices-forecast-long-term-2017-to-2030-data-and-charts>

⁷<http://www.energyscope.ch/>

⁸<https://doi.org/10.1016/j.trd.2017.07.012>

⁹<http://www.bfe.admin.ch>

¹⁰<http://www.bmwi.de/>

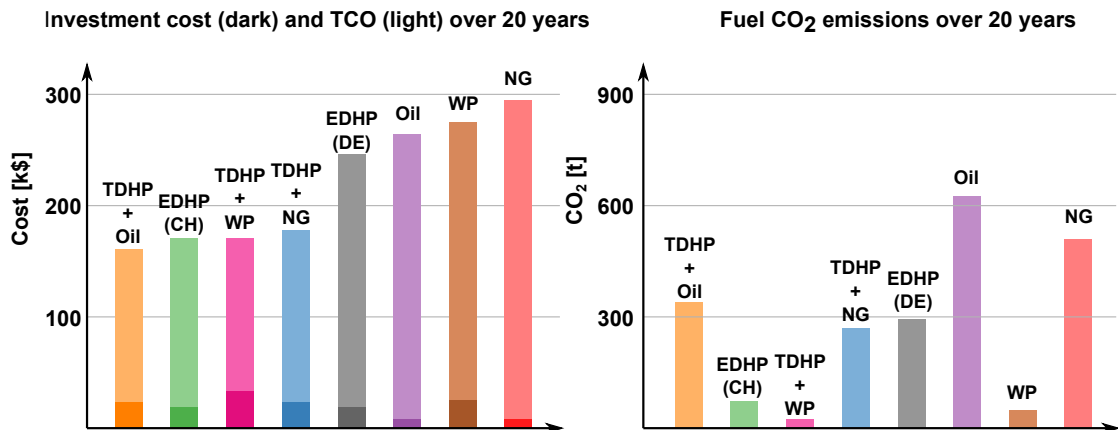


Figure 1.1 – Comparison of conventional heating systems with TDHP technologies

Ground source heat pumps are considered with a COP of 1.85 for TDHPs (maximum COP achieved in the investigation performed in this thesis) and a COP of 4.5 for EDHPs¹¹. The cost of the ground source drilling is supposed to be equal to \$10'000. The efficiency of the conventional boilers is estimated at 95%. The investment cost of the EDHPs and conventional boilers are taken from the catalog of the heating systems manufacturer Viessmann¹¹. The investment cost of the TDHP driven by fossil fuels is assumed to be equal to the absorption heat pumps found on the market¹². Since no data are available for absorption heat pumps coupled with wood pellets, it was assumed that an additional cost of \$10'000 would be considered, which is the difference between a conventional oil/gas boiler and a wood pellet boiler¹¹. The results of the comparative study are presented in Figure 1.1.

Compared to conventional oil and gas boilers, the TDHPs yield smaller TCOs and reduced CO₂ emissions over the system lifetime. Furthermore, since the cost per kWh of conventional fuels is lower than electricity, TDHPs are economically equivalent to EDHPs in Switzerland, and even less expensive than EDHPs in Germany. It is also interesting to note that, while EDHPs installed in Switzerland produce less CO₂ than TDHPs driven by fossil fuels, installing an EDHP in Germany would release 6.5% more CO₂ than a TDHP driven by natural gas, and 108% more than a TDHP driven by wood pellets. By being independent of the electrical power, TDHPs are a very promising alternative in countries such as Germany which have an energy mix with a significant part of fossil fuels. Finally, TDHPs driven by wood pellets present the lowest carbon intensity, suggesting reductions in CO₂ emissions from 48% (compared to conventional wood pellet boilers) up to 96% (compared to conventional oil boilers). TDHPs are, therefore, highly promising since they compete with conventional heating systems regarding operating cost and CO₂ emissions reductions.

¹¹<https://www.viessmann.ch/fr/services/liste-de-prix.html>

¹²<http://www.origen.ie/page/price-lists/26>

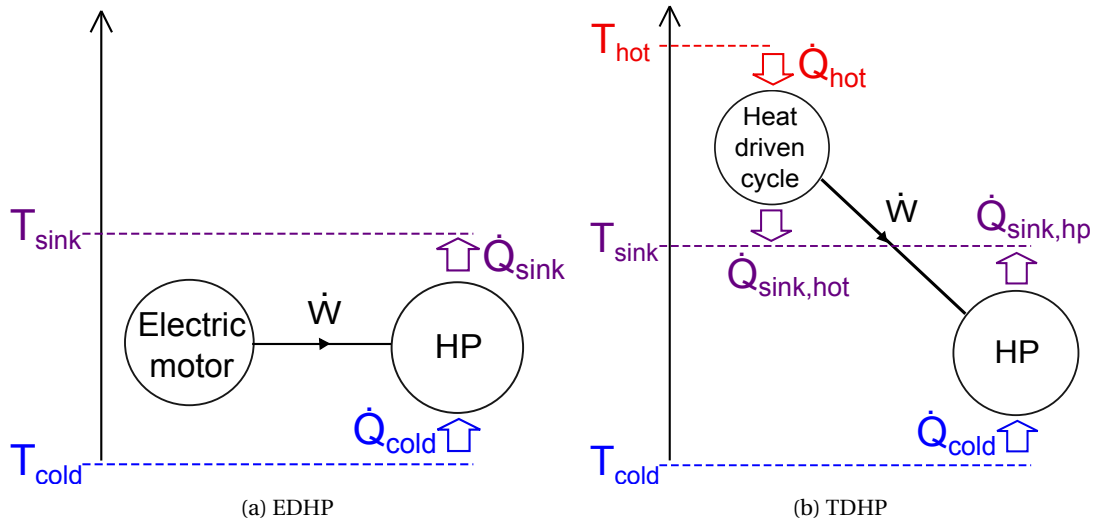


Figure 1.2 – Working principle of a EDHP (a) and a TDHP (b)

1.2 State of the art on Thermally Driven Heat Pumps (TDHPs)

The principle of TDHPs is shown in Figure 1.2 (right), as opposed to EDHPs (left). EDHPs upgrade the heating power absorbed from the environment \dot{Q}_{cold} at low temperature T_{cold} into a heating capacity \dot{Q}_{sink} at medium temperature T_{sink} . This compression step is driven by the power \dot{W} provided by an electric motor. TDHPs operate at three temperature levels. The heating power \dot{Q}_{hot} is supplied at high temperature T_{hot} into a heat driven cycle which releases a heating capacity $\dot{Q}_{sink,hot}$ at medium temperature T_{sink} . The heat driven cycle provides the compression power \dot{W} required to upgrade the heating power \dot{Q}_{cold} into $\dot{Q}_{sink,hp}$. The useful heat $\dot{Q}_{sink} = \dot{Q}_{sink,hp} + \dot{Q}_{sink,hot}$ is recovered in heating mode. TDHPs are capable of running either in cooling or heating mode.

1.2. State of the art on Thermally Driven Heat Pumps (TDHPs)

The performance of TDHPs is in practice measured by the Coefficient of Performance (COP) defined in equation 1.2 in heating mode and in equation 1.3 in cooling mode. For almost all types of TDHPs, electrical power \dot{W}_{el} is required to drive the pump(s) and other auxiliaries. In order to account for the primary energy consumption, \dot{W}_{el} is divided by 0.56, which corresponds to the conversion efficiency of modern combined gas power plants [2].

$$COP_{heat} = \frac{\dot{Q}_{sink}}{\dot{Q}_{hot} + \frac{\dot{W}_{el}}{0.56}} \quad (1.2)$$

$$COP_{cool} = \frac{\dot{Q}_{cold}}{\dot{Q}_{hot} + \frac{\dot{W}_{el}}{0.56}} \quad (1.3)$$

However, it is challenging to compare the COP from one TDHP technology to the other since their efficiencies strongly depend on their temperature levels. A thermodynamically more coherent metric is the evaluation of the exergetic efficiency, which enables to compare TDHP systems operating at different temperatures while assessing the thermodynamic quality of the system. The exergetic efficiency rates the maximum work output available from a heat source i providing a heating power \dot{Q}_i through a reversible cycle operating between the temperatures of the heat source T_i and the ambient T_a [3]. The exergetic efficiency η_{exe} is described by equation 1.4 for a TDHP in heating mode. It compares the exergy output $\dot{E}x_{sink}$ towards the exergy input $\dot{E}x_{hot}$ and the electrical power \dot{W}_{el} required to drive the cycle (pump(s) and other auxiliaries). The exergy $\dot{E}x_i$ corresponding to a heating power \dot{Q}_i is defined in equation 1.5.

$$\eta_{exe} = \frac{\dot{E}x_{sink}}{\dot{E}x_{hot} + \frac{\dot{W}_{el}}{0.56}} \quad (1.4)$$

$$\dot{E}x_i = \int_{in}^{out} \left(1 - \frac{T_a}{T_i} \right) \delta \dot{Q}_i = \left(1 - T_a \frac{\log \frac{T_{i,out}}{T_{i,in}}}{T_{i,out} - T_{i,in}} \right) \dot{Q}_i \quad (1.5)$$

The working principle of TDHPs consists in using the thermodynamic potential of a heat source to perform the compression power \dot{W} required to upgrade free heating power from the environment (Figure 1.2). The compression can be realized through three main mechanisms: (1) Thermal compression such as in sorption technologies, (2) kinetic energy driven compression such as in ejector systems, and (3) mechanical compression. In the following section, different TDHP concepts based on the compression mechanisms mentioned above are presented. The concepts are focused on domestic heating applications in the 40 kW power range, corresponding to a multi-dwelling residential building.

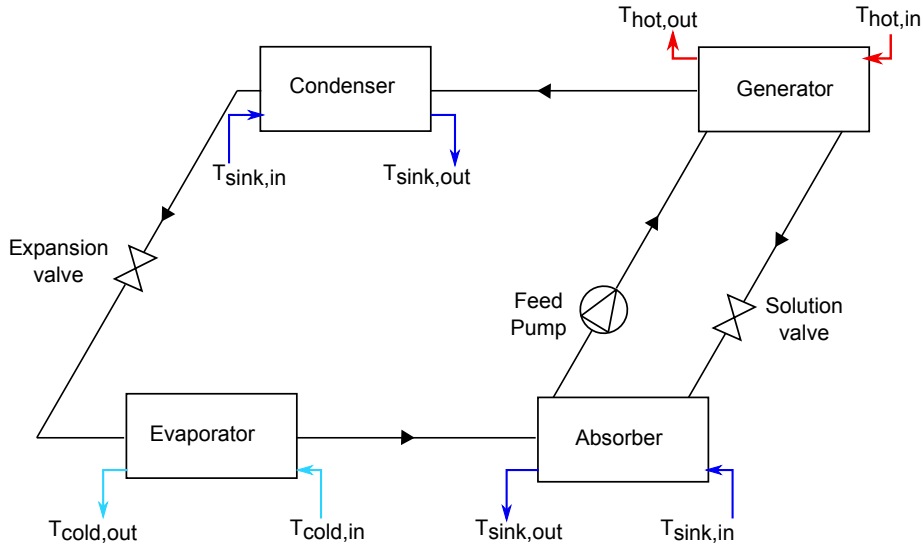


Figure 1.3 – Schematic layout of an Absorption Heat Pump (AHP) and its main components

1.2.1 Sorption technologies

For TDHPs the literature and the industrial market usually refer to sorption technologies, and particularly Absorption Heat Pumps (AHPs), which are represented in Figure 1.3. The working principle of a AHP is similar to a vapor compression heat pump since it uses a refrigerant that is evaporated at low pressure and condensed at high pressure, at the difference that no mechanical vapor compression is involved. The compression is made in three steps: First, the refrigerant is absorbed in a liquid sorption medium or absorbent at low pressure. The refrigerant-absorbent solution is then pumped to the high pressure level. Finally, the refrigerant is separated from the sorption medium (or desorbed) at high pressure in the generator (or desorber) by mean of heat addition. It is referred as a thermal compression mechanism. AHPs are free from the inherent problems due to rotating parts (wear, lubrication, and maintenance) but are unable to perform electrical power generation (cogeneration).

The selection of the working fluid pair is a key parameter for AHPs. Several working fluids are proposed in literature [4], but the most widely used refrigerant/absorbent pairs are water-lithium bromide ($\text{H}_2\text{O}-\text{LiBr}$) and ammonia-water ($\text{NH}_3-\text{H}_2\text{O}$). The ($\text{H}_2\text{O}-\text{LiBr}$) refrigerant pair is attractive for its low cost, high chemical stability, and its high environmental compatibility. Its application is, however, limited due to inherent challenges related to refrigerant freezing and solution crystallization, confining their use to low temperature lifts and high evaporating temperatures. In contrast, the ammonia-water ($\text{NH}_3-\text{H}_2\text{O}$) pair does not crystallize or freeze even at temperatures below -40°C . The latter can, therefore, be used for both cooling and heating applications within a wide operational range [5, 6]. The efficiency of AHPs can be further improved by the addition of generators (number of effects) or evaporator/absorber pairs (number of stages). Nevertheless, the efficiency increase comes with the penalty of additional cost and system complexity [7].

1.2. State of the art on Thermally Driven Heat Pumps (TDHPs)

Nowadays, AHP products operating with (NH₃-H₂O) are launched in the low to mid capacity range (between 5 kW and 50 kW) for applications such as residential heat pumps or chillers driven by solar or waste heat [8]. Manufacturers such as Robur¹³ and Bosch¹⁴ provide absorption systems for residential applications with heating capacities around 40 kW and nominal COPs in heating mode of 1.65 (air source at 7°C for heating water at 35°C). However, this technology is penalized by the selection of its refrigerant pair. The toxicity of ammonia on the environment [9] and health [10, 11], as well as its flammability and corrosion hazard, lead to the necessity of having additional safety measures and more complex maintenance.

More recently, new working fluid pairs have been investigated to overcome the safety issues of ammonia, for example by replacing the refrigerants or the absorbents by ionic liquids [12]. Ionic liquids are salts which are in the liquid state at near or below room temperature. They are appreciated for their unique properties, such as negligible vapor pressure, non-flammability, thermal stability, and good solubility. AHPs with ionic liquid pairs have, however, not reached the market yet.

Other sorption systems are adsorption heat pumps. In principle, they are similar to AHPs, mainly by presenting the same heat exchanger network configuration. They differ, however, by having the refrigerant adsorbed in the pores of a solid material instead of a liquid medium. Hence, adsorption heat pumps operate discontinuously. On the contrary to liquid absorbents, which are continuously pumped from the absorber to the desorber, the solid adsorbent cannot be moved quickly between the two heat transfer units. It leads to phases where the adsorbent must be regenerated, which decreases the heating/cooling production and hence depreciates the efficiency of the cycle [13]. Nonetheless, these systems are now reconsidered as they operate without moving components and offer a higher power density than AHPs in the 10 kW range [13]. Recently, heating system manufacturers Viessmann and Vaillant have developed a first commercial adsorption heat pump with a heating capacity between 1.8 and 11 kW^{15 16}. This product is, however, not yet available on the market.

1.2.2 Ejectors

Ejector Refrigeration Systems (ERS) are TDHPs operating at three levels of temperature and are currently investigated for cooling and heating capacities ranging from 0.5 [14] to 36 kW [15]. As shown in Figure 1.4, ERS are composed of an evaporator, a condenser, a generator, and an ejector. In the ejector, the high pressure fluid leaving the generator expands and accelerates through a supersonic nozzle placed in a suction chamber. The high-velocity fluid drives the low pressure fluid coming from the evaporator, before the two streams mix and condense.

¹³<http://www.robur.com/>

¹⁴<https://www.bosch-industrial.co.uk/products/renewables-range/ghpawo38.html>

¹⁵<http://trends.archiexpo.com/viessmann/project-789-224262.html>

¹⁶<http://www.bine.info/fileadmin/content/Publikationen/Projekt-Infos.html>

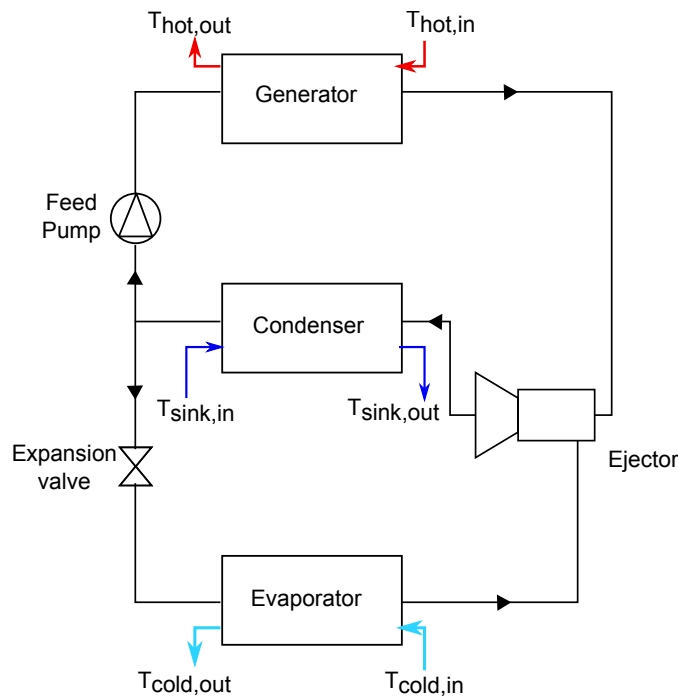


Figure 1.4 – Schematic layout of an Ejector Refrigeration System (ERS) and its main components

At the condenser exit, a fraction of the liquid refrigerant is expanded to the evaporator through a valve, and the other fraction is pumped to the generator. ERS are advantageous since they are not using any moving mechanical parts while having a high power density. However, the performance of ERS is low compared to conventional heating systems [16]. Various attempts have been made to enhance the performance of ERS by optimizing geometry features such as the nozzle area ratio and nozzle exit position. Nonetheless, since the optimum geometry features are strongly dependent on the operating conditions [16], ERS have difficulties to operate appropriately at off-design conditions. ERS configurations with additional jet pumps [17] or multi-stage evaporators [18] are proposed to adapt better to the nominal conditions. Yet, one of the most promising applications of ERS is when they are combined with conventional refrigeration systems with the goal of enhancing their efficiency. Sözen et al. [19] presented the combination of an ERS with a solar driven AHP, in which an ejector located between the absorber and the evaporator enabled COP improvements up to 20%. Similarly, as proposed by Sokolov et al. [20] and Zhu et al. [21], ERS increase the performance of vapor compression refrigeration cycles by taking over a part of the required pressure rise. While ERS are now triggering the interest of manufacturers such as DENSO¹⁷, they remain scarcely available on the market.

¹⁷<http://www.globaldenso.com/en/newsreleases/090519-01.html>

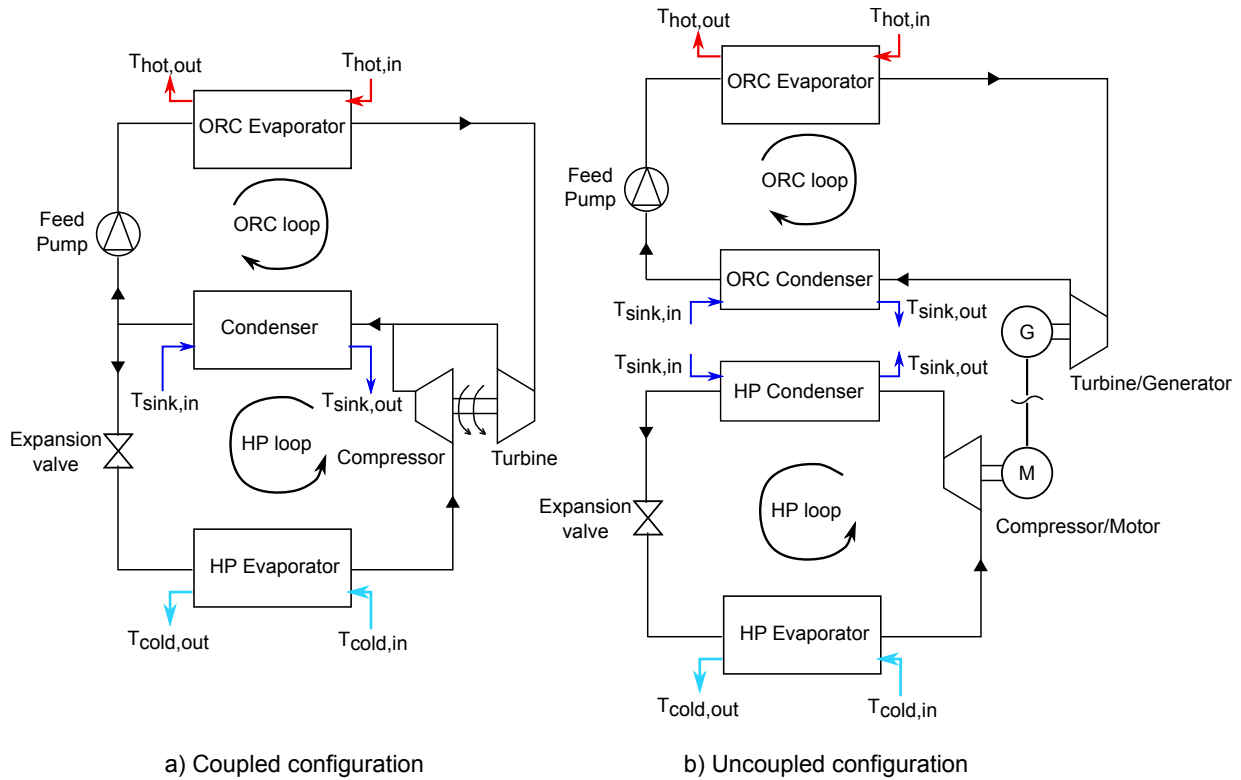


Figure 1.6 – Schematic layout of a HP-ORC and its main components in its (a) coupled and (b) uncoupled configuration

1.2.4 ORC driven Heat Pumps

An alternative TDHP technology consists in the combination of a power cycle to drive a vapor compression Heat Pump (HP), such as the Organic Rankine Cycle (ORC) driven Heat Pumps (HP-ORC). This technology is very similar to GEHPs, at the difference that the HP loop is driven by an ORC, as shown in Figure 1.6a, in which the turbine of the ORC drives the compressor of the HP directly. This technology is the main focus of this thesis. In the primary configuration presented here, the turbine and compressor are supported on the same shaft. In addition, the two cycles share the same condenser, and hence the same working fluid, offering a compact solution. Moreover, driving the vapor compression cycle with an ORC allows the use of low grade energy sources, such as biomass, waste heat or solar thermal, while having the possibility of providing cogeneration. For heating purposes, the HP-ORC systems have, therefore, a significant advantage compared to cogenerating ORC systems since they offer higher efficiencies while enabling trigeneration (electricity, heating, and cooling).

Another possible HP-ORC configuration consists in dissociating the ORC and HP loops, connecting them through an electrical transmission as shown in Figure 1.6b. Since the working fluid can be chosen independently in each loop, this configuration offers higher design and operational flexibility. Nonetheless, due to the presence of additional components (power conversion units and condensers), higher investment costs may be encountered.

1.2. State of the art on Thermally Driven Heat Pumps (TDHPs)

Table 1.2 – ORC driven Heat Pump (HP-ORC) concepts in literature

Type		COP	Application	T_{sink}	T_{cold}	T_{hot}	Reference
		-	-	[°C]	[°C]	[°C]	
Coupled	Experimental	1.17	Heating[12kW]	4	57	229	Strong [24]
	Experimental	1.6	Heating[100kW]	12	27	145	Biancardi [25]
	Theoretical	1.32	Cooling[N.A.]	10	45	100	Kaushik [26]
	Theoretical	1.55	Cooling[N.A.]	7	38	300	Jeong [27]
	Theoretical	0.47	Cooling[N.A.]	5	40	80	Aphornratana [28]
	Theoretical	0.4	Cooling [N.A.]	5	40	80	Li [29]
	Experimental	1.48	Heating[40kW]	5	35	100	Demierre [30]
Uncoupled	Experimental	0.5	Cooling[N.A.]	35	7.2	102	Prigmore [31]
	Theoretical	1.5	Heating[5kW]	24	67	190	Wang [32]

Table 1.2 summarized the different concepts of HP-ORC existing in literature. The concept has been first investigated by Prigmore et al. [31], with the testing of a solar driven residential air conditioning system prototype, operating with R113a and R22 in the ORC and HP loop, respectively. They measured a cooling COP of 0.5, which in 1975, was competing with absorption cycles. Later, Strong [24] designed a domestic HP-ORC using R114 in the two loops. The system used a CTU composed of a radial inflow turbine coupled to a single-stage centrifugal compressor rotating on gas bearings. Strong has achieved a measured heating COP of 1.17 for a heating output of 12.3 kW, condensing temperature of 57°C, HP evaporation temperature of 4°C, and rotational speeds up to 164 krpm. Unfortunately, issues with gas bearings have resulted in limited experimental data. Biancardi et al. [25] have tested a similar concept with a 100 kW solar driven HP-ORC, achieving heating COPs ranging from 1.4 to 2.5, with condensing temperatures up to 66°C and HP evaporation temperatures of 20°C, at the difference that rolling element bearings could be used.

Later, Kaushik et al. [26] performed theoretical studies on vapor compression systems driven by steam Rankine cycles. They tested various heat integration solutions and showed that implementing regenerative heat exchangers allowed to improve the efficiency significantly. Jeong et al. [27] investigated a HP-ORC in which the ORC expander and HP compressor are coupled on the same shaft, leading to more compact solutions with fewer design issues regarding sealing. They have shown that R123 achieved the highest theoretical efficiency when used in both thermal loops. Li et al. [29] investigated HP-ORCs running with natural refrigerants for their lower GWP (Global Warming Potential) than conventional working fluids, showing that R600 (n-butane) was the most promising one. Aphornratana et al. [28] proposed a HP-ORC system using a linear piston compressor/expander, allowing the system to operate with hot sources as low as 60°C. They showed that R22 resulted in higher COP than R134a and that the area ratio between the expander and the compressor pistons is critical to optimize the system performance. Wang et al. [32] investigated a 5 kW HP-ORC powered by renewable fuels reaching a theoretical cooling COP of 0.66, with condenser air temperature of 67°C and evaporator air temperature of 24°C. In their system, the ORC scroll expander drives a power generation unit that is used to drive the HP scroll compressor.

Chapter 1. Introduction

More recently, Demierre et al. [30] presented a 40 kW HP-ORC using a gas bearing supported Compressor Turbine Unit (CTU) running on R134a. Their system is similar to the one developed by Strong [24], avoiding, however, gas bearing issues as a result of a better choice of rotor and bearings material, hence limiting the risk of high-speed rotor seizures. They measured a heating COP of 1.48 with a condensing temperature of 35°C and HP evaporation temperature of 5°C, with rotor speeds up to 200 krpm. This prototype showed encouraging results for the technology, which combines high power density, high efficiency, and oil-free operation.

1.2.5 Summary

Different TDHP (Thermally Driven Heat Pump) concepts have been presented. The ORC driven Heat Pump (HP-ORC) is the target technology of this thesis and is qualitatively compared to the other TDHP concepts in Table 1.3. Domestic heating applications in the 40 kW power range are considered. The comparison criteria are performance, ability to perform cogeneration, the flexibility on the heat source selection (low grade and renewable), and the maturity of the technology.

All TDHP technologies yield similar performance, apart from the ejectors which are significantly lower. On the contrary to GEHPs (Gas Engine driven Heat Pumps), which are restricted to gas and liquid fossil fuels, the other TDHP technologies have a broader choice in the selection of their heat source, which can be renewable and at low temperature. Nonetheless, HP-ORCs are usually more limited by the heat source since they require a sufficient temperature at the turbine inlet to avoid liquid droplets, which may lead to premature wear and suboptimal operation. Furthermore, only HP-ORCs and GEHPs can provide cogeneration, giving them a considerable advantage compared to AHPs (Absorption Heat Pumps) and ejectors. Although they are still in the prototype phase, HP-ORCs are highly promising since they offer similar performance compared to AHPs and GEHPs while having flexibility on the heat source and being able of providing electricity.

Table 1.3 – Summary of the different TDHP concepts: 1 = Suitable/Good, 0.5 = Suitable/Poor, 0 = Not applicable

	Performance	Cogeneration	Low grade sources	Renewable sources	Market maturity	Total score
HP-ORCs	1	1	0.5	1	0.5	4
GEHPs	1	1	0	0	1	3
AHPs	1	0	1	1	1	4
Ejectors	0.5	0	1	1	0.5	3

1.3 HP-ORC based on gas bearing supported turbomachinery

The principle of the HP-ORC is explained in Figure 1.6. The system is composed primarily of heat exchangers units (HP/ORC evaporators and condenser(s)), a Compressor Turbine Unit (CTU), a pump, an expansion valve, and external sources (heat source at the ORC evaporator, cold source at the HP evaporator, and the heat sink at the condenser). The following section details the characteristics and main features of these components, except for the expansion valve, which is the same as in conventional electrically driven heat pumps.

1.3.1 External sources

The HP-ORC heat source can be fossil-based, biomass-based (wood), solar thermal or waste heat from a cogeneration unit, fuel cell or industrial process. The medium type for the sink and the cold source is either brine/water or air. Brine/water systems, such as in the Ground Source Heat Pumps (GSHPs), are commonly more efficient due to the higher heat transfer coefficient of water and brine compared to air. Moreover, when the considered cold source is air, the seasonal HP efficiency is significantly reduced in Winter due to the variation of the outside air temperature. GSHPs are, however, more expensive since they require the drilling of a ground heat exchanger.

1.3.2 Heat exchangers

In residential heat pumps, most of the heat exchangers are Plate Heat Exchangers (PHEs) for their high efficiency, low cost, and high compactness [33]. In ORC systems, PHEs are also widely used for the same reasons²⁰. However, when high pressures are combined with high temperatures, such as in the ORC evaporator, PHEs can be challenging on both safety and lifetime considerations due to high mechanical and thermal stress^{21 22}. To address these issues, the alternative for the HX selection is the shell tube or double tube coil type [33]. These two technologies have, however, increased cost, size, and mass [34]. PHEs are thus preferred, provided sufficient material resistance.

1.3.3 Compressor Turbine Unit

The HP-ORC is based on the combination of an ORC and HP cycle, in which the ORC expander drives the HP compressor directly. The proper selection of the expander and the compressor technology is, therefore, essential. In this thesis, a gas bearing supported Compressor Turbine Unit (CTU) is considered. It is composed of a radial inflow turbine and a centrifugal compressor which are integrated on the same shaft [35]. The shaft is supported on two radial bearings and one axial bearing.

²⁰<https://www.swep.net/applications/case-stories/clean-power-when-orc-system-recovers-waste-heat/>

²¹<https://www.swep.net/solutions/co2/>

²²<https://www.swep.net/products/b18/>

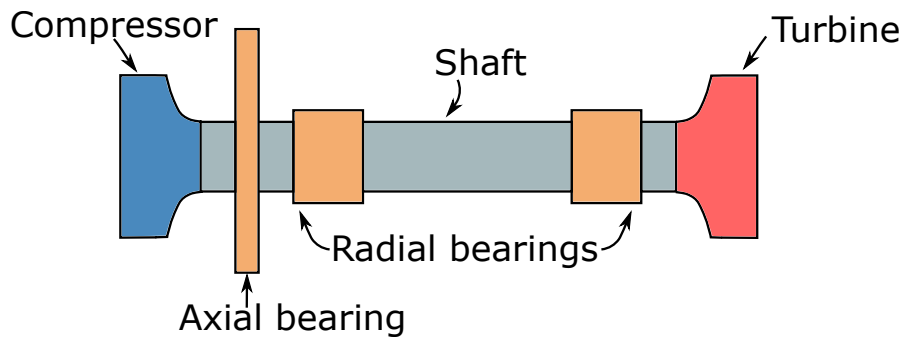


Figure 1.7 – Schematic of the HP-ORC CTU

Figure 1.7 shows the schematic of the system. The following section explains why these technological features have been chosen.

Expander/Compressor selection

Currently, small capacity ORC and HP cycles are predominantly using volumetric expander and compressor technologies, which are mainly scroll, screw, and reciprocating machines [36,37]. These systems are praised for their low cost, high robustness, and reliability. However, the disadvantage of such expansion and compression devices is that they require oil for lubricating the moving parts and for sealing purposes. Zehnder [38] showed that oil from the compressor is likely to migrate through the cycle. If the oil supply is ill-managed, the loss of lubrication in the compression unit could ultimately lead to the system seizure. Furthermore, the heat exchanger efficiency decreases due to the oil pollution. The latter effect is due to the thermodynamic properties differences between oil and organic working fluid regarding the evaporation temperature and viscosity, which implies decreasing heat transfer coefficients and increasing pressure losses [39, 40].

The use of dynamic machines is, therefore, a promising way of increasing efficiency. Indeed, their operating principles do not involve parts sliding against each other, except for bearings, where contact-less technologies such as magnetic bearings or gas bearings can be used. Moreover, dynamic machines offer higher power density and higher theoretical efficiencies compared to volumetric machines, which are limited by their volume ratio capacity, and hence see their performance depreciated at off-design conditions [41]. Nonetheless, for low power applications, dynamic machines tend to be small-sized and need to run at very high speed, which increases the design complexity [42]. Recent developments in small-scale oil-free dynamic centrifugal compressors [43] and radial inflow turbines [35] integrated into vapor compression heat pumps and ORCs demonstrated that isentropic efficiencies up to 80% with pressure ratios of 3 and 4.5 could be reached. These systems are supported on gas lubricated bearings, which allows operating without oil lubrication.

Bearing selection

An essential technical constraint of the compression/expansion device lies in the selection of proper bearings, which depends on the expected system lifetime, maintenance, rotational speed ranges, and radial loads. Rolling Element Bearings (REBs) are widely used to support volumetric machines, such as scroll compressors and screw expanders. REBs are, however, generally not suitable for supporting dynamic machines that run at much higher rotor speeds than volumetric ones. Moreover, REBs operate at the condition of being continuously lubricated, implying oil pollution in the thermal cycle. The alternative is to implement contact-less technologies such as Active Magnetic Bearings (AMBs) or Fluid Film Bearings (FFBs). Since they allow operating oil-free, contact-less bearings ensure a theoretically infinite lifetime and thus a zero-maintenance. AMBs present large load capacity and stability owing this to their active control system but are, however, bulky and expensive. FFBs are categorized as externally pressurized and as dynamic self-acting bearings. Since externally pressurized bearings rely on a constant supply of pressurized fluid to carry the load, they are not appealing for energy conversion applications. One of the most used dynamic self-acting FFBs are Herringbone Grooved Journal Bearings (HGJBs) for their lower cross-coupled stiffness and high viscous damping, and hence enhanced stability compared to plain bearings [44, 45]. HGJBs have been selected for this thesis work.

1.3.4 Pump

The selection of a suitable ORC pump technology is challenging. The chosen pump must deliver the required mass flow and pressure difference while ensuring an oil-free environment, which is one of the key arguments of using a gas bearing supported CTU. Very few pump data are available, on the market and in literature, in the regions where small capacity ORCs are operating, which are defined by low volumetric flow rates and high pressure ratios [41]. The most widespread liquid pump technologies are the diaphragm, the centrifugal, and the piston pumps. The diaphragm pumps, which are activated by piston compressed oil, are robust and can achieve high pressure differences but can pollute the cycle. The centrifugal pumps are less likely to contaminate the system with oil but need many stages to achieve high pressure differences, thus increasing the cost and the size of the system. Piston pumps, which are widely used in the water-pumping industry, are a promising alternative, provided that they can achieve sufficient hydraulic lubrication with the working fluid without the use of oil.

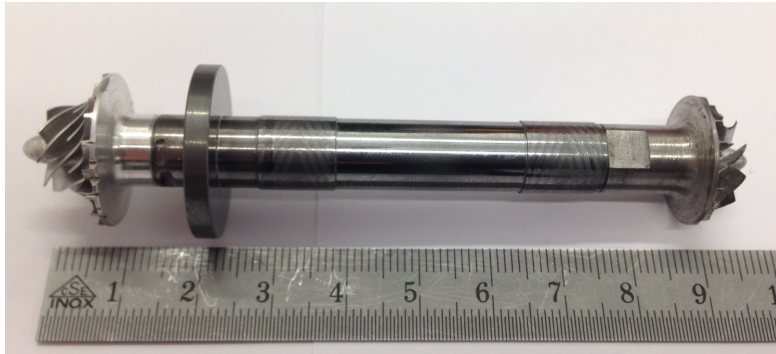


Figure 1.8 – Picture of the CTU including the centrifugal compressor (left), the shaft and bearings (center), and the radial turbine (right)

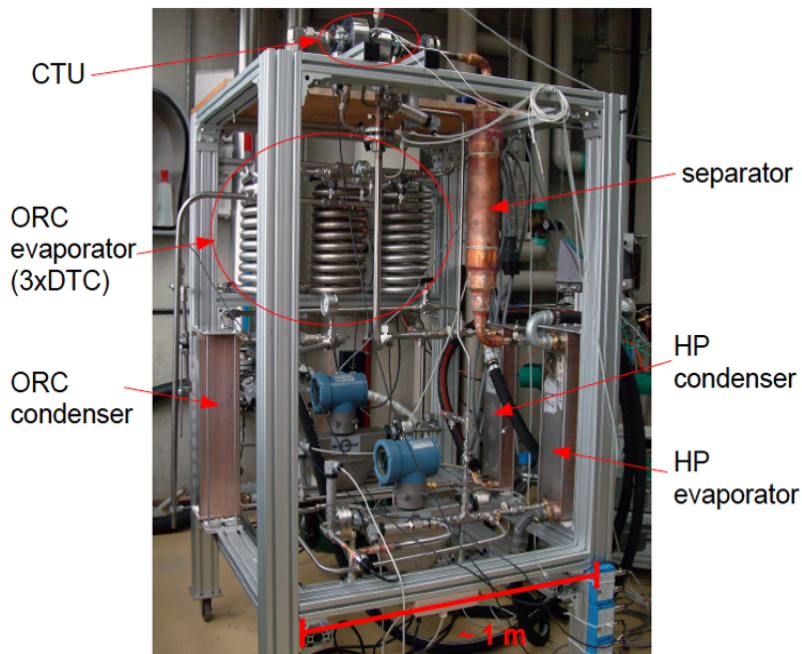


Figure 1.9 – Picture of the HP-ORC prototype as tested by Demierre et al. [30]

1.4 Experimental proof of concept

A first prototype of a HP-ORC operating with a small-scale gas bearing supported CTU (Compressor Turbine Unit) has been designed and tested by Demierre et al. [2, 35]. The CTU is composed of an 18 mm radial inflow turbine made of steel, coupled to a 20 mm centrifugal compressor made of aluminum. The compressor and turbine are connected through a gas bearing supported shaft made of Tungsten Carbide. Figure 1.8 shows a picture of the current CTU, with the compressor on the left and the turbine on the right. This CTU design is based on a domestic HP compressor investigated and tested by Schiffmann [46], on which a radial turbine has been adapted to replace the compressor motor.

Figure 1.9 shows a picture of the first version of the HP-ORC prototype. The unit was tested with R134a for different operating conditions including HP evaporation temperatures, condensing temperatures, and ORC evaporation temperatures. Two condensers have been implemented instead of a single one to have more operational flexibility between the ORC and HP loops. The ORC evaporator is composed of three Double Tube Coil (DTC) heat exchangers in parallel, heated up by thermal oil Syltherm XLT. The HP evaporator and condensers are Plate Heat Exchangers (PHEs), supplied by cooling water. The highest performance has been achieved at a COP in heating mode of 1.58, with an HP evaporation temperature of 20°C, an ORC evaporation temperature of 100°C, a condensing temperature of 36°C, a rotational speed of 147 krpm, and turbomachinery efficiencies up to 70% [35]. These results suggest a promising preliminary test phase since they consist in the first proof of concept for HP-ORCs based on gas bearing supported turbomachinery.

However, several issues have been encountered during the experimental investigation.

- The refrigerant was not entirely evaporated at higher mass flow rates in the ORC evaporator. The three DTCs have then been installed in series rather than in parallel.
- The current ORC evaporator design is undersized since the system could not provide temperatures above 120°C at the turbine inlet.
- High leakage rates have been encountered in the CTU, from the turbine inlet (90 to 120°C) to the compressor outlet (35 to 45 °C). This leakage rate has been estimated at 15% of the turbine mass flow rate through an energy balance around the bearing cavity [35].
- In addition to the mechanical power loss triggered by the fluid leakage, thermal leakages have most likely been encountered [35]. Indeed, the preliminary results showed that the compressor isentropic efficiency was lower than the 1D model prediction and than the results achieved with the same compressor driven by an electrical motor [43].
- The mass flow measurement was missing in the HP loop due to a limited sub-cooling after the HP condenser.
- The turbine was adapted to a centrifugal compressor previously designed by Schiffmann [47]. An adequate integrated CTU design is currently missing, suggesting a certain potential to improve the CTU performance.

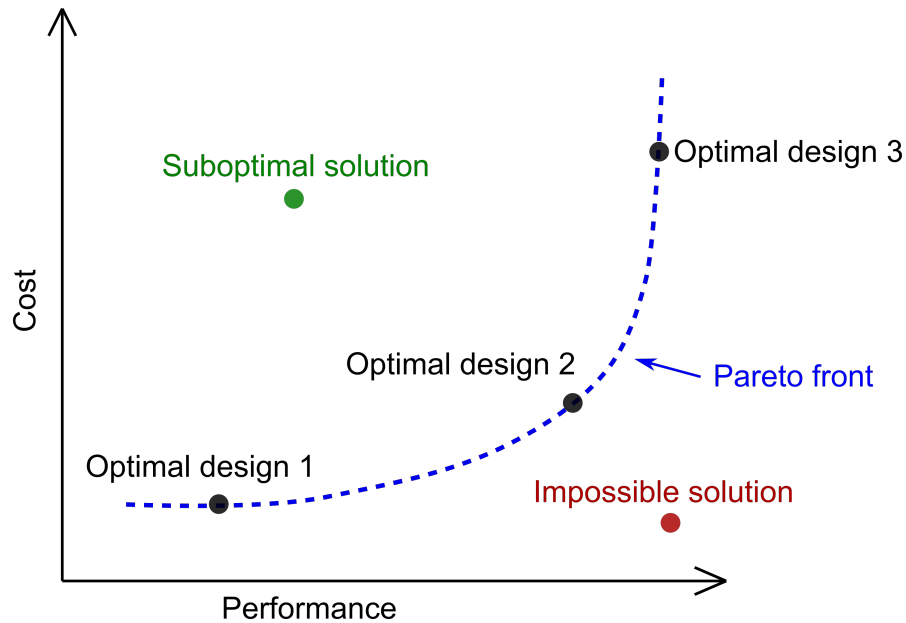


Figure 1.10 – Pareto front of a two-objective optimization

1.5 Optimization and design of complex energy systems

The optimization of energy and mechanical systems is complex. Such problems usually have more than one objective to satisfy and are so-called Multi-Objective Optimization (MOO) problems. The optimum solutions are located on a Pareto frontier, which represents the solutions offering the best trade-off between the considered competitive objectives. An example of a typical Pareto front is depicted in Figure 1.10, in which the two conflicting objectives cost and performance are minimized and maximized, respectively. Furthermore, the optimization of energy and mechanical systems deals with models presenting different local optima and regions where no solution is possible due to physical constraints (compressor surging, bearing seizure, fluid decomposition due to too high temperatures,...). Moreover, mechanical design problems are often characterized by a large number of decision variables.

Evolutionary algorithms such as the Queuing Multi-Objective Optimization (QMOO) developed by Leyland are well-indicated for performing the integrated design optimization of such systems [48, 49]. Starting from a random population of solutions, QMOO converges towards the optimum Pareto frontier by applying individual selection inspired from biologic evolution, such as recombination, crossover, and mutation, while continuously removing individuals that do not fit at best the two objectives. These algorithms allow finding the best trade-off between conflicting objectives while exploring the whole design space.

The HP-ORC based on gas bearing supported turbomachinery is a highly complex system (various components such as heat exchangers, dynamic turbomachinery, and self-acting gas bearings) that is characterized by conflicting objectives of performance, cost, and feasibility. Since the integrated design optimization of the technology is currently missing, QMOO has

been used in this thesis work for providing optimum integrated designs, and hence, for assessing the potential of the system.

The drawback of evolutionary algorithms, such as QMOO applied to such complex problems as HP-ORCs, is that a large number of function evaluations to obtain satisfactory convergence is required. Therefore, the models that are implemented for the different HP-ORC components need to be accurate and of reduced order to mitigate the evaluation computation time.

1.6 Objectives and structure of the thesis

The goal of this thesis is to answer the following question: What are the potential and challenges of the ORC driven Heat Pump concept (HP-ORC) based on gas bearing supported turbomachinery?

The work is divided into four chapters in which the specific objectives are presented as follows. Figure 1.11 represents a graphical summary of the thesis structure.

Chapter 2: Pre-design models for small-scale radial turbomachinery

Accurate and reliable reduced order models for the various system components are highly beneficial for improving the automated design process. Such models are, however, currently missing for small-scale radial turbomachinery. Hence, updated reduced order models for small-scale radial inflow turbines and centrifugal compressors are developed in a first step. The objectives of chapter 2 are:

1. Updated 0D turbomachinery models allowing a quick and accurate pre-design phase
2. Insights into the aerodynamic phenomena that govern the turbomachinery performance
3. Identified dimensions that have a major role in the design of small-scale turbomachinery

Chapter 3: Integrated design optimization of the Compressor Turbine Unit

Using the turbomachinery pre-design models developed in chapter 2, the integrated design optimization of the CTU is performed in this third chapter. The objectives of chapter 3 are:

1. The predicted stability/performance gain obtained by using integrated design optimization procedures compared to the proof of concept prototype
2. Design guidelines for small-scale gas bearing supported turbomachinery
3. Insights into the robustness of gas bearing supported turbomachinery regarding off-design effects, fluid leakage, tip clearances, and manufacturing errors

Chapter 1. Introduction

Chapter 4: Integrated design optimization of the HP-ORC cycle

Chapter 4 deals with the thermo-economic optimization of the HP-ORC cycle, including the design of the small-scale turbomachinery based on the reduced order models presented in chapter 2. The objectives are:

1. Thermo-economic optimum cycle design solutions of the HP-ORC
2. The potential of the technology towards other TDHPs such as Absorption Heat Pumps
3. The predicted cost/performance gain provided by the optimization procedure compared to the proof of concept cycle

Chapter 5: Application examples

In chapters 2 to 4, new reduced order models and optimization strategies are put in place for investigating the potential of the HP-ORC technology based on gas bearing supported turbomachinery. In chapter 5, all these tools are combined and applied to three application examples. The objectives of chapter 5 are:

1. Proven and efficient optimization procedure providing cycle and CTU designs with maximum performance, minimum investment cost, and proven feasibility
2. An assessment potential of the technology in domestic heating, agricultural greenhouse heating, and air conditioning of helicopter cabins

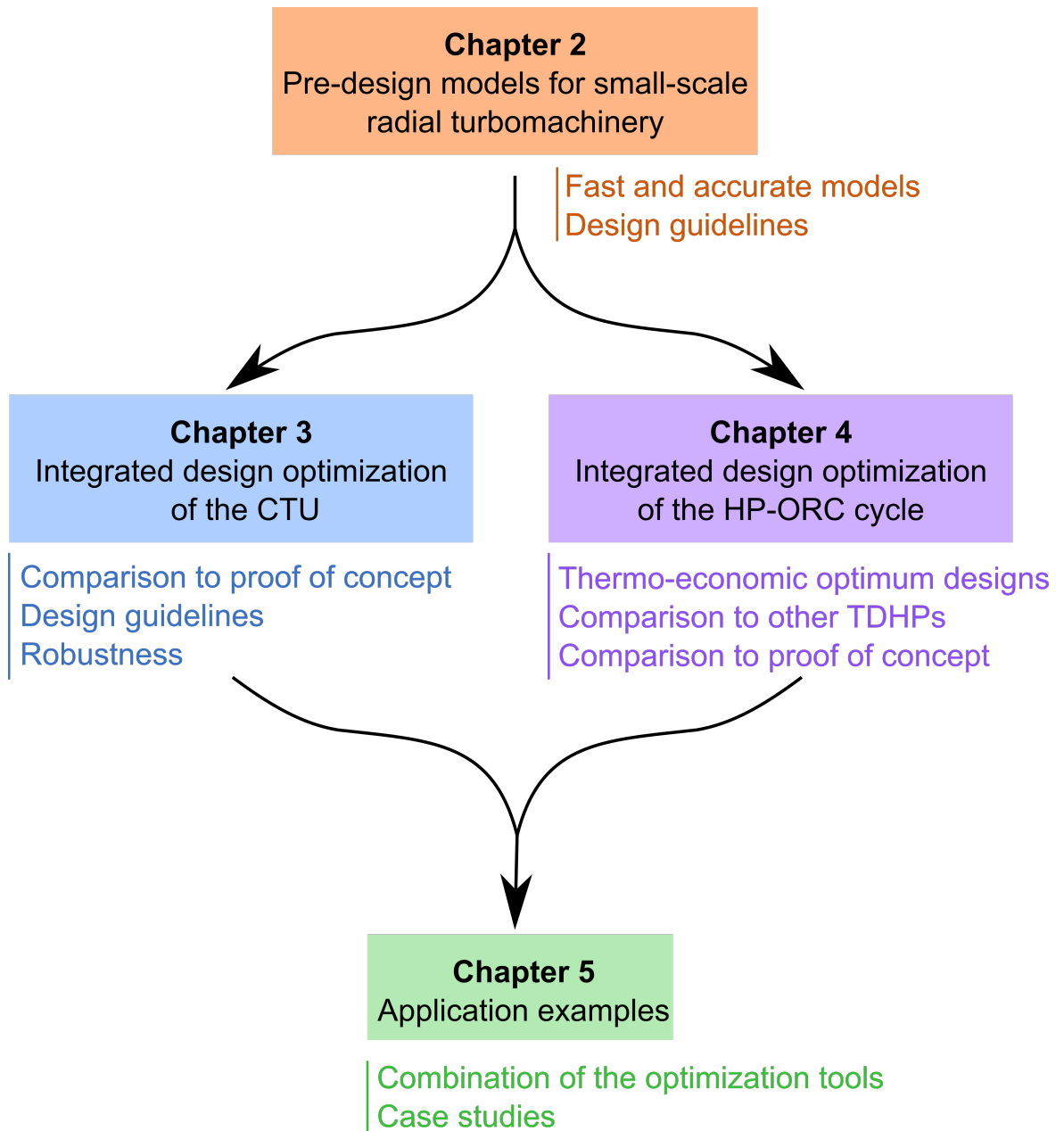


Figure 1.11 – Graphical summary of the thesis structure and objectives

2 Pre-design models for small-scale radial turbomachinery

This chapter aims at providing updated turbomachinery pre-design models since the ones available in literature are more and more challenged, in particular for small-scale systems operating with organic media.

The updated reduced order models for evaluating small-scale radial turbomachinery are obtained from the evaluation of experimentally validated 1D models, which are fed with a set of equally distributed thermodynamic and geometrical variables through a Monte Carlo simulation.

Section 2.5 presents an updated pre-design model for transonic radial inflow turbines. The efficiency contours are described by a polynomial function $\eta_{is} = f(Ns, Ds, PR)$, where Ns and Ds are the specific speed and diameter, and PR is the pressure ratio. The aerodynamic phenomena that are shaping the Ns - Ds contours are presented in section 2.5.4. A sensitivity analysis performed in section 2.5.5 identifies the key design variables and presents a comparison towards the current efficiency chart of Balje. Finally, an external validation of the turbine pre-design model is shown in section 2.5.6.

Section 2.6 carries out the same procedure for providing a pre-design model of centrifugal compressors. A model $\eta_{is} = f(Ns, PR, \zeta)$ is built, where $\zeta = \frac{b_4}{r_4}$ is the compressor blade height to tip radius ratio. An analysis of the phenomena shaping the efficiency contours of the pre-design model is presented in section 2.6.3. A sensitivity analysis of the updated compressor model and a comparison with existing literature are presented in sections 2.6.4 and 2.6.5. The influence of the working fluid and the model validation are discussed in sections 2.6.6 and 2.6.7.

In this chapter, the proposed turbomachinery pre-design models are indicated with the following terminologies, which are equivalent: Pre-design model, pre-design map, efficiency map, performance map, reduced order model, and 0D model.

By default, the isentropic efficiency η_{is} refers to the total-to-total isentropic efficiency.

Part of the work presented in this chapter has been published in:

- Mounier V., Olmedo L.E., Schiffmann J., *Small scale radial inflow turbine performance and pre-design maps for Organic Rankine Cycles*. Energy 2018
- Mounier V., Picard C., Schiffmann J., *Data-driven Updated Pre-design Tool for Small Scale Centrifugal Compressors In Refrigeration*. Turbo Expo: Power for Land, Sea, and Air, Oslo, 2018, accepted with journal recommendation

2.1 Introduction

Various authors have contributed to the optimization of ORC and HP cycles, mainly by investigating optimum working fluids towards a specific application [50–55]. Often, they do not include any design features of the compressor/expander and impose fixed isentropic efficiencies instead, regardless of the operating condition. Nonetheless, as shown recently by Mounier et al. [56], coupling the thermodynamic optimization with the ORC turbine/HP compressor preliminary design offers valuable insights into the trade-off mechanisms. In previous work by Demierre [2] and Schiffmann [47], 1D models have been built for radial inflow turbines and centrifugal compressors and both validated with experimental data. The motivations behind these 1D simulation tools were to provide optimal and accurate turbomachinery solutions when integrated into complex thermodynamic simulations. Although the 1D evaluation is much faster than the other design steps such as the 2D or 3D approach, its computation time may remain too large when embodied in integrated design optimizations. An alternative is to use a 0D model, or a pre-design model, usually based on polynomial functions, and hence orders of magnitude faster. In literature, the most widely used pre-design methods are the performance maps proposed by Balje [57] and Cordier [58], which are both based on similarity concepts. These design charts were obtained assuming air as a working fluid and applied to large-scale applications. As a consequence, these pre-design models are more and more challenged since they are most likely not suitable for small-scale turbomachinery operating with organic working fluids. The goal of this chapter is to propose newly tailored pre-design (or 0D) models for radial turbines and centrifugal compressors, generated through experimentally validated 1D models. These models will be used in the following chapters of the thesis to tackle the optimization of the HP-ORC.

2.2 Small-scale turbomachinery: Terminology

In this chapter, updated reduced order models for small-scale radial turbomachinery are proposed. Literature usually refers as small-scale turbomachinery systems which have a shaft mechanical power in the range [100-10'000] W. In this thesis, small-scale is restricted to systems above 1 kW of shaft mechanical power, such as the one presented by Demierre et al. [35] (2 kW turbocompressor at 200 krpm) which is well adapted to domestic refrigeration applications. The Reynolds numbers for the [1-10] kW power range are in the order of $Re = 10^5$.

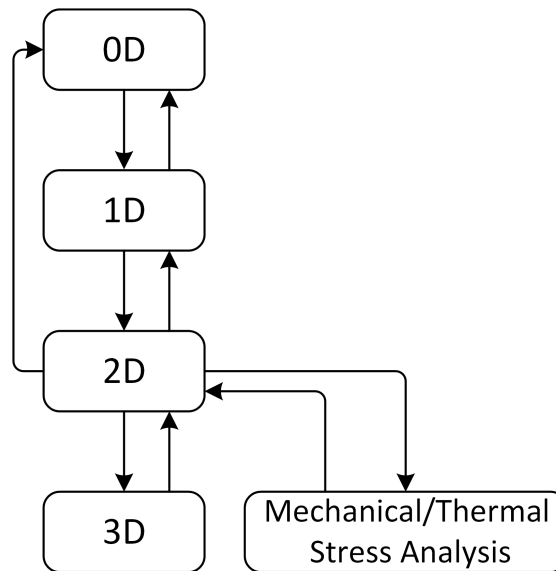


Figure 2.1 – Main steps of the turbomachinery design process

2.3 Classic design steps for turbomachinery

The turbomachinery design undergoes four major steps, each of them adding more geometrical details.

- **0D design** yields the overall scale of the compressor/turbine with a first estimation of the tip diameter, the rotor speed, and the efficiency. This step is based on performance maps and Cordier lines.
- **1D design** or mean-line design adds geometrical information on the inlet and the exhaust areas of the turbomachinery design and allows predicting operation maps and efficiency, based on loss correlations.
- **2D design** enables through-flow calculations, often based on the streamline curvature methodology, to define and tune the complete rotor blade geometry between the inlet and the exhaust. At this stage, the geometry of the turbomachinery is entirely determined, including channel passage and blade angles along the streamline.
- **3D design** allows analyzing and optimizing detailed flow patterns. The 3D design approach is the most accurate but also the most expensive in computational time, which makes it unpractical for integrated optimization procedures.

The typical turbomachinery design process summarized in Figure 2.1 is complex and highly iterative. Hence, the initial 0D pre-design stage has to be accurate since the better the initial guess, the faster the procedure converges to an optimal design.

The Cordier line [58] is commonly used for the pre-design of centrifugal compressors [59]. It is built from the analysis of existing centrifugal compressors and displays – in a specific speed N_s and specific diameter D_s diagram – the configurations of machines achieving best efficiency. More recent expressions for the Cordier line are given by Bommès et al. [60] and Gülich [61] for radial machines (compressors and pumps), and by Casey and Marty [62] for industrial multi-stage compressors with shrouded impellers. Regarding the pre-design of radial turbines, the N_s - D_s performance maps presented by Balje [57] are usually preferred. These pre-design methods are based on the principle of dimensional analysis and offer a convenient and practical approach to predict sizing, rotor speed, and performance when operating at nominal conditions. However, these methods are challenged for the following reasons:

- **Reduced scale** The pre-design methods found in literature are valid for large-scale machines ($Re = 10^6$) [57]. Capata et al. [63] proposed a re-scaling of the original Balje maps for small-scale radial turbomachinery ($Re = 10^5$) by applying a Stodola correction factor fitted with CFD simulations. The numerical results suggest a 14.4 to 10-point efficiency drop compared to the original Balje maps. Therefore, it is likely that the current pre-design methods are not valid for small-scale turbomachinery. As summarized by Schiffmann [47], this is due mainly to increased relative roughness, larger tip clearances, and non-adiabatic effect [64, 65].
- **Influence of the working fluid** The current pre-design tools are obtained for non-organic media (air and combustion gases). Therefore, they are often challenged when organic working fluids are targeted [66] since they present higher expansion ratios (high Mach number) and are subject to real gas effects. Da Lio et al. [67, 68] proposed tailored performance maps for single-stage axial stage turbines, based on the most recent loss correlations. They have shown that, while the axial turbine performance maps follow the same qualitative trend for different organic working fluids, efficiency deviations in the order of 1.5% are predicted from one fluid to the other. Furthermore, the effect of the working fluid on current compressor pre-design models is barely addressed in literature.
- **Validity of the design** The shortcomings of the current pre-design approaches are that little information about the conditions at which the best compressors and turbines were tested (machine size, pressure ratio, and operating limits) is available. The feasibility and optimality of the obtained pre-design solutions are, therefore, not guaranteed.
- **Level of design detail** With the usual pre-design methods, there is limited design information available since only an indication of the optimum rotor speed and tip diameter is given. Therefore, the designer is forced to use more complex and time consuming design tools to extend the level of design detail.

As a consequence, using the classic turbomachinery pre-design methods increases the risk of a misleading design starting point, hence leading to an unnecessarily high number of time-consuming design iteration steps. To address these shortcomings, the generation of updated pre-design models for small-scale turbomachinery are proposed, with the goal of (1) obtaining more accurate models and (2) extending the design information.

2.4 Generation of the turbomachinery pre-design models

The fundamental requirement of a turbomachinery pre-design model is to provide an accurate and quick estimation of the turbomachinery efficiency and design parameters for a given duty. Pre-design tools are surrogate models that are built from data obtained with more complex models [69]. According to Schmidt et al. [70], these data-driven approaches make extensive use of machine learning or evolutionary computation principles and show promising results.

The behavior of radial turbomachinery can be captured through experimental, 3D, 2D, and mean-line (1D) analysis data. All of which could, in theory, be used to build a detailed data-driven model [69]. Bamberger et al. [71] proposed a novel CFD data-driven design method for a centrifugal fan impeller having a given operating rotor speed and tip diameter. Their models allow meeting the design target with enhanced efficiency and higher accuracy than with classic methods. However, since the data-driven approaches require a large number of points to be sufficiently accurate, validated 1D models are better indicated than CFD models since the performance of numerous turbomachinery designs and operating conditions can be estimated within a reasonable amount of time and accuracy.

In this chapter, a Monte Carlo simulation approach is used to evaluate, through experimentally validated 1D models, a dataset of randomly and equally distributed possible turbomachinery design solutions. From this dataset, a reduced order model to predict the turbomachinery performance is built using multi-variate polynomial functions.

Following best practice to describe turbomachinery behavior, the rotational speed ω and the turbomachinery tip diameter D are replaced with the dimensionless specific speed N_s and diameter D_s , defined in equation 2.1 [57, 59]. The volumetric flow rate \dot{V} and the isentropic enthalpy difference Δh_{is} characterize the turbomachinery duty, while ω and D are the required design variables to achieve this duty. This substitution reduces the complexity of the data-driven models while capturing various possible turbomachinery operating conditions. The volumetric flow rate is calculated at the compressor inlet and turbine outlet, respectively.

$$N_s = \frac{\omega \dot{V}^{0.5}}{\Delta h_{is}^{0.75}} \tag{2.1}$$
$$D_s = \frac{D \Delta h_{is}^{0.25}}{\dot{V}^{0.5}}$$

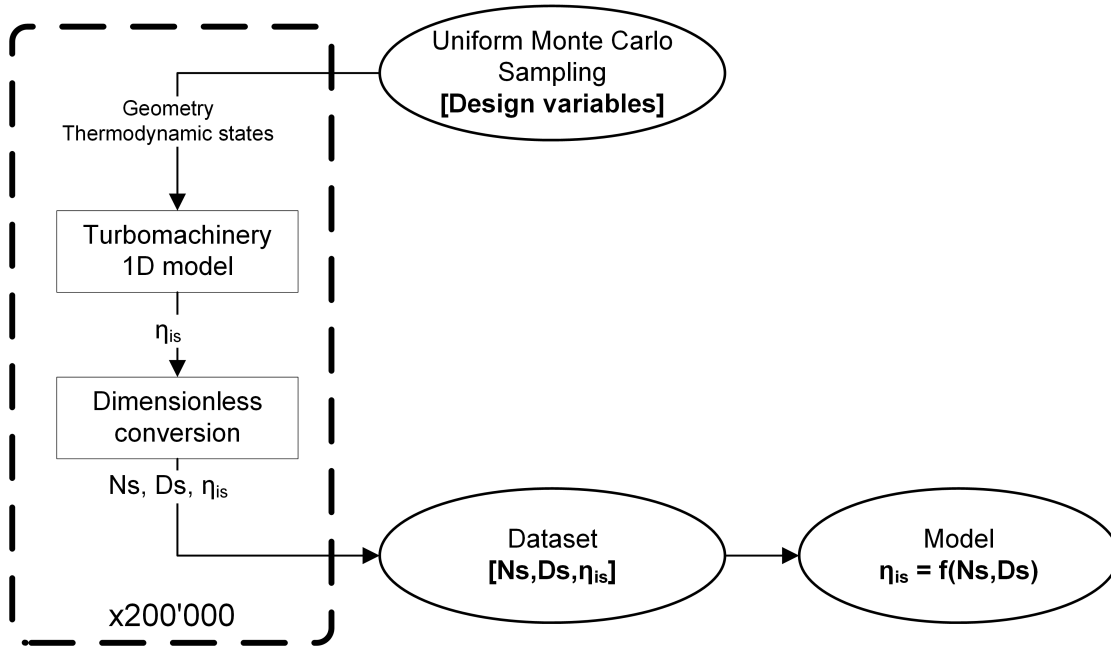


Figure 2.2 – Procedure for generating the turbomachinery pre-design models

The procedure for generating the turbomachinery pre-design models is summarized in Figure 2.2 when 200'000 equally distributed turbomachinery solutions (different geometry and thermodynamic conditions) are used to generate a model of the form $\eta_{is} = f(Ns, Ds)$. Ns and Ds are the dimensionless form of the turbomachinery rotor speed and tip diameter.

Note that, in literature, other dimensionless parameters such as the head and flow coefficients for compressors [59], and the volume expansion ratio and size parameter for turbines [72] are commonly used. In this thesis, only the specific speed and diameter are investigated, hence offering a direct comparison with the work of Balje [57] and Cordier [58].

2.5 Radial inflow turbine

2.5.1 Generation of the reduced order model

Figure 2.3 shows the radial inflow turbine layout, its main components and the geometry parameters required for a mean-line (1D) evaluation. The considered 1D model developed in MATLAB [73] has been validated both with CFD [2] and experimental data obtained with a 2 kW 18 mm tip diameter radial inflow turbine used in a HP-ORC running on R134a [35]. As shown in Figure 2.4, the predicted turbine isentropic efficiency and the measured data yield a deviation of $\pm 2.5\%$ for pressure ratios below 4.2 and for rotor speeds ranging from 150 to 200 krpm, suggesting a good agreement between predicted and experimental data. However, for pressure ratios above 4.2, the 1D model underestimates the turbine isentropic efficiency by up to 10-pt.

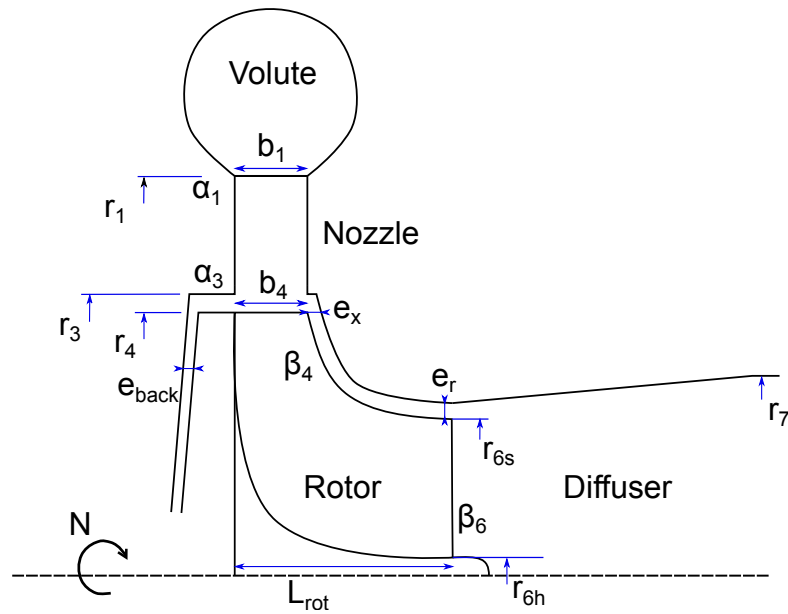


Figure 2.3 – 1D layout of a radial inflow turbine

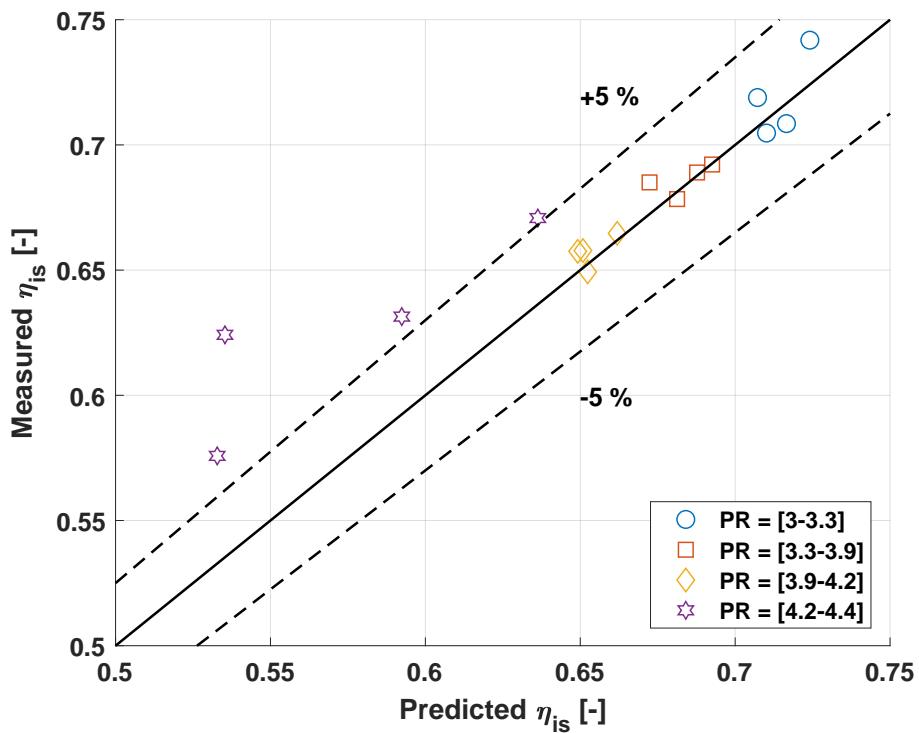


Figure 2.4 – Predicted and measured turbine isentropic efficiency for different turbine pressure ratios as obtained by Demierre et al. [35]

Chapter 2. Pre-design models for small-scale radial turbomachinery

For the reduced order model used in this analysis, the aerodynamic performance is corrected by loss correlations introduced by Baines [74]. These correlations account for (1) nozzle and interspace losses, (2) incidence, passage, tip clearance and trailing edge losses on the rotor, and (3) diffusion losses. The 1D model inputs are the turbine geometry and thermodynamic conditions, and its output is the turbine performance assessed by the total-to-total isentropic efficiency η_{is} . More details about the 1D radial inflow turbine code can be found in [2, 35]. In addition, the evaluated solutions are subject to the following constraints:

- The vapor quality must be above unity at each station within the turbine stage in order to avoid flashing
- The turbine geometry needs to achieve the specified pressure ratio within a $\pm 0.5\%$ deviation

Table 2.1 presents the variables used for generating the turbine pre-design model. The turbine tip diameter and rotor speed ranges have been set for a mechanical shaft power range of [1-10] kW based on the existing Balje maps. The turbine inlet temperature is set to small-scale ORC systems ranges. The turbine outlet pressure is calculated from ORC condensation temperatures ranging from 20°C to 60°C while a variable pressure ratio from 1.5 to 8.5 sets the turbine inlet pressure. Note, however, that the 1D mean line model was experimentally validated with a good agreement for pressure ratios up to 4.2 (Figure 2.4). Nonetheless, higher pressure ratios are considered for exploring a wider application range of the radial inflow turbine, which is of particular interest when considering ORC driven Heat Pumps.

The other 1D dimensions are defined as constant values or as dependent parameters (diameters, angles, blade heights, and blade number), and are selected based on design guidelines given by Balje [57] and Baines [74]. Finally, it has been assumed that the turbine operates at the onset of choke conditions in the transonic nozzle throat. This condition maximizes the turbine stage work output and enables to achieve higher turbine pressure ratios. Therefore, for each operating condition, the geometric nozzle outlet angle α_3 is adapted in a way that the choked mass flow at the nozzle throat is the same as the specified mass flow rate \dot{m}_{turb} , as proposed in equation 2.2, neglecting the effect of the nozzle blade trailing edge thickness. With the use of advanced nozzle designs with variable throat areas [75], a radial turbine could adapt to different choked mass flows, which is of particular interest at part load.

$$\alpha_3 = \arccos\left(\frac{A_{noz,choke}}{2\pi r_3 b_3 (1 - B_{throat,noz})}\right) \quad (2.2)$$

$$A_{noz,choke} = \frac{\dot{m}_{turb}}{\rho_{throat,noz,choke} C_{throat,noz,choke}}$$

In equation 2.2, $\rho_{throat,noz,choke}$ and $C_{throat,noz,choke}$ are the fluid density and absolute velocity at the nozzle throat in choked conditions. $B_{throat,noz}$ represents the aerodynamic blockage coefficient of the nozzle [2].

Table 2.1 – 1D turbine inputs for the reduced order generation based on the original Balje maps [57], small-scale ORC operating conditions, and geometrical design guidelines recommended by Baines [74]

Term	Symbol	Range	Unit
Model design variables			
Rotational speed	N	50-400	[krpm]
Rotor tip radius	r_4	5-75	[mm]
Turbine Inlet temperature	$T_{turb,in}$	90-250	[°C]
Condensation temperature	T_{cond}	20-60	[°C]
Pressure Ratio	PR	1.5-8.5	[-]
Mass flow rate	\dot{m}_{turb}	20-400	[g.s ⁻¹]
Fixed parameters			
Nozzle inlet angle	α_1	60	[deg]
Rotor inlet angle	β_4	0	[deg]
Rotor outlet angle	β_6	-60	[deg]
Rotor blades number	Z_{blades}	9	[-]
Rotor splits blades number	Z_{split}	9	[-]
Nozzle blades number	Z_{noz}	5	[-]
Dependent parameters			
Nozzle outlet blade height	b_3	$0.11 r_4$	[mm]
Nozzle inlet blade height	b_1	b_3	[mm]
Rotor blade height	b_4	b_3	[mm]
Nozzle outlet radius	r_3	$1.055 r_4$	[mm]
Nozzle inlet radius	r_1	$2 r_4$	[mm]
Nozzle outlet angle	α_3	equation 2.2	[deg]
Rotor exit shroud radius	r_{6s}	$0.7 r_4$	[mm]
Rotor exit hub radius	r_{6h}	$0.3 r_{6s}$	[mm]
Diffuser exit radius	r_7	$1.1 r_{6s}$	[mm]
Rotor radial clearance	e_r	$\max(0.08, 0.02 b_4)$	[mm]
Rotor axial clearance	e_x	$\max(0.08, 0.02 b_4)$	[mm]
Rotor back-face clearance	e_{back}	$\max(0.08, 0.02 b_4)$	[mm]
Rotor length	L_{rot}	$0.56 r_4$	[mm]

The Monte Carlo simulation was performed by using 65'000 randomly and equally distributed geometrical and operational turbine configurations. Only the feasible solutions are kept for generating a 6th degree polynomial pre-design model as follows:

$$\eta_{is,turb} = f(Ns, Ds, PR) \quad (2.3)$$

The data have been generated for four organic working fluids (R134a, R245fa, R152a, and R600a). These working fluids present a wide range of critical temperatures (ranging from 101°C to 154°C) and speeds of sound (ranging from 157.7 and 221.6 m.s⁻¹ at $T_{turb,in} = 160^\circ\text{C}$, $T_{cond} = 35^\circ\text{C}$, and $PR=4$) in order to assess their effect on the turbine pre-design model.

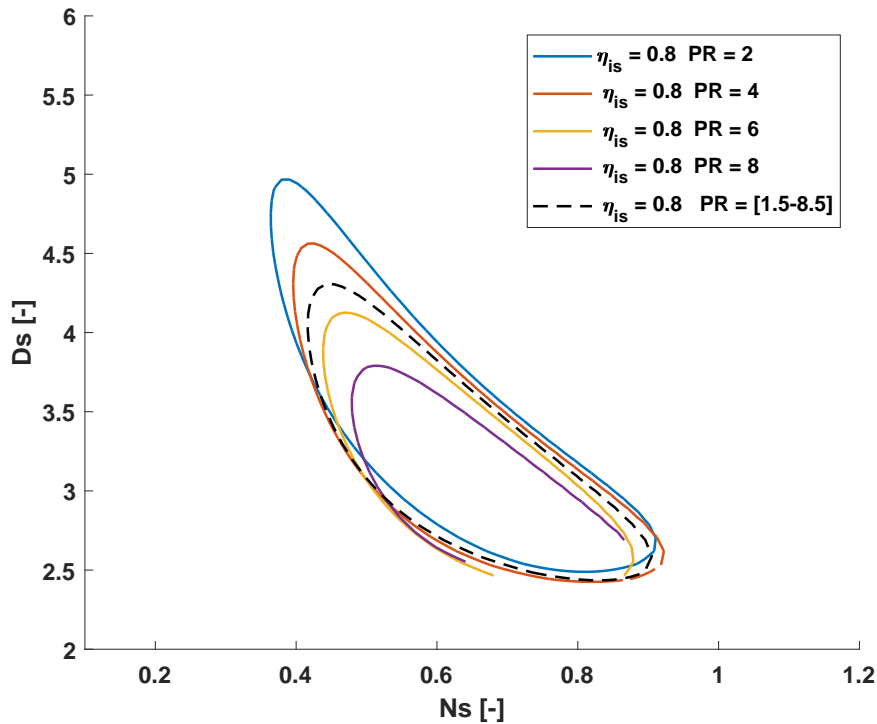


Figure 2.5 – Iso-efficiency contours in the Ns-Ds diagram generated at fixed pressure ratios (colored lines) and for a varying pressure ratio (black line) for R134a working fluid

2.5.2 Influence of the pressure ratio

Figure 2.5 represents the 80% isentropic efficiency contours in a Ns-Ds diagram obtained for fixed pressure ratios across the turbine and R134a working fluid. The surface of the iso-efficiency contours is suggested to decrease while a shift towards lower specific diameters D_s and higher specific speeds N_s is observed with increasing pressure ratios. In addition, while the maximum N_s and minimum D_s seem unaffected by the pressure ratio, the maximum specific diameter decreases and the minimum specific speed increases with pressure ratio. The accuracy of the 0D performance map is affected when different pressure ratios are used for its generation. Indeed, when using a polynomial fit with all points independently of the pressure ratio (black line on Figure 2.5), the N_s and D_s values are averaged, meaning that the isentropic efficiency gets underestimated at low pressure ratios, and vice versa at high pressure ratios. To capture this effect, the turbine pressure ratio is included as an input variable of the pre-design model. Using a multivariate 6th degree polynomial fitting, a new tailored equation rating the total-to-total isentropic efficiency is built as a function of N_s , D_s , and PR ($\eta_{is} = f(N_s, D_s, PR)$). As highlighted in Figure 2.6, this model presents a R^2 over 0.985 and a RMSE of 0.016. The polynomial equation of the model is provided in Appendix A.

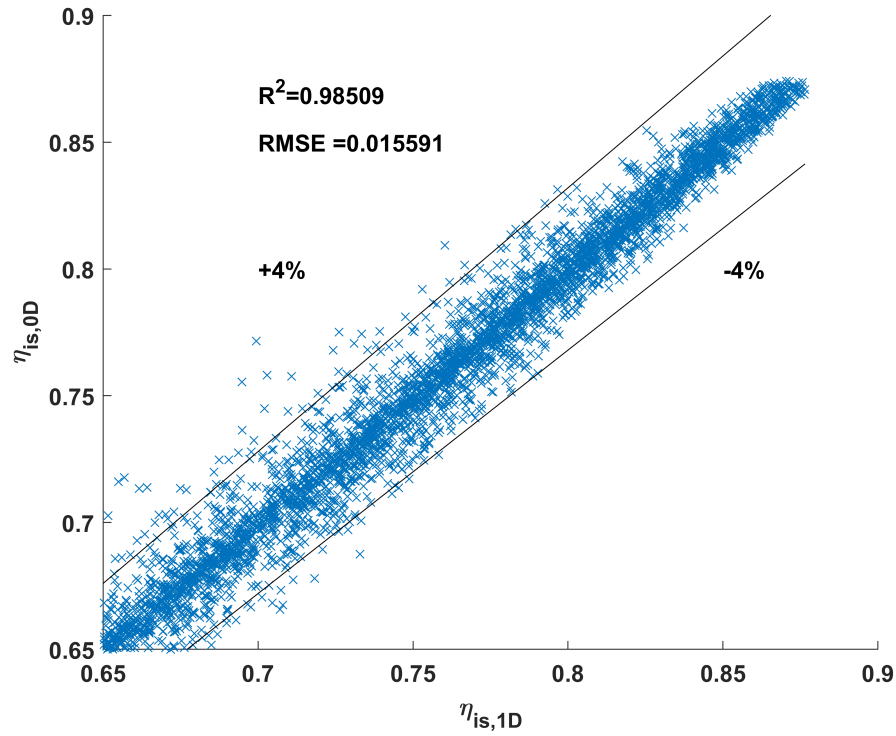


Figure 2.6 – Goodness of fit of the $\eta_{is,0D} = f(Ns, Ds, PR)$ model for R134a working fluid

In order to further simplify the turbine design, it is common practice to approximate the ideal radial inflow turbine design variables along the “efficiency ridge”, which is often approximated by the $NsDs=2$ curve [74]. This correlation, similar to the Cordier line for compressors, is represented in Figure 2.7 for different pressure ratios. Although this correlation fits the original Balje diagrams well, it leads to suboptimal designs when state-of-the-art turbine design guidelines are considered (Table 2.1). As a consequence, a new set of polynomial equations along the “efficiency ridge” estimating the isentropic efficiency (equation 2.4) and specific diameters (equation 2.5) as a function of both pressure ratio and specific speed is introduced. These equations are obtained by retrieving the optimum values of the isentropic efficiency η_{is} and specific diameters Ds for each value of Ns and PR .

$$\eta_{is} = 0.45 + 1.64Ns - 0.05PR - 2Ns^2 + 0.15NsPR + 0.63Ns^3 - 0.07Ns^2PR - 0.003NsPR^2 \quad (2.4)$$

$$Ds = 9.42 - 18.3Ns - 0.16PR + 17.8Ns^2 + 0.24NsPR + 0.001PR^2 - 6.37Ns^3 - 0.13Ns^2PR + 0.001NsPR^2 \quad (2.5)$$

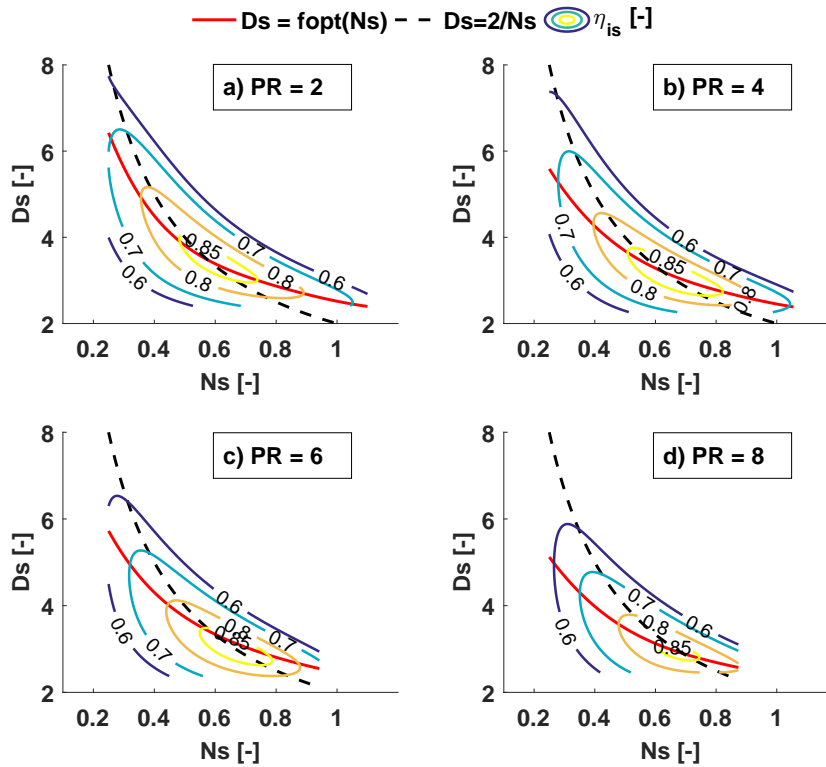


Figure 2.7 – Iso-efficiency contours in the N_s - D_s diagram generated at fixed pressure ratios superimposed by the theoretical curve $N_s D_s = 2$ for R134a working fluid

The resulting curves along the new “efficiency ridges” in the N_s - D_s diagram are also plotted in Figure 2.7 highlighting the difference with the classic $N_s D_s = 2$ curve. The selection of the specific speed optimizing the turbine efficiency (equation 2.4) immediately leads to the appropriate specific diameter and hence turbine tip diameter. However, this method might depreciate the overall system design since the turbine diameter and speed might need to be adjusted when additional constraints such as volume, mass or rotordynamic stability have to be met.

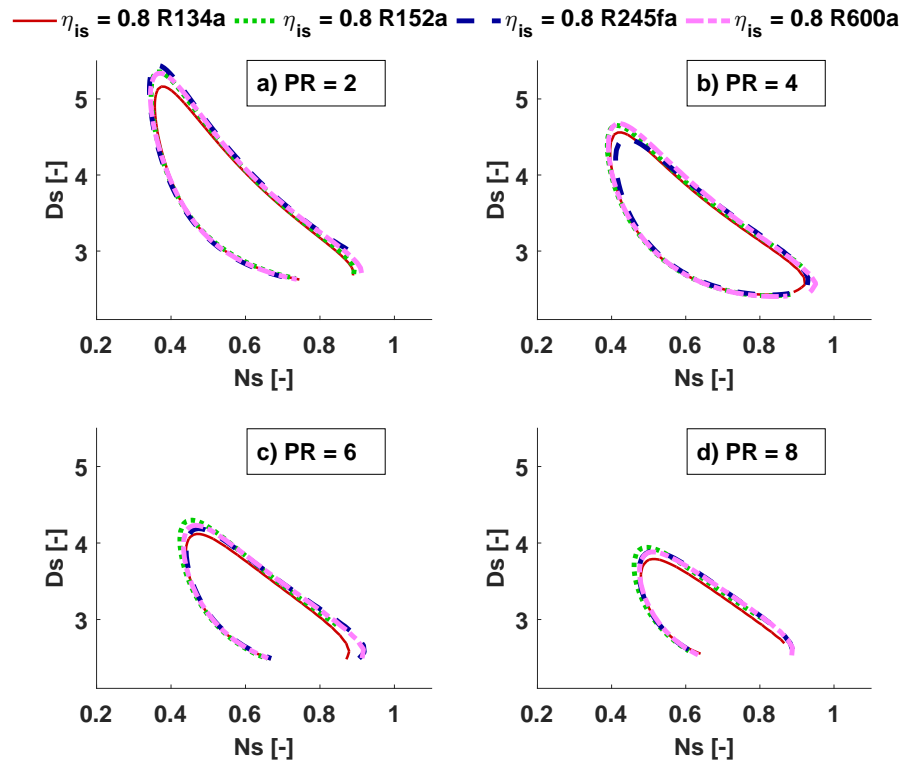


Figure 2.8 – Iso-efficiency contours in the N_s - D_s diagram for various pressure ratios and for four organic working fluids suggesting only limited influence of the working fluid on the efficiency contours

2.5.3 Influence of the working fluid

Figure 2.8 shows similar efficiency contours obtained for the investigated fluids as a function of pressure ratio across the turbine. The maximum RMSE between the polynomial fits built for each working fluid is equal to 0.012, which is below the accuracy of the pre-design model as shown in Figure 2.6 (RMSE=0.016). This results in maximum average absolute deviations below 1-pt in isentropic efficiency from one fluid to the other. This corroborates with observations by Da Lio [68]. Since these performance maps are used for pre-design purposes, the results suggest that the proposed model based on R134a is reasonably well suited to a wide variety of organic working fluids (critical temperatures ranging from 101 to 154 °C).

2.5.4 Influence of the turbine loss mechanisms on the efficiency contours

In order to investigate and highlight the underlying phenomena leading to the characteristic iso-efficiency contours shape in the turbine Ns-Ds diagram, the different loss mechanisms are analyzed in detail. The losses are normalized with the isentropic enthalpy drop across the nozzle or the rotor depending on their nature (stationary nozzle or rotor).

Nozzle and interspace passage losses

Figures 2.9a and 2.9b represent the relative nozzle and interspace passage losses for various pressure ratios. The plots suggest that the overall turbine efficiency drops with high Ds values due to the loss increase in the nozzle and the interspace passage (space between the nozzle and the rotor). The Loss Ratio LR, defined by equation 2.6 for the nozzle stage, is a function of ξ , which represents the nozzle/interspace loss coefficient defined by Baines [74] and is defined by equations 2.7 and 2.8. The expressions for o_{noz} , c_{noz} , and s_{noz} , which are the nozzle throat opening, nozzle blade chord length, and nozzle blade spacing, can be found in [2]. The Reynolds number Re is based on the flow velocity and blade height at the nozzle throat.

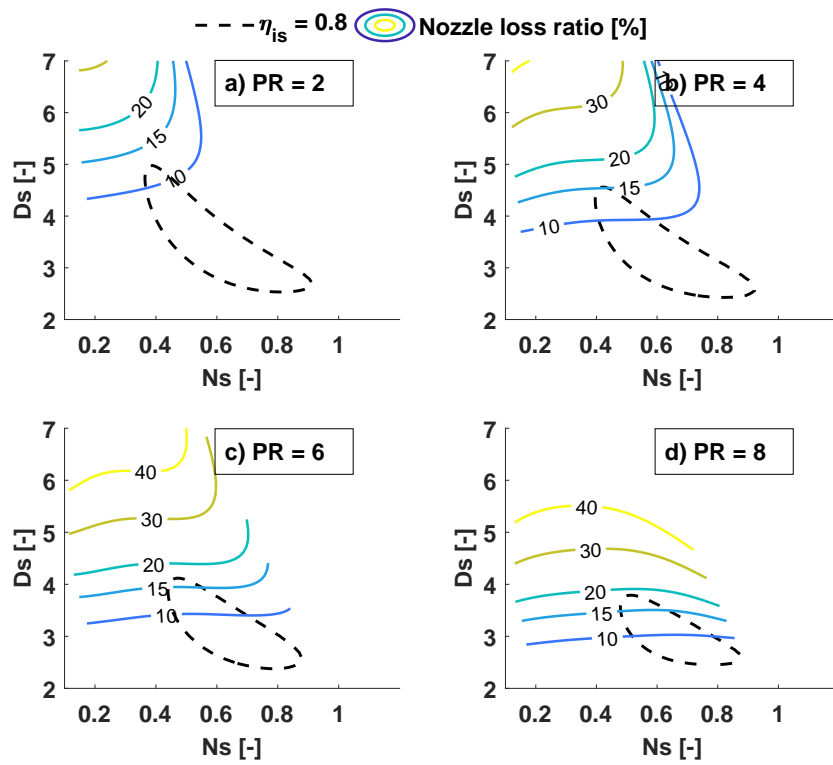
$$LR = \frac{\Delta h_{loss,noz}}{\Delta h_{is,noz}} = \frac{\xi C_2^2}{2\Delta h_{is,noz}} = \frac{\xi}{\xi + 1} \quad (2.6)$$

$$C_2^2 = \frac{C_{2,is}^2}{\xi + 1} = \frac{2\Delta h_{is,noz}}{\xi + 1} \quad (2.7)$$

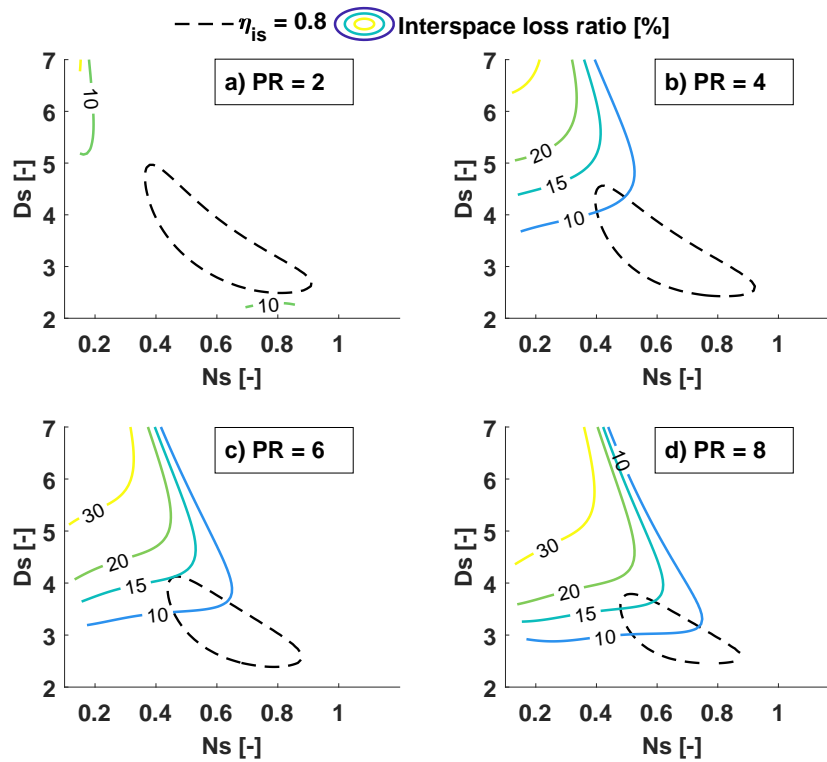
$$\xi = \frac{0.05}{Re^{0.2}} \left(\frac{\tan(\alpha_3)^2}{s_{noz}/c_{noz}} + \frac{o_{noz}}{b_3} \right) \quad (2.8)$$

The nozzle losses are governed primarily by the geometric nozzle outlet angle α_3 , which is adapted to obtain a choked flow at the specified mass flow rate (equation 2.2). With a diameter increase and a volume flow rate reduction, which both lead to higher Ds values, the nozzle outlet angle α_3 grows, and the nozzle losses increase as a consequence. This effect is amplified with the pressure ratio due to the higher density at the throat (equation 2.2). Therefore, for a given mass flow, an increased pressure ratio decreases the required area (α_3 increase) for achieving choked nozzles.

The evolution of the relative interspace losses in the Ns-Ds diagram is represented for various pressure ratios in Figure 2.9b. Similarly to the nozzle losses, the interspace losses are driven by the absolute flow angle at the rotor inlet α_4 , which is governed primarily by α_3 . Hence, higher flow angles driven by increased diameter and reduced volume flows increase the interspace losses, and the loss contours follow the same trend as for the nozzle losses in Figure 2.9a. For a pressure ratio of 2 the interspace losses are negligible, and hence no contours are visible.



(a) Nozzle loss ratio



(b) Interspace loss ratio

Figure 2.9 – Evolution of the turbine nozzle loss ratio (a) and interspace loss ratio (b) at different pressure ratios

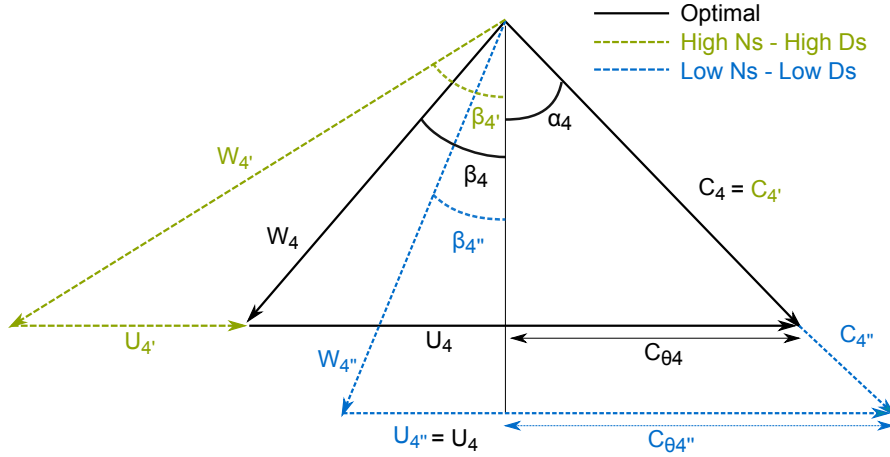


Figure 2.10 – Velocity triangle at the turbine rotor inlet and evolution of the relative speed W_4 at optimal, high Ns-Ds, and low Ns-Ds conditions

Rotor incidence losses

The rotor blade incidence losses are calculated based on a model proposed by Wasserbauer et al. [76] and are described by equation 2.9.

$$\Delta h_{inc} = 0.5 [W_4 \sin(\beta_4 - \beta_{4,opt})]^2 \quad (2.9)$$

where $\beta_{4,opt} = -40^\circ$ is the optimal flow angle at the rotor inlet [77] and W_4 is the relative flow speed defined by:

$$W_4 = \sqrt{C_4^2 + U_4^2 - 2C_4U_4 \sin \beta_4} \quad (2.10)$$

Figure 2.10 shows the evolution of the relative inlet speed W_4 when either U_4 or C_4 increases. The evolution of the relative incidence losses in the Ns-Ds diagram is represented in Figure 2.11. The incidence loss ratio contours coincide with the evolution of the relative Mach number at the rotor inlet $M_{rel,4} = \frac{W_4}{a_4}$ as represented in Figure 2.12a, which suggests that these losses depend mainly on W_4 . At high Ns and Ds values, and hence high rotor speeds and tip diameters, the rotor tip speed $U_4 = r_4\omega$ increases, which also increases β_4 and, therefore, the incidence losses. However, at low Ns and Ds values, as the tip speed U_4 gets lower, the rotor absolute inlet velocity C_4 needs to be increased to match the required pressure ratio, which also leads to an increase in W_4 (Figure 2.10). This corroborates with the evolution of the absolute rotor inlet Mach number $M_{abs,4} = \frac{C_4}{a_4}$ presented in Figure 2.12b.

Although the absolute rotor inlet Mach number increases with pressure ratio, the latter has little impact on the incidence losses. Both tip speed and absolute velocity increase with the pressure ratio to match the required turbine specific work. Nonetheless, their effect on W_4 is compensated by the $2U_4C_4 \sin(\beta_4)$ term, which increases with pressure ratio as well.

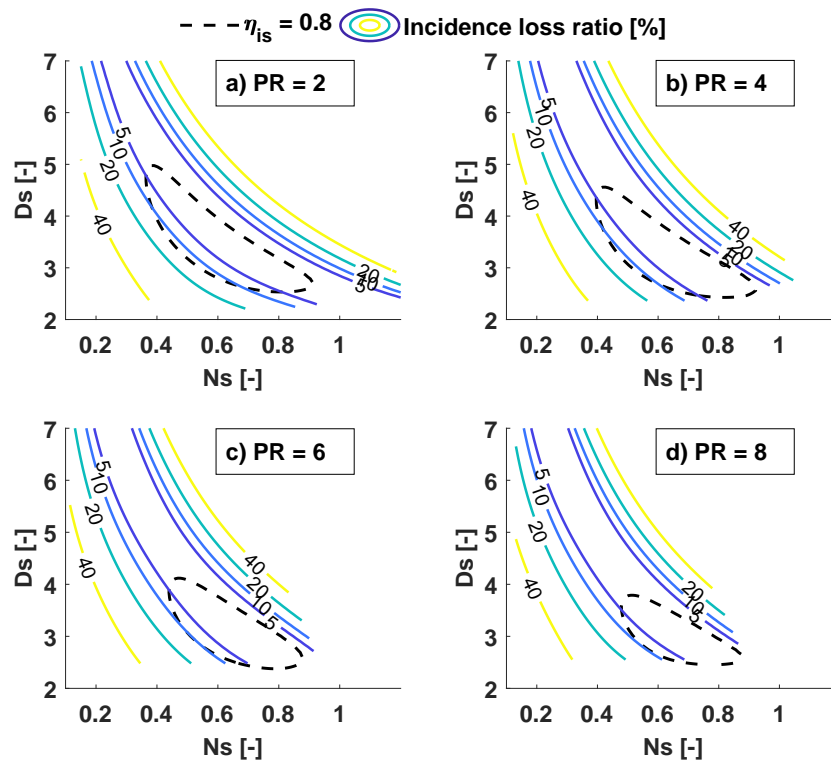
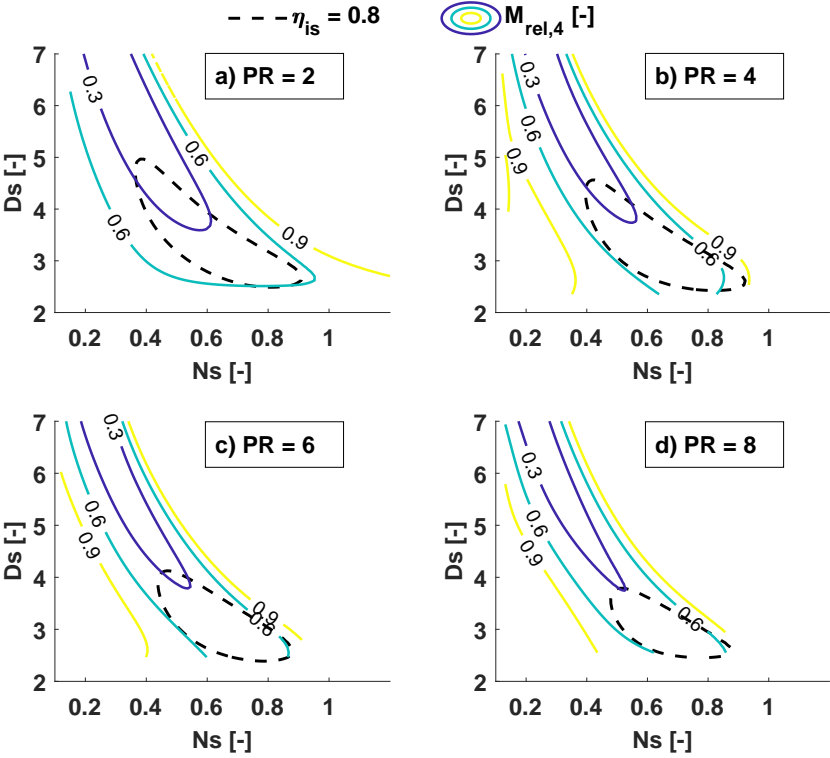
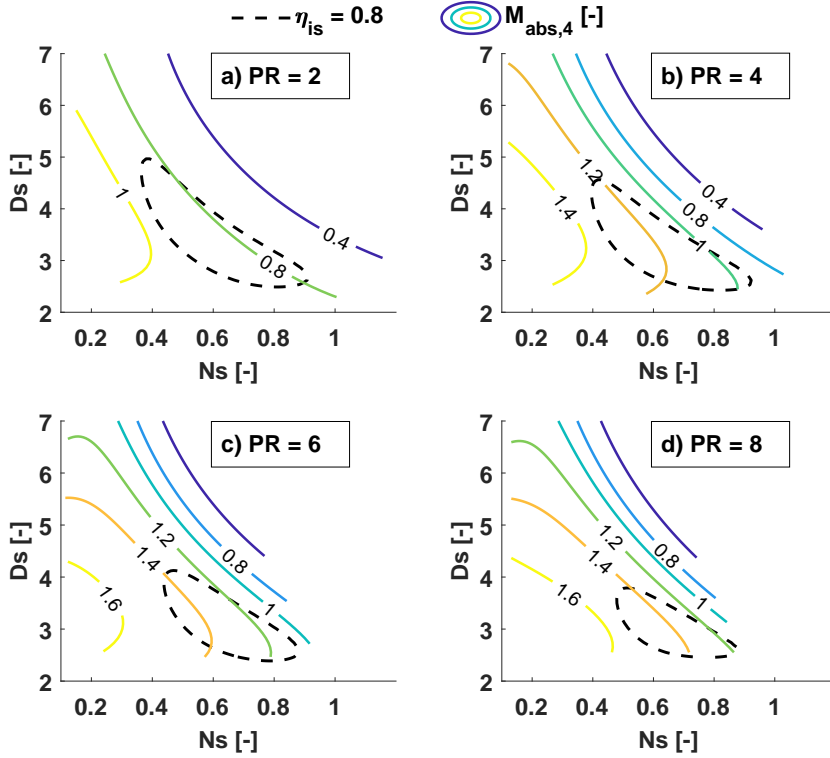


Figure 2.11 – Evolution of the turbine incidence loss ratio at different pressure ratios



(a) Relative Mach number at rotor inlet



(b) Absolute Mach number at rotor inlet

Figure 2.12 – Evolution of the (a) relative and (b) absolute Mach numbers at the turbine rotor inlet at different pressure ratios

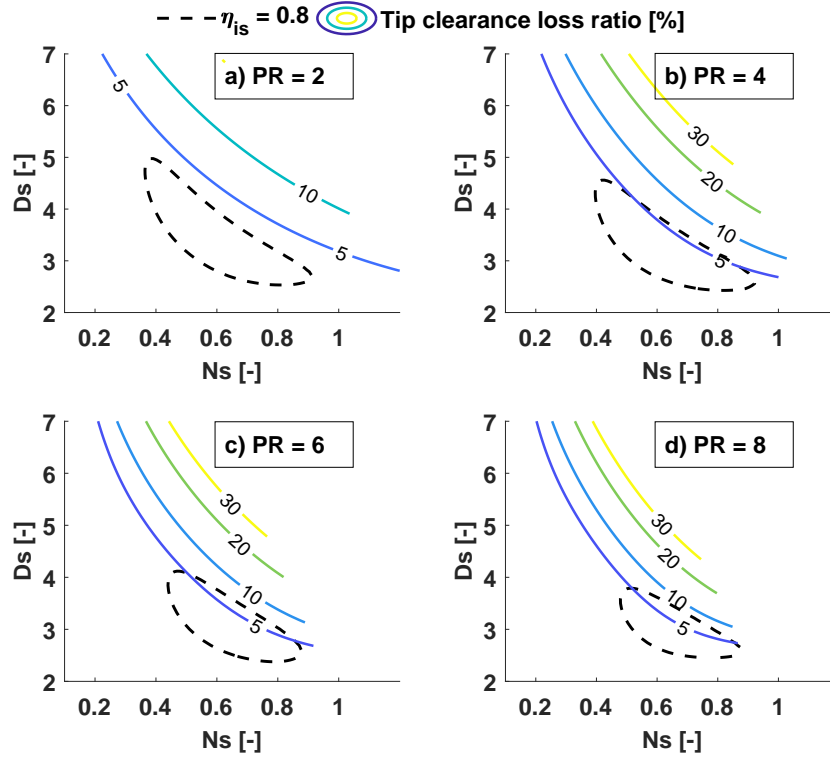


Figure 2.13 – Evolution of the turbine tip clearance loss ratio at different pressure ratios

Tip clearance losses

The tip clearance losses are predicted through the correlation given by Baines [74] and described by equation 2.11. The axial and radial tip clearances e_x and e_r are defined by $e_{r,x} = \max(80\mu m, 0.02b_4)$. The discharge parameters values $K_x = 0.4$, $K_r = 0.75$, and $K_{rx} = -0.3$ are recommended based on experimental data [74]. The expressions of G_x and G_r can be found in [2, 35]. Since they are driven mainly by the tip speed U_4 , the tip clearance losses increase for high values of N_s and D_s . These losses increase with the imposed pressure ratio, as the tip speed U_4 increases to match the required Euler work defined by equation 2.12. This results in narrower N_s - D_s contours when the required pressure ratio increases, as shown in Figure 2.13.

$$\Delta h_{cl} = \frac{U_4^3 (Z_{blades} + 0.5Z_{split})}{8\pi} \left(K_r e_r G_r + K_x e_x G_x + K_{xr} \sqrt{e_r e_x G_x G_r} \right) \quad (2.11)$$

$$\Delta h_{rot} = C_{\theta 4} U_4 - C_{\theta 6} U_6 \quad (2.12)$$

Rotor passage losses

The passage losses refer to all losses occurring inside the blade passage and are expressed as a generic term embracing all possible contributions. This includes the losses due to the secondary flows, the growth of the boundary layers, separation, and mixing. On the contrary to axial turbines, profile and secondary flow losses are, therefore, combined in one single expression [74]. Figure 2.14a represents the evolution of the passage loss ratio, which tends to rise towards low D_s and high N_s values and towards both high D_s and N_s values. The correlation for the passage losses implemented in the turbine 1D model is proposed by Futral et al. [78], Benson [79], and Wasserbauer et al. [76] as follows:

$$\Delta h_{pass} = 0.5K_{pass} [W_4^2 \cos^2(\beta_4 - \beta_{4,opt}) + W_6^2] \quad (2.13)$$

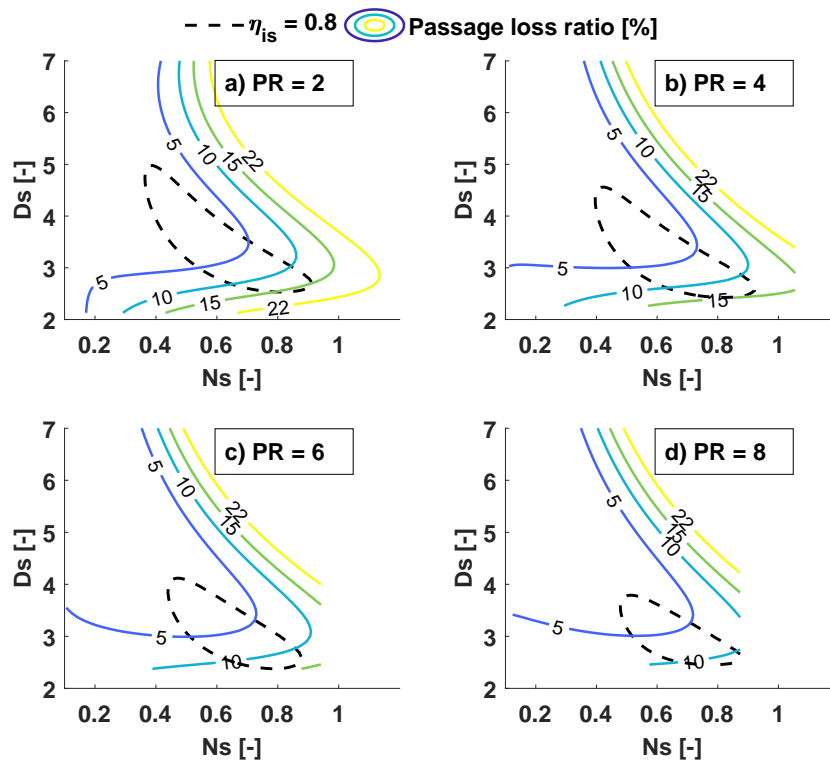
where $K_{pass} = 0.3$ has been identified experimentally. The passage loss ratio is governed by the relative rotor outlet velocity W_6 , which corroborates with the evolution of the relative Mach number at the turbine outlet $M_{rel,6} = \frac{W_6}{a_6}$ shown in Figure 2.14b. A decrease of the specific diameter D_s due to the drop of the tip diameter r_4 , reduces both the exhaust hub and shroud diameters r_{6h} and r_{6s} , and hence the rotor throat area, thus forcing the relative exhaust velocity to increase. On the other hand, an increase of both N_s and D_s results in higher tip speeds, which drive both the relative inlet and the exhaust velocities.

In addition, W_6 is suggested to rise with pressure ratio, which is an inherent consequence of the increased specific turbine work (equation 2.12). Indeed, higher pressure ratios lead to higher tip speeds U_4 , which inevitably increase U_6 . An analysis of the exhaust velocity triangle as presented in Figure 2.15 shows that W_6 needs to increase with U_6 to minimize the exhaust swirl $C_{\theta 6}$. In spite of having W_6 increasing with the pressure ratio, it has a limited effect on the passage losses though. This is due to the $\cos^2(\beta_4 - \beta_{4,opt})$ term, which decreases with pressure ratio (β_4 increases with pressure ratio - see Figure 2.10), thus counterbalancing the W_6 rise.

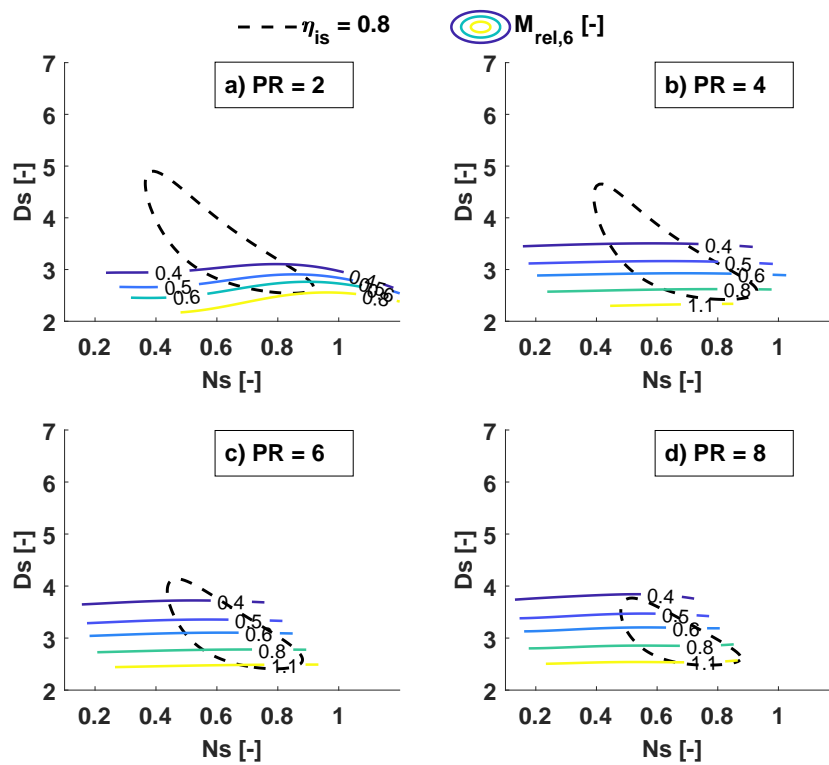
Finally, if W_6 is high enough to choke the rotor throat, the throat flow angle is corrected to allow for a supersonic expansion. As shown in Figure 2.14b, $M_{rel,6}$ is limited to Mach 1.1 since only a limited amount of over-expansion can be achieved in the rotor passage. This is due to the axial Mach number at the rotor outlet that cannot exceed unity.

Trailing edge losses

The trailing edge losses, which are described by Baines [74], are presented in a N_s - D_s diagram in Figure 2.16. These losses are one order of magnitude lower compared to the other rotor and nozzle losses and have, therefore, a negligible effect on the efficiency contours in the N_s - D_s diagram.



(a) Passage loss ratio



(b) Relative Mach number at rotor outlet

Figure 2.14 – Evolution of the passage loss ratio (a) and relative Mach number at the turbine rotor outlet (b) at different pressure ratios

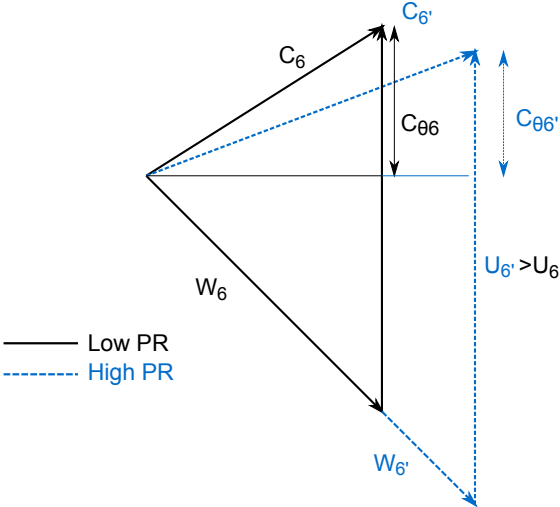


Figure 2.15 – Velocity triangle at the turbine rotor outlet and evolution of the relative speed W_6 at low and high pressure ratio

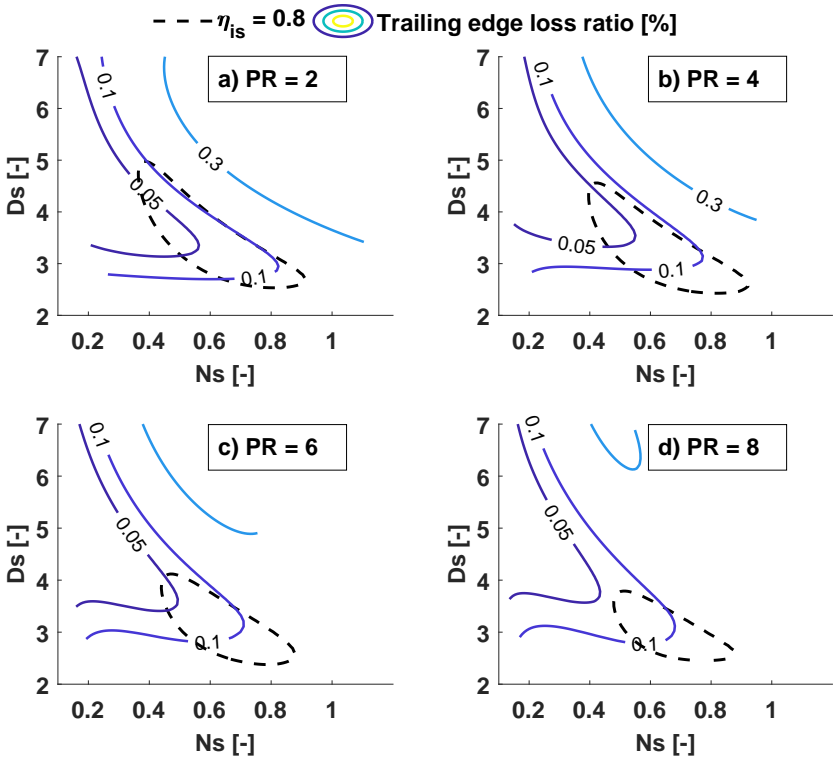


Figure 2.16 – Evolution of the turbine trailing edge loss ratio at different pressure ratios

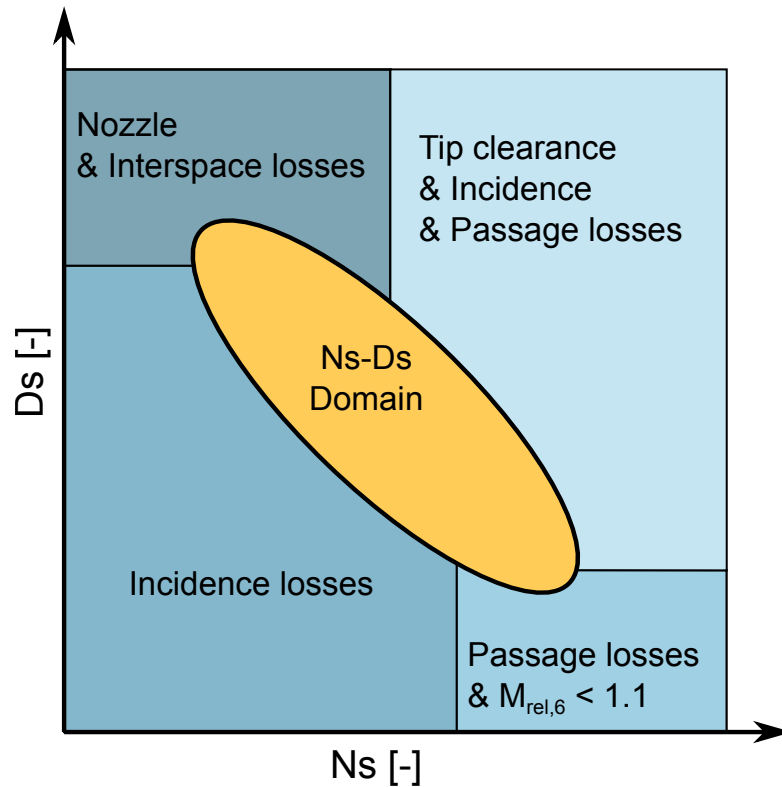


Figure 2.17 – Underlying phenomena imposing the shape of the turbine efficiency contours

Summary

As summarized in Figure 2.17, analyzing each loss mechanism individually along the turbine flow path has allowed identifying the key aerodynamic phenomena that influence the shape of the efficiency contours in the Ns - Ds diagram as follows:

- The nozzle outlet angle α_3 limits the map towards high values of Ds due to its influence on the nozzle losses.
- The tip speed U_4 drives mainly the tip clearance losses and increases the rotor losses at high specific diameters and speeds.
- The relative velocity W_4 at the rotor inlet drives the incidence losses and constrains the width of the elliptic iso-efficiency contours, elongating them along a constant Ns - Ds product.
- The relative velocity W_6 at the rotor outlet limits the contours towards low Ds values due to increasing passage losses and Mach number at the rotor throat.

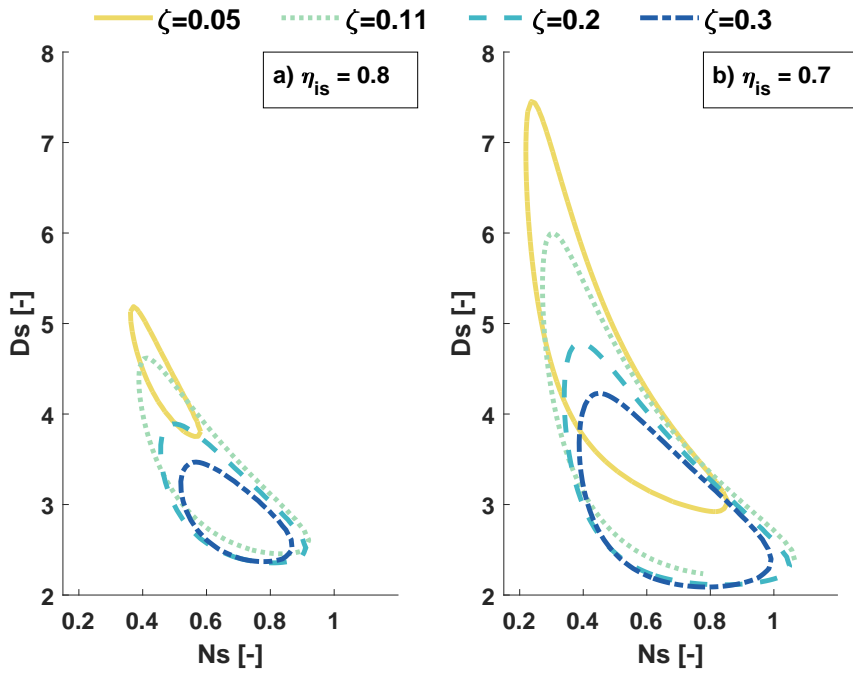


Figure 2.18 – Ns-Ds contours when performed at different blade height to tip radius ratios $\zeta = \frac{b_4}{r_4}$ for isentropic efficiencies of 0.8 and 0.7 and for PR=4

2.5.5 Sensitivity Analysis

With the nozzle outlet angle α_3 being adapted to each operating condition, the turbine design is fully determined by the values of rotational speed and diameters obtained with the presented Ns-Ds map. The following section presents a sensitivity analysis showing the influence of geometrical design dependencies that have been set as constant values to generate the map according to best engineering practices such as suggested by Baines [74]. This analysis is performed on the blade height to tip radius ratio $\zeta = \frac{b_4}{r_4}$, the clearance ratio $CR = \frac{e_{r,x}}{b_4}$, and on the shroud to tip radius ratio $\epsilon = \frac{r_{6s}}{r_4}$. The efficiency contours obtained by the sensitivity analysis are plotted for a pressure ratio of 4.

Figure 2.18 shows the impact of the blade height to tip radius ratio $\zeta = \frac{b_4}{r_4}$ on the 0.8 and 0.7 efficiency contours, with ζ ranging from 0.05 to 0.3. The previous performance maps were obtained at $\zeta=0.11$ (see Table 2.1). At high ζ ratios the nozzle outlet angle α_3 increases due to the higher area at the rotor tip (equation 2.2). Higher nozzle angles, however, increase the nozzle losses, which get compensated by a decrease in the specific diameters Ds to obtain the same isentropic efficiency. As a consequence, the results suggest that smaller blade height ratios allow increasing the iso-efficiency surface in the Ns-Ds diagram. Nonetheless, for $\zeta=0.05$, higher values of Ds are reached, at the expense of the iso-efficiency surface decrease though. Indeed, decreasing ζ increases the relative speed W_4 at the rotor inlet, which leads to increased incidence and passage losses. Therefore, $\zeta=0.11$ is found to be optimal.

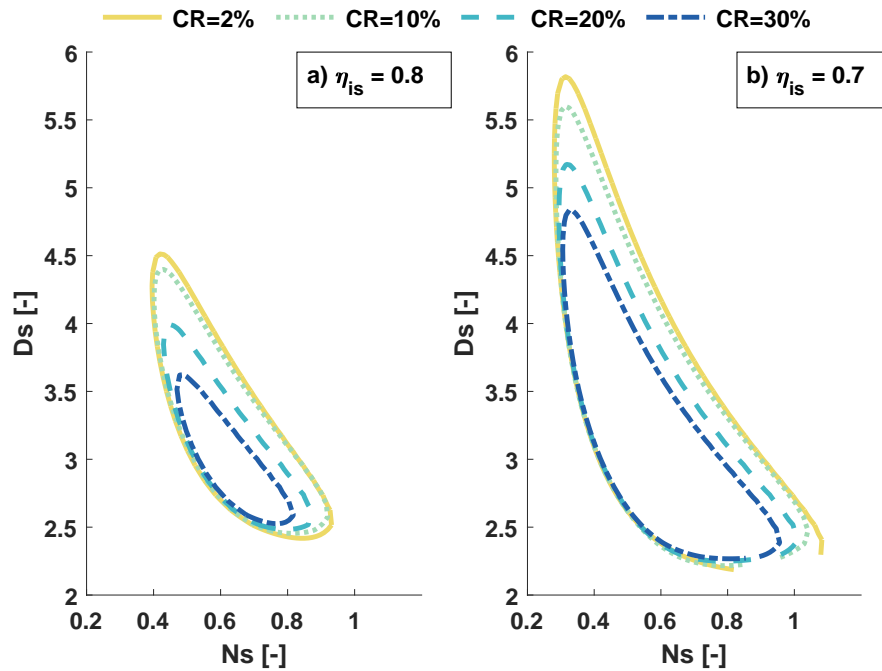


Figure 2.19 – Ns-Ds contours when performed at different clearance ratios CR for isentropic efficiencies of 0.8 and 0.7 and for PR=4

Figure 2.19 represents the 0.8 and 0.7 efficiency contours obtained at different clearance ratios $CR = \frac{e_{r,x}}{D_4}$, ranging from 2 (value used for the map generation - see Table 2.1) to 30%. The increase of the clearance ratio tends to shift the Ns-Ds map towards lower values of Ns and Ds, due to the influence of the tip speed in equation 2.11. Moreover, one can observe that the values of Ds are required to be smaller at high clearance ratios to ensure an isentropic efficiency of 0.8 at a given specific speed. This can be explained by the fact that the clearance losses are driven by both the tip speed and the tip clearance (equation 2.11). Hence, at a larger tip clearance, the tip speed needs to be reduced to keep the efficiency constant. Note that these contours could increase even further without the clearance minimum set to $80 \mu\text{m}$ for taking into account manufacturing and assembly issues.

Finally, Figure 2.20 represents the 0.8 and 0.7 efficiency contours obtained for shroud to tip radius ratios $\epsilon = \frac{r_{6s}}{r_4}$ ranging from 0.4 to 0.9. The maps presented before were obtained with $\epsilon = 0.7$ (see Table 2.1). The results suggest that tuning the shroud to tip radius ratio allows operating at higher specific speeds (increased ϵ) and higher specific diameters (decreased ϵ), which may offer interesting design options in cases where constraints due to operating conditions or manufacturing need to be taken into account. Note, however, that only ϵ values ranging from 0.5 to 0.8 allow achieving efficiencies over 0.8. In addition, for a shroud to tip radius ratio of 0.7, the surface of the 0.8 and 0.7 efficiency contours are larger than for the other values, which may offer higher design flexibility. This shift is governed mainly by the evolution of the passage losses since when ϵ decreases, the rotor outlet area decreases as well, and thus W_6 increases (equation 2.13).

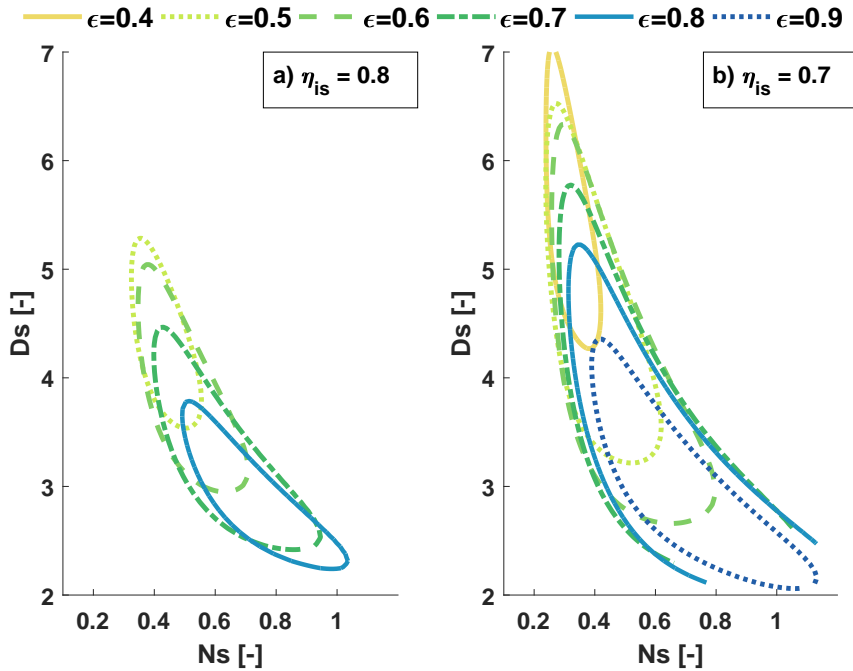


Figure 2.20 – Ns-Ds contours when performed at different shroud to tip radius ratios $\epsilon = \frac{r_{6s}}{r_4}$ for isentropic efficiencies of 0.8 and 0.7 and for PR=4

In order to take into account the shroud to tip radius ratio in the pre-design phase, new sets of equations can be built as follows:

- For four discrete ϵ values, a 6th degree polynomial fit $\eta_{is,\epsilon=[0.5,0.6,0.7,0.8]} = f(Ns, Ds, PR)$ is implemented. The designer can evaluate the efficiency for each ϵ and keep the one offering the best system efficiency. All these functions have a similar goodness of fit shown in Figure 2.6 for $\epsilon=0.7$.
- The ϵ parameter can be implemented in the model, thus leading to a 6th degree polynomial fit $\eta_{is} = f(Ns, Ds, PR, \epsilon)$. The goodness of fit is presented in Figure 2.21. Using this model offers more flexibility in the choice of ϵ and could lead to better design trade-offs. However, the fit is less accurate due to the addition of one model parameter and might increase the complexity of the pre-design exploration.

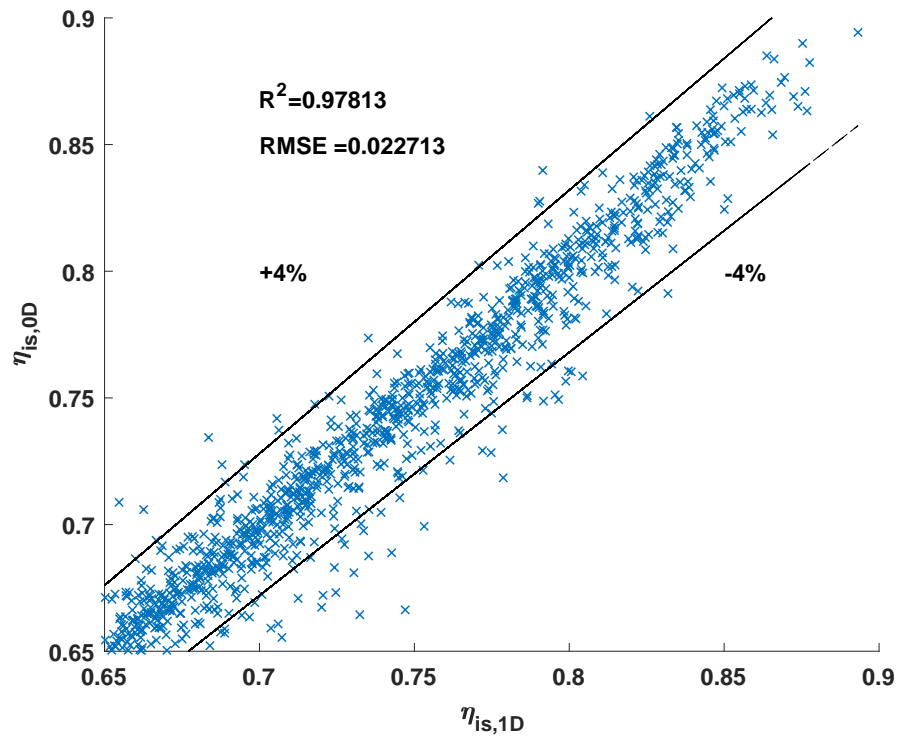


Figure 2.21 – Goodness of fit of the $\eta_{is,0D} = f(Ns, Ds, PR, \epsilon)$ model

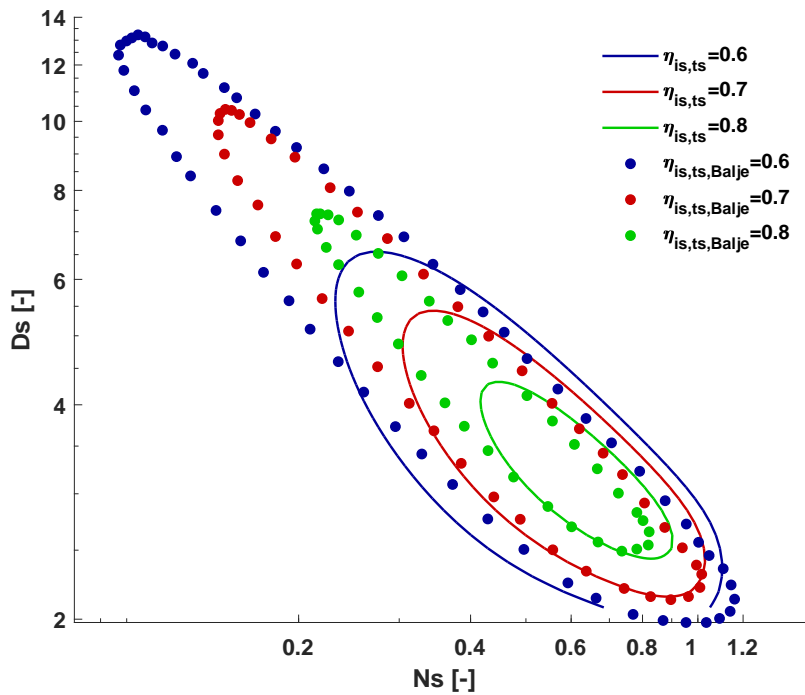


Figure 2.22 – Comparison of the new performance map ($\epsilon = \frac{r_{6s}}{r_4} = 0.7$) with the original map of Balje [57]

In addition, these results provide keys to understanding why, when compared to the original Balje performance map, the updated radial turbine isentropic efficiency contours delimit smaller N_s - D_s surfaces for a given total-to-static isentropic efficiency $\eta_{is,ts}$, such as shown in Figure 2.22:

- In order to compute the maps, Balje used varying shroud to tip radius ratios ϵ with values ranging from 0.4 to 0.8, as opposed to a fixed value of 0.7 used in this investigation and recommended by Baines [74].
- The original Balje maps were computed using a tip clearance ratio of 2%. In the frame of this investigation, reduced scale rotors are considered. Hence the minimum tip clearance is limited to $80 \mu\text{m}$ to stay within realistic manufacturing tolerances. In some cases, this threshold leads to tip clearance ratios approaching 20%, leading to similar results illustrated by Figure 2.19. Moreover, while Balje considered leakage losses as a part of the end wall friction losses [57], the correlation used for the present N_s - D_s map consists in a more fundamental experimentally validated analysis of the flow through the clearance gap [74].
- The Balje maps were computed for large-scale air machines operating with significantly lower pressure ratios than the ones considered in this analysis, which tends to increase the efficiency contours in the N_s - D_s diagram as suggested in Figure 2.5.

2.5.6 Pre-design model validation

Compared to the 1D radial inflow turbine model, the pre-design maps (or 0D model) represent a significant reduction of the model order. To assess the effect of these simplifications the ratings obtained by the 0D and the 1D models are compared for a radial inflow turbine with a 18 mm tip diameter. The pre-design models with a fixed $\epsilon = \frac{r_{6s}}{r_4}$ of 0.7 have been considered. The operating conditions summarized in Table 2.2 were investigated, which correspond to typical values of a small capacity ORC without regeneration [80]. The turbine mass flow rate is computed through the evaporator power input, assuming that all the heat transfers are isobaric. Further assumptions used to calculate the cycle are steady-state flow conditions and an isentropic pump efficiency of 60%.

Table 2.2 – Boundary conditions for the turbine pre-design model validation

Term	Range	Unit
ORC evaporator power	20-32	[kW]
Turbine inlet temperature	160	[°C]
ORC condensation temperature	35	[°C]
Turbine pressure ratio	2-8	[-]
Turbine diameter	18	[mm]
Working fluid	R134a	[-]

Two different calculations are implemented for the evaluation of the 0D model. The first calculation checks whether the optimum design configuration exists in the original dataset used to generate the 0D model. These constrained solutions are retrieved by using a classification method which verifies whether the design solution lies within the convex envelope (or convex hull) delimited by the original dataset. This approach allows discarding the points of the search space which are extrapolated outside of the feasibility domain. When the pre-design solutions are not tested against the convex hull of the original dataset (hence, the whole search space is explored), they are annotated as unconstrained solutions.

Figure 2.23 illustrates a convex hull envelope generated from a uniform 2D dataset, indicated as "Original Dataset". If another set of data is analyzed over the whole search space, the convex hull method enables to sort the valid points (those inside the convex envelope of the original dataset) from the extrapolated ones. The valid points satisfy the following expression:

$$[A_{conv}]X_{var} \leq [b_{conv}] \tag{2.14}$$

where X_{var} describes the design variables used to generate the convex hull envelope (in Figure 2.23, $X_{var} = (x_1, x_2)$), and $[A_{conv}]$ and $[b_{conv}]$ describe the inequality equations defining the convex hull envelope. In the particular case of the proposed turbine pre-design model, $X_{var} = (\eta_{is}, N, D, \dot{m}_{turb}, PR, T_{turb,in}, P_{turb,out})$. Therefore, validating equation 2.14 ensures that, for a given set of operating conditions (\dot{m}_{turb} , PR, $T_{turb,in}$, and $P_{turb,out}$), the predicted optimum isentropic efficiency η_{is} can be achieved with the optimum rotational speed and diameter (N, D) found by the pre-design model.

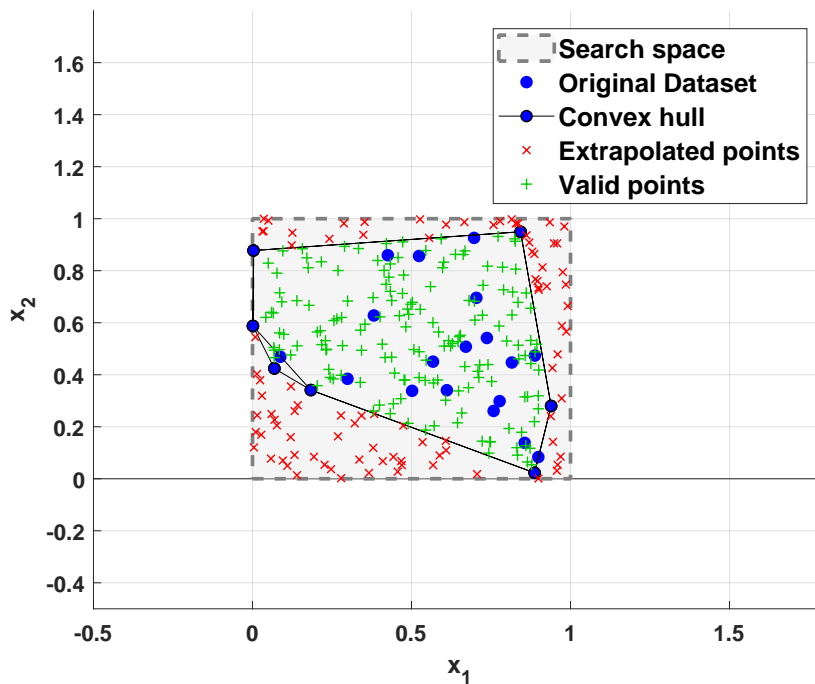
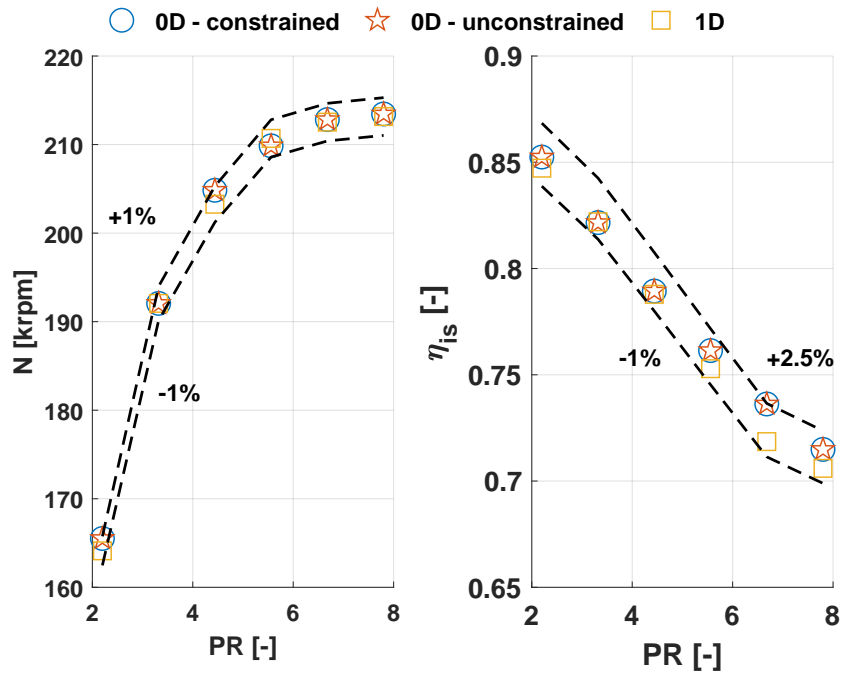


Figure 2.23 – Example of a convex hull generated from a random set of variables x_1 and x_2

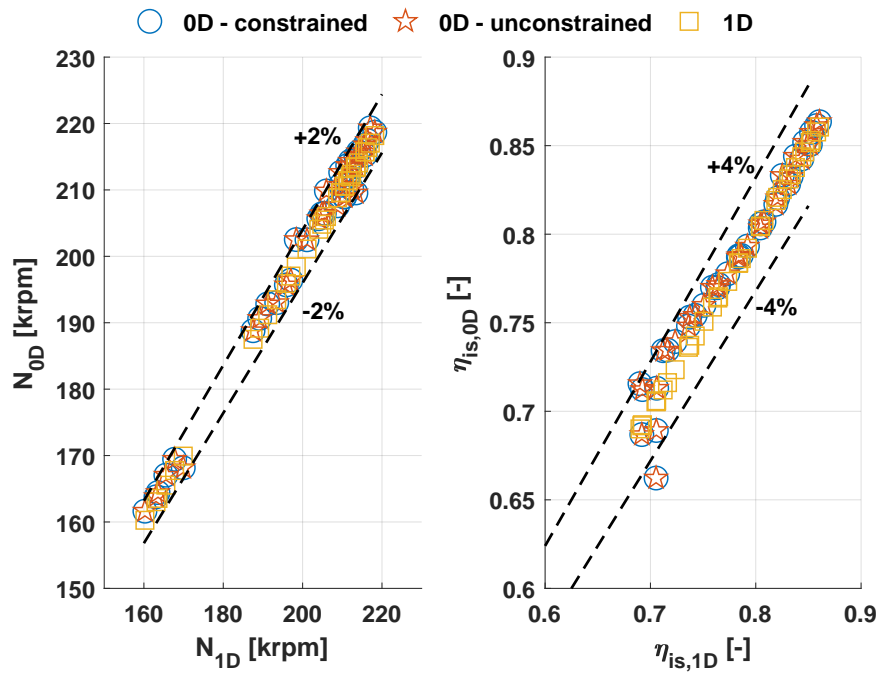
Figure 2.24a compares the optimum isentropic efficiencies and rotational speeds as a function of the pressure ratio resulting from both the 0D and the 1D models, for a constant ORC evaporator power of 22 kW. Both unconstrained and constrained solutions are displayed. As expected, the isentropic efficiency decreases with pressure ratio as a consequence of the increased nozzle, interspace, and tip clearance losses. Similarly, the rotational speed increases with the pressure ratio to match the new turbine power requirements. Compared to the 1D predictions, both the optimum 0D predicted rotational speeds and isentropic efficiencies are contained within a deviation band of ± 1 and $\pm 2.5\%$, respectively. Therefore, the prediction performance of the new 0D tool is remarkable, in particular considering the significant reduction in model order, since the evaluation time of the 0D model is in average 1500 times faster than the 1D mean line model.

Figure 2.24b compares the optimum rotor speeds and isentropic efficiencies obtained by the 0D and the 1D models independently of the evaporation power. The 1D and 0D based predictions are contained within a deviation band of ± 2 and $\pm 4\%$ for the rotor speed and the isentropic efficiency, respectively.

Finally, no significant difference occurs between the constrained and unconstrained solutions, meaning that the new radial turbine 0D models can be used on a wide range of operating conditions to pre-design small-scale radial inflow turbines without incurring significant prediction errors.



(a) Fixed ORC heat input at 22 kW



(b) Varied ORC heat input

Figure 2.24 – Comparison of the optimum rotational speeds and efficiencies between the 0D (constrained and unconstrained) and the 1D model with (a) fixed ORC heat input at 22 kW and (b) varied ORC heat input

2.5.7 Limitations of the turbine pre-design model

The updated 0D pre-design model for the radial turbine is generated through the evaluation of an experimentally validated 1D model and offer a significant reduction of the evaluation time (few orders of magnitude) while ensuring satisfactory accuracy due to the inclusion of the pressure ratio in the evaluation of the isentropic efficiency. This methodology presents, however, the following limitations:

- **Level of design detail** The new pre-design model includes the rotational speed N , the tip diameter D , and the shroud to tip radius ratio ϵ as design variables. Hence blade number, hub to shroud radius, and blade angles are fixed. Adding these variables in the pre-design model may yield higher turbine efficiencies and improved design flexibility.
- **Validity of the 1D enthalpy loss correlations** The 1D enthalpy losses have been calculated with empirical loss correlations, which have not been extensively studied in the small-scale domain. More experimental data on a broader range of turbine geometries, working fluids, and operating conditions are needed to further refine and validate the individual loss correlations at the reduced scale. In particular, an extended validation is required for pressure ratios above 4.2, for which the considered 1D model underestimates the isentropic efficiency compared to the experimental data as shown in Figure 2.4.
- **Choke condition at the turbine nozzle throat** The present method imposes the turbine to operate at the onset of choke. While this condition maximizes the work output by increasing the value of $C_{\theta 4}$ and avoids a mismatch between the nozzle and the rotor design, it may induce higher losses in the nozzle passage, in particular for low pressure ratios ($1.5 < PR < 3$), which could easily be achieved without a choked nozzle.
- **Off-design aspects** While the updated reduced order model offers a powerful pre-design tool, it cannot be used for rating off-design operations since it considers the adaptation of the nozzle outlet angle to each operating condition. Nonetheless, this shortcoming could be addressed with the use of variable nozzle geometries, in which the nozzle outlet angle could be adapted to each operating condition.

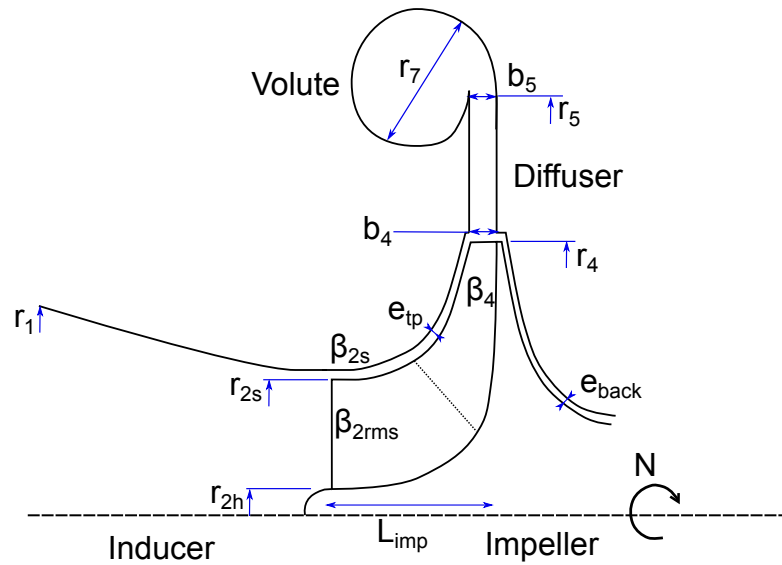


Figure 2.25 – 1D layout of a centrifugal compressor

2.6 Centrifugal compressor

2.6.1 Generation of the reduced order model

Figure 2.25 shows the layout of a centrifugal compressor, its main components, and the geometry parameters required for a mean-line (1D) evaluation. The centrifugal compressor 1D models are based on the same principles as the ones adapted for radial turbines. A 1D model written in MATLAB [73] and experimentally validated by Schiffmann [46] has been used for the generation of the compressor reduced order model. For a given geometry, the 1D model calculates the velocity triangles at the inlet and exhaust of each compressor station. The flow is corrected using the enthalpy loss collection introduced by Galvas [81], which includes: (1) The inducer losses, (2) the impeller losses including incidence, skin friction, blade loading, disc friction, and outlet recirculation losses, (3) the diffuser losses, and (4) the volute losses. In this work, the effect of the volute is neglected. The 1D model inputs are the compressor geometry and the thermodynamic inlet conditions. The outputs are the compressor performance, assessed by the total-to-total isentropic efficiency η_{is} and the achieved pressure ratio PR. In addition, the evaluated solutions are subject to the following constraints:

- In order to avoid flashing, the vapor quality must be above unity at each station.
- Choke and surge conditions are prohibited. When the flow is choked in the compressor passage, the system performs very poorly, while surge generates high unsteady flow regions, which might lead to the failure of the compressor system.
- The maximum pressure ratio is limited to 5 to stay within realistic values considering a single-stage centrifugal compressor.

Chapter 2. Pre-design models for small-scale radial turbomachinery

Table 2.3 presents the variables and their range that have been used to generate the compressor dataset. Note that only a subset of available geometry parameters is taken into account, including the tip radius r_4 and the blade height ratio $\zeta = \frac{b_4}{r_4}$. These dimensions are the main variables to adjust the outlet impeller flow passage area, which influence the enthalpy losses and the choke and surge limits. The other dimensions are defined as constant values or as dependent parameters based on best engineering practice [82] and on existing prototypes [35]. The ranges of the compressor mass flow rate \dot{m}_{comp} , tip radius r_4 , rotor speed N , and the evaporation temperature T_{evap} are adapted to domestic refrigeration applications (7–25 kW of heating capacity). Similarly to the radial turbine pre-design model, four organic working fluids (R134a, R245fa, R152a, and R600a) have been investigated.

Table 2.3 – Description of the inputs of the centrifugal compressor 1D model indicating the ranges considered for the generation of the reduced order model

Term	Symbol	Range	Unit
Model design variables			
Rotational speed	N	30-400	[krpm]
Rotor tip radius	r_4	5-75	[mm]
Impeller blade height ratio	b_4/r_4	0.015-0.3	[-]
Evaporation temperature	T_{evap}	-10-10	[°C]
Inlet super-heating	ΔT_{in}	5-20	[K]
Mass flow rate	\dot{m}_{comp}	20-400	[g.s ⁻¹]
Fixed parameters			
Impeller outlet angle	β_4	-40	[deg]
Impeller inlet angle	β_{2rms}	-45	[deg]
Impeller shroud inlet angle	β_{2s}	-60	[deg]
Inducer roughness	Ra_{ind}	1.2e-5	[-]
Impeller roughness	Ra_{imp}	1.2e-5	[-]
Compressor blades number	Z_{blades}	9	[-]
Compressor split blades number	Z_{split}	9	[-]
Dependent parameters			
Inducer inlet radius	r_1	$1.1r_{2s}$	[mm]
Impeller shroud radius	r_{2s}	$0.56r_4$	[mm]
Impeller hub radius	r_{2h}	$0.35r_{2s}$	[mm]
Vaneless diffuser outlet radius	r_5	$1.5r_4$	[mm]
Impeller tip clearance	e_{tp}	$\max(0.08, 0.02b_4)$	[mm]
Impeller back-face clearance	e_{back}	$\max(0.08, 0.02b_4)$	[mm]
Impeller length	L_{imp}	$1.5r_4$	[mm]

Using a Monte Carlo simulation approach, 200'000 randomly and equally distributed solutions are evaluated. A dataset of feasible compressor designs that satisfy the constraints previously mentioned is thus generated. From this dataset, a 5th degree polynomial model to predict the compressor performance is built as follows:

$$\eta_{is,comp} = f(Ns, Ds, \zeta, PR) \quad (2.15)$$

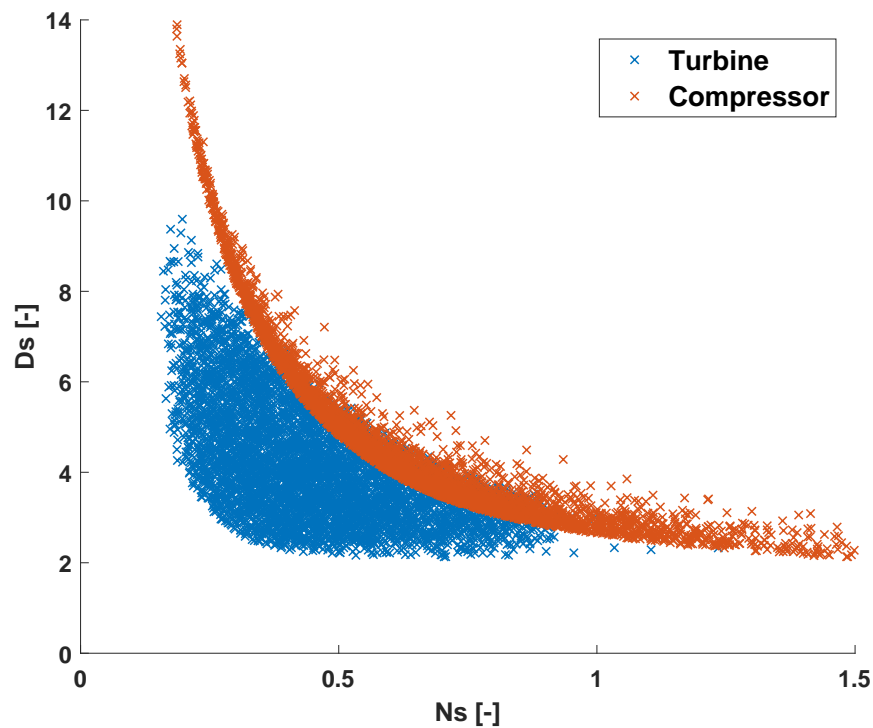


Figure 2.26 – Repartition of the compressor and turbine feasible points in a Ns-Ds diagram for R134a working fluid

With the remaining geometry variables set in Table 2.3, the compressor geometry is then fully characterized, i.e., the tip diameter, inlet and exhaust areas, and the required rotor speed are known.

2.6.2 Reduced order model in the Ns-Ds design space

Figure 2.26 represents the repartition of the feasible designs generated by the compressor dataset regardless of their efficiencies in a Ns-Ds diagram, together with the radial turbine dataset and for R134a working fluid. The plot suggests that, in contrast to radial turbines, the feasible compressor designs lie within a narrow band of Ns and Ds configurations, which echoes with the extensively cited Cordier line [58]. This is due to the compressor flow physics, which prevents sensible designs from existing in regions of low Ns and Ds, and vice versa [59]. It follows that the specific diameter can be expressed as a function of the previously identified model inputs without incurring significant errors.

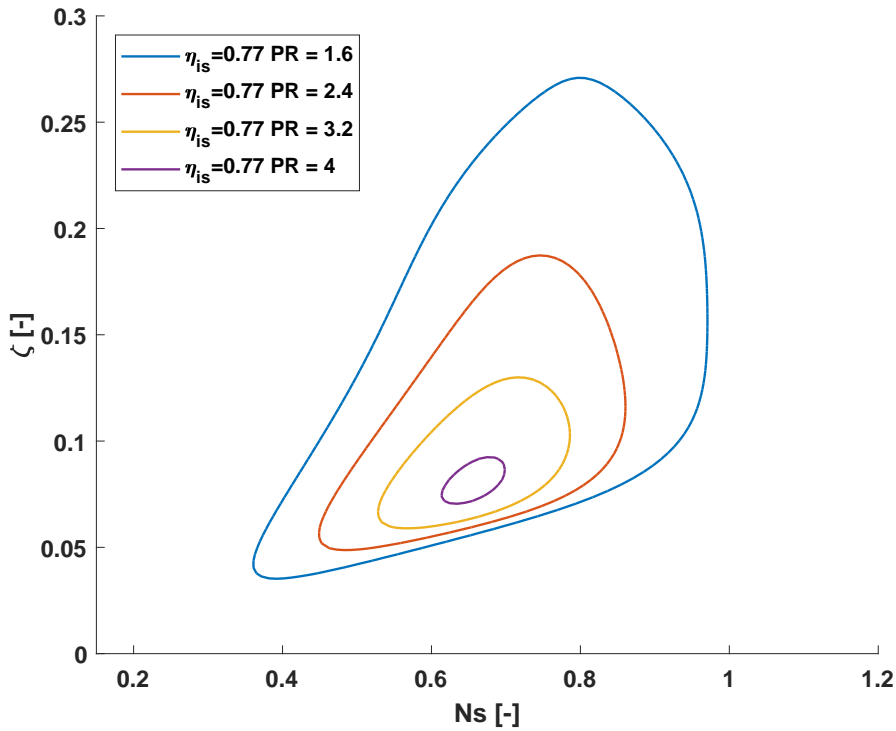
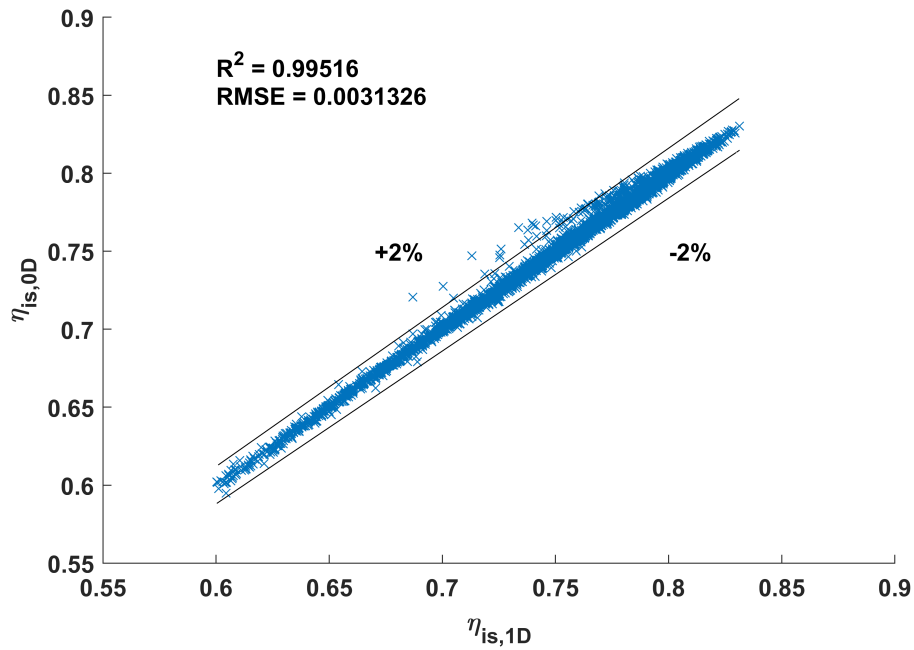


Figure 2.27 – 77% iso-efficiency contours in the compressor Ns - ζ diagram generated at different pressure ratios for R134a working fluid

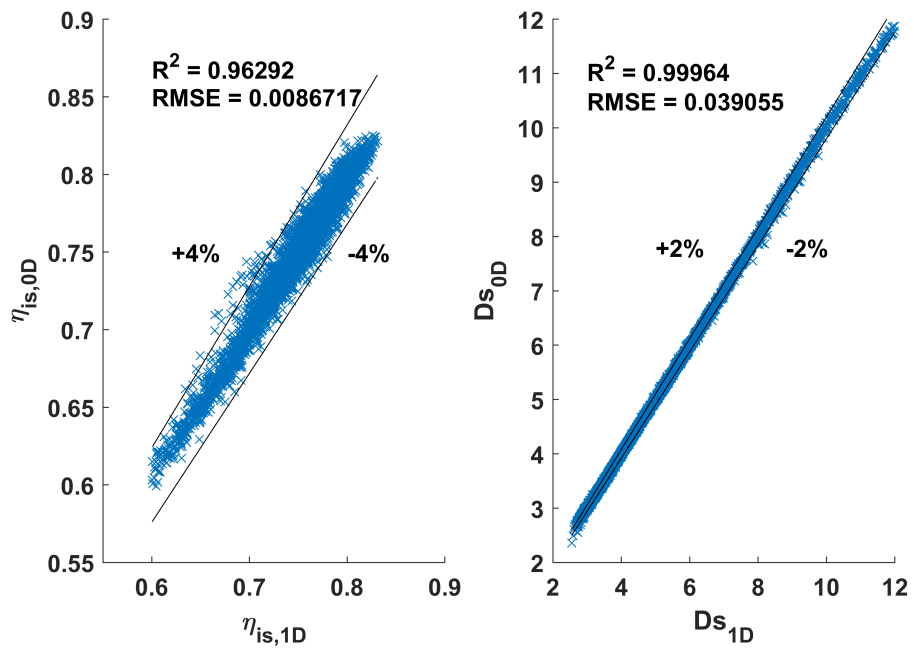
In light of the previous observations, two fitting methodologies are possible.

- A 5^{th} degree polynomial fit $\eta_{is} = f(Ns, Ds, PR, \zeta)$. This methodology allows optimizing Ns and Ds simultaneously although they lie within a narrow design space. The goodness of fit is represented in Figure 2.28a.
- Two 5^{th} degree decoupled polynomial fits $\eta_{is} = f(Ns, PR, \zeta)$ and $Ds = f(Ns, PR, \zeta)$. The goodness of fit corresponding to these two equations are shown in Figure 2.28b. This second procedure is less accurate due to the inherent regression errors that occur when correlating Ns and Ds . Since the number of parameters is decreased, the search for the compressor isentropic efficiency optimum is faster though.

Since Ns and Ds are correlated, there is no longer an interest in representing the compressor efficiency contours in a Ns - Ds diagram. An updated performance chart representing the isentropic efficiency in a Ns - ζ domain is proposed instead, as shown in Figure 2.27 for R134a working fluid. This first graph suggests (1) that different combinations of Ns and ζ are possible to achieve the same isentropic efficiency, and that (2) the surface covered by the Ns and ζ iso-efficiency lines decreases with increasing pressure ratio.



(a) $\eta_{is,0D} = f(Ns, Ds, PR, \zeta)$



(b) $\eta_{is,0D} = f(Ns, PR, \zeta)$ and $Ds_{0D} = f(Ns, PR, \zeta)$

Figure 2.28 – Goodness of fit: (a) $\eta_{is,0D} = f(Ns, Ds, PR, \zeta)$ model (b) $\eta_{is,0D} = f(Ns, PR, \zeta)$ and $Ds_{0D} = f(Ns, PR, \zeta)$ models - obtained for R134a working fluid

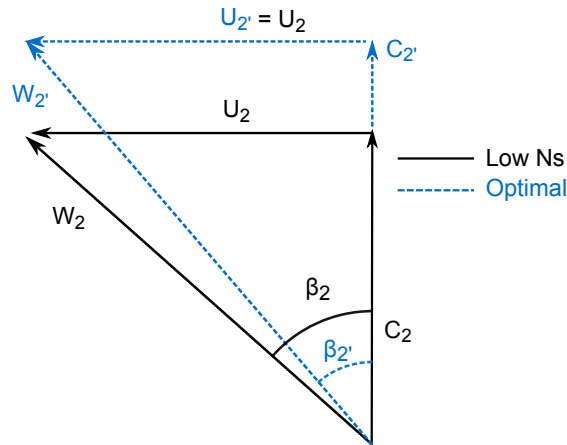


Figure 2.29 – Velocity triangle at the compressor impeller inlet assuming a zero-swirl at optimal and low Ns conditions

2.6.3 Influence of the compressor loss mechanisms on the efficiency contours

The following section aims at explaining the underlying phenomena that are shaping the efficiency contours of the compressor pre-design model in the Ns- ζ diagram shown in Figure 2.27. Each enthalpy loss normalized with the stage isentropic enthalpy rise is analyzed and superimposed on the efficiency contours in the Ns- ζ diagram. Only the losses occurring in the impeller are represented. The considered working fluid is R134a.

Internal impeller losses

The internal impeller losses include the incidence, skin friction, tip clearance, and blade loading losses.

Incidence losses The incidence losses are estimated with a correlation proposed by Galvas [81] and are represented in Figure 2.30, where it is observed that they increase towards low Ns values. The incidence loss correlation is given in equation 2.16.

$$\Delta h_{inc} = 0.5 [W_2 \sin(|\beta_2 - \beta_{2,opt}|)]^2 \quad (2.16)$$

The incidence losses are due to the deviation of the flow incidence from its optimum angle $\beta_{2,opt}$. At low specific speeds, the relative flow angle $\beta_2 = -\arctan \frac{U_2}{C_2}$ increases due to the decrease of the absolute inlet velocity $C_2 = \frac{\dot{m}_{comp}}{\pi(r_{2s}^2 - r_{2h}^2)\rho_2}$, as shown in the impeller inlet velocity triangle in Figure 2.29, which assumes zero-swirl conditions. The more β_2 moves away from its optimum value, the higher the incidence losses. With a fixed U_2 , β_2 is primarily driven by C_2 . Therefore, the incidence losses are linked to the mass flow rate and the impeller inlet area (a constant $\frac{r_{2s}}{r_4}$ is assumed here). When Ns decreases, \dot{m}_{comp} decreases as well, and since low specific speeds Ns correspond to high specific diameters Ds, the impeller inlet area tends to increase as well.

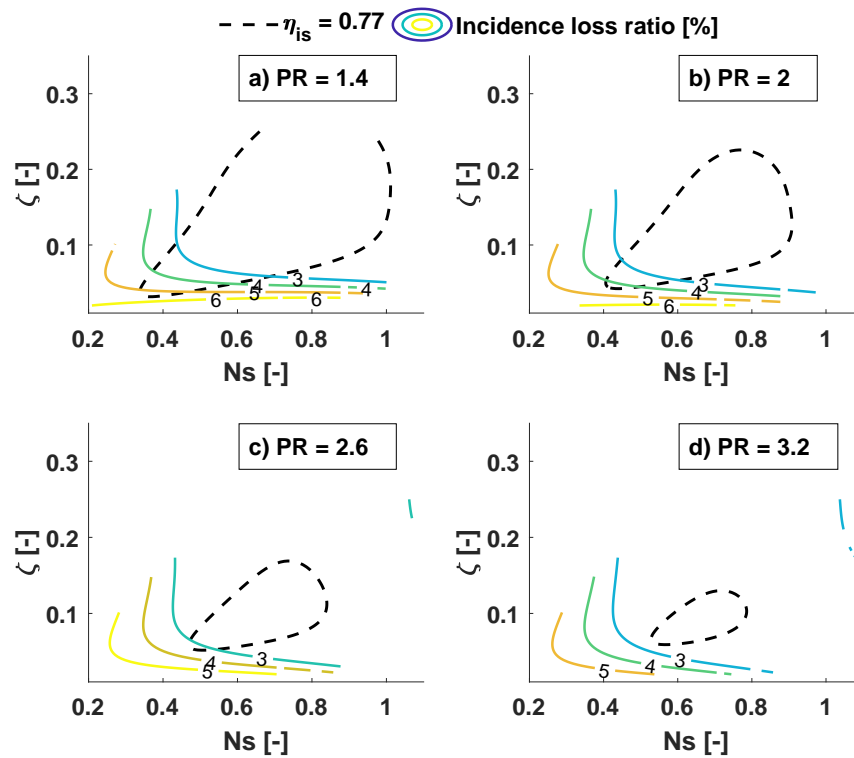


Figure 2.30 – Evolution of the compressor incidence loss ratio in the N_s - ζ diagram at different pressure ratios

Since the impeller inlet conditions are not affected by the pressure rise and by the discharge geometry, the pressure ratio and the blade height ratio ζ do not affect the incidence losses. On the other hand, while the incidence losses increase at low N_s , the relative inlet Mach number $M_{rel,2} = \frac{W_2}{a_2}$ increases at high N_s , as shown in Figure 2.31. This effect explains why the compressor performance is limited in regions of high N_s , where the flow comes closer to the choking limit at its inlet. When choosing the feasible range of N_s , a trade-off is thus to be met between high incidence losses and choked flow at the impeller inlet, when considering a constant $\frac{r_{2s}}{r_4}$.

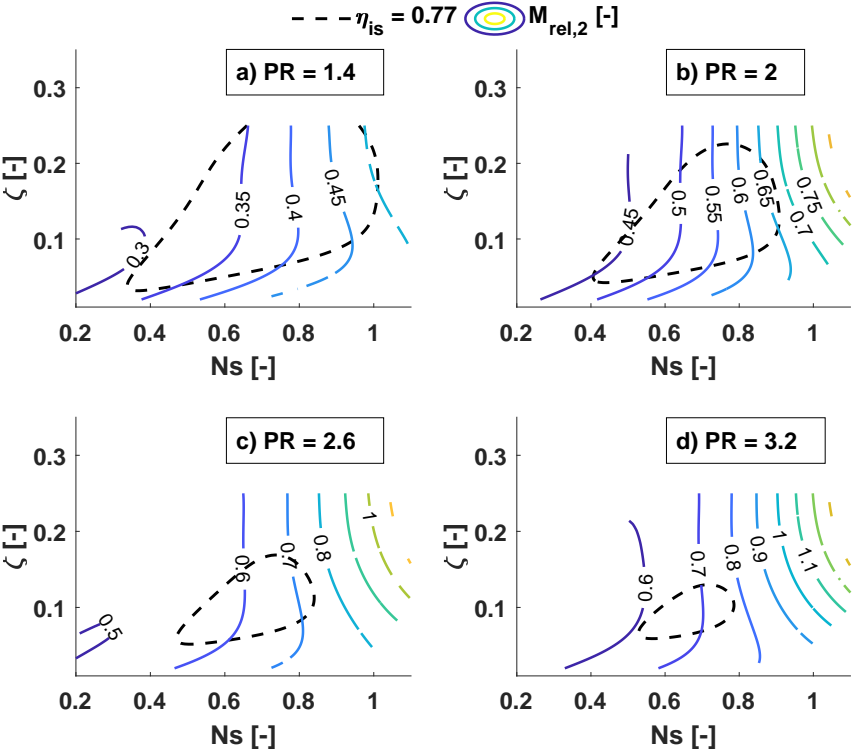


Figure 2.31 – Evolution of the relative Mach number at the compressor impeller inlet in the N_s - ζ diagram at different pressure ratios

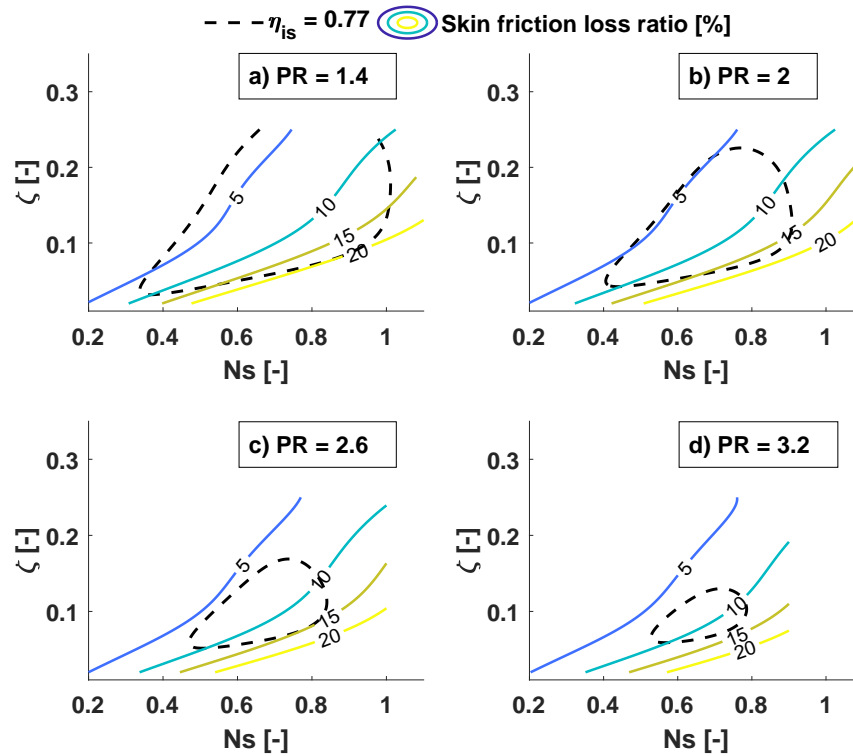


Figure 2.32 – Evolution of the compressor skin friction loss ratio in the N_s - ζ diagram at different pressure ratios

Skin friction losses Figure 2.32 represents the evolution of the skin friction loss ratio with N_s and ζ . These losses are described through the correlation proposed by Jansen [83] and Coppage [84] as follows:

$$\Delta h_{sf} = \frac{C_f L_h (W_4 + W_2)^2}{2d_h} \quad (2.17)$$

where d_h and L_h are the hydraulic diameter and channel length, and C_f the friction coefficient. The expression of C_f is given by Galvas [81]. The analysis shows that the skin friction losses are governed mainly by the relative outlet velocity W_4 , as corroborated by Figure 2.33, which represents the evolution of the impeller outlet relative Mach number $M_{rel,4} = \frac{W_4}{a_4}$ in the N_s - ζ diagram.

Figure 2.34 shows the velocity triangle at the compressor outlet at different operating conditions and for a fixed geometric impeller outlet angle β_4 . For a given β_4 and tip speed U_4 , W_4 is driven by $C_{m4} = \frac{\dot{m}_{comp}}{2\pi r_4 b_4 \rho_4}$. Therefore, W_4 increases with an augmentation of the mass flow and a diminution of the outlet surface area defined by $A_4 = 2\pi b_4 r_4$. These conditions are met at high specific speeds and low blade height ratio ζ . Finally, W_4 increases with pressure ratio to match the required compressor impeller work.

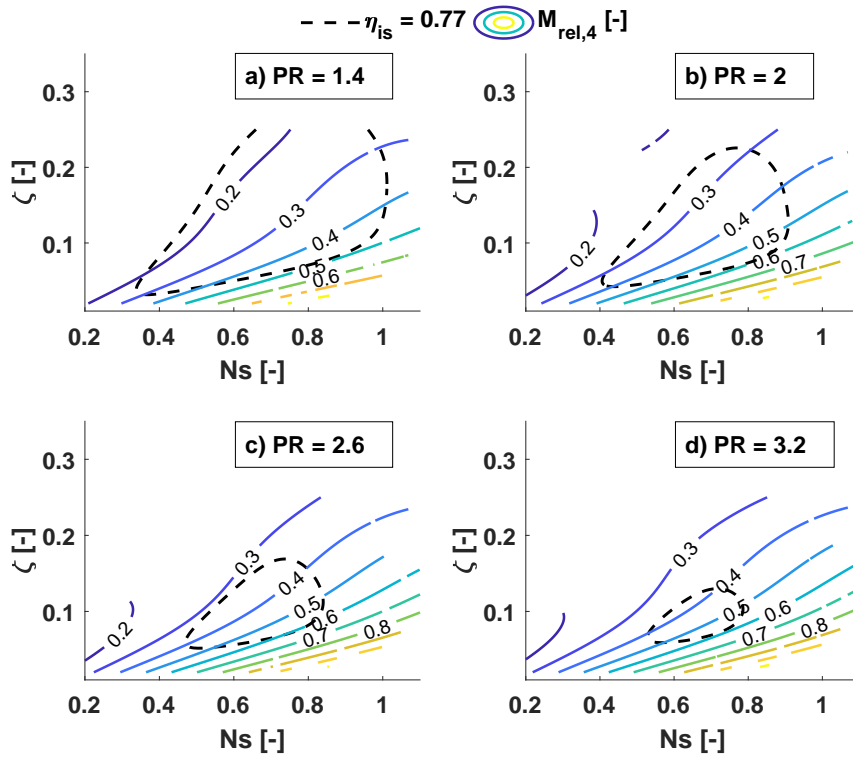


Figure 2.33 – Evolution of the relative Mach number at the compressor impeller outlet in the N_s - ζ diagram at different pressure ratios

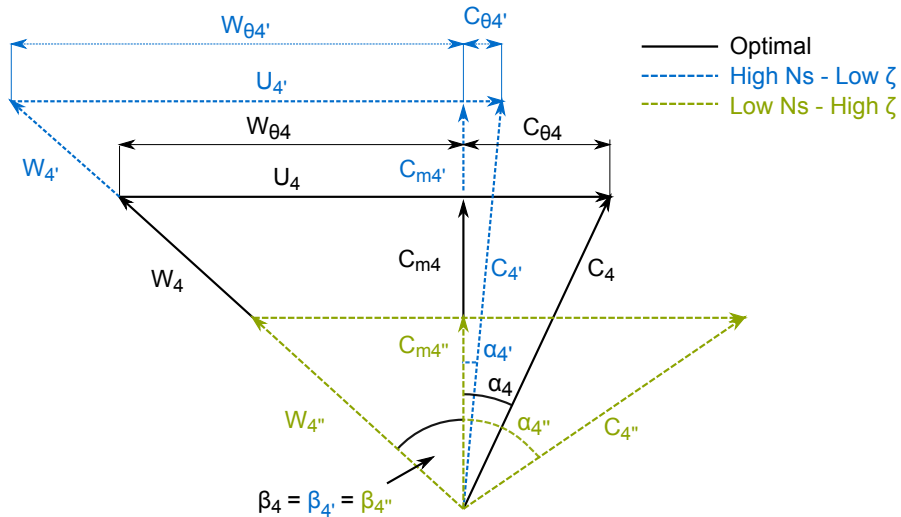


Figure 2.34 – Velocity triangle at the compressor impeller outlet assuming a fixed impeller outlet angle β_4 at optimal, high N_s -low ζ , and low N_s -high ζ conditions

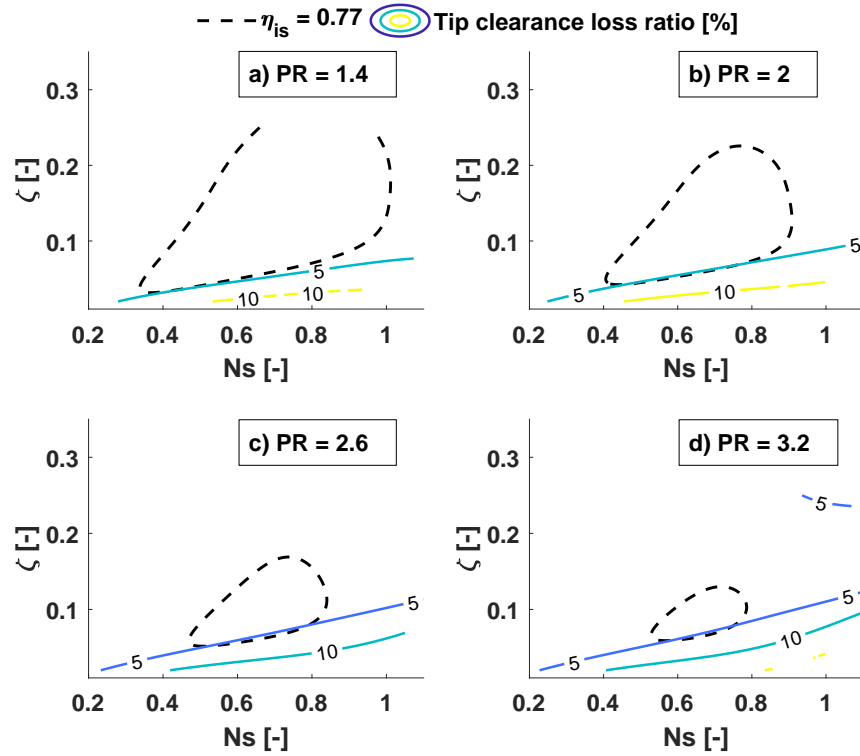


Figure 2.35 – Evolution of the compressor tip clearance loss ratio in the N_s - ζ diagram at different pressure ratios

Tip clearance losses The evolution of the tip clearance loss ratio with N_s and ζ is represented in Figure 2.35. These losses are evaluated using a model presented by Brasz [85], which is given in equation 2.18. Similarly to the skin friction losses, the tip clearance losses become dominant in the regions of high N_s and low ζ . The analysis identifies $\frac{C_{\theta 4} C_{m 2}}{b_4}$ as being the dominating term of the correlation, explaining why the losses increase at low $\zeta = \frac{b_4}{r_4}$ and high N_s due to the contribution of \dot{m}_{comp} in $C_{m 2}$. The reason why these losses increase with the pressure ratio is due to the contribution of $C_{\theta 4}$, which increases to match the required compressor work.

$$\Delta h_{cl} = 0.6 \frac{e_{tp} C_{\theta 4}}{b_4 + \frac{e_{tp}}{2}} \sqrt{\frac{4\pi C_{\theta 4} C_{m 2}}{\left(b_4 + \frac{e_{tp}}{2}\right) Z_{blades}} \left[\frac{r_{2s}^2 - r_{2h}^2}{(r_4 - r_{2s}) \left(1 + \frac{\rho_4}{\rho_2}\right)} \right]} \quad (2.18)$$

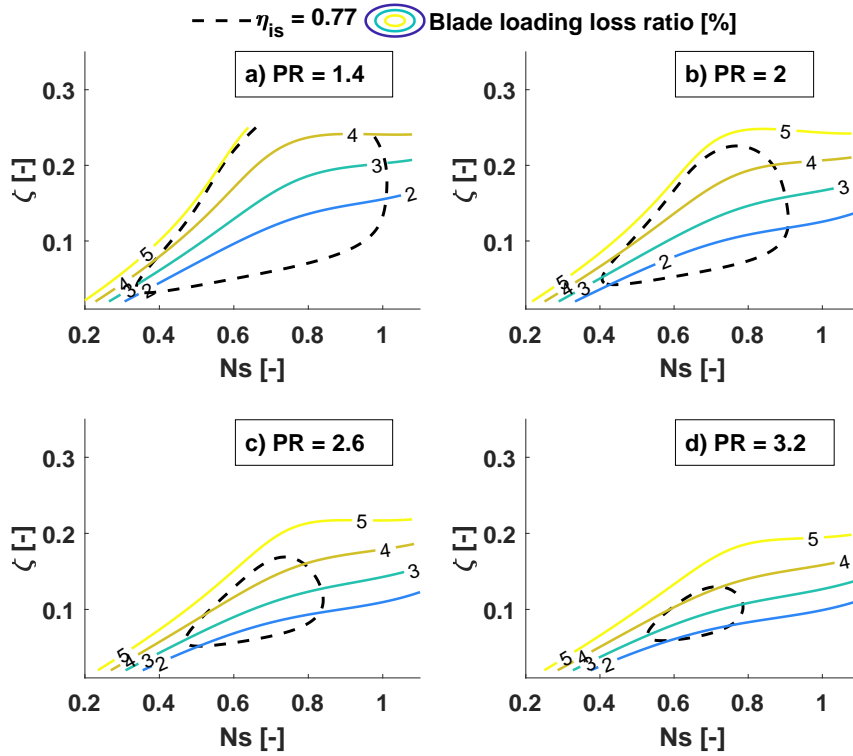


Figure 2.36 – Evolution of the compressor blade loading loss ratio in the N_s - ζ diagram at different pressure ratios

Blade loading losses The losses associated with blade loading in the impeller passage are estimated with the correlation proposed by Rodgers [86, 87] and are described by equation 2.19.

$$\Delta h_{bl} = 0.05 U_4^2 D_f^2 \quad (2.19)$$

When ζ increases and N_s decreases, leading to lower W_4 , the blade loading losses represented in Figure 2.36 increase. These losses describe the enthalpy rise depreciation caused by the boundary layer growth, the flow separation, and secondary flows in the impeller. This phenomenon is related to a diffusion coefficient D_f given by equation 2.20. Through the analysis of its different terms, the blade loading losses are driven mainly by $1 - \frac{W_4}{W_{2rms}}$ in the expression of D_f , explaining why they increase with dropping W_4 in Figure 2.36.

$$D_f = 1 - \frac{W_4}{W_{2rms}} + \frac{\pi r_4 \Delta h_{is}}{Z_{blades} L_h U_4 W_{2rms}} + 0.1 \frac{(r_{2s} - r_{2h} + b_4) \left(1 + \frac{W_4}{W_{2rms}}\right)}{2(r_4 - r_{2s})} \quad (2.20)$$

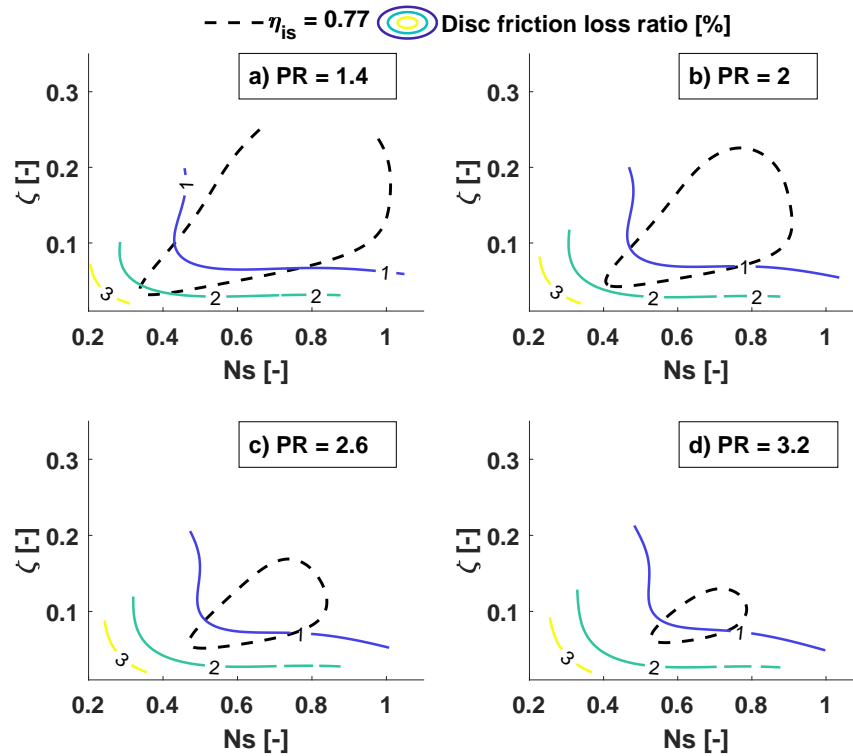


Figure 2.37 – Evolution of the compressor disc friction loss ratio in the N_s - ζ diagram at different pressure ratios

Impeller external losses

The previous enthalpy losses are categorized as internal losses, involving both an entropy rise and a pressure drop at the impeller outlet. The external losses do not affect the pressure at the compressor outlet but increase the enthalpy rise needed to satisfy the compressor work, and hence depreciate the isentropic efficiency. Figures 2.37 and 2.38 represent the evolution of the disc friction and recirculation losses in the N_s - ζ diagram.

Disc friction losses The disc friction losses are evaluated with a model proposed by Daily and Nece [88] and are given in equation 2.21. These losses are dominated by $\frac{r_4^3}{\dot{m}_{comp}}$, which increases in regions of high D_s values, and hence in regions of low N_s values. However, the disc friction losses are much smaller than all other enthalpy losses.

$$\Delta h_{df} = 0.25 \rho_4 U_4^3 r_4^2 K_f \frac{1}{\dot{m}_{comp}} \quad (2.21)$$

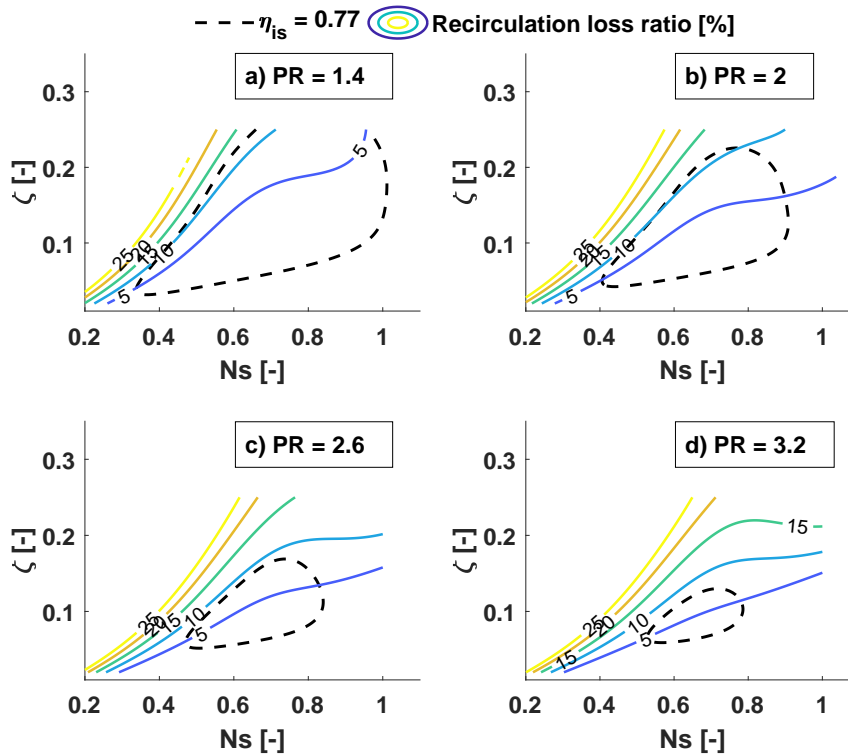


Figure 2.38 – Evolution of the compressor recirculation loss ratio in the N_s - ζ diagram at different pressure ratios

Recirculation losses The recirculation losses have been approached by Coppage et al. [84] and are described by equation 2.22. These losses describe the compressor work depreciation in regions where the flow at the compressor outlet does not have enough kinetic energy to overcome the pressure rise in the diffuser. These losses are governed mainly by the diffusion factor D_f defined in equation 2.20, and hence increase in regions of high ζ and low N_s values, which correspond to low relative velocities W_4 . Furthermore, since the recirculation losses are also influenced by the absolute flow angle $\alpha_4 = \arctan \frac{C_{\theta 4}}{C_{m4}}$ this effect is emphasized even further, due to the increase of α_4 with decreasing W_4 (see Figure 2.34), eventually leading to surge [89].

$$\Delta h_{rc} = 0.02 D_f^2 U_4^2 \tan(\alpha_4) \quad (2.22)$$

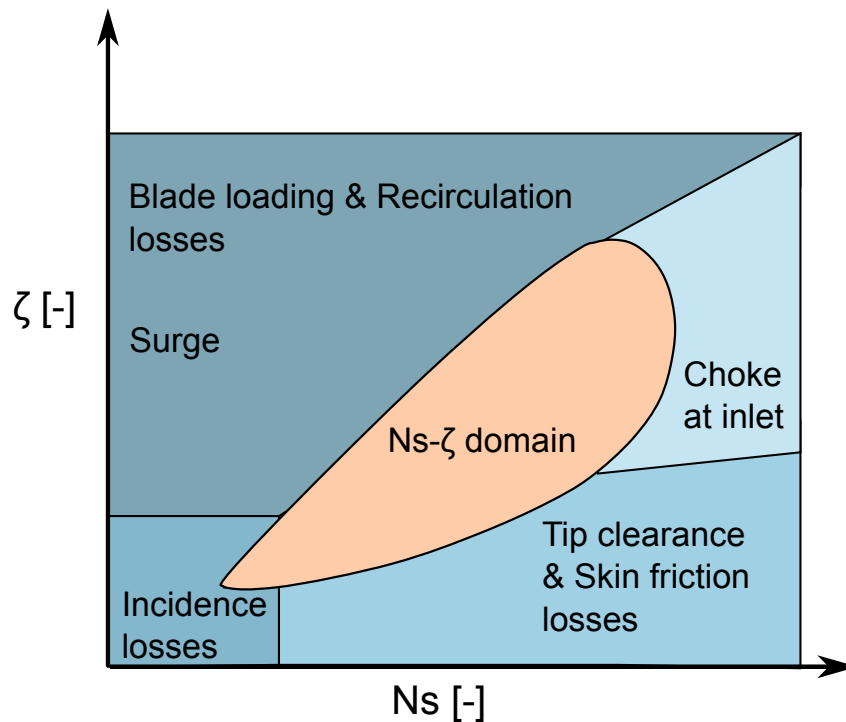


Figure 2.39 – Underlying phenomena shaping the efficiency contours of the compressor pre-design model in the N_s - ζ diagram

Summary

Similarly to the radial turbine, analyzing each loss mechanism individually along the compressor flow has allowed identifying the key aerodynamic phenomena that influence the shape of the compressor efficiency contours in the N_s - ζ diagram.

- The skin friction and tip clearance losses prevail in regions of high N_s and low ζ . This is the consequence of an increased relative outlet velocity W_4 .
- With decreasing N_s and increasing ζ , W_4 decreases, leading to increased blade loading and recirculation losses.
- The incidence and disc friction losses prevent efficient compressor operation at low specific speeds N_s .
- The choke limit at the impeller inlet prevents the compressor to operate at high specific speeds N_s .

Figure 2.39 summarizes these limitations and the corresponding loss mechanisms in the N_s - ζ diagram.

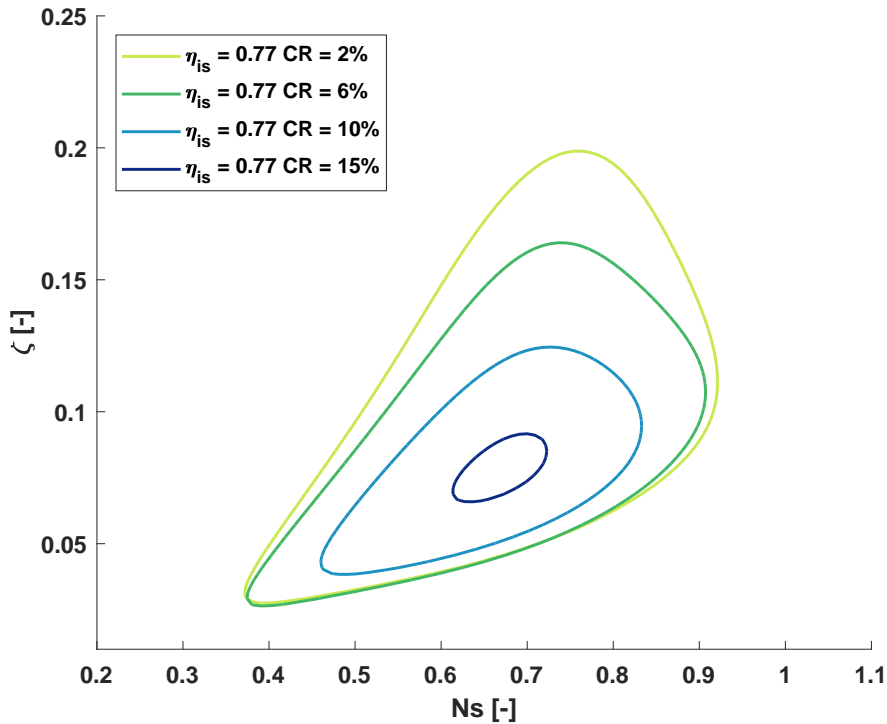


Figure 2.40 – Influence of the tip clearance ratio CR on the compressor efficiency contours at PR=2.5

2.6.4 Sensitivity analysis

The updated compressor reduced order model considers the compressor tip diameter and the blade height to tip radius ratio $\zeta = \frac{b_4}{r_4}$ as geometry inputs. The following section presents a sensitivity analysis highlighting the influence of two additional compressor dimensions: The tip clearance ratio $CR = \frac{e_{tp}}{b_4}$ and the shroud to tip radius ratio $\epsilon = r_{2s}/r_4$. The considered working fluid is R134a.

Figure 2.40 shows the influence of the tip clearance ratio, defined by $CR = \frac{e_{tp}}{b_4}$, on the model efficiency contours for a pressure ratio of 2.5. In this case, the minimum clearance limit at $80 \mu\text{m}$ was removed to capture better the effect of the clearance ratio on the efficiency. The efficiency contours suggest that the higher the clearance ratio, the smaller the surface covered by Ns and ζ , due to the impact of the tip clearance losses, which increase with $\frac{e_{tp}}{b_4}$ (equation 2.18). These results suggest that this parameter should be as small as possible.

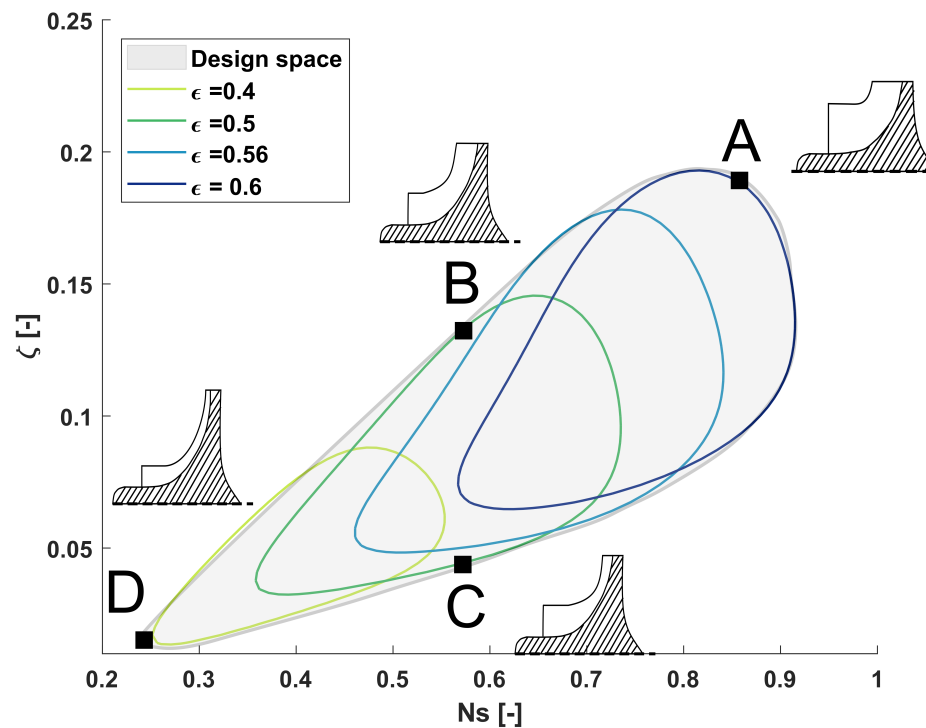


Figure 2.41 – 77% iso-efficiency contours in the compressor N_s - ζ diagram at $PR=2.5$ and varying $\epsilon = \frac{r_{2s}}{r_4}$

The previous results were performed with a fixed shroud to tip radius ratio $\epsilon = \frac{r_{2s}}{r_4} = 0.56$. Figure 2.41 shows the influence of ϵ , ranging from 0.4 to 0.6, on the centrifugal compressor performance in the N_s - ζ domain, and at a pressure ratio of 2.5. The results suggest that tuning this geometry parameter allows covering a wider design space since it adapts the flow conditions at the impeller inlet. If ϵ increases, higher mass flows can enter the compressor before choke occurs, hence extending the design domain towards higher specific speeds. However, the absolute velocity C_2 gets lower, and hence incidence losses increase at low N_s as explained above. On the other hand, decreasing ϵ will mitigate the blade loading and incidence losses (improved inlet design) and hence allow to explore lower N_s regions, at the penalty of decreasing the limit to choke though.

Points A to D in Figure 2.41 present possible compressor designs that achieve the same efficiency. Compressor geometries of type C present high tip radii, small shroud to tip radius ratios, and low blade height ratios, resulting in long and narrow compressor blade channels. On the other hand, compressors of type A, which yield the same performance as type C, present an entirely different geometry, with smaller tip radii and shorter yet larger blade channels. This flexibility in geometrical design is obtained by varying the repartition of enthalpy losses and margins to choke and surge within the compressor design space.

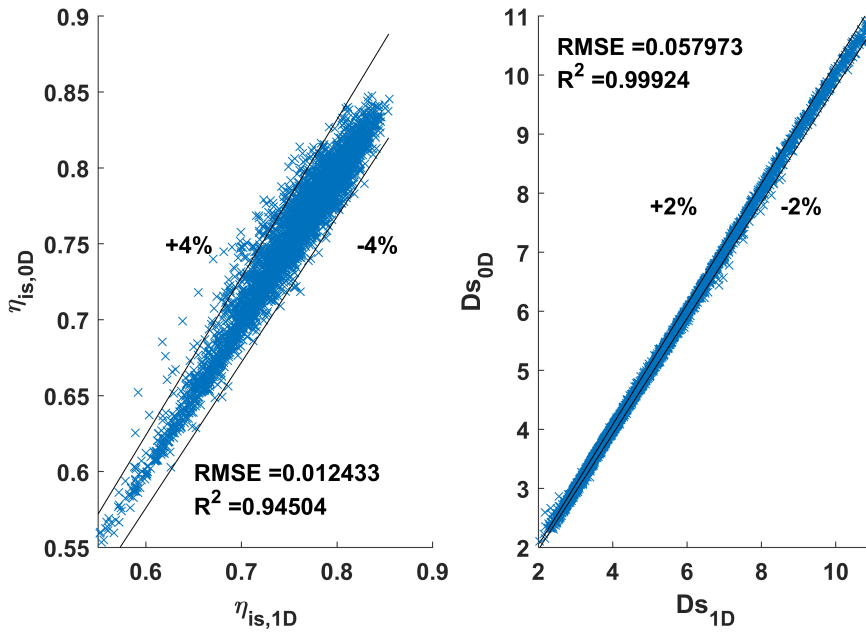


Figure 2.42 – Goodness of fit of the $\eta_{is,0D} = f(Ns, PR, \zeta, \epsilon)$ and $Ds_{0D} = f(Ns, PR, \zeta, \epsilon)$ models

In order to take into account the shroud to tip radius ratio in the pre-design phase, new sets of equations can be built as follows:

- For each ϵ value, a 5th degree polynomial fit $\eta_{is,\epsilon=[0.4,0.5,0.56,0.6]} = f(Ns, PR, \zeta)$ is implemented. The designer can evaluate the isentropic efficiency for each ϵ and select the one offering the best system efficiency. All these functions have similar goodness of fit than the one highlighted in Figure 2.28b.
- The ϵ parameter can be implemented in the model, thus leading to a 6th order polynomial fit $\eta_{is} = f(Ns, PR, \zeta, \epsilon)$ and $Ds = f(Ns, PR, \zeta, \epsilon)$. The goodness of fit of the two models are presented in Figure 2.42. Using this model offers more flexibility in the choice of ϵ and could lead to better design trade-offs. However, the fit is less accurate due to the addition of one model parameter and might increase the complexity of the pre-design exploration.

2.6.5 Comparison with literature

Using the reduced order models presented above, the best efficiency designs can be retrieved and compared with the existing pre-design methods available in literature. Figure 2.43 presents the optimum efficiencies and specific diameters versus the specific speeds, comparing the proposed model, obtained with R134a working fluid, with the expressions given by Balje and Cordier. The $\eta_{is} = f(Ns, PR, \zeta, \epsilon)$ and $Ds = f(Ns, PR, \zeta, \epsilon)$ models are used. According to Balje, a specific speed around one is optimal for centrifugal compressors. However, discrepancies are observed since the new model, which is adapted to small-scale turbomachinery, draws an optimum for specific speeds between 0.35 and 0.45. The maximum efficiency achieved by Balje is also higher than the ones obtained with the present pre-design model (0.87 against 0.82 for a pressure ratio of 3.2), which is a consequence of the reduced scale application. It is noted, however, that the qualitative shape of the efficiency curves remain comparable, suggesting that the trade-offs between the different loss mechanisms remain similar, yet leading to a shift in optimality.

The discrepancies between the Ns-Ds correlations are also significant, especially at high specific speeds where deviations up to 25% are highlighted. Furthermore, in the Ns-Ds diagram, the pressure ratio has no significant influence on the predicted curves, which all collapse into a single line –annotated by “0D model”. On the other hand, the isentropic efficiency plotted as a function of the specific speed in the right-hand graph of Figure 2.43 shows a clear variation with pressure rise. This is in agreement with observations made by Rodgers [90], who suggests both a drop in efficiency with increasing pressure ratio and a shift of optimum efficiency towards lower specific speeds compared to Balje. These graphs are, therefore, questioning the validity of the correlations proposed in the current literature for the targeted application.

In addition to prior work, the new pre-design model provides the values of ζ and ϵ that achieve the best isentropic compressor efficiency for each Ns, as shown in Figure 2.44 for a fixed pressure ratio of 2.5. The results suggest that a low specific speed machine requires high Ds, low ζ and ϵ , and vice versa when operating at high specific speeds. The optimum design curves of Figure 2.44 offer an alternative to the methods available in literature and can be used to start the compressor design procedure. However, note that using the design curves of Figure 2.44 does not offer the increased design flexibility provided by the presented reduced order model, which allows the fine-tuning of the compressor rotor speed N, tip diameter D, and geometry parameters ζ and ϵ . Indeed, this increased design flexibility is of great interest when other constraints such as rotordynamic stability, off-design effects or rotor speeds matching have to be met.

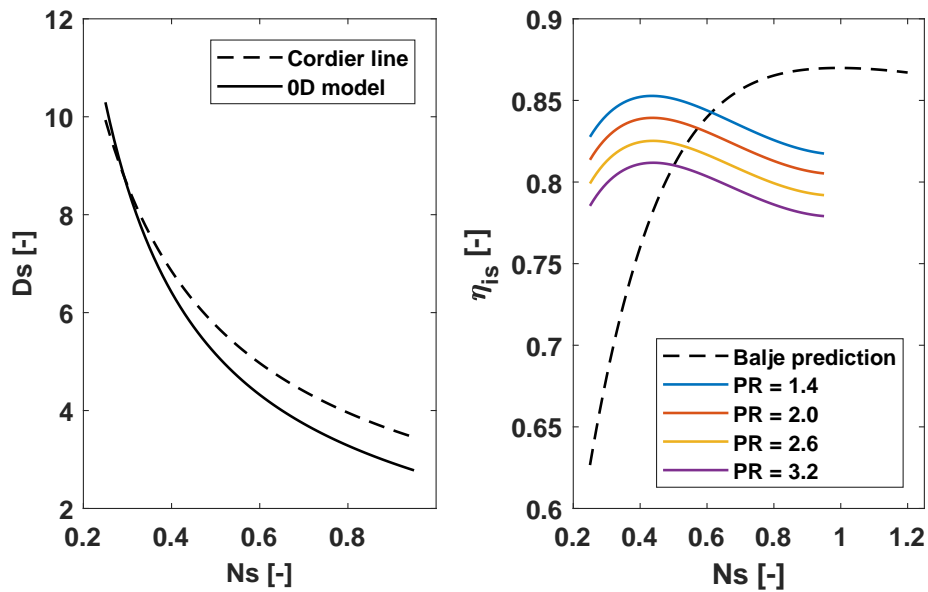


Figure 2.43 – Comparison of the predicted optimum D_s with respect to the Cordier line [58, 59] (left) and of the predicted best efficiency with respect to Balje’s prediction [57] (right)

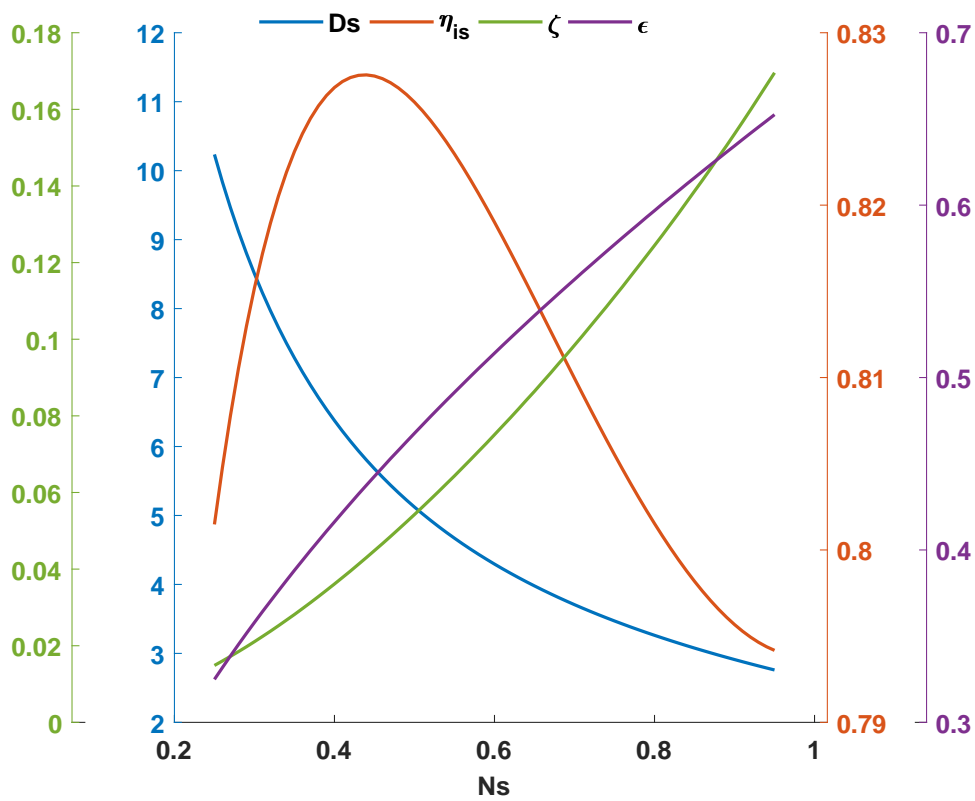


Figure 2.44 – Optimum D_s , ζ , ϵ , and η_{is} for the best efficiency points along N_s for PR=2.5

2.6.6 Influence of the working fluid

The analyses presented above were valid for R134a working fluid. On the contrary to the radial turbine pre-design model, discrepancies occur in the pre-design model efficiency contours depending on the working fluid, as shown in Figures 2.45a and 2.45b, which display the $\eta_{is} = f(Ns, PR, \zeta)$ and $Ds = f(Ns, PR, \zeta)$ contours for different working fluids and pressure ratios.

If the contours of $Ds = f(Ns, PR, \zeta)$ are similar from one fluid to the other, non-negligible variations are observed when estimating the efficiency. As a consequence, if a global model $\eta_{is} = f(Ns, PR, \zeta)$ is made based on a dataset built with a collection of the proposed fluid data (R134a, R152a, R600a, and R245fa), the goodness of fit represented in Figure 2.46a is obtained, which is lower than the ones obtained based on R134a as shown in Figure 2.28b (RMSE of 0.01 instead of 0.008, and R^2 of 0.93 instead of 0.96).

This resulting inaccuracy is triggered mainly by the limit imposing minimum clearances of $80 \mu\text{m}$, which may lead to clearance ratios above 2% of the blade height. This is confirmed by the evolution of the tip clearance losses for the four different working fluids evaluated at a pressure ratio of 2.5, as shown in Figure 2.46b. At similar operating conditions, the diameter of R245fa will be higher due to its lower density. The $80 \mu\text{m}$ limit is then less likely to be activated than for the other fluids. When operating with different working fluids, either a specific correlation should be used for each fluid, or one should consider the clearance ratio as an additional variable of the pre-design model.

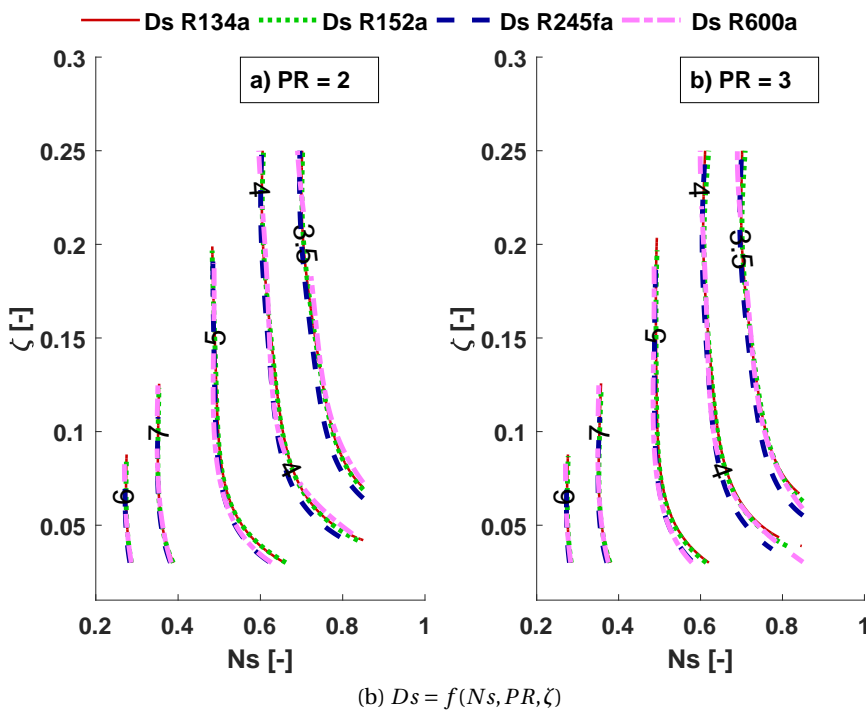
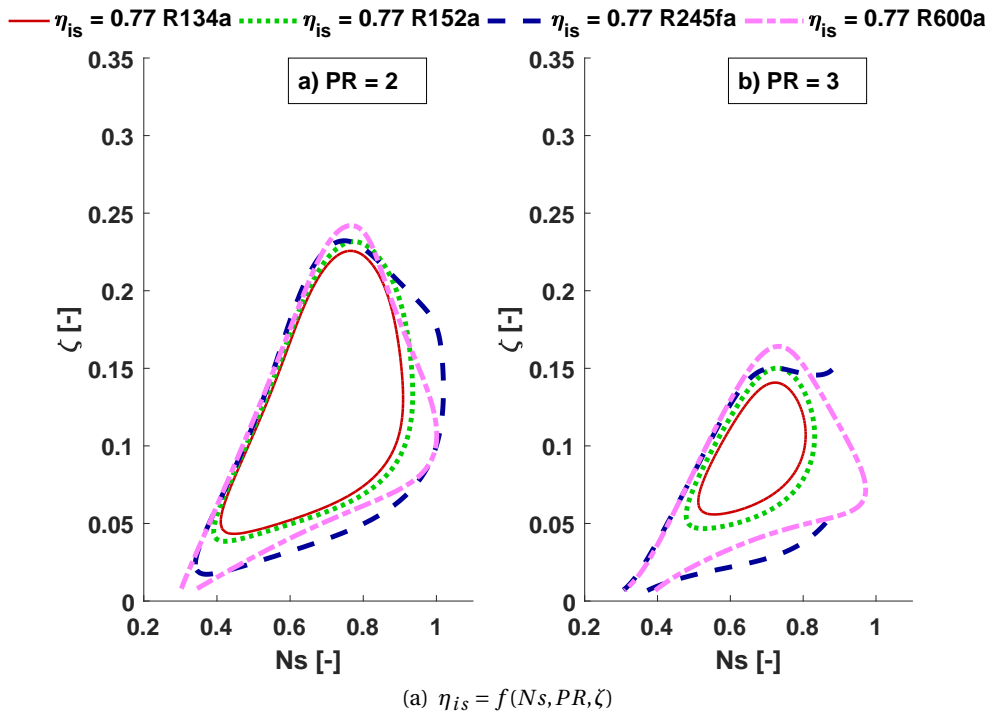
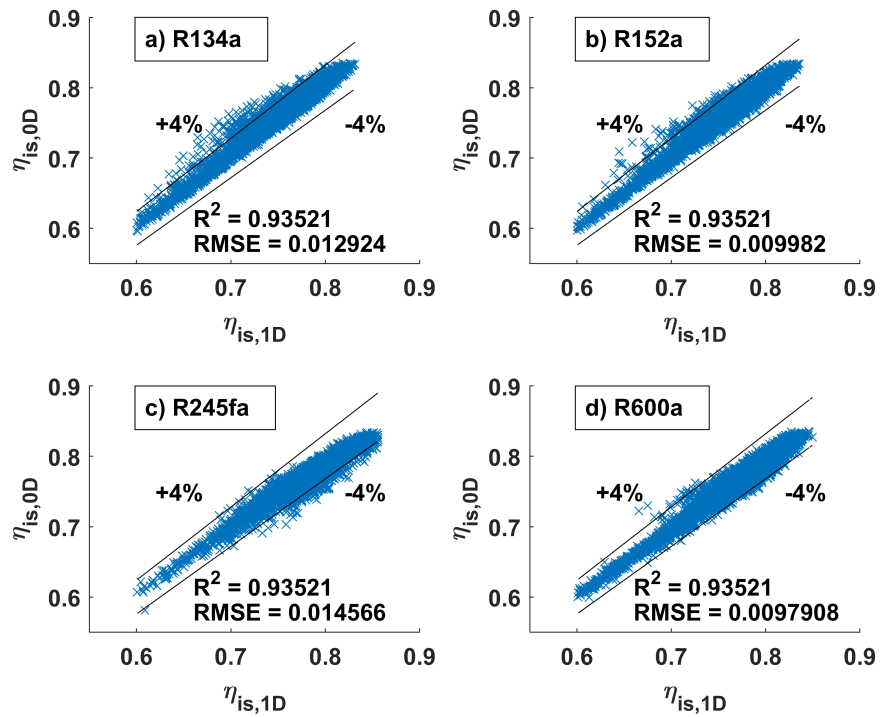
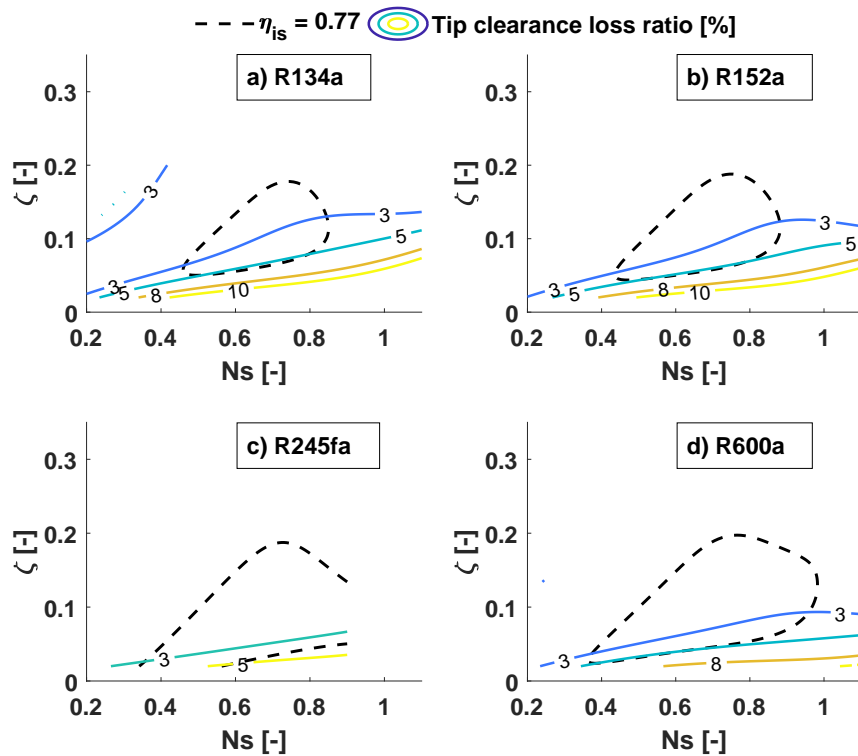


Figure 2.45 – (a) Isentropic efficiencies and (b) specific diameters in the Ns - ζ domain at different working fluids and pressure ratios



(a) Goodness of fit of $\eta_{is} = f(Ns, PR, \zeta)$ for different working fluids



(b) Tip clearance loss ratio for different working fluids a PR=2.5

Figure 2.46 – (a) Goodness of fit of the $\eta_{is,0D} = f(Ns, PR, \zeta)$ model (based on a dataset built with a collection of the proposed fluid data) for different working fluids and (b) evolution of the compressor tip clearance loss ratio in the Ns - ζ diagram

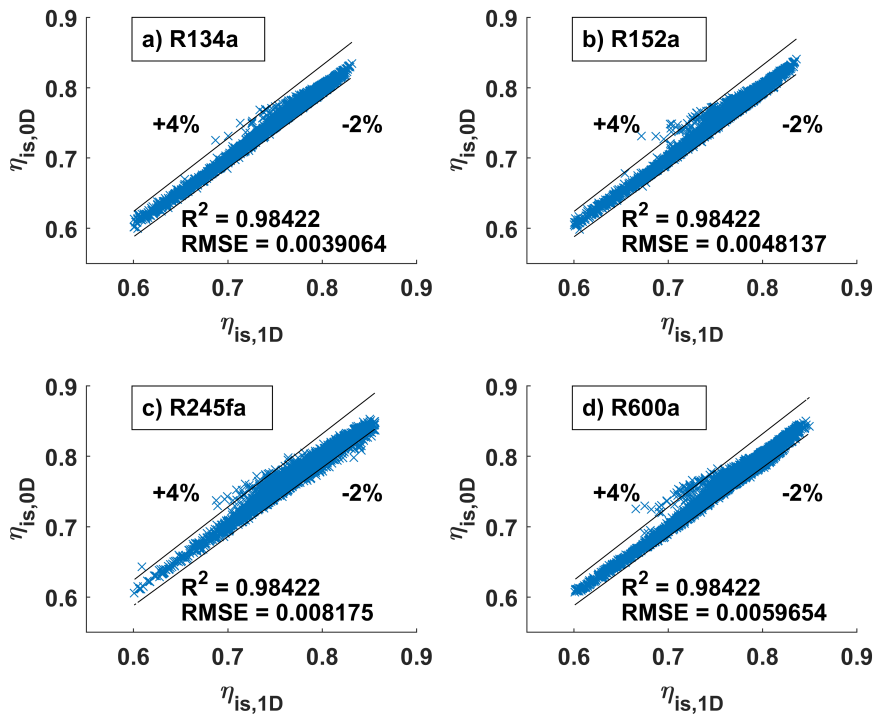


Figure 2.47 – Goodness of fit of the $\eta_{is,0D} = f(Ns, PR, \zeta, CR)$ model for different working fluids

Therefore, a new equation of the form $\eta_{is} = f(Ns, PR, \zeta, CR)$ is built. The corresponding goodness of fit when applied to each working fluid are shown in Figure 2.47, presenting higher R^2 and lower RMSEs than when the clearance ratio is not included (see Figure 2.46a). In addition, this new model presents a better accuracy for R134a than the $\eta_{is} = f(Ns, PR, \zeta)$ model shown in Figure 2.28b.

2.6.7 Pre-design model validation

In order to assess the validity of the proposed compressor pre-design (0D) model, the isentropic efficiency ratings evaluated by the 0D and the 1D models are compared. Different operating points within the conditions summarized in Table 2.4 have been assessed, which correspond to typical values of a residential heat pump cycle. For each operating point, the specific speed N_s and the blade height ratio ζ that maximize the isentropic efficiency are retrieved and then fed into the 1D model.

Table 2.4 – Boundary conditions for the compressor pre-design model validation

Term	Range	Unit
HP evaporator power	5-20	[kW]
Compressor inlet temperature	15	[°C]
HP evaporation temperature	5	[°C]
Compressor pressure ratio	2-4.5	[-]
Compressor tip diameter	20	[mm]
Working Fluid	R134a	[-]

Figure 2.48 compares both the optimum isentropic efficiencies and rotational speeds as a function of the pressure ratio resulting from both the 0D ($\eta_{is} = f(N_s, PR, \zeta, CR)$ & $D_s = f(N_s, PR, \zeta, CR)$) and 1D models for a constant HP evaporator power of 12 kW. The models with a fixed ϵ of 0.56 have been tested, and similarly to the radial turbine evaluation, both constrained and unconstrained 0D solutions are displayed.

As expected, the isentropic efficiency decreases with pressure ratio as a consequence of the increased losses. Similarly, the rotational speed increases with the pressure ratio to match the compressor power requirements. Compared to the 1D predictions both the optimum constrained 0D rotational speeds and isentropic efficiencies are contained within a deviation band below $\pm 1\%$ and $\pm 2\%$, suggesting an excellent agreement between the 0D and the 1D method.

However, in contrast to the turbine evaluation, a significant discrepancy occurs between the unconstrained and constrained solutions. The unconstrained isentropic efficiency is constant and always at its optimum independently of the operating point. The reasons are twofold: (1) The 5th order polynomial fit is diverging outside the dataset on which the model is built, and (2) the compressor is characterized by unfeasible operating regions (choke and surge). Therefore, as highlighted in Figure 2.49, which shows the model efficiency contours overlaying the original dataset and its convex hull, using the model blindly cannot render the compressor flow physics described in the 1D model. It is thus paramount to validate the optimum solutions with the original dataset by using a classification method, such as the convex hull used in this work (equation 2.14). This imposes additional constraints to the designer since the access to the convex hull inequality equations is required. Yet, the 0D method has an evaluation time 1500 times faster than the 1D approach, hence offering a significant advantage when embodied in simulations requiring many iterations.

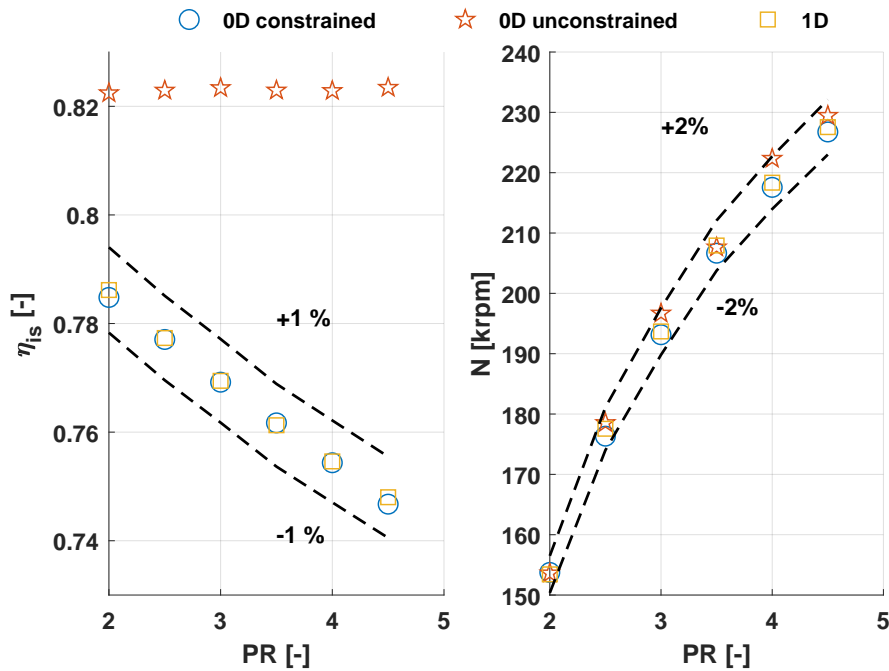


Figure 2.48 – Comparison of the optimum rotational speeds and efficiencies versus the pressure ratio between the 0D (constrained and unconstrained solutions) and the 1D model for a centrifugal compressor operating at a fixed HP evaporator power of 12 kW

Figure 2.50 compares the optimum rotor speeds and isentropic efficiencies obtained by the 0D and the 1D models this time independently of the HP evaporator power. Again, the results suggest a very good match between the 1D and 0D based predictions since they are contained within a deviation band of ± 1.5 and $\pm 3\%$ for the isentropic efficiency and the rotor speed, respectively.

Finally, Figure 2.51 captures the model validation for different working fluids, using the model equations $\eta_{is} = f(Ns, PR, \zeta, CR)$ and $Ds = f(Ns, PR, \zeta, CR)$. 100 equally distributed thermodynamic conditions within the ranges defined in Table 2.4 were simulated, at the difference that the tip diameter of the compressor is this time optimized as well. The deviation between the 0D and the 1D models is always below 2.5%, showing a good agreement with the 1D model for the four working fluids. R245fa presents the highest deviation, due to the construction of the $\eta_{is} = f(Ns, PR, \zeta, CR)$ model, which is built from the collection of R245fa, R134a, R600a, and R152a compressor data. Since R134a, R152a, and R600a have more thermodynamic similarities than with R245fa, the accuracy of the model is penalized when R245fa is used.

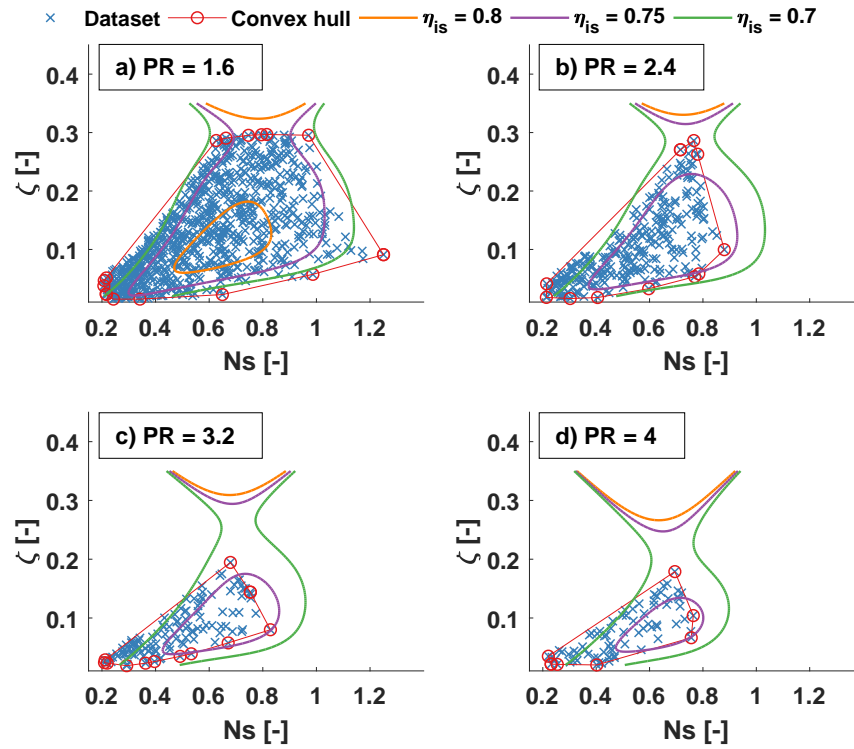


Figure 2.49 – Efficiency contours of $\eta_{is} = f(N_s, PR, \zeta)$ versus the the original dataset

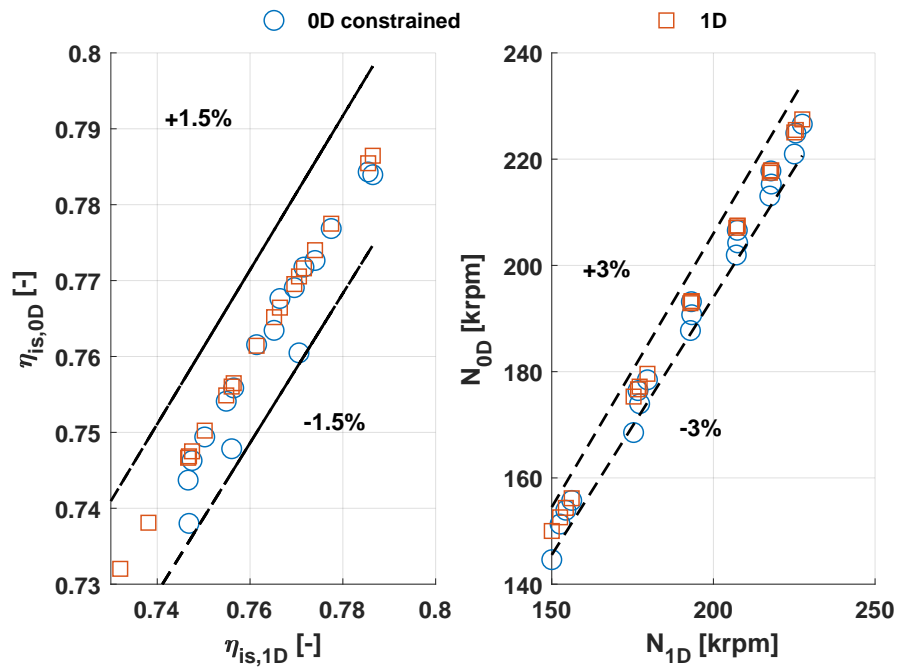


Figure 2.50 – Comparison of the optimum rotational speeds and efficiencies between the 0D and the 1D model for a centrifugal compressor operating at different HP evaporator powers

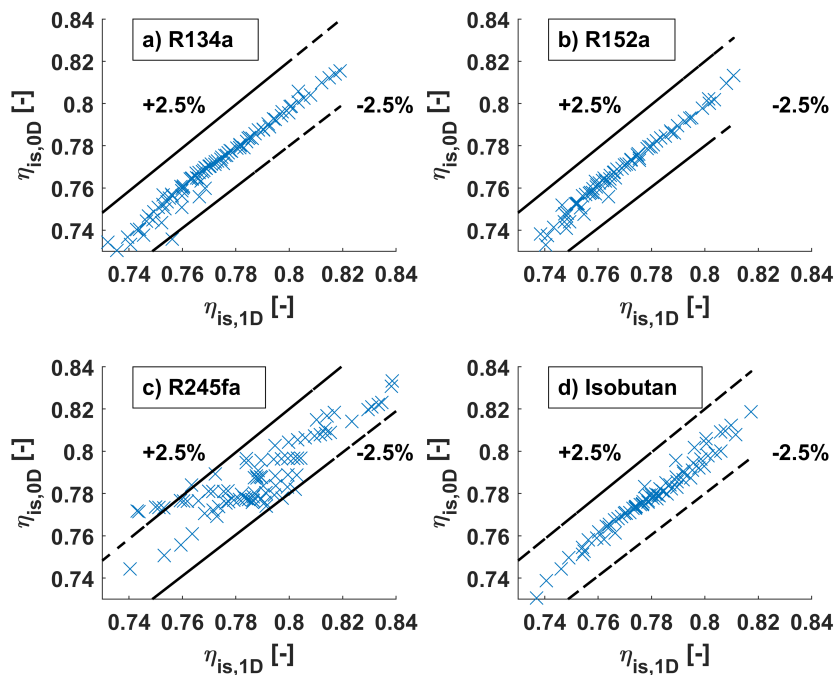


Figure 2.51 – Comparison of optimum efficiencies predicted by the 0D and by the 1D model for a centrifugal compressor operating with different working fluids

2.6.8 Limitations of the compressor pre-design model

The proposed compressor pre-design model is subject to the same limitations already introduced for the turbine, and specific ones as follows:

- **Model extrapolation** On the contrary to the turbine, the compressor pre-design model must be coupled with a classification method. As a consequence, the original dataset on which the different compressor pre-models are built is required. This effect is due to the nature of the compressor flow physics, which includes binary operation regions determined by the limits to choke and surge and by the use of a high degree polynomial function. Testing other data-driven modeling tools inducing fewer extrapolation errors, such as interpolation or symbolic regression tools [91], may overcome this issue.
- **Influence of the working fluid** It has been observed that, while the compressor pre-design model offers similar accuracies between the working fluids R134a, R152a, and R600a, it presents higher prediction errors for R245fa, which has less thermodynamic similarities than with the others. In order to overcome this shortcoming and being able to offer a more generic compressor pre-design model, an investigation in a broader scope of refrigeration working fluids is required. Moreover, additional thermodynamic variables that characterize the working fluids such as the heat capacity ratio γ could be introduced in the model fit, at the penalty of increasing its complexity though.

2.7 Summary and conclusions

Reduced order models have been developed for small-scale turbomachinery, focusing on radial inflow turbines and centrifugal compressors. The procedure to generate these updated pre-design tools is based on experimentally validated 1D models, used to build datasets through a Monte Carlo approach. Multi-variate polynomial regression models are further applied to the generated datasets to capture the turbomachinery isentropic efficiency. Using similarity concepts, a model of the form $\eta_{is} = f(Ns, Ds, PR)$ is built for the radial turbine, in which Ns is the specific speed, Ds the specific diameter, and PR the pressure ratio. For the compressor, a model of the form $\eta_{is} = f(Ns, Ds, \zeta, PR)$ is generated, where $\zeta = \frac{b_4}{r_4}$ is the blade height to tip radius ratio.

While providing satisfactory accuracy (R^2 over 0.985 and RMSEs below 0.016), these reduced order models allow a faster turbomachinery evaluation, which is paramount when embodied in complex simulations, such as multi-objective optimizations, which require a significant number of iterations. Furthermore, these pre-design models offer a better understanding of the underlying aerodynamic phenomena yielding the characteristic efficiency contours of radial turbomachinery.

In radial turbines, the nozzle and interspace losses set an upper limit for the values of specific diameter Ds due to the effect of the nozzle outlet angle. The tip clearance losses prevent efficient operation at high values of Ds and Ns . The turbine rotor incidence losses are limiting the width of the elliptic shape of the Ns - Ds contours, due to the increase of the absolute and relative velocities at the rotor inlet. Finally, the passage losses and choking conditions at the rotor throat limit the turbine operation towards lower values of Ds . The results further suggest that a broader coverage of the Ns - Ds design space is enabled by tuning the shroud to tip radius ratio $\epsilon = \frac{r_{6s}}{r_4}$.

Centrifugal compressors operating at low Ns and high blade height ratio ζ are defined by high blade loading and recirculation losses and are closer to the surge limit. On the other hand, compressors running on low ζ and high Ns are subject to high tip clearance and skin friction losses. The compressor design space is finally limited to high Ns due to the appearance of choke at the compressor inlet, while high incidence losses occur at low Ns . Similarly to the turbine, tuning the shroud to tip radius ratio $\epsilon = \frac{r_{2s}}{r_4}$ allows exploring a wider design space.

Furthermore, the proposed models present an alternative to the current pre-design methods found in literature, commonly based on the Cordier line and Balje performance maps. They offer a higher level of design detail by considering the effect of the pressure ratio and by including additional design variables such as the blade height ratio ζ (compressor) and the shroud to tip radius ratio ϵ (compressor and turbine). Therefore, the updated pre-design models provide the designer with more flexibility while offering more accurate starting points for the turbomachinery design process. Finally, fine tuning of the turbomachinery geometry parameters is enabled, which is of great interest when additional system constraints have to be met.

Chapter 2. Pre-design models for small-scale radial turbomachinery

The generated models have been validated with the 1D models at small-scale conditions, presenting isentropic efficiencies deviations below 4% for the radial turbine (with the $\eta_{is,turb} = f(Ns, Ds, PR)$ model) and below 2.5% for the centrifugal compressor (with the $\eta_{is,comp} = f(Ns, PR, \zeta, CR)$ model). Finally, the developed models will serve the optimizations which are implemented in the next chapters.

Table 2.5 – Summary of the proposed turbomachinery pre-design models

Component	Fluid validity	Model	R ²	RMSE
Turbine	Multiple	$\eta_{is,\epsilon=[0.4,0.6,0.7,0.8]} = f(Ns, Ds, PR)$	0.985	0.016
		$\eta_{is} = f(Ns, Ds, PR, \epsilon)$	0.978	0.0255
Compressor	R134a	$\eta_{is,\epsilon=[0.4,0.5,0.56,0.6]} = f(Ns, Ds, PR, \zeta)$	0.995	0.003
		$\eta_{is,\epsilon=[0.4,0.5,0.56,0.6]} = f(Ns, PR, \zeta)$	0.963	0.009
		$\eta_{is} = f(Ns, PR, \zeta, \epsilon)$	0.945	0.012
	Multiple	$\eta_{is,\epsilon=[0.4,0.5,0.56,0.6]} = f(Ns, Ds, PR, \zeta, CR)$	0.989	0.005
$\eta_{is,\epsilon=[0.4,0.5,0.56,0.6]} = f(Ns, PR, \zeta, CR)$		0.984	0.006	
		$\eta_{is} = f(Ns, PR, \zeta, CR, \epsilon)$	0.944	0.011

Table 2.5 summarizes the different models and their corresponding goodness of fit described in this chapter. The pre-design models for the turbine are found in Ref. [92] and the ones for the compressor in Ref. [93]. For both turbine and compressor, two alternative models are proposed whether the shroud to tip radius ratio ϵ is a discrete or continuous variable. The latter choice may lead to better design trade-offs but at the penalty of offering less good model accuracies, especially for the compressor. Since Ns and Ds are correlated for centrifugal compressors, the isentropic efficiency is captured with two methods, which include or not the specific diameter Ds . The models that do not account for Ds are less accurate but faster to evaluate. Furthermore, while the turbine pre-design model is valid for the four tested organic fluids - R134a, R152a, R600a, and R245fa - significant discrepancies occur within the compressor model if the clearance ratio CR is not included. Finally, the results suggest that the estimation of the compressor pre-design model must be coupled with a classification method, such as the convex hull used in this thesis. The convex hull inequalities equations for each working fluid can be found in Ref. [93].

The expressions of the polynomial fits $\eta_{is,turb} = f(Ns, Ds, PR)$ at $\epsilon_{turb}=0.7$, and $\eta_{is,comp} = f(Ns, PR, \zeta, CR)$ at $\epsilon_{comp}=0.56$ are presented in Appendix A.

3 Integrated design optimization of the Compressor Turbine Unit

This chapter describes the integrated design optimization process of the Compressor Turbine Unit (CTU), including the design of the turbomachinery, shaft, and bearing components. The models of the CTU components are described in section 3.2. The integrated approach based on a trade-off between performance and rotordynamic stability is introduced in section 3.3. Different levels of design complexity have been investigated. The results of the optimization are presented in section 3.4 where the obtained Pareto fronts and the evolution of the design variables between the different optimization levels are compared. Finally, the design robustness is investigated in section 3.5, where the impacts of (1) off-design considerations, (2) the turbomachinery tip clearances, (3) the fluid leakage, and (4) of the manufacturing errors are discussed.

3.1 Introduction

As shown in the introduction chapter, the Compressor Turbine Unit (CTU) is one of the core elements of the HP-ORC system since it serves as both the ORC expander and the HP compressor. The bearings are of gas-dynamic types (or self-acting). Demierre et al. [35] have experimentally tested a gas bearing supported CTU for a 40 kW HP-ORC, composed of an 18 mm turbine rotor and a 20 mm compressor impeller, serving as a proof of concept. The CTU shaft is supported by two radial Herringbone Grooved Journal Bearings (HGJB) and by an axial Spiral Grooved Thrust bearing (SGTB). Figure 3.1 shows a schematic of the CTU with its main components and geometry parameters. In his thesis, Demierre [2] designed the turbine while the shaft, compressor, and bearings were designed by Schiffmann [47, 94]. Therefore, no proper integrated design of the CTU had been performed for the considered HP-ORC application. Nonetheless, Schiffmann [95] has demonstrated that implementing an integrated design procedure of a heat pump turbocompressor, compared to a standard fragmented design methodology, leads to a significant improvement (up to 12 points of efficiency gain) of the heat pump seasonal efficiency.

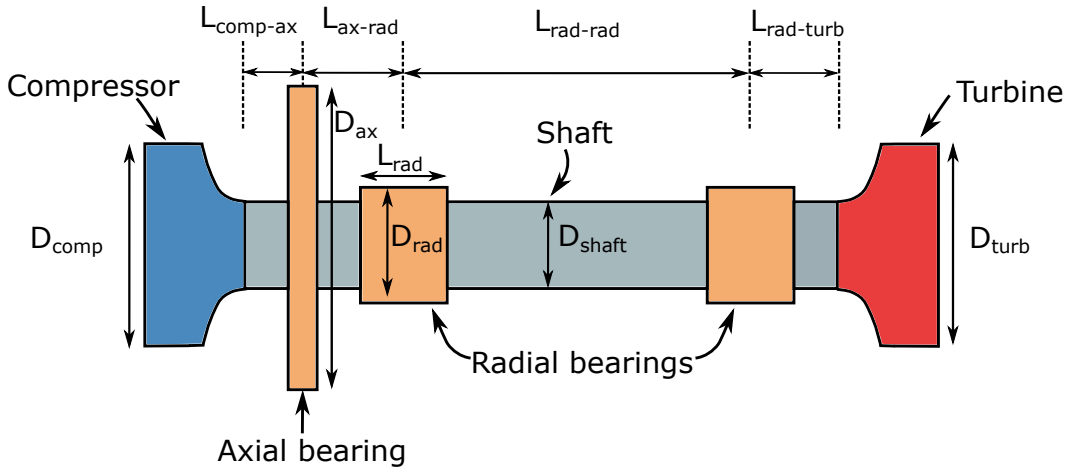


Figure 3.1 – CTU schematic with its main components and dimensions

In the present thesis, the same methodology as presented by Schiffmann [95] has been implemented, yet in this case for a HP-ORC Compressor Turbine Unit. Based on experimentally validated reduced order models of the different CTU components, a multi-objective design optimization is performed. A set of six distinct optimization problems with increased design complexity have been implemented in order to identify at which point it is worthwhile to make the optimization process more complex to get meaningful results. Moreover, the present thesis includes novel features in the CTU component modeling: Updated reduced order models for the turbomachinery, a fluid leakage model, and an updated axial load model. The robustness of the obtained optimum design is further analyzed, particularly with regards to off-design effects, turbomachinery tip clearances, fluid leakage, and manufacturing errors. The focus is set on the aerodynamic and mechanical design of the CTU for fixed operating conditions that have been encountered experimentally with R134a [35]. Therefore, the effect of the working fluid and the cycle operating parameters are not investigated in this chapter.

3.2 CTU modeling

The following section details the performance indicators as well as the models used for the integrated design optimization of the CTU. The geometry parameters and models of the CTU components, which are the radial bearings, axial bearing, shaft, and turbomachinery - as shown in Figure 3.1 - are described. For designing rotating machines used in energy conversion applications, optimum system feasibility and performance is aimed. The feasibility of gas bearing supported rotors is commonly measured by the rotordynamic stability, computed through the rigid-body analysis of the system shown in Figure 3.2, and described in equation 3.1.

$$[M]\ddot{q} + ([C] + [G])\dot{q} + [K]q = f \quad (3.1)$$

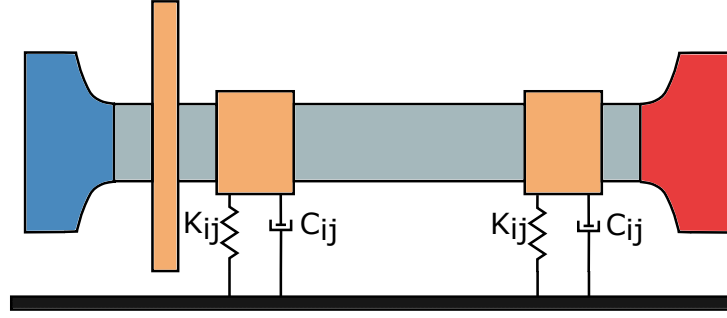


Figure 3.2 – Rigid-body model of the CTU rotor supported on two radial journal bearings. K_{ij} represents the stiffness coefficients and C_{ij} the damping coefficients

where $[M]$ is the system inertia, $[K]$ the bearing stiffness coefficients, $[C]$ the bearing damping coefficients, and $[G]$ the gyroscopic effects. The evaluation of the rotordynamic stability depends on the rotor total mass, polar and transverse inertias, and on the radial bearing features (location of mid-planes, type, and geometry). By solving the eigenvalue problem shown in equation 3.1, the rotordynamic stability is estimated through the logarithmic decrement $\Gamma_{CTU,j}$ defined by equation 3.2, where $\Omega_j\omega$ is the damped natural frequency, and λ_j the damping coefficient corresponding to the rotordynamic system rotating at the speed ω . Stable operations are reached for $\Gamma_{CTU} > 0$. With the evaluation of the eigenvectors of equation 3.1, the natural modes of the system are also retrieved.

$$\Gamma_{CTU,j} = -\lambda_j \frac{2\pi}{\Omega_j\omega} \quad (3.2)$$

Apart from the system stability, the designer aims at maximizing the efficiency, reached by minimizing the mechanical losses and by maximizing the isentropic efficiencies of the turbomachinery components. The CTU efficiency η_{CTU} is defined by equation 3.3, where $\eta_{is,turb}$ and $\eta_{is,comp}$ are the isentropic efficiencies of the turbine and compressor, \dot{E}_{turb} the mechanical power delivered by the turbine, and \dot{E}_{loss} the sum of the mechanical losses occurring in each component of the shaft (equation 3.4). \dot{E}_{rad} represents the mechanical losses occurring in the radial bearings, \dot{E}_{ax} in the axial bearing, and \dot{E}_{shaft} the mechanical losses produced by the friction of the rotating shaft.

$$\eta_{CTU} = \eta_{is,turb}\eta_{is,comp}\eta_{mech} = \eta_{is,turb}\eta_{is,comp} \frac{\dot{E}_{turb} - \dot{E}_{loss}}{\dot{E}_{turb}} \quad (3.3)$$

$$\dot{E}_{loss} = \dot{E}_{rad} + \dot{E}_{ax} + \dot{E}_{shaft} \quad (3.4)$$

The CTU efficiency η_{CTU} and stability Γ_{CTU} are competing design objectives. Indeed, while some shaft and bearing features allow reducing the mechanical losses (e.g., smaller radial bearing spacing $L_{rad-rad}$ and higher radial clearances), they tend to depreciate the stability [95].

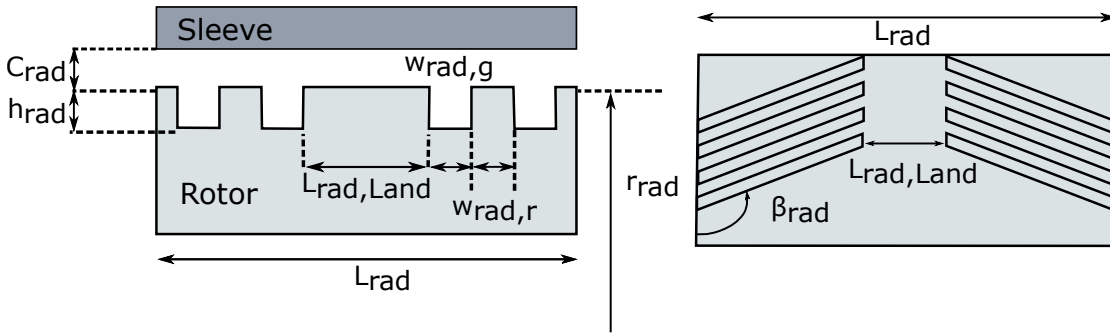


Figure 3.3 – Schematic of a Herringbone Grooved Journal Bearing (HGJB)

3.2.1 Shaft model

As shown in Figure 3.1, the shaft is composed of two radial gas bearings and of an axial bearing. The different shaft sections joining the bearing and turbomachinery elements are subject to windage losses \dot{E}_{shaft} and centrifugal growth, which are described in [35]. To facilitate manufacturing, the shaft and the bearing components are made of the same material. Since energy related applications require a high number of operational cycles, the shaft and bearing material should be sufficiently resistant to wear (sufficient hardness and low friction coefficient). Furthermore, sufficiently high Young modulus to density ratios are required to obtain natural system frequencies in excess of the maximum rotor speed while mitigating the shaft centrifugal growth [47]. Tungsten Carbide is used since its mechanical properties match these specifications well (compared to uncoated stainless steel in Table 3.1).

Table 3.1 – Shaft material properties

Material	Young Modulus	Density	Friction coefficient	Hardness
	[GPa]	[kg.m ⁻³]	[-]	[HV]
Tungsten Carbide	630	14900	0.2-0.25	1200-1700
Stainless Steel	210	7800	0.5-0.8	150-220

3.2.2 Radial bearing model

The radial bearings are self-acting fluid film bearings and more specifically Herringbone Grooved Journal Bearings (HGJBs). The geometry features of HGJBs enable the generation of a fluid film pressure, governed by the Reynolds equations, to support the shaft. The aerodynamic groove effects are captured through the Narrow Groove theory. This grooved geometry builds a stiffness $[K]$ and a damping coefficient $[C]$ in the bearing region, further used in equation 3.1 to compute the system stability and natural frequencies. These coefficients are deeply influenced by the bearing geometry itself. The basic dimensions of a HGJB are shown in Figure 3.3. More details about the governing equations and rotordynamic effects of the HGJBs, as well as their mechanical losses \dot{E}_{rad} , can be found in [35, 47].

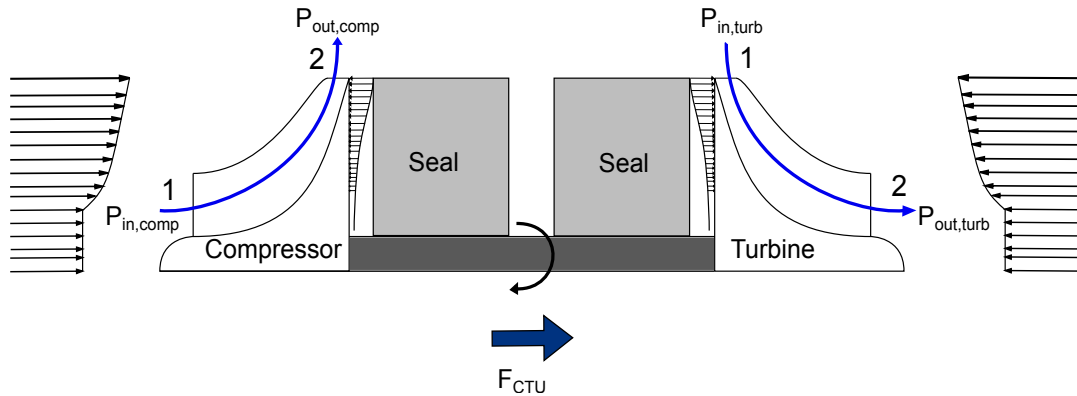


Figure 3.4 – Axial force generation across the Compressor Turbine Unit

3.2.3 CTU axial load and axial bearing models

The prediction of the axial load applied to radial turbomachinery is challenging since it is highly dependent on the flow conditions in the rotor/impeller blade passage. The literature is sparse for predicting the axial load in turbochargers, relying mainly on empirical models and CFD as proposed by Zhang et al. [96]. In the previous work by Demierre and Schiffmann, a similar model has been implemented, considering that the pressure varies linearly on the impeller front side and is constant on the impeller backplate [47].

In this thesis, a new model to predict the CTU axial load based on the turbine and compressor 1D models developed by Demierre et al. [35] is presented. This model predicts the axial pressure distribution along the compressor impeller and the turbine rotor, which are integrated over the impeller area to obtain the total axial force. Figure 3.4 shows a schematic of the CTU with the location of the axial pressure profiles. One occurs on the front side, due to the pressure evolution in the blade passage, and the other takes place in the space between the turbine/compressor backplate and the seal.

On the turbine/compressor front side, the axial force is composed of a block pressure field in the inducer/diffuser region $F_{frt,block}$ and of a pressure profile in the blade region $F_{frt,blade}$. The axial force occurring in the inducer/diffuser region can be written as follows:

$$F_{frt,block} = P_{1,2} \pi r_{1,2rms}^2 \quad (3.5)$$

where $P_{1,2}$ is the static pressure at the turbine outlet and compressor inlet. $r_{1,2rms}$ is the root mean square radius at the turbine outlet and compressor inlet.

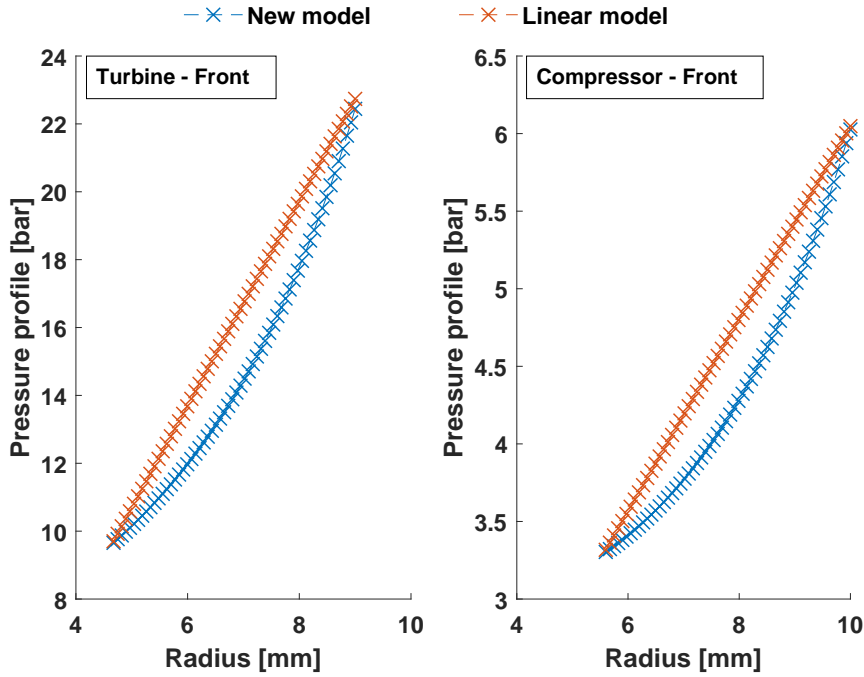


Figure 3.5 – Pressure distribution profile on the turbomachinery front side for an operating condition tested by Demierre et al. [35]

In order to evaluate the static pressure evolution within the blade region, the principle of static isentropic rothalpy conservation, described by equation 3.6, is used [97].

$$h_s(r) - h_{1,2} = \frac{1}{2} ((W(r)^2 - W_{1,2}^2) - (r_{1,2}^2 \omega^2 - r^2 \omega^2)) \quad (3.6)$$

where $h_s(r)$ is the isentropic static enthalpy evolution along the blade, ω the shaft rotational speed, and $W(r)$ the relative flow velocity along the blade passage. In the turbomachinery 1D codes, only inlet (1) and outlet (2) conditions are known. The evolution of $W(r)$ and of the internal enthalpy losses are assumed to vary linearly with the radius r . Using REFPROP [98], the static enthalpy evolution $h(r)$, and hence the static pressure $P_{blade}(r)$, is calculated as a function of the radius and further fitted with a 2^{nd} degree polynomial function which presents R^2 in excess of 0.99. Figure 3.5 represents the pressure distribution for both the turbine and compressor side and compared them to the linear model proposed by Schiffmann [47] for an operating condition tested by Demierre et al. [35]. The axial force in the blade region $F_{f_{rt,blade}}$ and the total axial force applied to the turbomachinery front side $F_{f_{rt}}$ are calculated following equation 3.7.

$$F_{f_{rt,blade}} = \int_{r_1}^{r_2} P_{blade}(r) 2\pi r dr \quad (3.7)$$

$$F_{f_{rt}} = F_{f_{rt,blade}} + F_{f_{rt,block}}$$

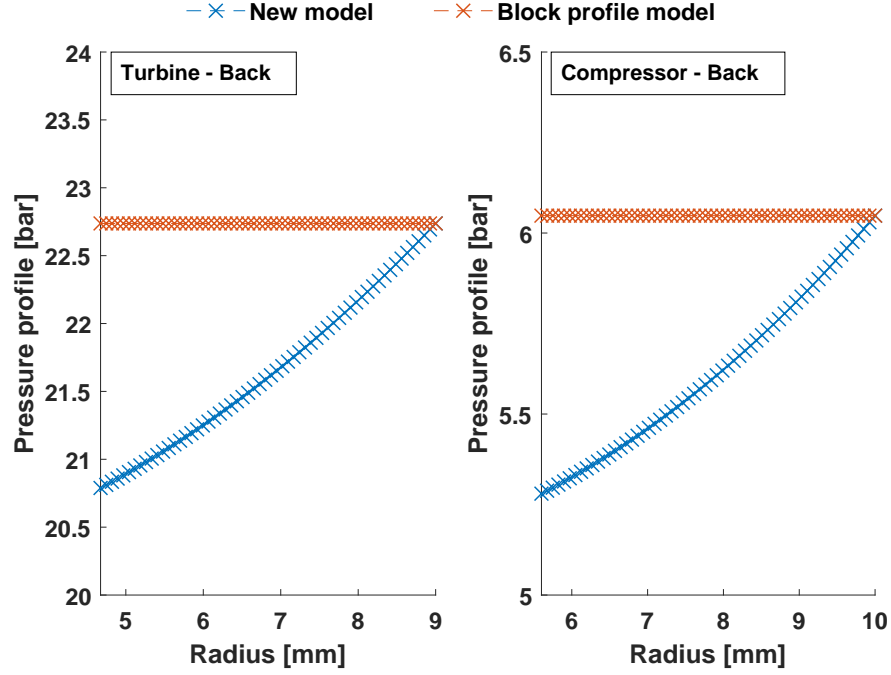


Figure 3.6 – Pressure distribution profile on the turbomachinery backside for an operating condition tested by Demierre et al. [35]

On the turbomachinery backside, the fluid is supposed to be in steady-state with no recirculation. Fluid leakages are neglected, and the fluid is assumed to be compressible and to follow an isothermal process considering that the system is micro-scaled. Furthermore, it is assumed that the pressure gradient is governed by the centrifugal forces and that the flow velocity is purely circumferential and constant at $\omega_{back} = \frac{\omega}{2}$ [99], where ω is the shaft rotational speed. The pressure distribution $P_{back}(r)$ and the total axial force F_{back} are, therefore, obtained as follows:

$$P_{back}(r) = P_{1,2} \exp \frac{\omega_{back}^2 (r^2 - r_{1,2}^2)}{2R} \quad (3.8)$$

$$F_{back} = \int_{r_{shaft}}^{r_2} P_{back}(r) 2\pi r dr$$

Figure 3.6 represents the corresponding pressure distribution for both turbine and compressor backsides and compares them to a block pressure profile [47] for a given operating condition tested by Demierre et al. [35]. Finally, the total forces on the compressor and turbine are retrieved as shown in equation 3.9.

$$F_{tot,comp} = F_{frt,comp} - F_{back,comp}$$

$$F_{tot,turb} = F_{back,turb} - F_{frt,turb} \quad (3.9)$$

$$F_{CTU} = F_{tot,comp} + F_{tot,turb}$$

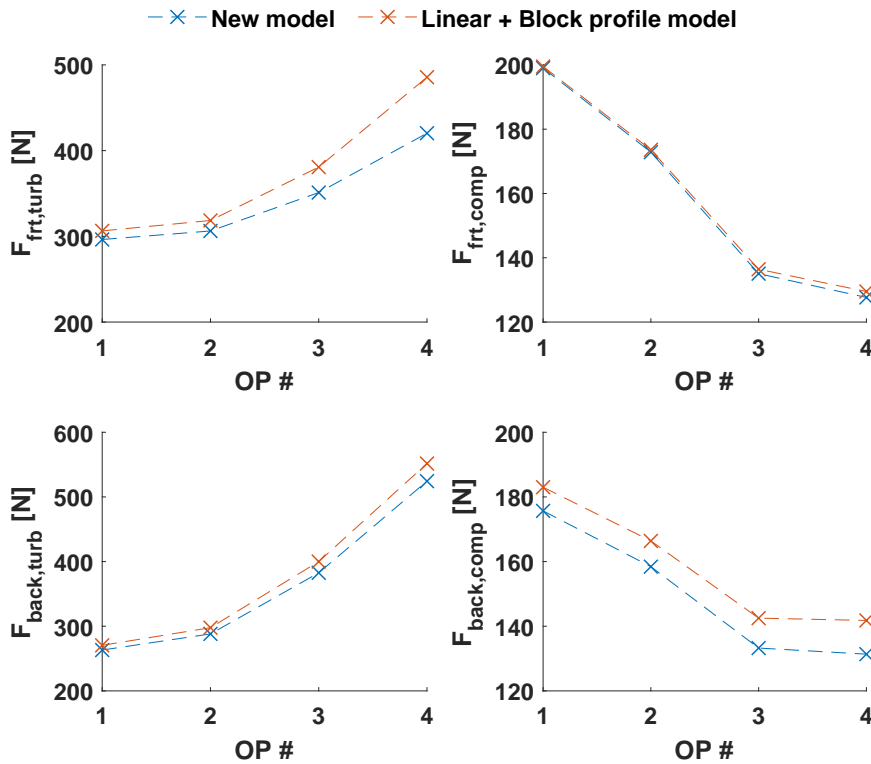


Figure 3.7 – Axial forces applied to the turbomachinery for four different operating points (OP) performed by Demierre et al. [35]

Figures 3.7 and 3.8 show the force repartition and the total force F_{CTU} across the CTU for four experimental runs performed by Demierre et al. [35] and compare them to the model proposed by Schiffmann [47]. The details about the thermodynamic conditions of these Operating Points (OP) can be found in Table 3.2. The proposed axial force model presents significant discrepancies towards the linear model, predicting lower loads by 10 N for OP1 and OP2 but higher ones by up to 50 N for OP4.

Once the CTU axial load F_{CTU} is known, the axial thrust bearing needs to be designed accordingly to avoid any touchdowns during the system operation. The axial thrust is a self-acting bearing, and is more specifically an inward pumping Spiral Grooved Thrust Bearing (SGTB). The model developed by Schiffmann [47] applies the Narrow Groove theory in order to retrieve the pressure field produced by the SGTB inward pumping effect. The pressure field is integrated over the thrust diameter to obtain the axial load capacity F_{SGTB} . Figure 3.9 shows the SGTB layout and its main dimensions. More details about the governing equations, rotordynamic considerations, and mechanical losses \dot{E}_{ax} of the SGTB can be found in [47].

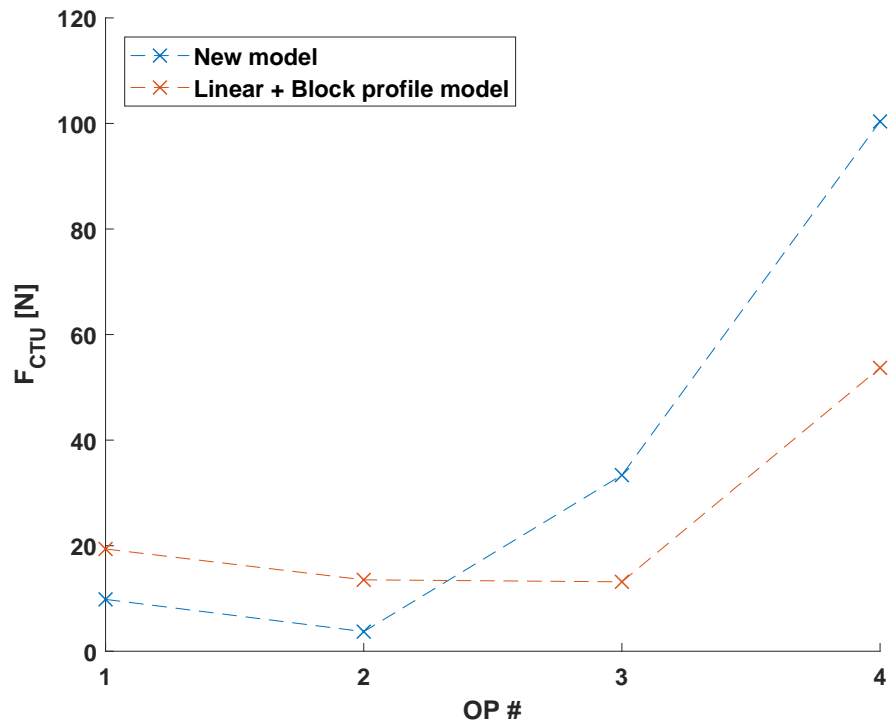


Figure 3.8 – Total axial force applied to the CTU for four different operating points (OP)

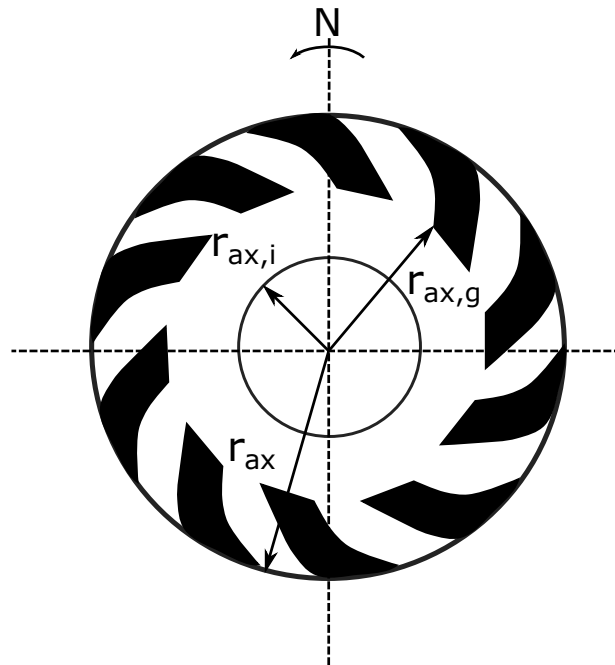


Figure 3.9 – Schematic of a Spiral Groove Thrust Bearing (SGTB)

3.2.4 Turbomachinery models

Updated pre-design (0D) models for both centrifugal compressors and radial inflow turbines have been introduced in chapter 2. These pre-design tools are based on experimentally validated 1D models and allow a drastic reduction of the turbomachinery evaluation time compared to a mean-line analysis. In this chapter both 0D and 1D models, which are described below, have been used for the CTU optimization.

0D model - Turbine

Equation 3.10 has been used for the evaluation of the radial inflow turbine. The efficiency is computed at different shroud to tip radius ratios ϵ ranging from 0.5 to 0.8, which allows exploring a broader range of feasible operating regions of specific speeds (Figure 2.20). In chapter 2, a turbine blade height to tip radius ratio ζ of 0.11 was found optimal to ensure higher iso-efficiency surfaces covered by Ns and Ds (Figure 2.18). The model which includes ϵ as a continuous variable ($\eta_{is} = f(Ns, Ds, PR, \epsilon)$) is not considered due to a lower goodness of fit (see Table 2.5).

$$\eta_{is,turb} = f(Ns, Ds, PR), \epsilon = [0.5, 0.6, 0.7, 0.8] \quad (3.10)$$

0D model - Compressor

Equation 3.11 has been used for the evaluation of the centrifugal compressor. This correlation showed a good match with the 1D model, at the condition to couple the evaluation with a classification method (see Figure 2.48). The model including the Clearance Ratio CR , which is valid for different working fluids, has been implemented. Similarly to the turbine evaluation, the efficiency is performed at different shroud to tip radius ratios ϵ . The model which includes ϵ as a continuous variable ($\eta_{is} = f(Ns, PR, \zeta, CR, \epsilon)$) is not considered due to a lower goodness of fit (see Table 2.5).

$$\begin{aligned} \eta_{is,comp} &= f(Ns, PR, \zeta, CR), \epsilon = [0.4, 0.5, 0.56, 0.6] \\ Ds_{comp} &= f(Ns, PR, \zeta, CR), \epsilon = [0.4, 0.5, 0.56, 0.6] \end{aligned} \quad (3.11)$$

1D model - Compressor and Turbine

The 0D turbomachinery evaluation methods allow obtaining a preliminary design, including the tip diameters, shroud diameters, and the optimum rotational speed of the CTU. However, the turbomachinery isentropic efficiencies may be enhanced even further by a full and integrated optimization of their 1D dimensions, including hub radii and blade angles. To achieve this level of design detail, the experimentally validated 1D models of both turbines and compressors are embodied in the optimization procedure.

3.3 Multi-objective optimization

The integrated design optimization of the CTU is performed by coupling a multi-objective evolutionary algorithm with the models presented above. As discussed earlier, the CTU optimization objectives are the maximization of the system efficiency η_{CTU} and of the rotor-dynamic stability Γ_{CTU} .

Six distinct optimization problems summarized in Figure 3.10 have been addressed, each of them representing a different level of design complexity. At each optimization stage, designated by Opt1, Opt2, Opt3.1, Opt3.2, Opt3.3, and Opt4, new components and variables are added into the design process: Only the bearings in Opt1; shaft and bearings in Opt2; shaft, bearings, and turbomachinery in Opt3 and Opt4. The goal of this approach is to identify how much design complexity is needed to obtain meaningful results and to devise design guidelines with regards to the optimization and modeling of small-scale turbomachinery systems. These optimization levels are described as follows:

Optimization level 1 (Opt1)

The first optimization level is restricted to the radial and axial bearings. The turbomachinery data (isentropic efficiencies, diameters, and rotor speeds) and shaft geometry are retrieved from the prototype tests performed by Demierre et al. [35]. The mathematical formulation of the optimization level 1 problem is described by equation 3.12. G_{rad} and G_{ax} represent vectors of geometry variables defining the design of the radial and axial bearings, respectively. The layout of the optimization problem is presented in Figure 3.11a. Since the shaft design is not included in this optimization level, G_{shaft} is fixed.

$$[\max(\eta_{CTU}), \max(\Gamma_{CTU})] = f_{Opt1}(G_{rad}, G_{ax}) \quad (3.12)$$

Optimization level 2 (Opt2)

The second optimization level is an extension of the previous one, with the addition of the shaft geometry (lengths, bearing positions, and diameters). Its mathematical expression is described by equation 3.13 and the same simulation layout depicted in Figure 3.11a is followed, this time by having G_{shaft} as an additional set of variables.

$$[\max(\eta_{CTU}), \max(\Gamma_{CTU})] = f_{Opt2}(G_{rad}, G_{ax}, G_{shaft}) \quad (3.13)$$

Chapter 3. Integrated design optimization of the Compressor Turbine Unit

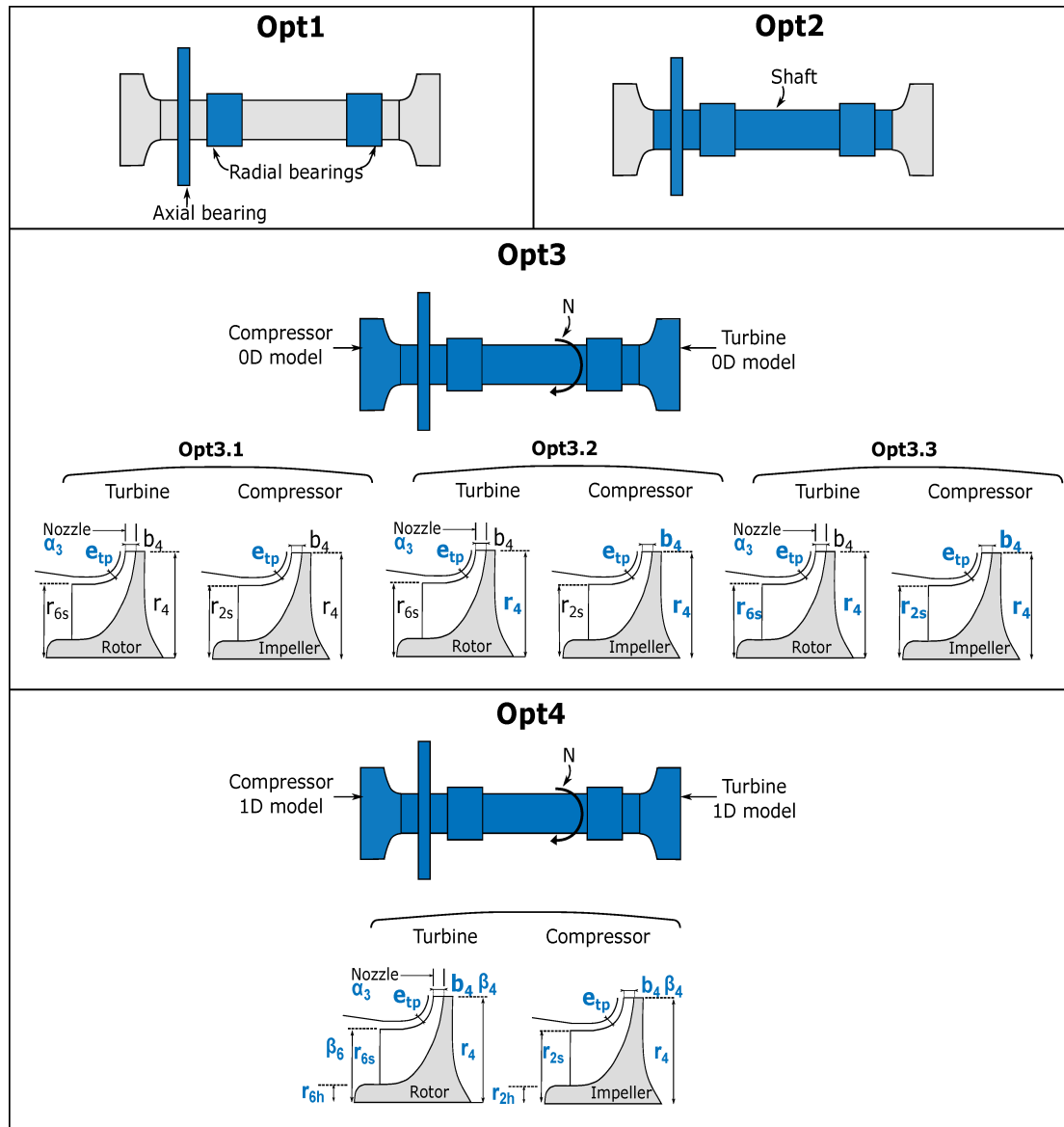


Figure 3.10 – Summary of the different CTU optimization levels. In blue are represented the components/variables of the considered optimization stage

3.3. Multi-objective optimization

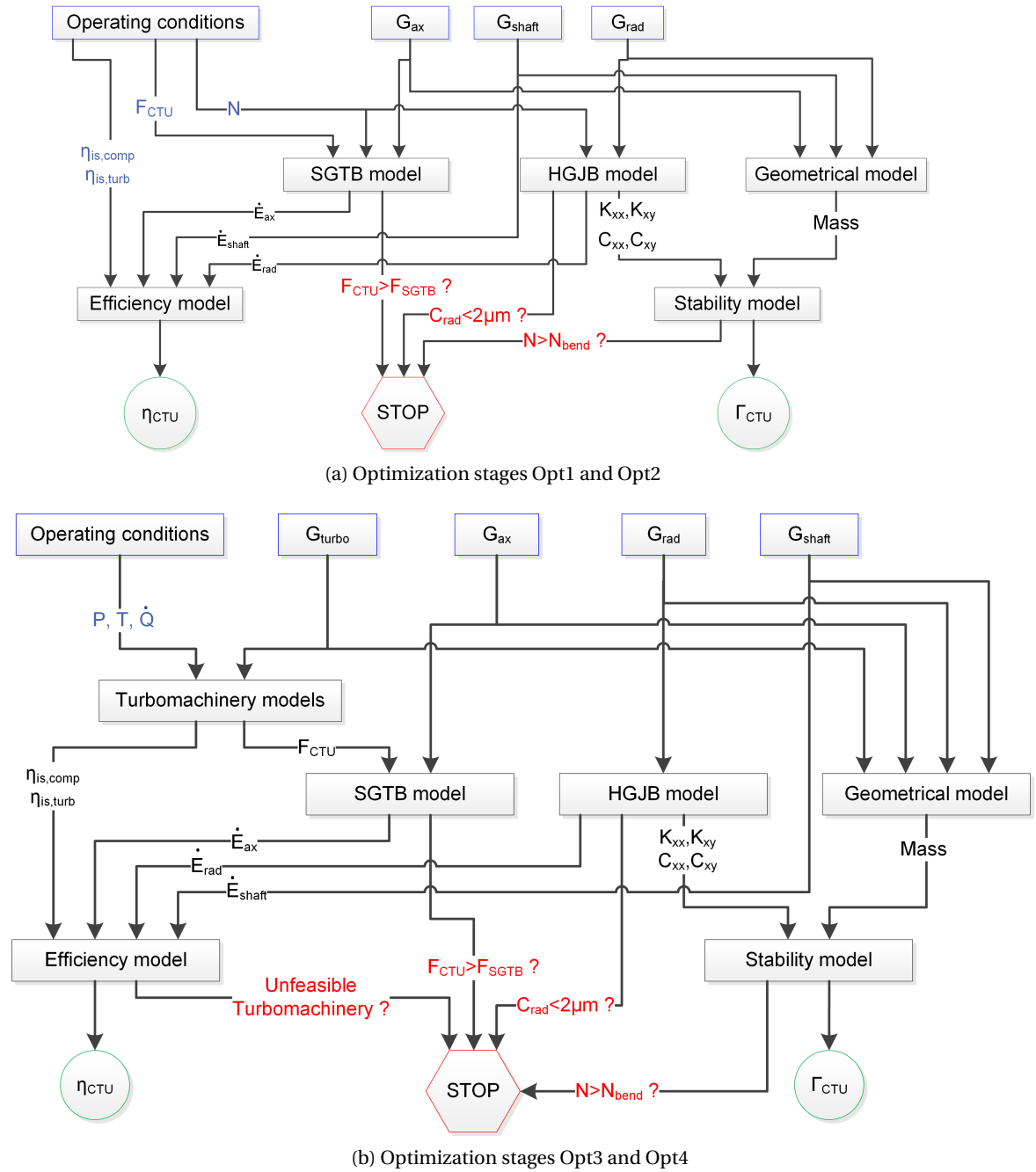


Figure 3.11 – Layout of the optimization levels (a) Opt1 and Opt2, (b) Opt3 and Opt4

Optimization level 3 (Opt3)

This level extends the previous optimization layers by adding the design of the turbomachinery components, which are estimated through the 0D model presented in chapter 2. This optimization layer offers augmented diversity in the design by adding features that influence the turbomachinery geometry, and hence playing on the isentropic efficiencies in equation 3.3. It is, however, more time consuming since the evaluation of the turbomachinery is included. Its mathematical expression is defined in equation 3.14 and its layout in Figure 3.11b.

$$[\max(\eta_{CTU}), \max(\Gamma_{CTU})] = f_{Opt3}(G_{rad}, G_{ax}, G_{shaft}, G_{turb-0D}, G_{comp-0D}) \quad (3.14)$$

The optimization level 3 is further divided into three distinct problems:

- **Optimization level 3.1 (Opt3.1)** The turbomachinery geometry features are the same as the prototype (18 mm turbine, 20 mm compressor with a blade height ratio of 0.12 [35]). Applying the turbomachinery pre-design models allows getting the optimum rotational speed and isentropic efficiency at the considered design point. The Opt3.1 level gives insights into the possible efficiency gain if the system, while operating with the same turbine and compressor geometry, was performing at the conditions set by the pre-design models.
- **Optimization level 3.2 (Opt3.2)** The optimization receives now as variables the turbomachinery geometry features (turbine tip diameter, compressor tip diameter, and compressor blade height ratio). At this stage, the shroud to tip radius ratio ϵ is fixed to 0.7 for the turbine and 0.56 for the compressor, such as in the proof of concept [35] and following best design practice for radial turbines [74].
- **Optimization level 3.3 (Opt3.3)** The Opt3.3 level is an extension of the previous design stage by including additional flexibility on the ϵ values for both turbomachinery.

Optimization level 4 (Opt4)

The last optimization layer includes the same elements as the previous levels but with the evaluation of the turbomachinery with the 1D model instead. This leads to the addition of new 1D turbomachinery design variables, such as the hub to shroud radius ratios and blade angles. Based on the required operating conditions, the compressor efficiency is first calculated for a range of possible rotational speeds. The turbine is computed such that it would match the compressor rotor speed and fulfill the CTU power balance, accounting for the shaft and bearing mechanical losses. Although this optimization stage is the most complete regarding integrated design, it is also the most time-consuming one. The simulation layout is similar to the optimization level 3 (Figure 3.11b), using a 1D model for the compressor and turbine instead of the 0D pre-design models. Its mathematical expression is the following:

$$[\max(\eta_{CTU}), \max(\Gamma_{CTU})] = f_{Opt4}(G_{rad}, G_{ax}, G_{shaft}, G_{turb-1D}, G_{comp-1D}) \quad (3.15)$$

3.3. Multi-objective optimization

All optimizations levels are subject to the following constraints:

$$\left\{ \begin{array}{l} C_{rad} > 2\mu m \\ F_{SGTB} > F_{CTU} \\ N < 1.2N_{bend} \end{array} \right\}$$

These constraints ensure that the SGTB load capacity F_{SGTB} is sufficient to overcome the CTU axial load F_{CTU} , that the operational rotational speed is lower than the first critical bending speed, and that the HGJB clearance C_{rad} is always higher than $2 \mu m$, accounting for centrifugal expansion growth. When the geometry of the turbomachinery is added such as for the optimizations Opt3.1, Opt3.2, Opt3.3, and Opt4, the optimization is subject to additional constraints related to unfeasible operations. For both turbine and compressor, this results in avoiding the presence of two-phase flows that could lead to premature blade erosion and a bearing failure. In addition, the compressor must not operate in choke or surge conditions.

Table 3.2 – Boundary conditions of the CTU optimization

#	$T_{turb,in}$	$P_{turb,in}$	$P_{turb,out}$	$T_{comp,in}$	$P_{comp,in}$	$P_{comp,out}$	\dot{Q}_{cond}	\dot{Q}_{cold}	\dot{Q}_{hot}	N
-	[°C]	[bar]	[bar]	[°C]	[bar]	[bar]	[kW]	[kW]	[kW]	[krpm]
1	103	31	10	34	5.7	9.4	31	11.8	19	147
2	101	32.5	9.8	28	4.8	9.4	29	9.7	19	161
3	113	42.4	10.1	23	3.7	8.9	39	11.9	26	190
4	123	50.2	11.3	27	3.3	9.4	42	12	30	206

The optimization procedure has been applied to the operating conditions experimented by Demierre et al. [35], in which the CTU was part of an ORC driven Heat Pump operating with R134a. Table 3.2 presents the thermodynamic and CTU boundary conditions of the selected experimental points, which have been chosen since they are relatively well spread regarding rotor speeds and turbine pressure ratios. The design variables and their ranges used for the different optimization levels are summarized in Table 3.3.

Chapter 3. Integrated design optimization of the Compressor Turbine Unit

Table 3.3 – Design variables of the CTU optimization

Component	Term	Range	Unit
Radial bearing G_{rad}	$\frac{D_{rad}}{D_{shaft}}$	[1-3]	[-]
	C_{rad}	[3.5-15]	[μm]
	$H_{rad} = \frac{h_{rad} + C_{rad}}{C_{rad}}$	[1.1-5]	[-]
	$\alpha_{rad} = \frac{w_{rad,g}}{w_{rad,g} + w_{rad,r}}$	[0.4-0.6]	[-]
	β_{rad}	[110-170]	[deg]
	$\gamma_{rad} = \frac{L_{rad} - L_{rad,land}}{L_{rad}}$	[0.6-0.9]	[-]
	L_{rad} Material	D_{rad} Tungsten Carbide	[mm]
Axial bearing G_{ax}	$D_{ax} = 2r_{ax}$	[10-30]	[mm]
	C_{ax}	[5-20]	[μm]
	H_{ax}	[1.1-5]	[-]
	α_{ax}	[0.4-0.6]	[-]
	β_{ax}	[110-170]	[deg]
	$D_{ax,g}$	$0.6D_{ax}$	[mm]
	L_{ax} Material	$0.2D_{ax}$ Tungsten Carbide	[mm]
Shaft G_{shaft}	D_{shaft}	[8-20]	[mm]
	$\frac{L_{ax-rad}}{D_{shaft}}$	[0.2-2]	[-]
	$\frac{L_{rad-rad}}{D_{shaft}}$	[1-3]	[-]
	$\frac{L_{rad-turb}}{D_{shaft}}$	[0.2-2]	[-]
	$L_{comp-ax}$	$0.3D_{shaft}$	[mm]
	C_{shaft} Material	$0.01D_{shaft}$ Tungsten Carbide	[mm]
Turbine 0D $G_{turb-0D}$	r_4	[5-20]	[mm]
	$\epsilon_{turb} = \frac{r_{6s}}{r_4}$	[0.5;0.6;0.7;0.8]	[-]
Turbine 1D $G_{turb-1D}$	r_4	[5-20]	[mm]
	$\frac{r_4}{r_3}$	[0.005-0.1]	[-]
	$\zeta_{turb} = \frac{b_4}{r_4}$	[0.1-0.25]	[-]
	$\epsilon_{turb} = \frac{r_{6s}}{r_4}$	[0.3-0.85]	[-]
	$\frac{r_{6h}}{r_4}$	[0.1-0.5]	[-]
	$\frac{r_{6s}}{r_7}$	[1.1-2]	[-]
	$\frac{r_{6s}}{r_{6s}}$ β_6 Material	[-60 -40] Stainless Steel	[deg]
Compressor 0D $G_{comp-0D}$	r_4	[5-20]	[mm]
	$\zeta_{comp} = \frac{b_4}{r_4}$	[0.03-0.25]	[-]
	$\epsilon_{comp} = \frac{r_{2s}}{r_4}$	[0.4;0.5;0.56;0.5]	[-]
Compressor 1D $G_{comp-1D}$	r_4	[5-18]	[mm]
	$\zeta_{comp} = \frac{b_4}{r_4}$	[0.03-0.25]	[-]
	$\epsilon_{comp} = \frac{r_{2s}}{r_4}$	[0.3-0.8]	[-]
	$\frac{r_{2h}}{r_{2s}}$	[0.15-0.5]	[-]
	β_4 Material	[-45-0] Aluminum	[deg]

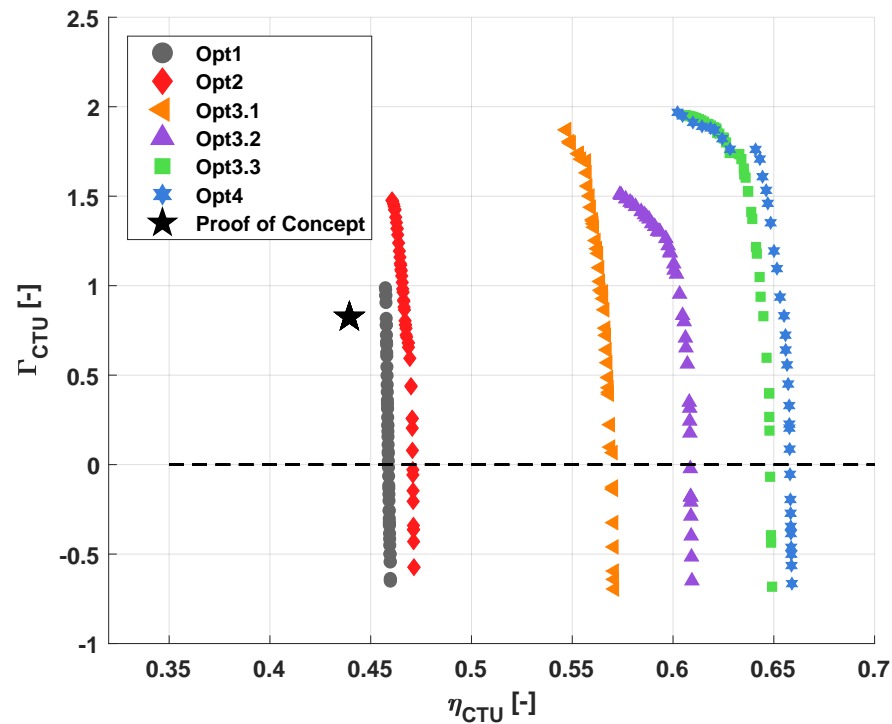


Figure 3.12 – Pareto optimum curves for different optimizations levels applied to the operating condition OP3 and compared to the Proof of Concept

3.4 Results and discussion

The more diverse and complete the optimization problem, the more time consuming it becomes. The goal of this section is to evaluate how much the different optimization levels applied to the CTU enable to gain performance compared to the existing prototype (Proof of Concept).

3.4.1 Pareto optimum curves for the operating point OP3

The Pareto fronts resulting from the CTU optimization performed at the operating point OP3 (see Table 3.2) are presented in Figure 3.12. The fronts for the different optimizations levels are displayed and compared to the current performance and stability level of the tested Proof of Concept. The fronts of optimization stages Opt1, Opt2, and Opt3.1 present a particular shape since they are composed mostly of two main slopes, where the stability decreases very rapidly for small variations of performances and vice versa. For the optimization levels Opt1 and Opt2, the optimizer is barely finding regions with trade-offs between rotordynamic stability and performance. With the optimization levels Opt3.2, Opt3.3, and Opt4, the enhanced design diversity introduced by the turbomachinery parameters enable to identify a higher number of trade-off families for rotordynamic stabilities above one.

Chapter 3. Integrated design optimization of the Compressor Turbine Unit

In addition, the results highlight the followings points:

- **Comparison to the proof of concept** The Pareto fronts are compared with the experimental efficiency and rotordynamic stability obtained with the proof of concept design ($\Gamma_{CTU}=0.82$). The results show that the CTU performance can be enhanced significantly with a suitable integrated design optimization procedure (up to 19.5 points in efficiency gain with the Opt3.3 stage when considering the same rotordynamic stability as the proof of concept).
- **Contribution of each optimization level** When staying at the same stability as the proof of concept, the optimization levels Opt1 and Opt2 allow a 1.7- and 2.7-pt efficiency gain. A more significant 12-pt efficiency increase is achieved with the optimization level Opt3.1. This is the contribution of applying the rules the pre-design models are based on (optimized rotational speed, clearance ratios, and turbine nozzle outlet angles). The optimization level Opt3.2 includes the turbomachinery geometry parameters with a fixed shroud to tip radius ratio and achieves an additional 5-pt increase (17-pt to Proof of Concept). The optimization level Opt3.3 enables to add more diversity by varying the shroud to tip radius ratio, leading to a CTU efficiency of 64.4% at $\Gamma_{CTU}=0.82$ (+2.5-pt compared to a fixed ϵ ratio). Finally, the last optimization level Opt4, which includes the integrated design of the other 1D dimensions, enables an additional 1-pt performance gain.
- **Comparison 0D/1D methods** While the optimization level Opt4 presents the highest efficiency in outperforming the Opt3.3 level (0D model based optimization) by 1-pt, it is at the penalty of being the most time-consuming. Indeed, considering the same cluster with ten cores running in parallel, the optimization level Opt1 performs 10'000 function evaluations in two hours, the optimization level Opt3.3 in four hours, and the Opt4 in eighteen hours. It follows that using the low order models for the turbomachinery designs is more than satisfying to achieve efficient and accurate integrated design of the complex turbomachinery system supported on gas lubricated bearings within a reasonable amount of time.

The following sections analyze and compare the design variables resulting from the proposed optimization levels.

3.4.2 Shaft and bearing design variables

Figure 3.13 represents the geometrical values of the radial bearing design resulting from the optimum Pareto curves Opt2 and Opt3.3 in Figure 3.12 compared to the proof of concept design. These plots highlight that α_{rad} and γ_{rad} converge towards one single value, which is the same as the current prototype. The angle β_{rad} slightly increases from 155 to 165 degrees to increase the rotordynamic stability. Similarly, the groove depth ratio H_{rad} increases to reach higher stabilities. However, H_{rad} increases also in the low stability regions (around $\Gamma_{CTU}=0$), most likely to mitigate the stability loss incurred by the augmentation of the radial clearance C_{rad} . Indeed, tuning C_{rad} seems to be one of the very last resorts for the optimizer to increase the CTU efficiency, which, however, leads to a dramatic drop of Γ_{CTU} . Finally, similar trends are observed between the Opt2 and Opt3.3 stages, although the latter has a higher degree of design detail.

Figure 3.14 presents the evolution of the optimal axial bearing dimensions function of the CTU rotordynamic stability. In contrast to the radial bearings, it is suggested that the axial bearing geometry of the proof of concept is suboptimal. Design solutions are found at lower thrust bearing diameters (20 mm instead of 26 mm) and higher axial clearances (18 μm in the Opt3.3 stage instead of 10 μm), due to a better adaptation of the spiral groove geometry (C_{ax} , H_{ax} , β_{ax} , and α_{ax}) to the axial forces of the system.

Figure 3.15 displays the Pareto-optimum geometrical dimensions of the shaft versus the CTU stability. Along the Pareto front, the shaft diameter D_{shaft} and the relative positions of the radial bearings towards the turbine and the axial thrust ($\frac{L_{rad-turb}}{D_{shaft}}$ and $\frac{L_{ax-rad}}{D_{shaft}}$) are converging to single values, advocating for smaller lengths and diameters than the current prototype. Furthermore, to maximize the efficiency (i.e., at minimum rotordynamic stability), the distance between the two radial bearings should be reduced. This variable, however, depreciates the stability due to its effect on the rotor mass and inertias around the center of gravity [47]. Finally, the optimizer suggests a larger radial bearing diameter than the shaft diameter in order to enhance the rotordynamic stability.

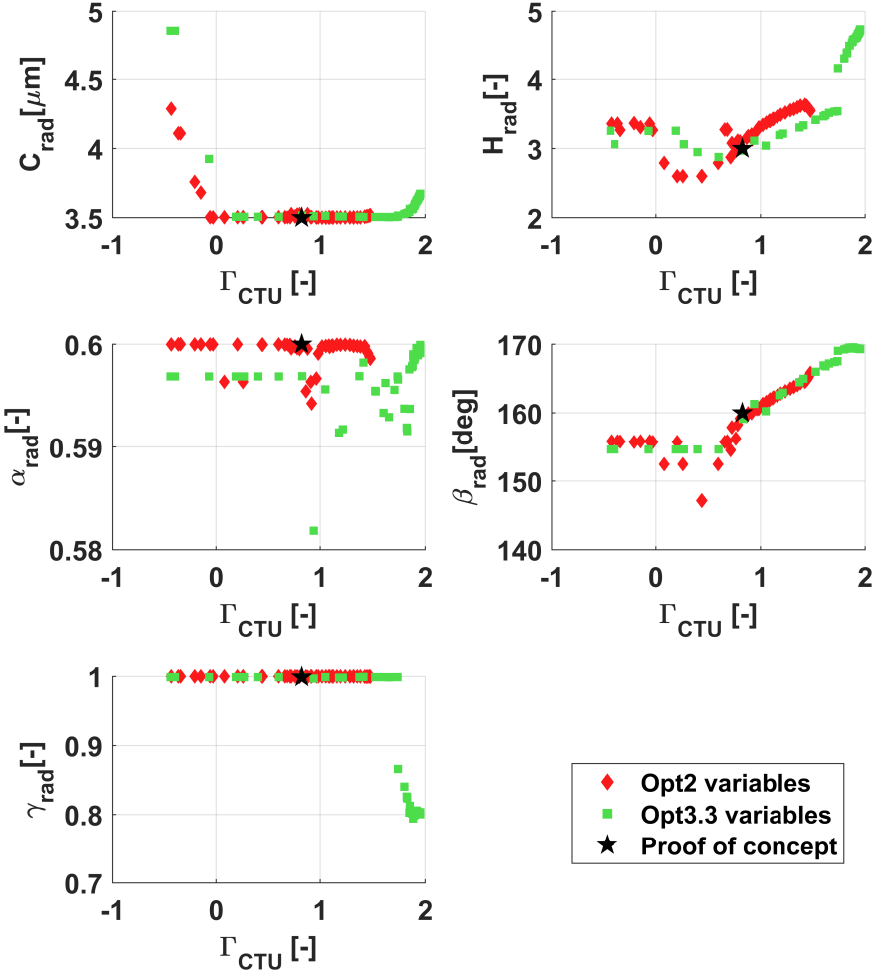


Figure 3.13 – Pareto optimum solutions of the radial bearing dimensions versus the CTU stability (levels Opt2 and Opt3.3 performed at OP3)

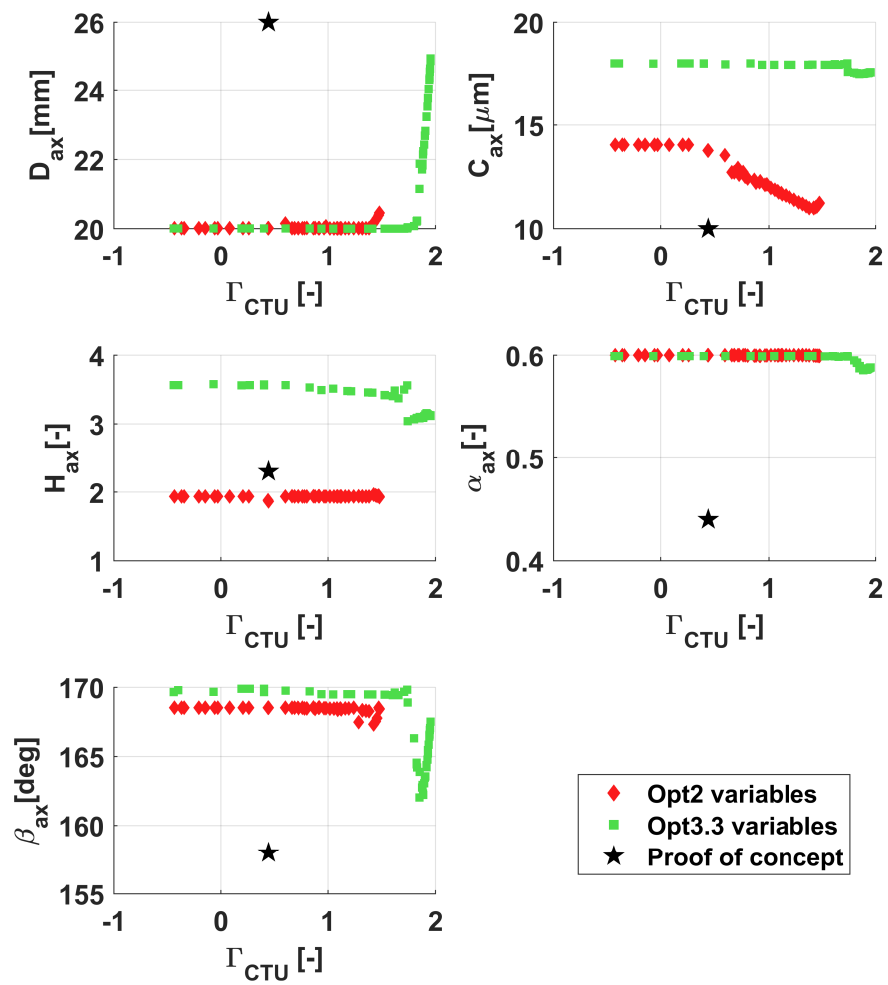


Figure 3.14 – Pareto optimum solutions of the axial bearing dimensions versus the CTU stability (levels Opt2 and Opt3.3 performed at OP3)

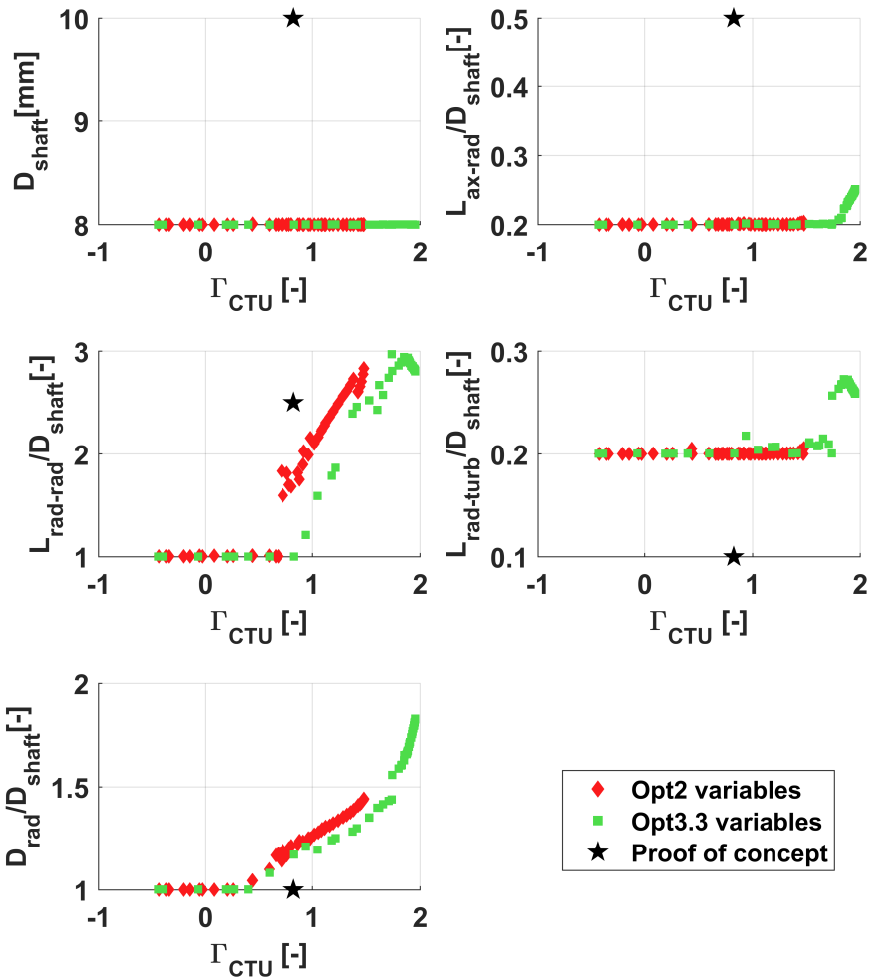


Figure 3.15 – Pareto optimum solutions of the shaft dimensions versus the CTU stability (levels Opt2 and Opt3.3 performed at OP3)

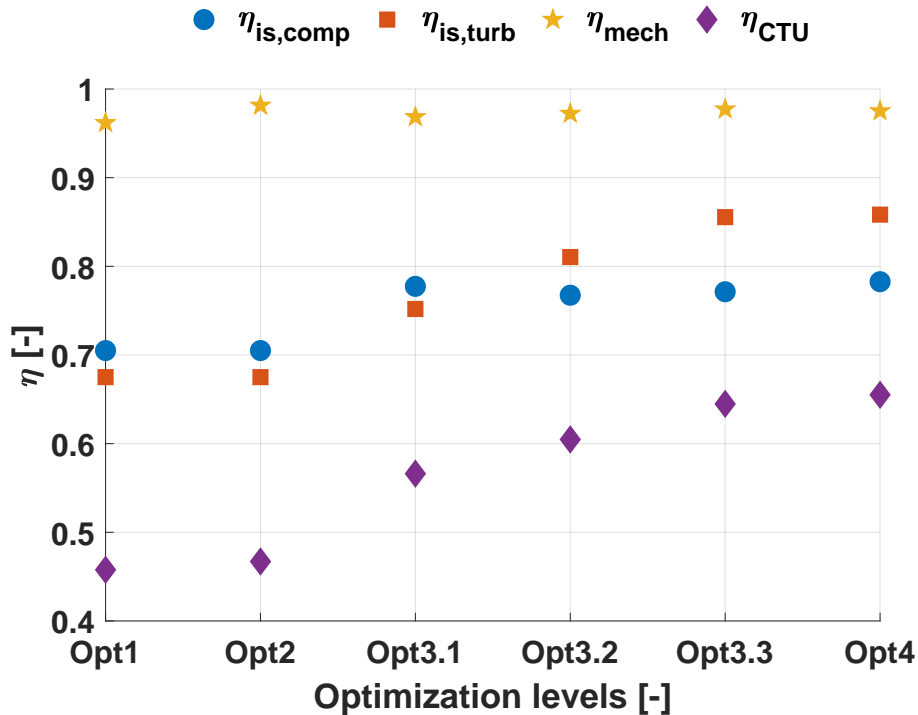


Figure 3.16 – Evolution of the mechanical efficiency and turbomachinery isentropic efficiencies throughout the optimization levels for a stability target equal to the one of the proof of concept ($\Gamma_{CTU}=0.82$)

3.4.3 Turbomachinery design variables

As observed in Figure 3.12, including the turbomachinery design has an impact on the system performance. Figure 3.16 shows the evolution of the turbomachinery isentropic efficiencies throughout the optimization levels when the same stability as the proof of concept is targeted ($\Gamma_{CTU}=0.82$). The CTU mechanical efficiency η_{mech} is displayed as well and presents only small variations from one level to the other. The highest efficiency gain comes from the first optimization stage Opt3.1, which includes the new turbomachinery pre-design models. In this level, the turbine nozzle outlet angle $\alpha_{3,turb}$ and the rotational speed N are optimized, and the turbomachinery tip clearances set to $\max(0.02b_4, 80\mu m)$. The turbine sees its efficiency rising due to the resizing of the tip diameter in the Opt3.2 stage, and increases further in Opt3.3 since a better match of rotor speeds is possible through the adaptation of the shroud to tip radius ratio ϵ . Regarding the compressor, the optimizer chooses to depreciate its efficiency from the Opt3.1 to the Opt3.2 stage at the benefit of the turbine performance. Similarly to the turbine, the Opt3.3 allows a small increase in the compressor efficiency due to the adaptation of the e value. Finally, the optimization of the 1D dimensions achieved by the Opt4 level enables to enhance further the compressor and turbine efficiencies, and hence η_{CTU} increases by 1-pt.

Chapter 3. Integrated design optimization of the Compressor Turbine Unit

Figure 3.17 presents the evolution of the design variables related to the turbomachinery 0D design. The dimensions of the proof of concept are displayed for the sake of comparison.

In the optimization level Opt3.1, the turbomachinery tip diameters, and hence their specific diameters D_s , are fixed. Since the compressor N_s and D_s lie within a narrow band, the optimum rotational speed of the system barely evolves during the optimization process but suggests that the rotational speed achieved during the experimental tests should be decreased. However, The nozzle outlet angle $\alpha_{3,turb}$ is very similar to the proof of concept design and hence is not responsible for the efficiency increase from the Opt2 to Opt3.1.

Since the Opt3.2 stage allows the modification of the turbine and compressor tip diameters, the rotational speed can be adjusted over a wider range. It shows that both the compressor and turbine diameters should be lower than what they are in the current prototype, and hence should run at higher rotor speeds (from 180 to 200 krpm).

In the Opt3.3 level, the ϵ values for both the compressor and the turbine are included as design variables, hence enabling a wider exploration of rotational speeds. Therefore, the optimizer finds higher efficiencies with higher turbine diameters, slightly lower compressor diameters, and with similar rotor speeds than the Opt3.2 stage. The optimizer explores these regions by changing the ϵ_{turb} value from 0.7 to 0.5, and the ϵ_{comp} value from 0.56 to 0.6.

Finally, the optimization level Opt4, which plays with a higher set of turbomachinery variables, enables to increase the CTU efficiency by 1-pt. The Opt4 optimum rotor speed, tip diameters, and ϵ values are similar to the ones of Opt3.3. The evolution of the Opt4 level 1D turbomachinery dimensions are shown in Figures 3.18 and 3.19, for the turbine and compressor, respectively. Figure 3.18 suggests that a turbine outlet rotor angle $\beta_6 = -60^\circ$ and a blade height to tip radius ratio $\zeta_{turb} = 0.1$ are optimal. As shown in Figures 3.18 and 3.19, the optimizer also converges towards the lowest compressor and turbine hub to shroud radius ratios ($\frac{r_{2h}}{r_{2s}}$ at 0.15 instead of 0.36 for the compressor, and $\frac{r_{6h}}{r_{6s}}$ at 0.1 instead of 0.32 for the turbine), hence leading to higher compressor impeller inlet and turbine rotor outlet areas. When the compressor impeller inlet area increases, the compressor absolute inlet velocity C_2 , and hence the relative velocity W_2 , decreases. In the compressor loss repartition, this leads to smaller skin friction losses since they are governed primarily by the average relative velocity $\frac{W_2 + W_4}{2}$ (see equation 2.17 in chapter 2). Similarly, since the rotor outlet area increases, the turbine outlet velocity W_6 and the associated rotor passage losses decrease (see equation 2.13 in chapter 2). Therefore, the results suggest that the turbomachinery hub to shroud ratios should be lower than in the current prototype, provided manufacturing feasibility.

Finally, Figure 3.20 summarizes the optimum compressor and turbine geometries corresponding to each optimization level for a stability target equal to the one of the proof of concept.

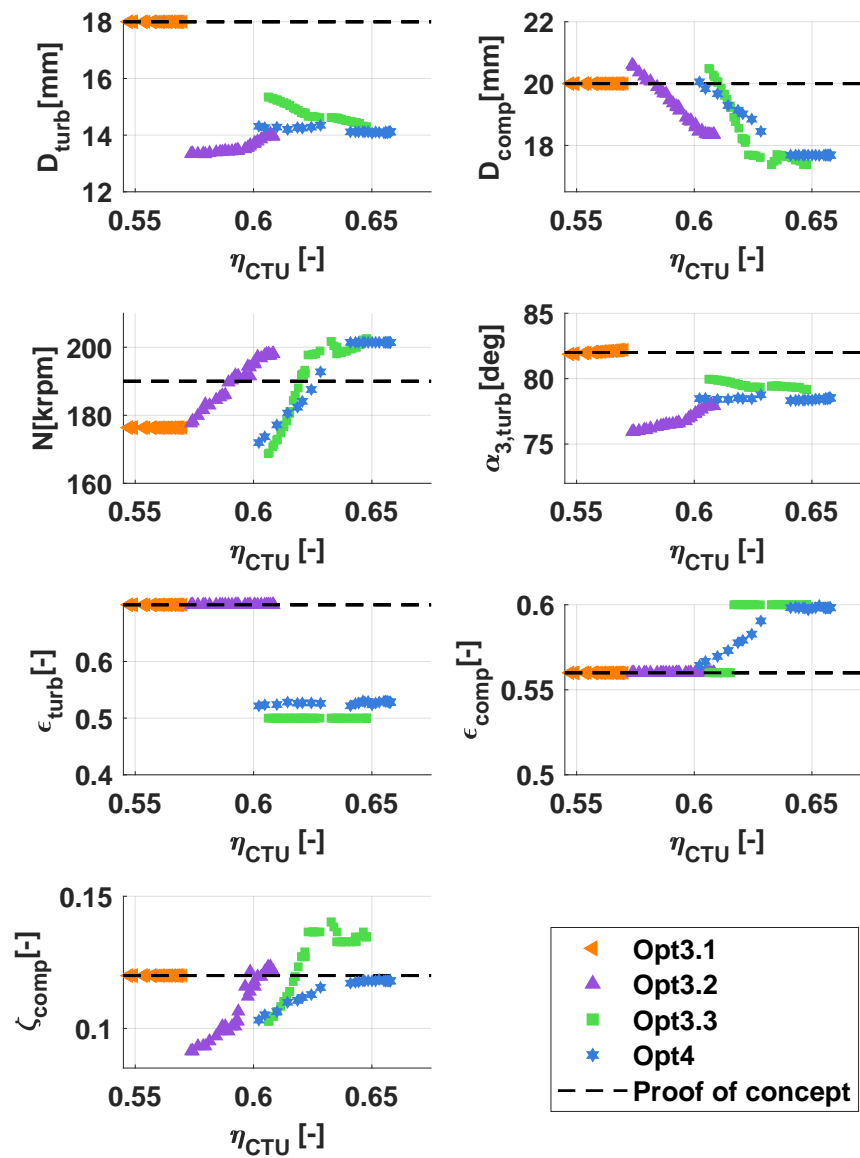


Figure 3.17 – Pareto optimum solutions of the 0D turbomachinery dimensions versus the CTU efficiency

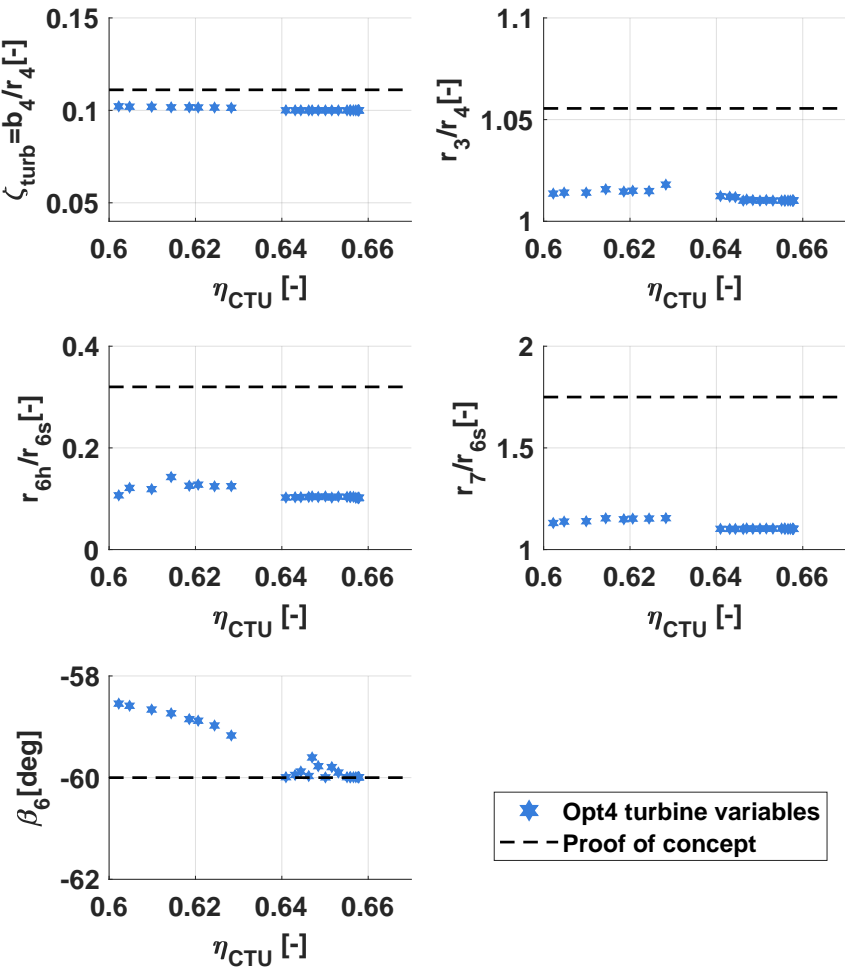


Figure 3.18 – Pareto optimum solutions of the 1D turbine dimensions versus the CTU efficiency

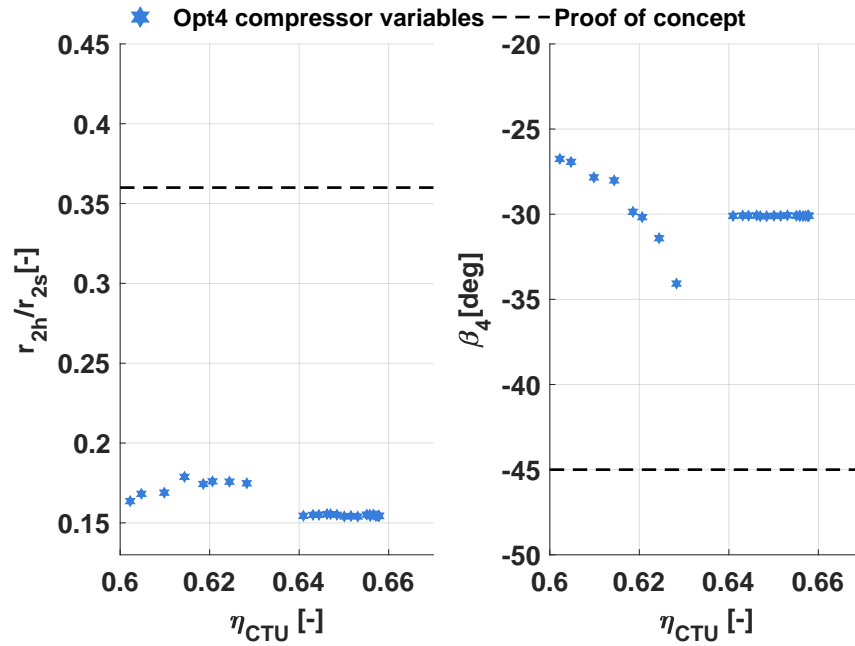


Figure 3.19 – Pareto optimum solutions of the 1D compressor dimensions versus the CTU efficiency

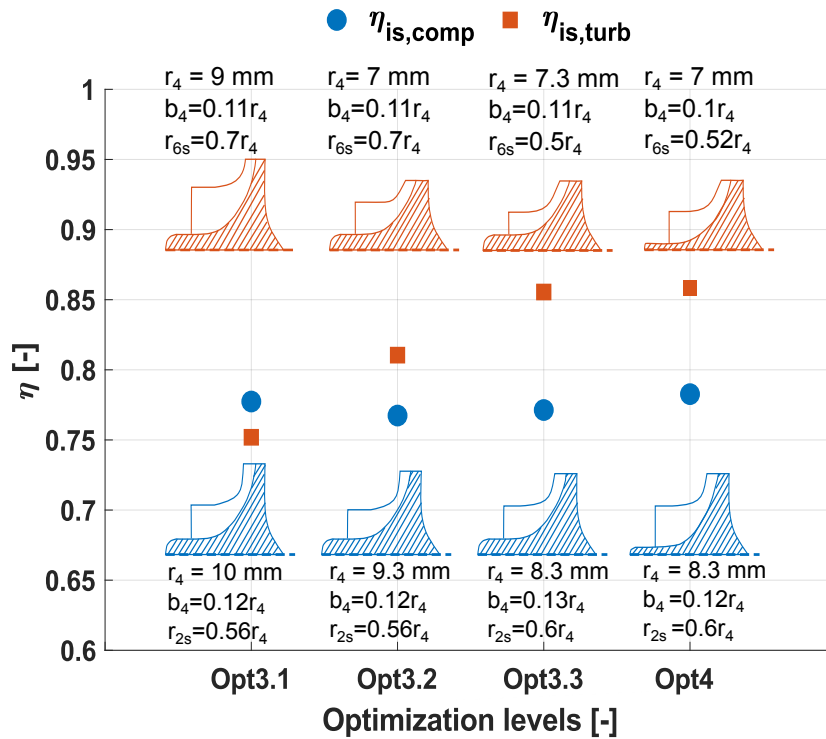


Figure 3.20 – Optimum turbomachinery designs for different optimization levels for a rotordynamic stability equal to the one of the proof of concept ($\Gamma_{CTU}=0.82$)

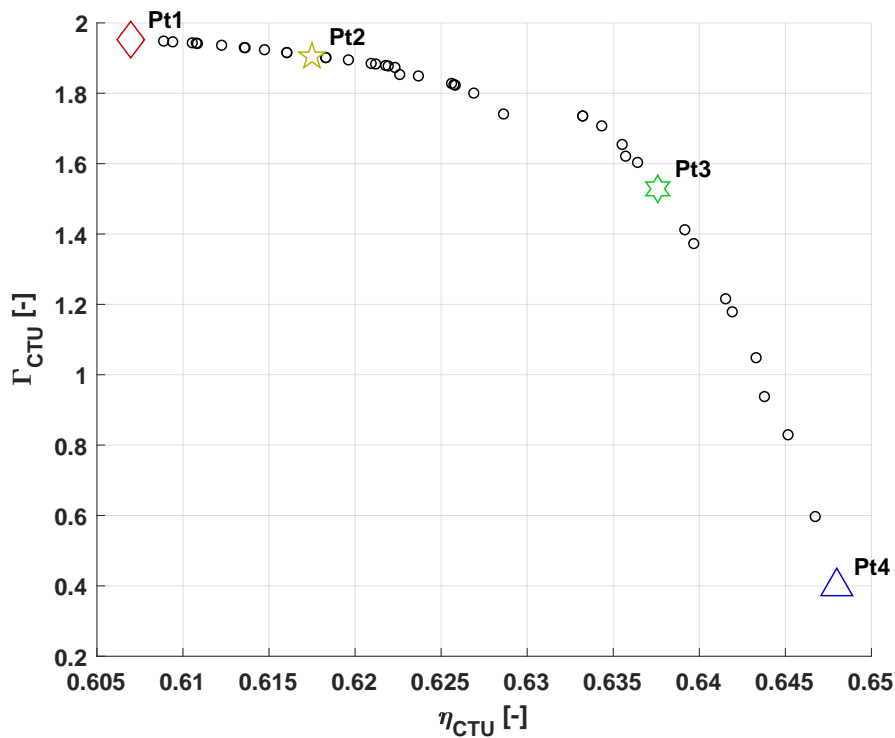


Figure 3.21 – Pareto optimum solution locations considered for the robustness analysis (Pareto front corresponding to the Opt3.3 stage performed on OP3)

3.5 Robustness analysis

In the Pareto curves shown in Figure 3.12, each point represents the best performance/stability trade-off design for a specific operating condition. However, insights into how design deviations affect the performance indicators are missing. In other terms, there is no information about the design robustness. In order to evaluate this effect, a set of sensitivity analyses is performed at different design solutions located on the Pareto front (Pt1 to Pt4), as shown in Figure 3.21. Since they yield the highest CTU performances in a reasonable amount of time, the results from the optimization level Opt3.3 are considered. Table 3.4 shows the design variables corresponding to these four possible Pareto optimum designs.

Table 3.4 – Optimum design variables at four different locations on the Opt3.3 Pareto front (Figure 3.21)

Component	Term	Pt1	Pt2	Pt3	Pt4	Unit
Stability	Γ_{CTU}	1.95	1.91	1.53	0.4	[-]
Efficiency	η_{CTU}	0.61	0.62	0.64	0.65	[-]
G_{rad}	$\frac{D_{rad}}{D_{shaft}}$	1.83	1.72	1.35	1	[-]
	C_{rad}	3.7	3.6	3.56	3.52	[μm]
	H_{rad}	4.74	4.59	3.42	2.95	[-]
	α_{rad}	0.6	0.6	0.6	0.6	[-]
	β_{rad}	169.3	169.4	166	154.6	[deg]
	γ_{rad}	0.8	0.88	0.98	0.98	[-]
G_{ax}	D_{ax}	25	22.2	20	20	[mm]
	C_{ax}	17.5	17.5	17.9	17.9	[μm]
	H_{ax}	3.12	3.12	3.42	3.57	[-]
	α_{ax}	0.59	0.59	0.6	0.6	[-]
	β_{ax}	167.5	163.6	169.5	169.6	[deg]
G_{shaft}	D_{shaft}	8	8	8	8	[mm]
	$\frac{L_{ax-rad}}{D_{shaft}}$	0.26	0.23	0.2	0.2	[-]
	$\frac{L_{rad-rad}}{D_{shaft}}$	2.8	2.9	2.5	1	[-]
	$\frac{L_{rad-turb}}{D_{shaft}}$	0.26	0.27	0.21	0.2	[-]
	r_4	7.7	7.5	7.3	7.2	[mm]
$G_{Turb-0D}$	$\epsilon = \frac{r_{6s}}{r_4}$	0.5	0.5	0.5	0.5	[-]
	N	170	188	205	210	[krpm]
	r_4	10.3	9.5	8.9	8.7	[mm]
$G_{Comp-0D}$	$\epsilon = \frac{r_{2s}}{r_4}$	0.56	0.6	0.6	0.6	[-]
	$\zeta = \frac{b_4}{r_4}$	0.1	0.12	0.13	0.13	[-]
	N	170	188	205	210	[krpm]

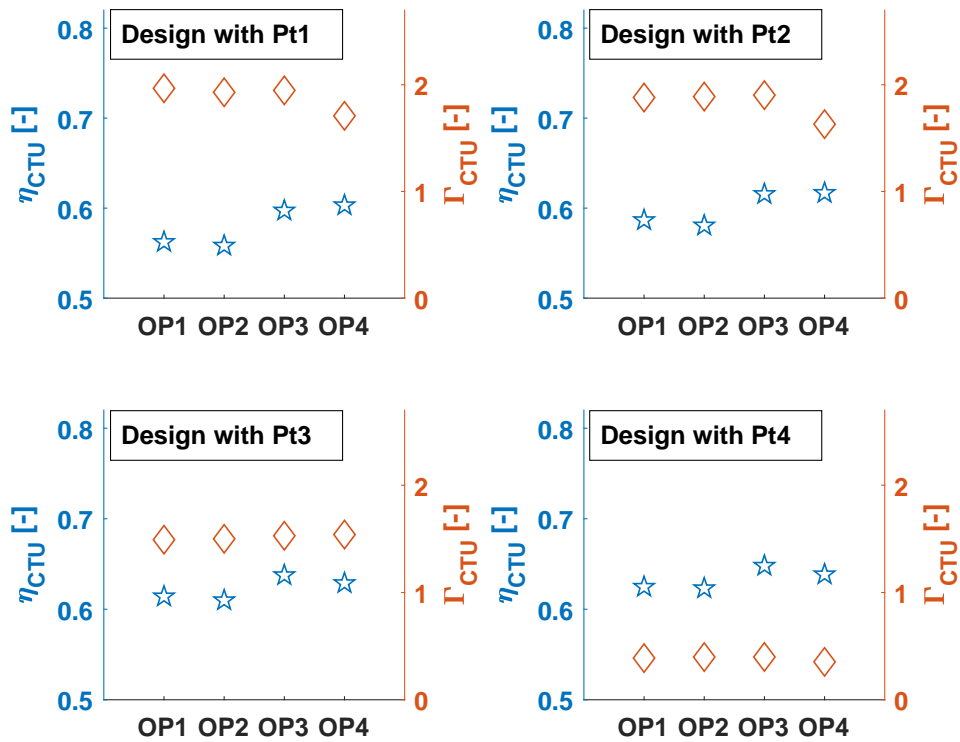


Figure 3.22 – CTU off-design performance and stability when Pareto optimum designs for OP3 are selected

3.5.1 Influence of the design point

The previous results analyzed the integrated design solutions for a specific operating condition - OP3 - described in Table 3.2. Figure 3.22 shows the CTU efficiency and stability for different operating conditions (OP1 to OP4, which are described in Table 3.2) when Pareto optimum designs tailored for OP3 are applied. The optimum designs corresponding to the Pareto locations Pt1 to Pt4 shown in Figure 3.21 are tested. Each design location presents a fixed shaft, bearing, and turbomachinery geometry (tip diameters, shroud diameters, and compressor blade height ratio). However, note that the CTU rotational speed and the turbine nozzle angle are adapted to each operating condition. The results suggest that selecting the design solutions Pt4 and Pt3 leads to less off-design performance and stability variations (0.2-pt on the efficiency) than with Pt1 and Pt2 (0.4-pt on the efficiency).

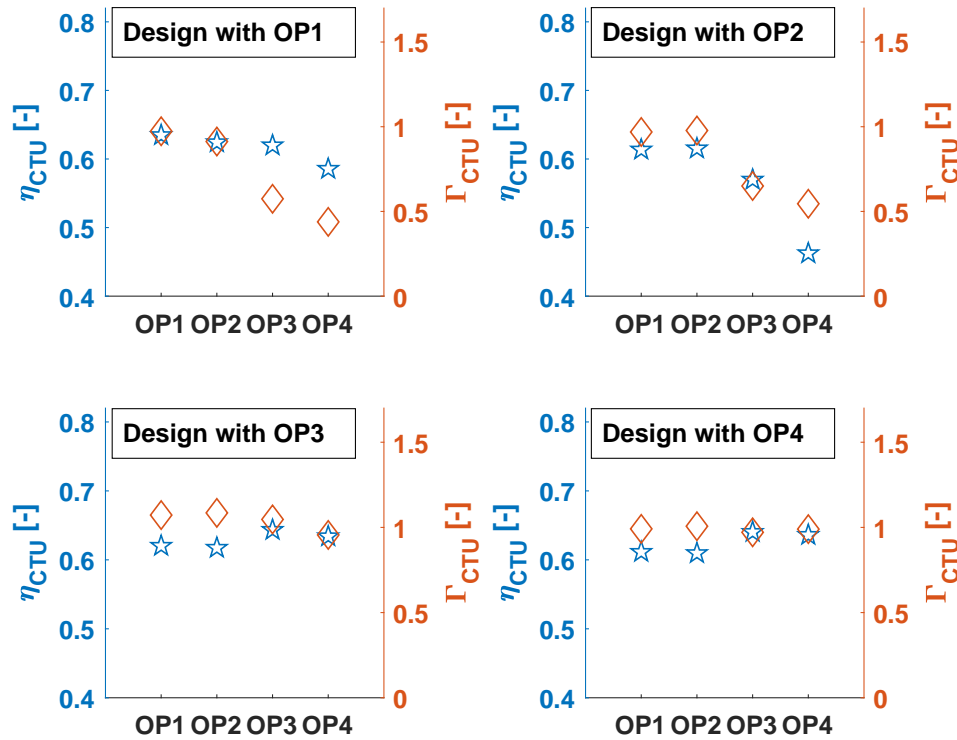


Figure 3.23 – CTU off-design performance and stability when Pareto optimum designs obtained at different OPs are selected at a stability target of $\Gamma_{CTU} = 1$

In a second step, the optimization procedure is applied to the different OPs described in Table 3.2 and the Pareto optimum designs are retrieved for each of them. Table 3.5 shows the optimum decision variables obtained at the different OPs described in Table 3.2, obtained at a rotordynamic stability $\Gamma_{CTU} = 1$. In order to estimate the off-design impact, the optimum designs for each OP are successively selected and assessed using the boundary conditions of the other considered OPs. Figure 3.23 shows the off-design effect on the CTU performance and rotordynamic stability.

The results suggest that choosing the optimum design adapted to OP3 or OP4 has a small off-design impact, with discrepancies up to 0.5% on both performance and rotordynamic stability. Choosing the optimum design for OP1 and OP2 are less interesting options since they trigger efficiency and stability drop up to 20%. Indeed, OP1 and OP2 operate with lower rotor speeds and tip diameters than OP3 and OP4, and hence, achieving satisfactory rotordynamic stability is less challenging. OP1 and OP2 have, therefore, higher C_{rad} , lower H_{rad} , and lower β_{rad} compared to OP3 and OP4, at the penalty to decrease their stability though.

Chapter 3. Integrated design optimization of the Compressor Turbine Unit

Table 3.5 – Optimum design variables of the CTU optimization achieved at $\Gamma_{CTU} = 1$ for different operating conditions

Component	Term	OP1	OP2	OP3	OP4	Unit
G_{rad}	$\frac{D_{rad}}{D_{shaft}}$	1.11	1.07	1.2	1.19	[-]
	C_{rad}	3.55	3.51	3.51	3.52	[μm]
	H_{rad}	2.36	2.3	3.04	3.07	[-]
	α_{rad}	0.59	0.6	0.59	0.59	[-]
	β_{rad}	149.2	158.2	160.2	160.9	[deg]
	γ_{rad}	0.99	0.98	0.99	0.98	[-]
G_{ax}	D_{ax}	20	20.4	20	21.4	[mm]
	C_{ax}	17.6	14.6	17.9	17.5	[μm]
	H_{ax}	3.43	2.81	3.42	2.69	[-]
	α_{ax}	0.59	0.59	0.6	0.57	[-]
	β_{ax}	166.3	168	168	165.4	[deg]
G_{shaft}	D_{shaft}	8	8	8	8	[mm]
	$\frac{L_{ax-rad}}{D_{shaft}}$	0.2	0.23	0.21	0.24	[-]
	$\frac{L_{rad-rad}}{D_{shaft}}$	1.55	2.11	1.6	1.56	[-]
	$\frac{L_{rad-turb}}{D_{shaft}}$	0.2	0.23	0.2	0.24	[-]
$G_{Turb-0D}$	r_4	7.3	6.8	7.2	7.2	[mm]
	$\epsilon = \frac{r_{6s}}{r_4}$	0.5	0.5	0.5	0.5	[-]
	N	170	198	200	211	[krpm]
$G_{Comp-0D}$	r_4	7.9	7.5	8.75	9	[mm]
	$\epsilon = \frac{r_{6s}}{r_4}$	0.6	0.6	0.6	0.6	[-]
	$\zeta = \frac{b_4}{r_4}$	0.18	0.16	0.13	0.13	[-]
	N	170	198	200	211	[krpm]

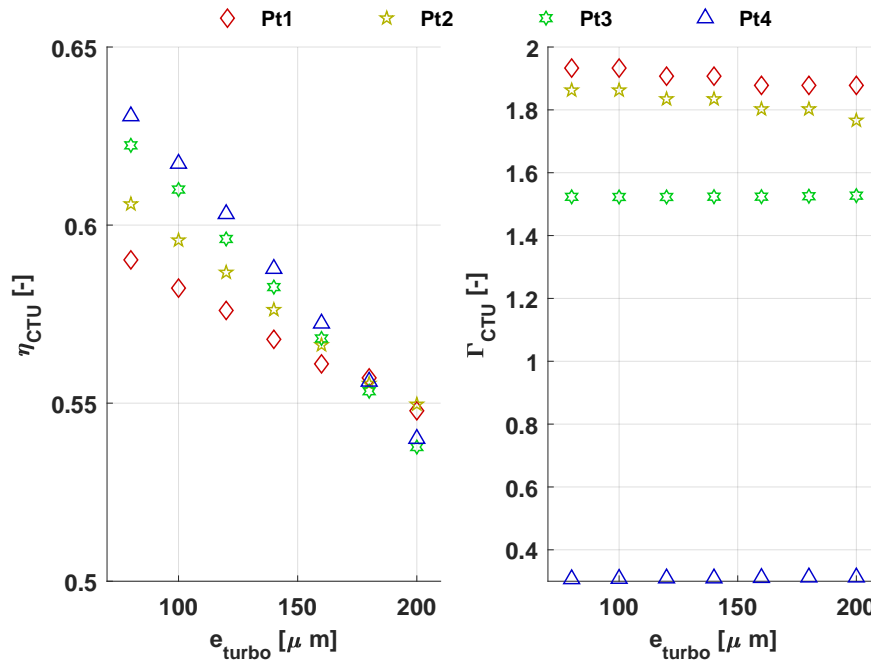


Figure 3.24 – Impact of the tip clearance e_{turbo} on the CTU efficiency and rotordynamic stability

3.5.2 Influence of the tip clearance

In the CTU optimization stages Opt3 and Opt4 performed above, the tip clearances for both compressor and turbine are set to $e_{turbo} = \max(0.02b_4, 80\mu m)$. However, as highlighted in chapter 2, this parameter has a strong influence on the turbomachinery performance and design. Moreover, since this value only depends on the mounting and manufacturing procedure, achieving the design tip clearance is in practice challenging. For the sake of safety, the experimentalist may also decide to increase the tip clearance for first prototype tests.

For the four Pareto optimum locations displayed in Figure 3.21, different tip clearances e_{turbo} ranging from 80 to 200 μm are tested, supposing that they are equal for both the compressor and the turbine. Figure 3.24 presents the evolution of η_{CTU} and Γ_{CTU} while Figure 3.25 shows the turbomachinery efficiencies and rotational speeds function of the tip clearance.

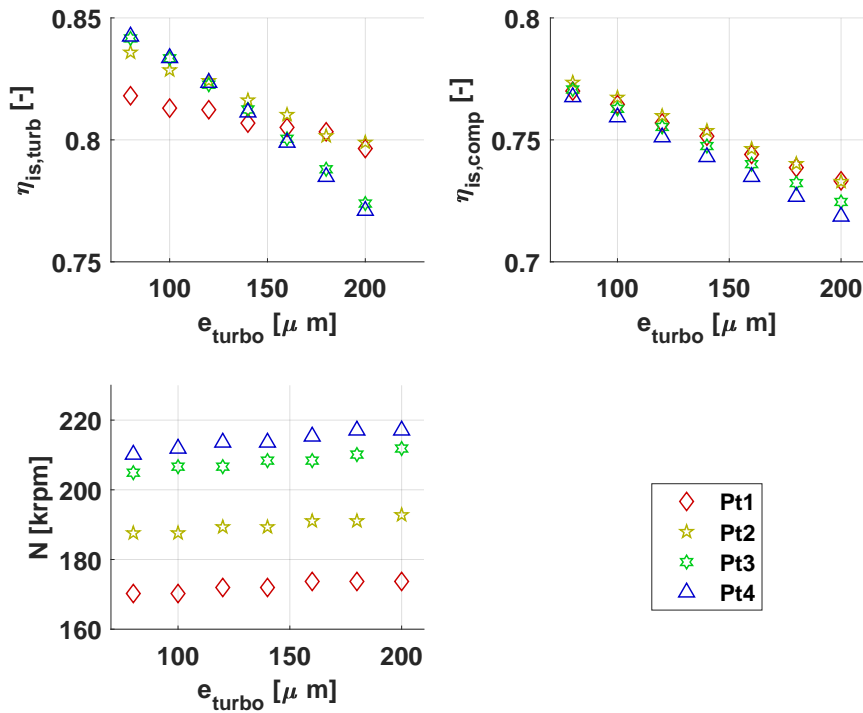


Figure 3.25 – Impact of the tip clearance e_{turbo} on the turbomachinery isentropic efficiencies and rotor speed

The results show that the tip clearance depreciates the CTU performance by a 10-pt efficiency drop from 80 to 200 μ m. This is due to the drastic isentropic efficiency drop of both turbomachinery components (with the Pt4 design, efficiencies drops by 6.4 and 4.4-pt for the turbine and the compressor, respectively). The rotordynamic stability is affected as well due to the required rotor speed adaptation. In addition, the results show that the tip clearance decrease is, in fact, the primary driver for the efficiency increase from optimization level Opt2 to Opt3.1 (Figure 3.16). Indeed the tip clearances were measured at 200 μ m in the proof of concept [35] while the Opt3.1 stage considers clearances at 80 μ m. Therefore, without optimizing the turbomachinery, decreasing the tip clearance in the current prototype would already lead to a significant efficiency improvement. Similarly, implementing a new CTU with optimized turbomachinery (Opt3.2 and Opt3.3), which allows a 7.5 points efficiency increase compared to the Opt3.1 stage, is only beneficial if the tip clearances are well adapted.

Finally, the results suggest that the design points Pt3 and Pt4 are more sensitive to a change in the tip clearance. This is driven mainly by the effect on the radial turbine. The Pt3 and Pt4 design points are characterized by higher rotor speeds and turbine pressure ratios - see Tables 3.2 and 3.4 - and hence present higher turbine tip speeds U_4 . Since the turbine tip clearance losses are driven mainly by the tip speed and the tip clearance (equation 2.11), the turbine isentropic efficiency tends to drop faster with e_{turbo} for the design points Pt3 and Pt4.

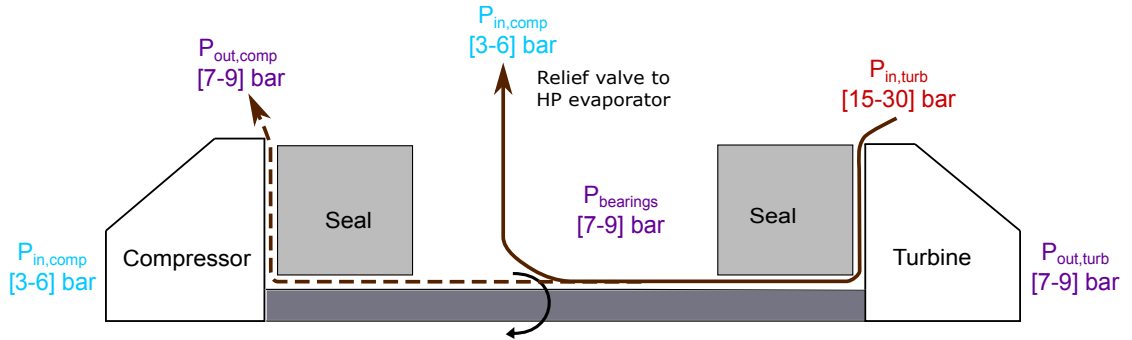


Figure 3.26 – CTU fluid leakage pathways and pressure levels encountered in the experimental data performed by Demierre et al. [35]

3.5.3 Influence of the fluid leakage

In the different optimizations performed above, the fluid leakage has been neglected. In practice, a contact-less labyrinth seal with a fixed clearance C_{seal} is present, which leads to an inevitable fluid leakage affecting the CTU efficiency.

Indeed, besides the axial force, the existence of pressure gradients throughout the CTU results in inevitable fluid leakage from the high pressure (turbine) to the low pressure side (compressor). As shown in Figure 3.26, after encountering the first seal on the turbine back-face, the fluid leakage can follow two particular paths, either to the compressor outlet or back into the cycle loop, generally to the HP evaporator. Since the pressures in the bearing cavity and at the compressor outlet are similar [35], it is assumed that the majority of the fluid leakage flows back into the cycle. This leakage is a direct mechanical power loss between the turbine and the compressor. To mitigate fluid leakages, an appropriate seal design is required, which should be contact-less due to the high rotor speeds that are encountered.

Since they fulfill these requirements and are widely used in the turbomachinery field, labyrinth seals are well indicated. Figure 3.27 shows the schematic of a labyrinth seal and its principal dimensions. These seals are made of a succession of cavities, separated by thin blades and spaced from the rotating shaft by a small clearance C_{seal} . The labyrinth seal cavities add pneumatic resistance in the fluid passage by degrading the flow kinetic energy. In order to estimate the leakage mass flow rate corresponding to a specific labyrinth seal geometry, a reduced order model is used. The model considers a seal with n cavities and with a fixed clearance C_{seal} . It is assumed that the flow is subject to isentropic expansions through each cavity. The flow tangential velocity through the seal is equal to $v_t = \frac{U}{2}$, where U is the rotor shaft tip speed. The meridional flow velocities are calculated for each i^{th} cavity following $v_{m,i} = \sqrt{v_i^2 - v_t^2}$ where $v_i = \sqrt{2(h_i - h_{i-1})}$. After few iterations, the leakage mass flow rate \dot{m}_{leak} is calculated at the n^{th} cavity as follows:

$$\dot{m}_{leak} = \rho_n v_{m,n} A_{seal} = \rho_n v_{m,n} 2\pi r_{shaft} C_{seal} \quad (3.16)$$

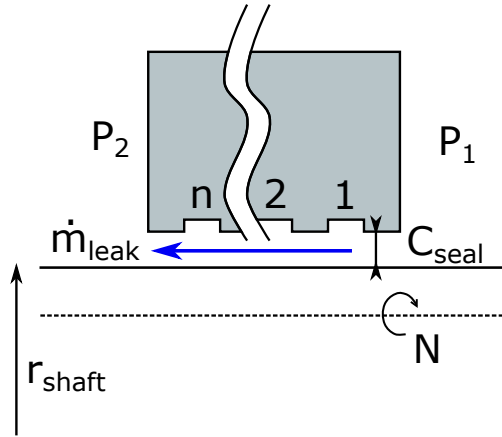


Figure 3.27 – Schematic of a labyrinth seal

The leakage mass flow rate is therefore governed mainly by the area A_{seal} and by the pressure gradient $\Delta P = P_1 - P_2$, which influences the meridional velocity $v_{m,n}$ through $v_i = \sqrt{2(h_i - h_{i-1})}$. In addition, the lower the rotor tip speed (and hence the higher $v_{m,n}$), the higher the fluid leakage.

The updated mechanical power balance of the CTU including the leakage losses is given as follows:

$$\dot{E}_{turb} = \dot{E}_{comp} + \dot{E}_{loss} + \dot{E}_{leak} \quad (3.17)$$

It follows that the CTU mechanical efficiency η_{mech} (equation 3.3) can be rewritten as follows:

$$\eta_{mech,leak} = \frac{\dot{E}_{comp}}{\dot{E}_{turb}} = \frac{\dot{E}_{turb} - \dot{E}_{loss} - \dot{E}_{leak}}{\dot{E}_{turb}} = \eta_{mech} - \frac{\dot{E}_{leak}}{\dot{E}_{turb}} \quad (3.18)$$

To capture the influence of the fluid leakage, a sensitivity analysis on the seal clearance C_{seal} is performed on the optimum designs highlighted in Figure 3.21. The dimensions of the simulated labyrinth seal are summarized in Table 3.6.

Table 3.6 – Sensitivity analysis boundaries on the labyrinth seal variables

Variable	Term	Range
Seal radial clearance	C_{seal}	[0-120] μm
Number of cavities	Z_{seal}	6
Seal diameter	D_{seal}	$D_{shaft} + 2C_{seal}$

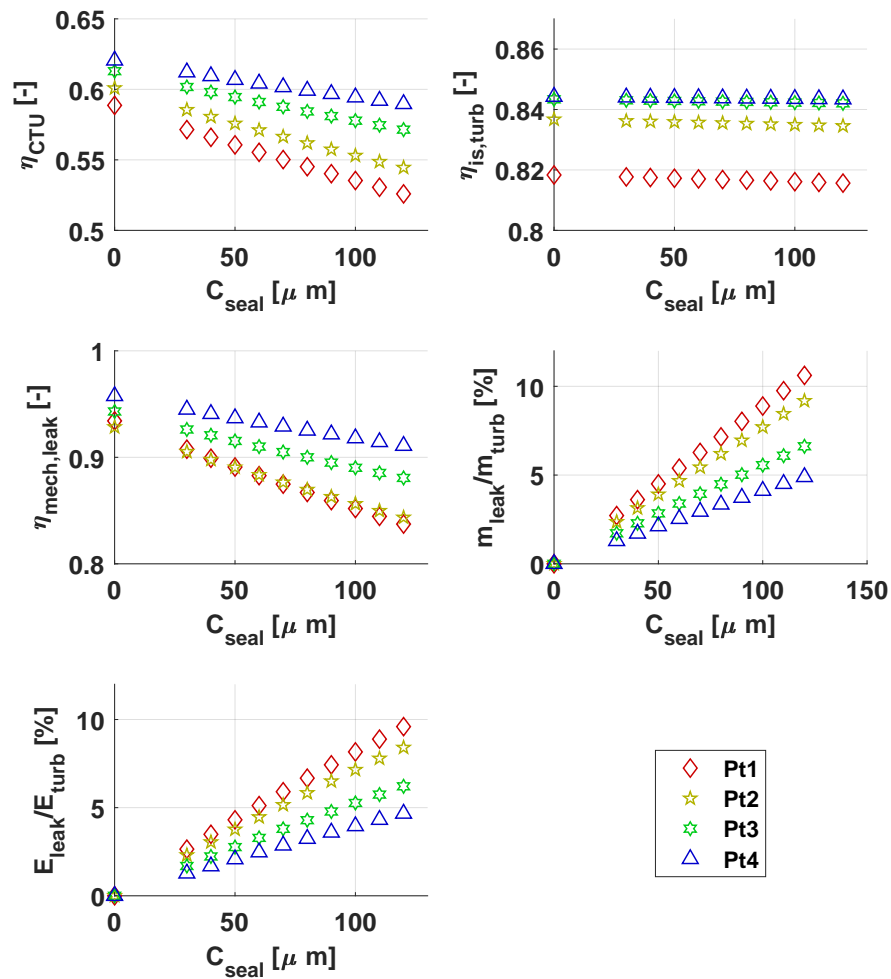


Figure 3.28 – Impact of the seal clearance on the CTU performance

Figure 3.28 highlights the effect of the seal clearance on the overall CTU performance η_{CTU} . The contribution on the turbine isentropic efficiency $\eta_{is,turb}$ and the mechanical efficiency $\eta_{mech,leak}$ is displayed. The relative fluid leakage ratio $\frac{\dot{m}_{leak}}{\dot{m}_{turb}}$ and the power loss ratio $\frac{E_{leak}}{E_{turb}}$ are also plotted. As suspected, the fluid leakage ratio increases linearly with the seal clearance, and hence depreciates the CTU efficiency η_{CTU} through a decrease of η_{mech} . From a seal clearance of 30 μm to 120 μm , the CTU efficiency suffers from a 3-pt drop for the Pt4 design, that can go up to a 7-pt drop when the Pt1 design is considered. The isentropic efficiency of the turbine is, however, barely affected. Finally, the design point Pt1 is subject to higher fluid leakage mass flows because of its lower rotor speed (see Table 3.4).

3.5.4 Influence of manufacturing errors

Radial bearings

Self-acting gas bearings allow oil-free operation without any additional auxiliary systems. Therefore, they are more interesting than pressurized gas bearings and active magnetic bearings for energy conversion applications. However, the drawback of these bearings is that they require tight radial clearances C_{rad} in the order of 3-20 μm for stable operation. Furthermore, very precise groove depths and geometries (defined by D_{rad} , h_{rad} , α_{rad} , and β_{rad} mainly) are required as well. In order to estimate the effect of manufacturing errors of C_{rad} , h_{rad} , and D_{rad} on η_{CTU} and Γ_{CTU} , a sensitivity analysis is performed on the four points located on the Pareto front shown in Figure 3.21. Each radial bearing variable is varied independently within ranges defined in Table 3.7. The results of the sensitivity analysis are represented in Figure 3.29.

Table 3.7 – Sensitivity analysis boundaries on the radial bearing variables

Variable	Term	Range
Radial clearance	C_{rad}	$C_{rad,nom} -3/+7 \mu\text{m}$
Groove depth	h_{rad}	$h_{rad,nom} \pm 7 \mu\text{m}$
Bearing diameter	D_{rad}	$D_{rad,nom} \pm 0.2 \text{ mm}$

Manufacturing errors occurring on C_{rad} and h_{rad} barely change the CTU mechanical efficiency but have a significant influence on the rotordynamic stability. Indeed, for the Pareto locations Pt1 to Pt3, a radial clearance 2 μm higher than its optimum value would ultimately lead to unstable systems ($\Gamma_{CTU} < 0$). For the Pareto location Pt4, which presents the lowest stability, this margin is less than a micron. While C_{rad} decreases, the stability tends to decrease as well but less drastically. However, it endangers the system towards its limit to centrifugal growth expansion that leads to possible touchdowns. There is, therefore, a narrow margin in which the radial clearance should be contained. Similarly, a 2 to 5 μm increase in the HGJB groove depth leads to an unstable CTU. Finally, the variations in the order of 0.2 mm on the radial bearing diameter have only a limited effect on both the CTU performance and stability.

Axial bearing

The pressure field generated by the axial bearing relies on the same working principle than the HGJB. Therefore, the spiral grooved thrust bearing SGTB requires small axial clearances C_{ax} and precise groove depths and diameters (defined by h_{ax} and D_{ax} , respectively). The same sensitivity analysis applied to radial bearings is performed on the axial bearing, and the effect of the manufacturing errors on the axial load capacity F_{SGTB} is reported. The results of the sensitivity analysis are displayed in Figure 3.30 for SGTB dimensions varying within ranges shown in Table 3.8.

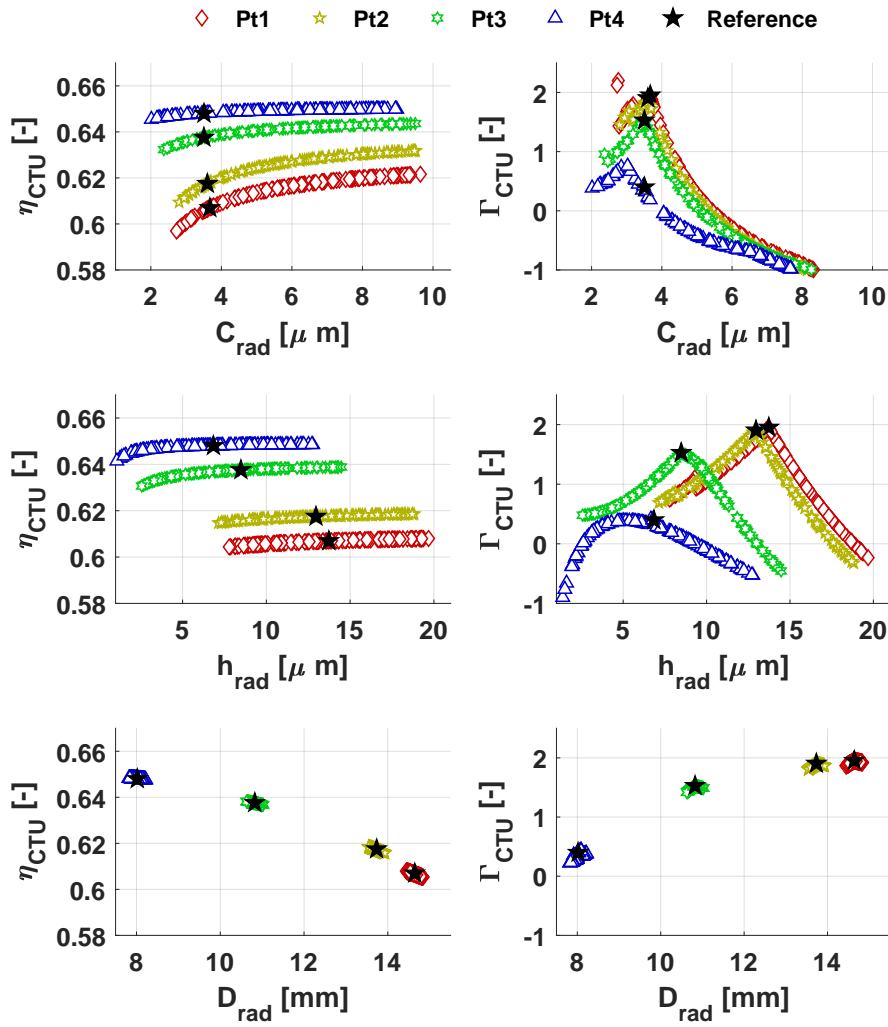


Figure 3.29 – Effect of the radial bearing manufacturing errors on the CTU performance and stability

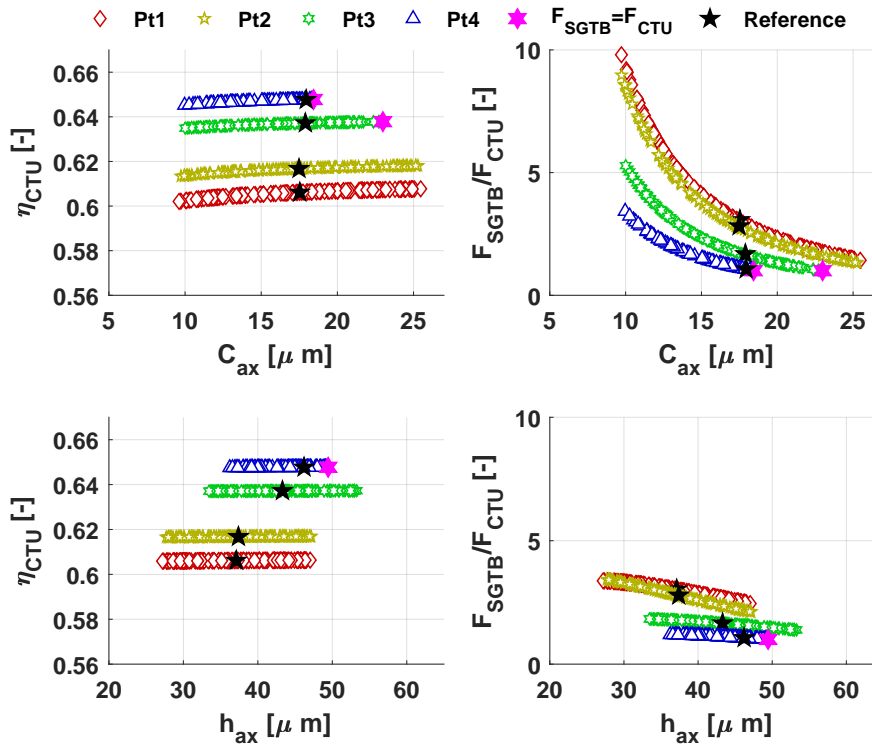


Figure 3.30 – Effect of the axial bearing manufacturing errors on the CTU performance and SGTB load capacity

Table 3.8 – Sensitivity analysis boundaries on the axial bearing variables

Variable	Term	Range
Axial clearance	C_{ax}	$C_{ax,nom} \pm 10 \mu\text{m}$
Groove depth	h_{ax}	$h_{ax,nom} \pm 10 \mu\text{m}$
Bearing diameter	D_{ax}	$D_{ax,nom} \pm 0.2 \text{ mm}$

Manufacturing errors in the order of 0.2 mm on the axial bearing diameter D_{ax} have a negligible effect on the system performance and feasibility, and hence, are not shown in Figure 3.30. Furthermore, similarly to the radial bearings, the manufacturing errors on C_{ax} and h_{ax} trigger marginal CTU efficiency variations. However, C_{ax} has a drastic impact on the SGTB load capacity F_{SGTB} . In particular, the CTU design in the Pareto locations Pt4 is highly sensitive to the axial clearance C_{ax} since a 1 μm increase does not allow to satisfy the condition $F_{SGTB} > F_{CTU}$, F_{CTU} being the axial load imposed to the CTU. This is due to the choice of the optimizer to select the smallest D_{ax} and highest C_{ax} to maximize at best the CTU efficiency (see Figure 3.14). The same effect appears when manufacturing errors of few microns occur on the axial bearing groove depth h_{ax} .

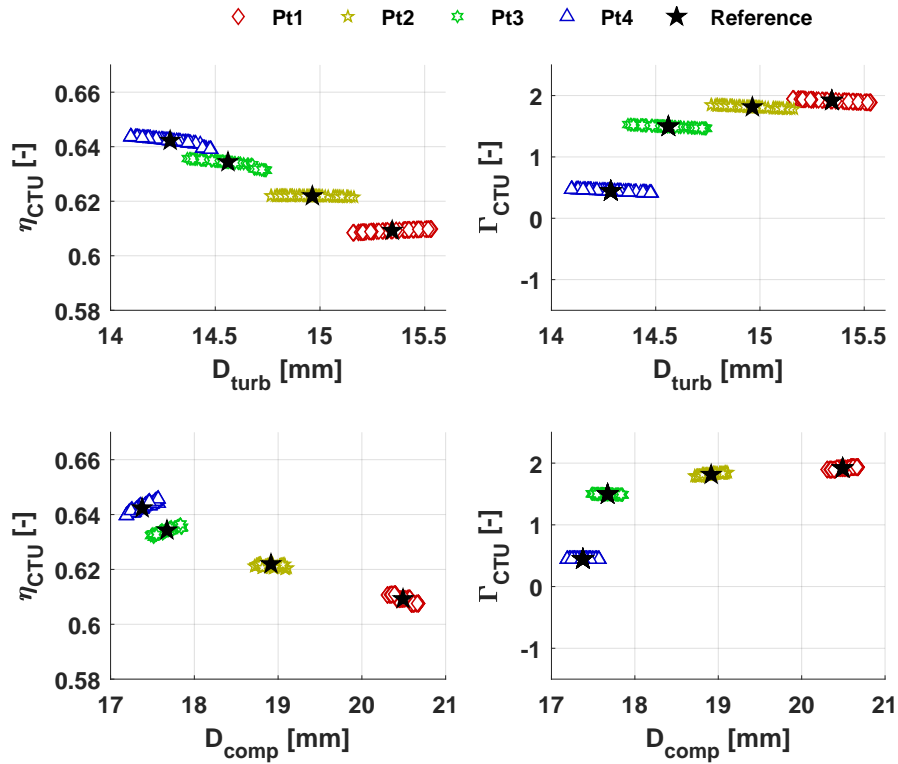


Figure 3.31 – Effect of the turbomachinery diameters manufacturing errors on the CTU performance and stability

Turbomachinery

Manufacturing errors occurring on the turbomachinery components may depreciate their isentropic efficiencies. This section evaluates the impact of dimensional errors on the turbomachinery diameters $D = 2r_4$, blade heights b_4 , and shroud diameters $r_{2s,6s}$. The considered manufacturing errors ranges are displayed in Table 3.9. The results of the sensitivity analysis are presented in Figures 3.31 and 3.32. The results suggest that manufacturing errors occurring on the turbomachinery geometry parameters within the range exposed in Table 3.9 lead to variations in the order of 0.3-pt for the CTU efficiency and of 0.2-pt for the CTU stability, which is considered acceptable.

Table 3.9 – Sensitivity analysis boundaries on the turbomachinery variables

Variable	Term	Range
Turbine tip diameter	$D_{turb} = 2r_{4,turb}$	$D_{turb,nom} \pm 0.2$ mm
Compressor tip diameter	$D_{comp} = 2r_{4,comp}$	$D_{comp,nom} \pm 0.2$ mm
Turbine blade height	$b_{4,turb}$	$b_{4,turb,nom} \pm 0.05$ mm
Compressor blade height	$b_{4,comp}$	$b_{4,comp,nom} \pm 0.05$ mm
Turbine shroud radius	$r_{6s,turb}$	$r_{6s,turb,nom} \pm 0.1$ mm
Compressor shroud radius	$r_{2s,comp}$	$r_{2s,comp,nom} \pm 0.1$ mm

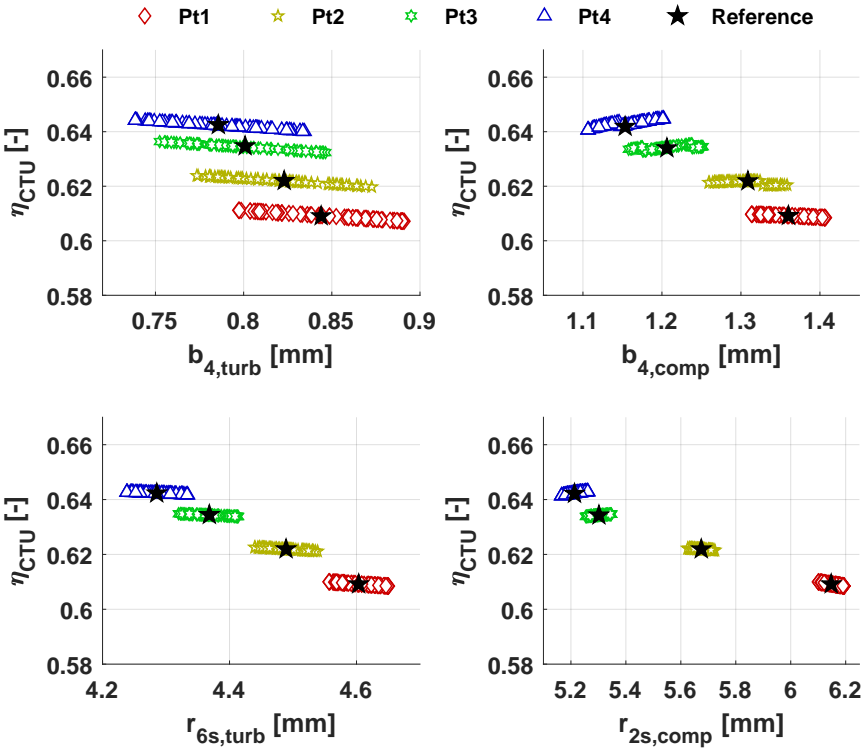


Figure 3.32 – Effect on the CTU performance of the manufacturing errors on the turbomachinery shroud diameters and blade heights

3.5.5 Tolerance ranges

Table 3.10 summarizes the recommendations on the manufacturing dimensions and tolerances to apply to each component. Since the impact of the manufacturing errors on the components diameters (D_{rad} , D_{ax} , D_{turb} , D_{comp} , and D_{shroud}) is considered negligible, a conservative tolerance of ± 0.05 mm is recommended. Similarly, a tolerance of ± 0.01 mm should be applied to the turbomachinery blade heights.

The manufacturing tolerances on C_{rad} and C_{ax} are more challenging though. Indeed, a tolerance range of 2 to 4 μm is required for C_{rad} to ensure a safe operation, which is in practice doable but challenging to obtain through grinding and honing process. C_{ax} requires tolerance ranges between 10 and 6 μm . Nonetheless, since C_{ax} is an axial clearance, it is common practice to use shims to set the correct dimensions. These shims are manufactured with leveling machines in which the control of fine tolerances is made easier. Furthermore, leveling is less expensive than fine grinding and honing processes. The groove depths h_{rad} and h_{ax} are made through laser etching, which can satisfy the suggested tolerances shown in Table 3.10. A labyrinth seal with six cavities and a 30 μm radial clearance, with a tolerance that does not exceed 20 μm in range, is suggested. Finally, the maximum tip and back-face clearances $e_{tp,back}$ should not exceed 80 μm with a tolerance range of 20 μm to ensure the highest CTU efficiency.

Table 3.10 – Recommended tolerances for the manufacturing of the CTU radial and axial bearings

Component	Term	Pt1	Pt2	Pt3	Pt4	Unit
G_{rad}	C_{rad}	3.5 ± 2	3.5 ± 2	3.5 ± 2	3.5 ± 1	$[\mu\text{m}]$
	h_{rad}	13.2 ± 4	12.6 ± 4	8.4 ± 4	7 ± 2	$[\mu\text{m}]$
G_{ax}	C_{ax}	16.5 ± 5	16.5 ± 5	17 ± 5	$17 +1/-5$	$[\mu\text{m}]$
	h_{ax}	37.1 ± 6	37.4 ± 6	43.3 ± 6	$46.2 +3/-6$	$[\mu\text{m}]$

3.6 Limitations of the integrated optimization procedure

- **Models** The different models used in the proposed integrated design procedure are 1D or 0D models, which enable to capture the aerodynamic features of the CTU with a reasonable computational effort while keeping a sufficient level of detail in the design. Some models, particularly the axial force and the fluid leakage models, which consist in first approximations, would gain in being investigated further and refined. In particular, 2D and 3D analyses may apprehend better the axial load occurring on a turbomachinery wheel, while bulk flow models, which account for skin friction losses, may offer a more realistic estimation of the fluid leakage through a labyrinth seal.
- **Off-design performance** The integrated design procedure has been tested on four experimental points measured by Demierre et al. [35], to identify the potential efficiency/stability gains. These measured experimental points cover a wide range of rotational speeds and turbine pressure ratios. Furthermore, it has been shown that the off-design performance across these four operating points is similar. To investigate more in-depth the off-design effect on the targeted application, more operating points should be tested with additional compressor pressure ratios and turbomachinery mass flow rates.
- **Heat transfer** Besides presenting high pressure gradients, the temperature difference between the turbine and the compressor is triggering heat transfer losses. Therefore, since a small-scale system is considered, the adiabatic assumption is no longer valid [64]. Non-adiabatic operations on a small-scale compressor cause an efficiency depreciation due to the temperature rise at the compressor outlet [100]. This phenomenon has been assumed as a possible cause of the isentropic efficiency mismatch between the compressor 1D model and experimental data provided by Demierre et al. [35]. Similarly, since non-adiabatic conditions tend to cool down the flow during the expansion process, hence decreasing the available enthalpy drop, heat transfer losses may depreciate the turbine isentropic efficiency as well, at a lesser effect than for compressors though [101, 102]. Therefore, since it may influence its trade-off mechanisms, the CTU integrated design optimization would gain in implementing heat transfer considerations.
- **Robustness** The results of the integrated design procedure suggest that the robustness is not to be neglected, especially when manufacturing errors on the radial and axial bearing clearances are suspected. In particular, the optimization algorithm tends to converge towards axial bearing designs that are just at the limit $F_{SGTB} = F_{CTU}$, in order to achieve maximum efficiencies. To operate within safer zones, it may be of interest to implement a safety factor applied to the axial force since the contribution of the SGTB on the overall CTU efficiency is relatively small. Moreover, the investigation of the manufacturing errors on the radial bearing design shows that both radial clearances and groove depths require very tight tolerances to ensure sufficient rotordynamic stability. This comes at the penalty of high manufacturing costs though. Future investigations could include the robustness as a third optimization objective.

3.7 Summary and conclusions

In this chapter, the integrated optimization of the gas bearing supported Compressor Turbine Unit (CTU) has been performed. The procedure consists in the simultaneous optimization of all the CTU components, including the shaft, the turbomachinery components (centrifugal compressor and radial inflow turbine), the radial bearings (of Herringbone groove Journal Bearing (HGJB) type), and the axial bearing (of Spiral Groove Thrust Bearing (SGTB) type). A Multi-Objective Optimization (MOO) procedure is applied, which aims at finding the best overall design to maximizing both the CTU efficiency η_{CTU} and rotordynamic stability Γ_{CTU} . The optimization procedure is divided into different levels of complexity to identify how much level of design detail is needed to devise meaningful guidelines with regards to the optimization and modeling of small-scale turbomachinery systems. The first level of complexity only includes the optimization of the bearings (radial and axial). The shaft design is considered in a second step. The third optimization stage adds the turbomachinery design features using the reduced order models presented in chapter 2. Finally, the final optimization stage includes a variety of 1D dimensions. While being more complete, the latter is also the most time-consuming.

The comparison of the obtained Pareto fronts for each optimization level reveals that the highest performance potential is achieved by focusing on the turbomachinery design, mainly by tuning the shroud to tip radius ratios ϵ of both compressor and turbine. The final optimization level, which uses the 1D turbomachinery models, enables to get an additional but marginal improvement (+1-pt), considering that the optimization results are retrieved with sufficient convergence within a week rather than a day when using the 0D turbomachinery models. The analysis of each design variable is further performed, which identifies the turbomachinery features as being the primary drivers of the CTU efficiency, while the radial bearing and rotor dimensions govern the rotordynamic stability.

Finally, a set of sensitivity analyses has been performed, aiming at evaluating the impact of off-design effects, tip clearance, fluid leakage, and manufacturing errors. The Pareto optimum solutions between four different operating conditions have been compared, suggesting that off-design considerations have a marginal effect on the system performance and rotordynamic stability. Controlling the turbomachinery tip clearances is, however, of great importance since a 100 μm increase is suggested to lead to a 4-pt CTU efficiency decrease. The impact of the fluid leakage is further analyzed, which presents a 2 to 5-pt CTU efficiency depreciation if a labyrinth seal clearance increases from 50 to 100 μm . Manufacturing errors are also to be carefully investigated. While variations on the shaft, bearings and turbomachinery components do not depreciate the CTU efficiency, they have a strong influence on the system feasibility. A difference of few microns in the radial bearing clearance and groove depth may lead to unstable rotors ($\Gamma_{CTU} < 1$). Similarly, errors of few microns in the axial bearing clearance and groove depth are likely to decrease the SGTB load capacity and lead to touchdowns. A thorough design of the shaft and bearings together with very tight manufacturing tolerances is essential, increasing the cost and complexity of the technology though.

4 Integrated design optimization of the HP-ORC cycle

While the previous chapter focused on the integrated design optimization of the Compressor Turbine Unit (CTU) for fixed working fluid and cycle operating parameters, this chapter aims at the optimization of the HP-ORC thermodynamic cycle, regarding objectives of maximum efficiency and minimum investment cost.

A detailed description of the HP-ORC cycle and its different components are given in sections 4.2 and 4.3. The economic model of the system, which is based on the components investment cost, is introduced in section 4.4. The multi-objective optimization procedure which finds the best thermo-economic trade-offs is presented in section 4.5, and its results in section 4.6. The investigation targets (1) the identification of the optimum trade-off designs for different performance indicators and boundary conditions, (2) the impact analysis of the component cost, and (3) the comparative study between two HP-ORC configurations (mechanically coupled or uncoupled). Finally, in section 4.7, the Pareto-dominant solutions are compared with a Single Effect Absorption Heat Pump (SEAHP), which is one of the most widespread technologies available on the TDHP market, and with the measured performance of the first prototype tests in section 4.8.

Part of the work presented in this chapter has been published in:

Mounier V, Mendoza L.C., Schiffmann J. *Thermo-economic optimization of an ORC driven heat pump based on small scale turbomachinery and comparison with absorption heat pumps*. Int. J. Refrig. 2017

4.1 Introduction

When designing ORC and HP systems, it is of common practice to look at the cycle features that optimize their performances, i.e., that maximize the COP for HPs and the maximum expander power output for ORCs. However, the best performance designs inevitably lead to higher investment costs. One of the primary drivers of this trade-off are the heat exchangers since the more efficient they are, the more expensive they get. When competing with other

technologies available on the market, assessing the optimum trade-off designs towards the investment cost and the system efficiency is, therefore, essential. Many references can be found in literature where parametric studies of ORCs including economic factors based on equipment cost are performed [103–108]. Nonetheless, few studies have considered true multi-objective optimization to identify the optimum trade-off families between investment cost and performance. Wang et al. [109] used an evolutionary algorithm to perform the thermo-economic optimization of an ORC based on component investment costs and exergetic efficiency, highlighting the optimum values of key thermodynamic parameters. Various authors have contributed to the research on HP-ORC cycles, mainly by investigating the working fluids that maximize the COP for a specific application [26–29]. However, the thermo-economic analysis of HP-ORCs is currently missing. Furthermore, the design of the expansion and compression device is often not considered thoroughly, and a fixed isentropic efficiency is used instead, regardless of the operating conditions. Nonetheless, as shown recently by Mounier et al. [56], designing small-scale ORC systems by coupling the thermodynamic and working fluid optimization with the turbo-expander preliminary design characteristics offers valuable insights into the trade-off mechanisms. Thanks to the reduced order turbomachinery models described in this thesis, it is possible to include the compressor and turbine design into the optimization process while keeping the computation time within reasonable bounds.

The goal of this chapter is to perform a thermo-economic optimization on the HP-ORC system based on gas bearing supported turbomachinery. In a first step, the thermodynamic steady-state model of the HP-ORC is introduced considering a ground source-based domestic heating application with a heating power of 40 kW. Using the radial turbomachinery pre-design models presented in chapter 2, the CTU design (rotational speed, tip, and shroud diameters) is included in the optimization process. However, since the shaft and bearing design variables have a limited effect on the system efficiency (see conclusions of chapter 3), they are not integrated into the optimization procedure described in this chapter. An economic model based on component investment cost is further developed. Catalog-based cost correlations (heat exchangers and boiler), manufacturers cost estimation (CTU), and average drilling costs for the Ground Heat Exchanger (GHX) are considered. From these models, a thermo-economic optimization using an evolutionary algorithm is performed. The results of this optimization highlight the ideal HP-ORC working fluid for different hot source temperatures and identify the optimal thermodynamic design (heat exchanger pinch, sub-cooling,...). The influence of the considered performance indicators (COP or exergetic efficiency η_{exe}) and of the component cost on the optimum design is further discussed.

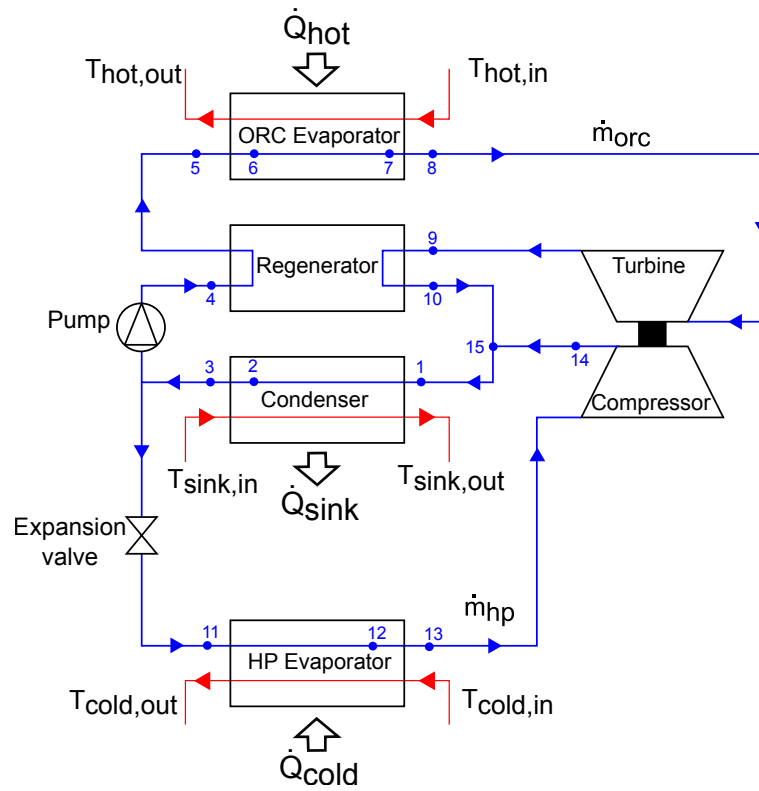
The thermo-economic comparison of two HP-ORC configurations (mechanically coupled and uncoupled) is performed, in order to identify which system offers the best investment cost/performance trade-off. The Pareto optimum HP-ORC systems are further compared with a competing TDHP technology, the Single Effect Absorption Heat Pump (SEAHP), in order to have more insights into the market potential of HP-ORCs. Finally, the optimum HP-ORC solutions are compared with the experimental data obtained by Demierre et al. [30], in order to assess the performance gain obtained with the present integrated optimization procedure.

4.2 HP-ORC description

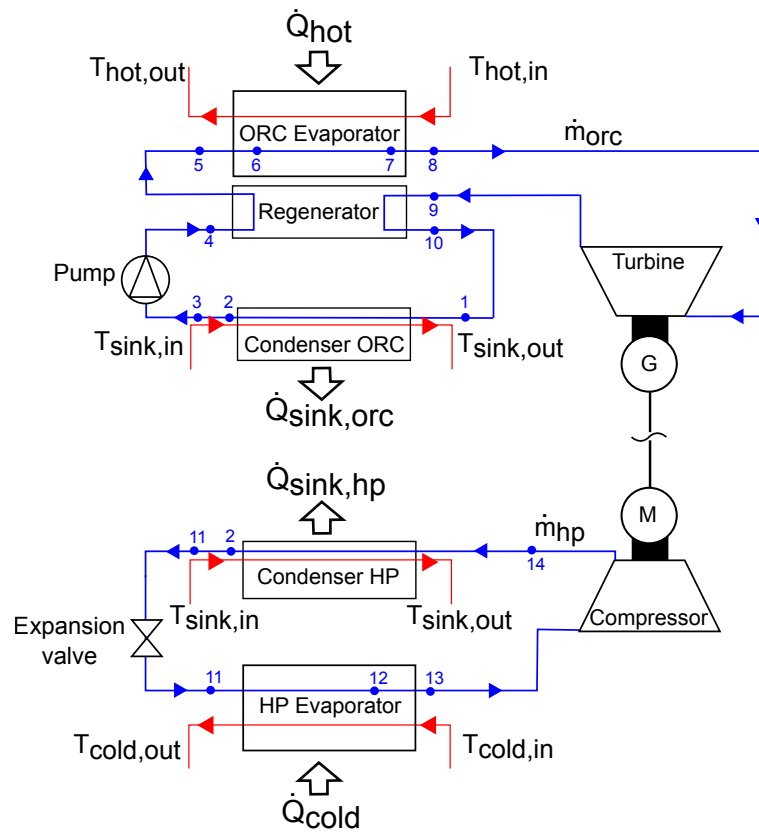
The ORC driven HP (HP-ORC) concept consists in the combination of an Organic Rankine Cycle (ORC) and a Heat Pump (HP). Two main configurations exist, one where the ORC and HP loops are mechanically linked (Figure 4.1a), and one where the two loops are uncoupled (Figure 4.1b).

The cycle illustrated in Figure 4.1a is composed of a topping ORC and a bottoming HP. The topping cycle described by the process (1-2-3-4-5-6-7-8-9-10-15) is composed of a pump (3-4), an ORC evaporator (sub-cooled section 5-6, evaporating section 6-7, and super-heated section 7-8 when subcritical), a turbine (8-9), a regenerator (4-5/9-10), and a condenser (super-heated section 15-1, condensing section 1-2, and sub-cooled section 2-3). The turbine drives directly the compressor of the bottoming HP cycle, described by the process (1-2-3-11-12-13-14-15), composed of an HP evaporator (evaporating section 11-12 and reheating section 12-13), a compressor (13-14), a condenser (super-heated section 15-1, condensing section 1-2, and sub-cooling section 2-3), and an expansion valve (3-11). The two vapor streams leaving the compressor and the turbine are adiabatically mixed in (15). \dot{Q}_{hot} is the heating power delivered from the hot source to the ORC evaporator, \dot{Q}_{cold} the heating power absorbed by the HP evaporator from the cold source, and \dot{Q}_{sink} the heating power released by the condenser to the ambient. The Compressor Turbine Unit (CTU) is composed of a single-stage radial inflow turbine and a single-stage centrifugal compressor, both linked through a gas bearing supported shaft. The coupled HP-ORC has, therefore, its expansion and compression devices supported on the same shaft, where the mechanical power harnessed by the ORC turbine is transferred directly to the HP compressor. Since only contact-less seals can be implemented with such a design, leakage is inevitable between the turbine and compressor as a consequence. Therefore, the ORC and HP loops must operate with the same working fluid and share the same condenser. Moreover, the addition of a regenerator in the ORC loop is discussed, since its adoption is highly dependent on the working fluid and cycle configuration [36, 110]. While the improvement of the ORC thermal efficiency can be limited in some cases, a regenerator helps to reduce the size of the condenser and of the ORC evaporator, and hence may lead to an economic interest [36].

The uncoupled HP-ORC (Figure 4.1b) has its expansion and compression devices mechanically dissociated and connected by an electrical transmission. The heating power recovered by the ORC is converted into electrical power via a generator (G), which is supplied to the HP compressor through a motor (M). The main advantage of such a system is its capability to have different working fluids in the two cycles, hence offering higher design flexibility. Moreover, such a system offers higher operational flexibility since the heating capacity and electricity generation can be uncoupled. However, the system efficiency may drop due to the addition of sources of mechanical and electrical power losses. Moreover, the system reaches higher costs since the condenser has to be split in two and the cost of the compressor motor, expander generator, and frequency converters has to be added. It is assumed that the power generation units (motor and generator) have a conversion efficiency of 96% each.



(a) Coupled HP-ORC



(b) Uncoupled HP-ORC

Figure 4.1 – HP-ORC schematic diagram of the topping Organic Rankine Cycle and the bottoming single-stage vapor compression heat pump cycle where the HP compressor and ORC turbine are (a) mechanically coupled and (b) uncoupled

4.3 Components modeling

4.3.1 Cycle model

The HP-ORC model considers a water-brine heat pump system driven by heat, where the cold source heating power is extracted from the ground with a brine composed of water and glycol (60%/40%). The heat sink is adapted to floor heating applications and is composed of a brine with the same composition as in the Ground Heat Exchanger (GHX). The 40 kW heat output is targeted for a small multi-dwelling building [2]. The cold source and heat sink temperatures have been set according to the European standards for brine/water heat pumps (EHPA [111]). The hot source is a thermal oil (Syltherm XLT) delivering temperatures from typical low grade hot sources for ORC systems [112]. Therefore, the hot source can be either a fossil-based boiler, biomass-based boiler or a solar thermal collector. In this investigation, for the sake of a simplified economic evaluation, it is assumed that the thermal oil is heated up by a conventional gas boiler. The thermal properties of water/glycol and Syltherm XLT, which are referred as auxiliary fluids, have been calculated using the incompressible fluids database of CoolProp [113]. The boundary conditions of the cycle are summarized in Table 4.1. The HP-ORC is simulated with the following assumptions:

- One dimensional and steady-state flow conditions are considered.
- The heating and cooling transformations are isobaric and adiabatic. The pressure drops are, therefore, neglected. More information about the validity of this assumption is available in Appendix B (Figures B.1 and B.2).
- The exergetic efficiency (equation 1.4) is calculated assuming a reference temperature (T_a) of 5 °C and pressure (P_a) of 101.3 kPa.

Table 4.1 – Boundary conditions of the HP-ORC

Term	Symbol	Value	Unit
Heat output	\dot{Q}_{sink}	40	[kW]
Pump isentropic efficiency	$\eta_{is,pump}$	0.60	[-]
Compressor inlet super-heating	$DT_{sh,comp}$	2	[K]
Condenser sub-cooling	DT_{sc}	7	[K]
Heat sink inlet temperature	$T_{sink,in}$	30	[°C]
Heat sink outlet temperature	$T_{sink,out}$	35	[°C]
Hot source inlet temperature	$T_{hot,in}$	[120;180]	[°C]
Hot source outlet temperature	$T_{hot,out}$	80	[°C]
Cold source inlet temperature	$T_{cold,in}$	7	[°C]
Cold source outlet temperature	$T_{cold,out}$	4	[°C]

Since the thermo-economic potential of the HP-ORC is investigated, a pinch analysis method is proposed, in which the evolution of the pinch point temperature difference DT_{min} in each heat exchanger unit is assessed. Indeed, the DT_{min} is governing the trade-off between efficiency and cost. As a matter of fact the smaller the pinch, the higher the HP-ORC overall efficiency. However, with decreasing pinch, the heat transfer area increases as well, leading to a higher heat exchanger investment cost. In addition, since HP-ORCs based on small-scale gas bearing supported turbomachinery are targeted in this work, the thermodynamic pinch analysis is coupled to a turbomachinery pre-design tool.

This results in two nested iteration loops as represented in Figure 4.2. This procedure allows identifying (1) the saturation temperatures in the evaporators and condenser, and (2) the detailed information on the turbomachinery geometry, efficiency, and rotor speed. The calculation is initialized with a best guess of the rotor speed ω , turbine and compressor isentropic efficiencies ($\eta_{is,turb}$, $\eta_{is,comp}$), and with a set of saturated temperatures for the condenser (T_2) and the evaporators (T_6 , T_{12}).

The first iteration layer adapts the evaporation and condensation temperatures ($T_{2,new}$, $T_{6,new}$, and $T_{12,new}$) to match the targeted pinches DT_{min} , which set the pressure levels in the cycle. To close the cycle simulation, additional variables impose the turbine inlet superheating ($DT_{sh,turb}$), the condenser sub-cooling (DT_{sc}) to avoid pump cavitation, and the super-heating of the HP evaporator ($DT_{sh,comp}$) to prevent liquid ingestion in the compressor. The values of DT_{sc} and $DT_{sh,comp}$ are constant (see Table 4.1), while DT_{min} and $DT_{sh,turb}$ are optimization variables. The second iteration layer is performed on the CTU to identify the new rotor speed ω and corresponding turbomachinery isentropic efficiencies ($\eta_{is,turb,new}$, $\eta_{is,comp,new}$). Using a nonlinear solver routine from MATLAB [73], the procedure is iterated until the power balance across the CTU and targeted pinches DT_{min} in the ORC evaporator, HP evaporator, and condenser are satisfied. The thermo-physical and transport properties of the HP-ORC working fluids are computed using REFPROP 9.1 [98]. Once the simulation is complete, since the thermodynamic properties are known in each station of the cycle, the performance and the heat transfer areas of the HP-ORC system can be retrieved.

Depending on the critical properties of the considered working fluid, the ORC evaporation process can be either subcritical or supercritical. Figure 4.3a shows the T-s diagram of two possible cycle design solutions for R600a working fluid at a hot source temperature of 180°C: At a COP in heating mode of 1.2 (subcritical ORC evaporation process) and of 1.85 (supercritical ORC evaporation process). Figure 4.3b represents the T-Q diagrams of each HX unit for these two cycle design solutions, along with the value and location of the pinch DT_{min} .

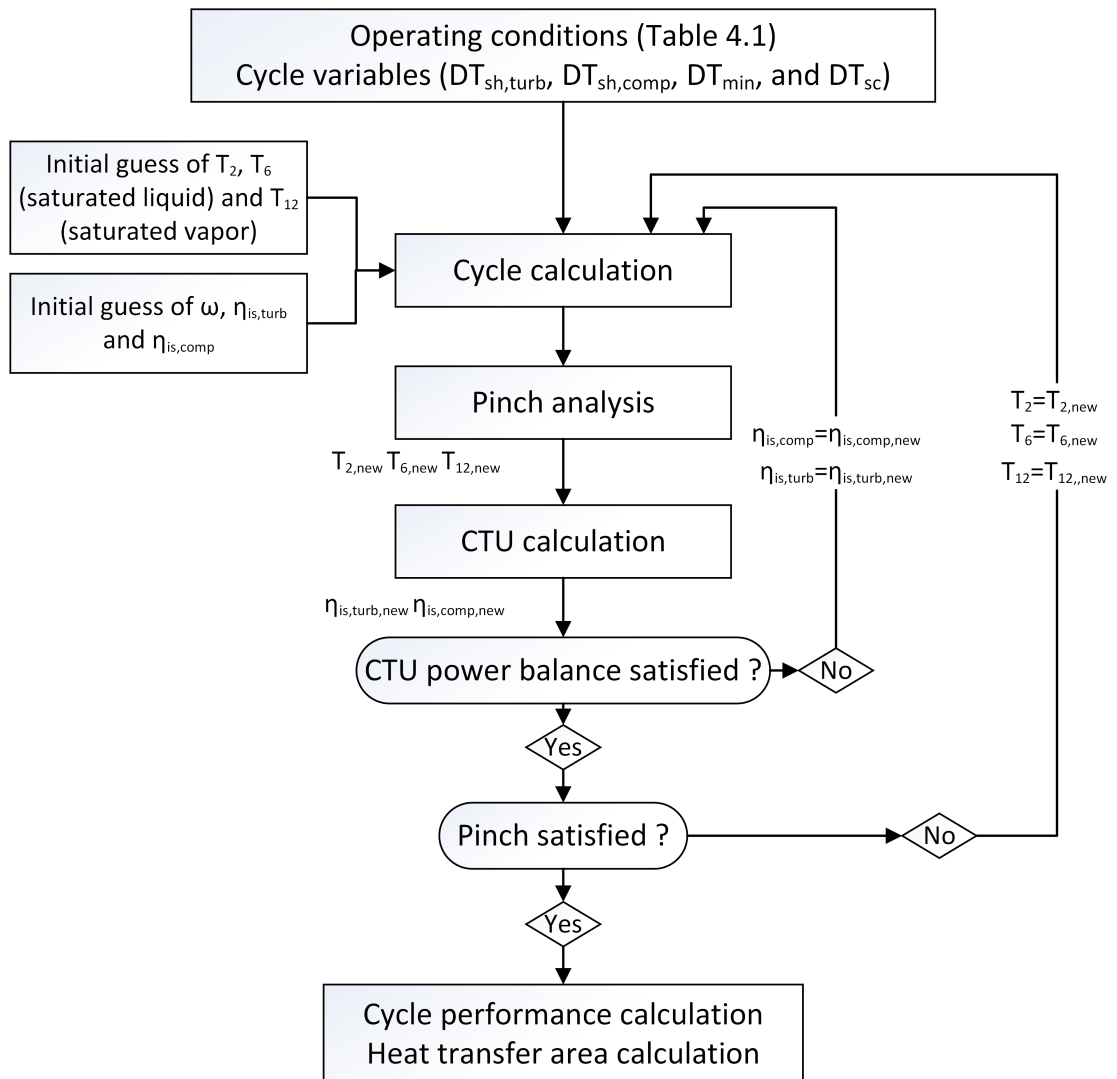
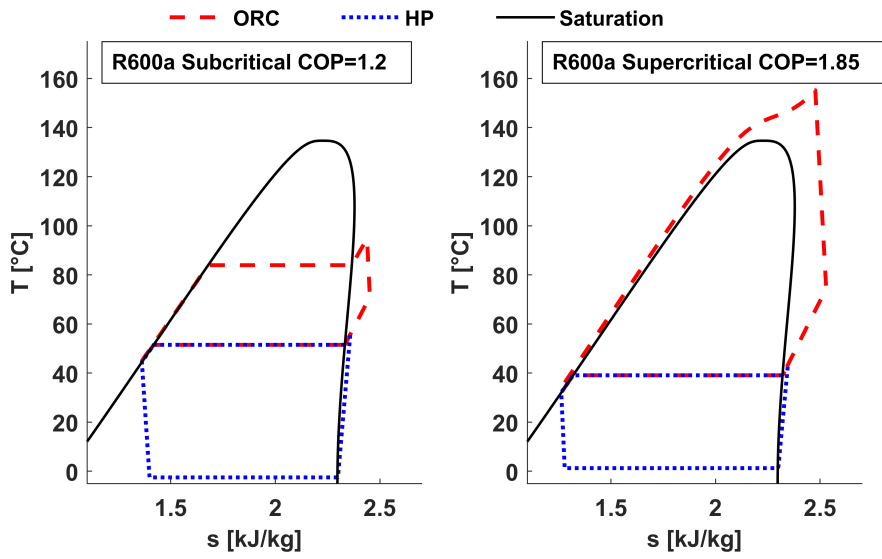
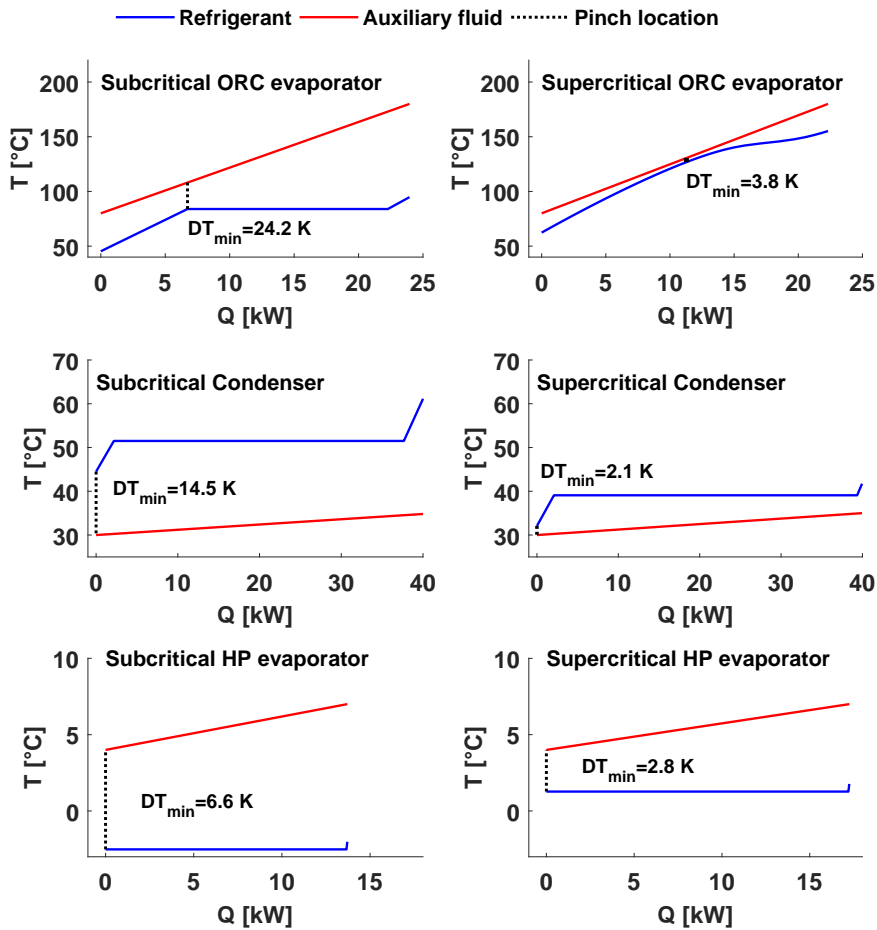


Figure 4.2 – Simulation layout of the coupled HP-ORC

Chapter 4. Integrated design optimization of the HP-ORC cycle



(a) T-s diagrams



(b) Heat exchangers T-Q diagrams

Figure 4.3 – (a) T-s and (b) HX T-Q diagrams of the HP-ORC operating with R600a at $T_{hot,in}=180^{\circ}\text{C}$ for two cycle design solutions: subcritical and supercritical ORC evaporation process.

4.3.2 CTU model

In chapter 3, the optimization of the CTU suggests that the shaft and bearing variables have a limited effect on the system efficiency. Since the goal of this chapter is to focus on the thermo-economic aspect of the HP-ORC technology, the CTU shaft and bearing design variables are not included in the optimization. In contrast, since the turbomachinery design has a considerable impact on the CTU performance (see chapter 3), their design features are part of the optimization process. The turbine and compressor are evaluated based on the updated reduced order turbomachinery models described in chapter 2. Given a specific operating condition, these pre-design models retrieve the turbomachinery design features offering the best CTU efficiency (equation 3.3). The corresponding isentropic efficiencies $\eta_{is,turb}$ and $\eta_{is,comp}$ are used to complete the overall cycle simulation.

Turbine model

Equation 4.1 has been used for the evaluation of the radial inflow turbine. Ns is the specific speed, Ds the specific diameter, and PR the pressure ratio across the turbine. In order to ensure a broader coverage of the Ns and Ds design space, the efficiency is evaluated at different shroud to tip radius ratios ϵ .

$$\eta_{is,turb} = f(Ns, Ds, PR), \epsilon = [0.5, 0.6, 0.7, 0.8] \quad (4.1)$$

Compressor model

Equation 4.2 has been used for the evaluation of the centrifugal compressor. In addition to Ns , Ds , and PR , the model considers the blade height to tip radius ratio $\zeta = \frac{b_4}{r_4}$ as an input. Additional diversity is reached by evaluating the efficiency at different shroud to tip radius ratios ϵ . As explained in chapter 2, since the clearance ratio defined as $CR = \max\left(\frac{80\mu m}{b_4}, 0.02\right)$ is taken into account, these correlations remain valid for different working fluids, at the condition that they are combined with a classification method to discard unfeasible design configurations. The convex hull inequalities (equation 2.14) equations valid for each working fluid, which can be found in Ref. [93], are fed into the simulation procedure.

$$\begin{aligned} \eta_{is,comp} &= f(Ns, PR, \zeta, CR), \epsilon = [0.4, 0.5, 0.56, 0.6] \\ Ds_{comp} &= f(Ns, PR, \zeta, CR), \epsilon = [0.4, 0.5, 0.56, 0.6] \end{aligned} \quad (4.2)$$

Shaft model

For each operating condition, the feasible turbine values of N_s and D_s (N_s and ζ for the compressor) are evaluated. The optimum values of N_s , D_s , ϵ , and ζ that maximize the overall CTU efficiency (equation 3.3) are retrieved. Therefore, in order to calculate the CTU efficiency accurately, the mechanical losses generated by the gas bearing supported shaft are included using the models introduced in chapter 3 (equation 3.4). Since the shaft and bearing design variables are not optimized along with the thermodynamic cycle, the HGJB and SGTB geometry parameters have been scaled with the rotor speed according to the existing prototype [35] as shown in Table 4.2.

Table 4.2 – Geometry parameters of the CTU shaft and bearings

Term	Symbol	Value	Unit
Shaft diameter	D_{shaft}	$\frac{2.1 \cdot 10^6}{N}$	[mm]
Shaft length	L_{shaft}	$5D_{shaft}$	[mm]
Shaft clearance	C_{shaft}	$0.01D_{shaft}$	[mm]
Radial bearing diameter	D_{rad}	D_{shaft}	[mm]
Radial bearing length	L_{rad}	D_{shaft}	[mm]
Radial bearing clearance	C_{rad}	$3.5 \cdot 10^{-4}D_{shaft}$	[mm]
Axial bearing diameter	D_{ax}	$2.6D_{shaft}$	[mm]
Axial bearing length	L_{ax}	$0.3D_{shaft}$	[mm]
Axial bearing clearance	C_{ax}	$3.8 \cdot 10^{-4}D_{ax}$	[mm]

4.3.3 Heat exchanger model

Since the heat exchanger cost is primarily driven by its area [114], an accurate model to predict the heat transfer area as a function of power and temperature pinch is needed to estimate the system investment cost. Plate Heat Exchangers (PHEs) are considered for all heat exchanger units for their high heat transfer performance, low cost, and compactness. The PHE geometry parameters are illustrated in Figure 4.4. Average values from literature [115,116] for the channel spacing b , wavelength of surface corrugation Λ , plate thickness δ , plate thermal conductivity k_{PHE} , and chevron angle β have been used for the calculations and are presented in Table B.1 (Appendix B). Equation 4.3 presents the expression of the PHE hydraulic diameters $d_{h,PHE}$ and the fluid mass flux G_{PHE} [33]. For each transfer unit, fixed values of plate number N_{ch} and plate width W have been set according to calculations made by SWEP for the considered application (see Table B.2 in Appendix B for details).

$$d_{h,PHE} = \frac{2b}{\phi} \quad (4.3)$$

$$\phi = 2b \left[\frac{1}{6} \left(1 + \sqrt{1 + \left(\frac{b\pi}{\Lambda} \right)^2} + 4 \sqrt{1 + \frac{1}{2} \left(\frac{b\pi}{\Lambda} \right)^2} \right) \right]^{-1}$$

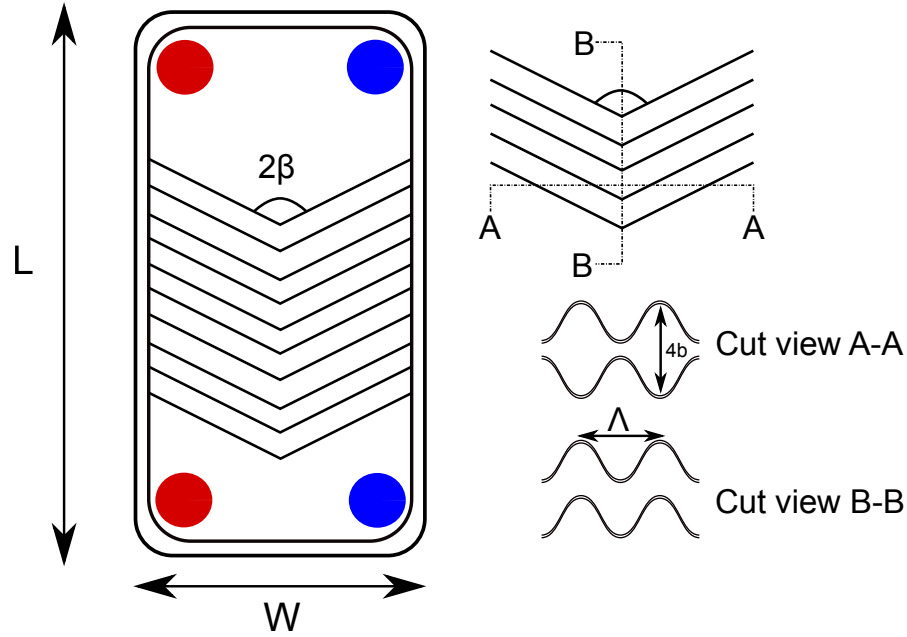


Figure 4.4 – Geometry parameters of a Plate Heat Exchanger

Since heat transfer coefficients strongly depend on local flow patterns, the model splits the heat exchanger into different sections j according to the occurring fluid phases. For each section, the heating power \dot{Q}_j , the overall heat transfer coefficient U_j , and the heat transfer area A_j are calculated separately. As an example, the ORC evaporator in a subcritical process is typically split into a liquid/liquid, a two-phase/liquid, and a vapor/liquid zone. It follows that, as shown in equation 4.4, the total heat exchanged \dot{Q}_{HX} corresponds to the sum of the heat transferred in each section \dot{Q}_j .

$$\dot{Q}_{HX} = \sum_j \dot{Q}_j \quad (4.4)$$

In order to predict the heat transfer area of each zone, the Logarithmic Mean Temperature Difference (LMTD) method has been used [117] as follows:

$$\dot{Q}_j = U_j A_j LMTD_j \quad (4.5)$$

For each heat exchanger section j of area A_j , the overall heat transfer coefficient U_j and the LMTD coefficient $LMTD_j$ are described by equations 4.6 and 4.7, respectively.

$$\frac{1}{U_j} = \frac{1}{h_{j,hs}} + \frac{1}{h_{j,cs}} + \frac{\delta}{k_{PHE}} \quad (4.6)$$

$$LMTD_j = \frac{\Delta T_{max,j} - \Delta T_{min,j}}{\log\left(\frac{\Delta T_{max,j}}{\Delta T_{min,j}}\right)} \quad (4.7)$$

Chapter 4. Integrated design optimization of the HP-ORC cycle

where $\Delta T_{max,j}$ and $\Delta T_{min,j}$ are the maximum and minimum temperature differences between the cold and hot streams while $h_{j,hs}$ and $h_{j,cs}$ are the heat transfer coefficients on the hot and cold side of section j . δ and k_{PHE} are the plate thickness and thermal conductivity.

The local heat transfer coefficients h_j depend on the flow pattern, which is categorized into single-phase flow (sub-cooled, super-heated, and supercritical) and two-phase flow (condensing and evaporating). For each flow pattern, individual correlations allow predicting the Nusselt number Nu as a function of the Prandtl Pr and Reynolds numbers Re . These correlations are valid whether the working fluid is a pure refrigerant or an auxiliary fluid (thermal oil and brine). The heat transfer coefficient h_j for each section j is calculated through the definition of the Nusselt number given in equation 4.8, where k_j is the fluid thermal conductivity and d_h the hydraulic diameter defined in equation 4.3.

$$h_j = Nu_j \frac{k_j}{d_h} \quad (4.8)$$

The correlations used in this work for evaluating the Nusselt numbers are given in Table 4.3, and detailed in Table C.1 (Appendix C). For single-phase flows, Martin [118] introduced semi-empirical correlations of the PHE heat transfer coefficient and pressure drop depending on the friction factor f , Reynolds numbers Re , and plate chevron angles β . For two-phase flows, Garcia et Cascales et al. [119] recommend the correlation of Yan et al. [120] for condensation, and Amalfi et al. [33] the model of Danilova et al. [121] for evaporation since they are suggested to best match data of an extensive PHE database. Since the Reynolds number varies significantly as a function of the local vapor quality in two-phase flow regions, the heat transfer process in this zone is divided into small sub-sections where the properties are assumed to remain constant. The individual sub-section area is then computed with the LMTD method [109].

Table 4.3 – Heat transfer correlations for PHEs

Single-phase	Condensing	Evaporating
Martin [118]	Yan et al. [120]	Danilova et al. [121]

In a first approximation, the PHE design has been conducted as follows: Given a fixed plate width W and a fixed number of plates N_{ch} , the heat transfer coefficients are calculated according to equation 4.8 using the Nusselt correlations given in Table 4.3. The heat transfer area is then computed using equation 4.5. The length of the plate L is further retrieved to match the required heat transfer area.

4.4 Economic model

The investment cost of the HP-ORC is governed by its internal (heat exchangers, CTU, pump, valves, working fluid, and piping) and external components (boiler and the Ground Heat Exchanger (GHX)). The cost of the CTU, pump, valves, and piping is assumed constant. However, since fixed costs do not influence the thermo-economic trade-off, they have not been considered in the thermo-economic optimization, at the exception of the CTU due to the differences occurring between the two HP-ORC configurations (see Figures 4.1a and 4.1b). Finally, the cost of the working fluid is assumed to be negligible due to the low charges required for domestic applications.

Heat Exchangers

The cost of the PHEs is estimated using the correlation presented by Henchoz et al. [122], which is based on catalog prices for CO₂ network brazed Plate Heat Exchangers.

$$\begin{aligned} C_{HX,j} &= 147 + 407 A_{HX,j} \text{ [\$]} \\ C_{HX} &= \sum_j C_{HX,j} \text{ [\$]} \end{aligned} \quad (4.9)$$

Ground Heat Exchanger (GHX)

In order to estimate the investment cost of Ground Source Heat Pumps (GSHPs), the cost of drilling and installation of the GHX is required. This cost has been estimated considering 100 m deep boreholes following $C_{bore} = 32 \text{ \$/m}$ [123] with a heat exchange rate $HR = 58 \text{ W.m}^{-1}$ [124].

$$C_{GHX} = C_{bore} \frac{\dot{Q}_{cold}}{HR} \text{ [\$]} \quad (4.10)$$

Boiler

The cost of the boiler is based on the customer catalog of the heating system manufacturer Viessmann¹. Depending on the boiler power range and its primary energy source, the investment cost of the boiler is estimated according to Table 4.4.

Table 4.4 – Boiler investment cost as a function of the primary fuel and the power range

Boiler primary source	Boiler cost C_{Boiler} (\$) per power range (kW)				
	2-13 kW	14-19 kW	20-26 kW	27-35 kW	> 35 kW
Gas	4'818	5'646	6'589	7'126	8'083
Wood logs	-	-	12'157	12'945	14'192
Wood pellets	-	15'000	15'420	17'900	18'716

¹<https://www.viessmann.ch/fr/services/liste-de-prix.html>

CTU

Since it is at a prototype stage and is operated at low shaft power (in the order of 2 kW [35]), no market-related correlations exist for the CTU investment cost. Based on prototyping cost and investigations with manufacturers, the CTU has been estimated to a unitary cost $C_{CTU} = \$500$, provided that a large number (above 1'000 units) can be produced annually. This estimation is valid for a turbocompressor that includes (1) the small-scale turbomachinery, (2) the gas-bearing supported shaft, and (3) the electrical machine. In the uncoupled HP-ORC configuration, this cost is accounted for twice. In the coupled HP-ORC, this cost has been applied as well, even though there is no electrical machine, yielding, therefore, a pessimistic cost estimation.

$$C_{CTU} = 500 \text{ [\$]} \quad (4.11)$$

To conclude, the component costs are divided into three main categories:

- **Fixed and discrete costs:** CTU and boiler
- **Costs depending on the heat exchanger surface area:** Heat exchangers
- **Costs depending on the cold source heating power:** GHX

4.5 Multi-objective optimization

Since the two objectives (maximum performance and minimum investment cost) are of conflicting nature, the ideal thermo-economic trade-off results in a Pareto curve. The HP-ORC performance can be evaluated either with the Coefficient of Performance (COP - equation 1.2) or the exergetic efficiency (η_{exe} - equation 1.4). The mathematical expression of the optimization problem is the following:

$$[\max(COP, \eta_{exe}), \min(C_{Tot})] = f_{thermoeco}(G_{HX}, G_{Fluid}) \quad (4.12)$$

where $f_{thermoeco}$ is the objective function including both the thermodynamic and the economic models introduced earlier. G_{HX} refers to the set of thermodynamic cycle variables related to the heat exchanger design, and G_{Fluid} related to the working fluid selection.

Table 4.5 presents the decision variables of the optimization problem and their range for optimizing the HP-ORC cycle where turbine and compressor are mechanically coupled (Figure 4.1a). The turbine inlet superheat, the HP-ORC condenser, HP evaporator, ORC evaporator, and regenerator pinches have an impact on the performance and the cost by varying the pressure levels, mass flows, and the heat transfer areas. Finally, an additional integer variable chooses whether a regenerator is considered or not.

4.5. Multi-objective optimization

Table 4.6 presents the decision variables of the uncoupled HP-ORC (Figure 4.1b). In this configuration, due to the presence of a second condenser, both pinches for the ORC and HP condensers are considered, and since the HP and the ORC loops are dissociated, the selection of the working fluid can be selected individually for each cycle.

Moreover, the HP-ORC optimization is in both cases subject to the following constraints, confining the optimization to realistic turbomachinery and cycle operating conditions:

$$\left\{ \begin{array}{l} PR_{turb} < 8.5 \ \& \ PR_{comp} < 5 \\ x_{turb,out} > 1 \ \& \ x_{comp,in} > 1 \ \& \ x_{comp,out} > 1 \\ U = \omega r < 400 \text{ m.s}^{-1} \\ P_{evo} < 70 \text{ bar} \end{array} \right.$$

The maximum pressure ratio for the radial turbine is limited to 8.5 and 5 for the single-stage centrifugal compressor, such as for the turbomachinery pre-design models described in chapter 2 (see Tables 2.1 and 2.3). The limitations on the vapor quality across the compressor and turbine ensure that no flashing occurs in the compression/expansion process, which may lead to premature blade erosion or bearing failure. The turbomachinery tip velocity U is limited to 400 m.s^{-1} , which is considered best practice to prevent excessive mechanical stress in turbomachinery impellers made of conventional aluminum and steel alloys. Finally, the pressure at the ORC evaporator P_{evo} is limited to 70 bar.

Table 4.5 – Design variables of the coupled HP-ORC optimization

Component	Variable	Term	Range	Unit
G_{HX}	Turbine inlet super-heating	$DT_{sh,turb}$	[10-100]	[K]
	Condenser pinch	$DT_{min,cond}$	[1-20]	[K]
	HP evaporator pinch	$DT_{min,evh}$	[1-20]	[K]
	ORC evaporator pinch	$DT_{min,evo}$	[1-20]	[K]
	Regenerator pinch	$DT_{min,reg}$	[1-20]	[K]
	Regenerator ?	Is_{reg}	Yes/No	[-]
G_{Fluid}	HP-ORC Working fluid	F_{HP-ORC}	Table 4.7	[-]

Table 4.6 – Design variables of the uncoupled HP-ORC optimization

Component	Variable	Term	Range	Unit
G_{HX}	Turbine inlet super-heating	$DT_{sh,turb}$	[10-100]	[K]
	HP Condenser pinch	$DT_{min,condh}$	[1-20]	[K]
	ORC Condenser pinch	$DT_{min,condo}$	[1-20]	[K]
	HP evaporator pinch	$DT_{min,evh}$	[1-20]	[K]
	ORC evaporator pinch	$DT_{min,evo}$	[1-20]	[K]
	Regenerator pinch	$DT_{min,reg}$	[1-20]	[K]
	Regenerator ?	Is_{reg}	Yes/No	[-]
G_{Fluid}	HP Working fluid	F_{HP}	Table 4.7	[-]
	ORC Working fluid	F_{ORC}	Table 4.7	[-]

Chapter 4. Integrated design optimization of the HP-ORC cycle

In order to analyze in detail the influence of each component, the investigation is divided into three main stages as follows:

- **Stage 1** The first stage gets insights into the optimum heat exchanger design and working fluid selection when considering the performance/economic trade-off driven by the heat exchangers.
- **Stage 2** The second stage analyzes the influence on the design of the other component costs (GHX, boiler and CTU).
- **Stage 3** The third stage is comparing the performance/economic trade-off between the two primary HP-ORC configurations (coupled and uncoupled).

4.6 Results and discussion

4.6.1 HP-ORC working fluid screening

The HP-ORC working fluid selection is based on different criteria related to the thermodynamic characteristics (critical properties, molar mass, and expansion behavior mainly), hazards (toxicity and flammability according to the ASHRAE standards) and environmental concerns (null-ODP² and low GWP³). Table 4.7 summarizes the working fluids that have been selected for this study as well as their thermodynamic properties. Since coupled HP-ORC configurations are considered (Figure 4.1a), the working fluid selection is challenging since it has to perform well in the two thermal loops, which are operating at different pressure levels. Therefore, conventional working fluids for both ORC and HP applications are investigated. Finally, only working fluids with a GWP equal or inferior to R134a were screened.

Table 4.7 – Working fluid selection

Working fluid	T_{cr}	P_{cr}	Molar mass	Expansion	GWP	ASHRAE standard 34	Application
-	[°C]	[bar]	[g.mol ⁻¹]	[-]	[-]	[-]	[-]
R134a	101	40.6	102.03	Wet	1430	A1	HP
R1234yf	94.7	33.8	114.04	Wet	1	A2L	HP
R152a	113	45.2	66.05	Wet	124	A2	HP
R600a	135	36.3	58.12	Wet	3	A3	HP
R245fa	154	36.5	134.05	Dry	1030	B1	ORC
R1233zd	166.5	36.2	130.5	Dry	5	A1	ORC

²Ozone Depletion Potential

³Global Warming Potential

4.6.2 Stage 1: Design selection based on the heat exchanger cost

As explained in the introduction, two indicators exist to assess the performance of a TDHP: The COP and the exergetic efficiency η_{exe} . This first optimization level aims at revealing the influence of these two performance objectives on the HP-ORC design. In this stage, only the cost of the heat exchangers is considered in the thermo-economic trade-off.

Thermo-economic trade-off

Figure 4.5 shows the Pareto curves highlighting the trade-off between HX investment cost and the HP-ORC performance objectives at two different hot source temperatures (thermal oil temperatures) $T_{hot,in}=120^{\circ}\text{C}$ and $T_{hot,in}=180^{\circ}\text{C}$, and as a function of the working fluids shown in Table 4.7. The results highlight a trade-off between cost and performance since higher exergetic efficiencies and COPs can only be achieved with higher heat exchanger areas, which comes at a higher cost though. The plots show that the system yields higher exergetic efficiency and lower cost when the hot source temperature decreases, while the opposite trend is observed when the comparison is based on the COP. Furthermore, the results suggest that the Pareto-dominant working fluids are different from one hot source temperature to the other. When the COP is maximized with a hot source temperature at 120°C , the Pareto front is determined by R134a and R152a, while at 180°C , the dominant fluid is R600a. When considering the COP as an objective, R245fa and R1233zd, which are ORC-based working fluids (Table 4.7), are always suboptimal. However, the optimum working fluids differ when the exergetic efficiency is considered. At 120°C , the trade-off is dominated by R245fa, and at 180°C , the Pareto front is shared between R245fa and R600a. This analysis, therefore, suggests that the working fluid selection depends (1) on the operating hot source temperature and (2) on the performance indicator.

Figures 4.7 and 4.8 present the evolution of the optimum decision variables with the exergetic efficiency and the COP at $T_{hot,in}=120^{\circ}\text{C}$ and $T_{hot,in}=180^{\circ}\text{C}$. As expected, decreasing the pinch DT_{min} and increasing the turbine inlet super-heating $DT_{sh,turb}$ leads to higher performances. It also demonstrates that the optimizer chooses to decrease simultaneously the pinch values in the condenser, ORC evaporator, and HP evaporator to get to the maximum performance. The consequence is that from a thermo-economic point of view it does not make sense to improve only one heat exchanger at a time, as shown in Figure 4.6, which presents the HX cost repartition along the Pareto fronts corresponding to the optimum working fluids. Finally, the results highlighted in Figures 4.6 to 4.8 reveal when it is economically worthwhile to implement a regenerator in the cycle. Since the regeneration potential is higher, there are more optimum configurations with a regenerator at 180°C than at 120°C . On the contrary to the other HX, the regenerator pinch is either fixed over the Pareto front or is not subject to a clear trend. This is caused by the lower impact of the regenerator on the thermo-economic trade-off.

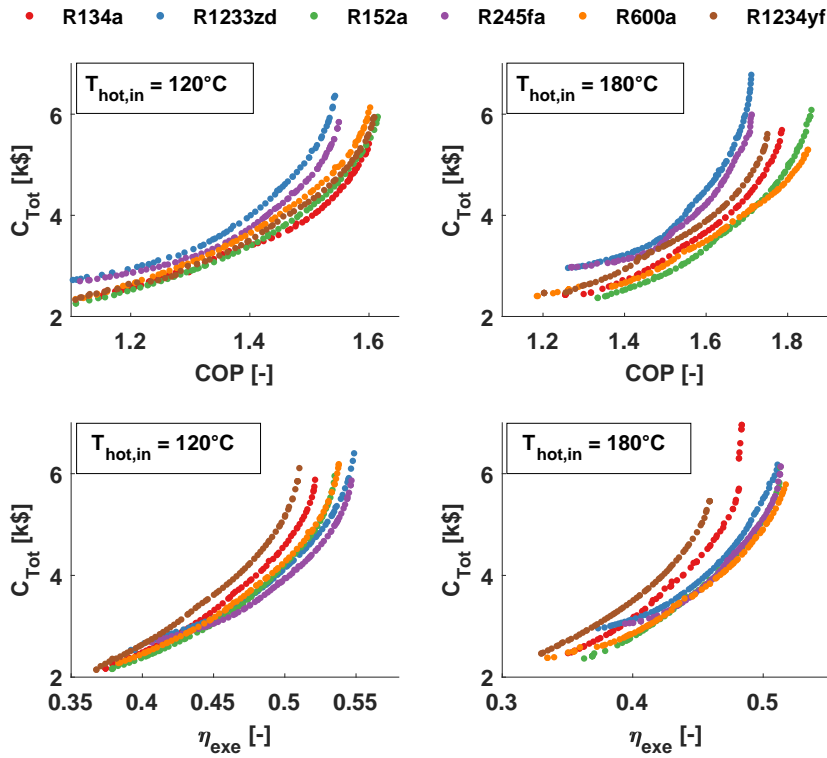


Figure 4.5 – Pareto curves of the selected working fluids for two performances objectives (COP and η_{exe}) and two hot source temperatures

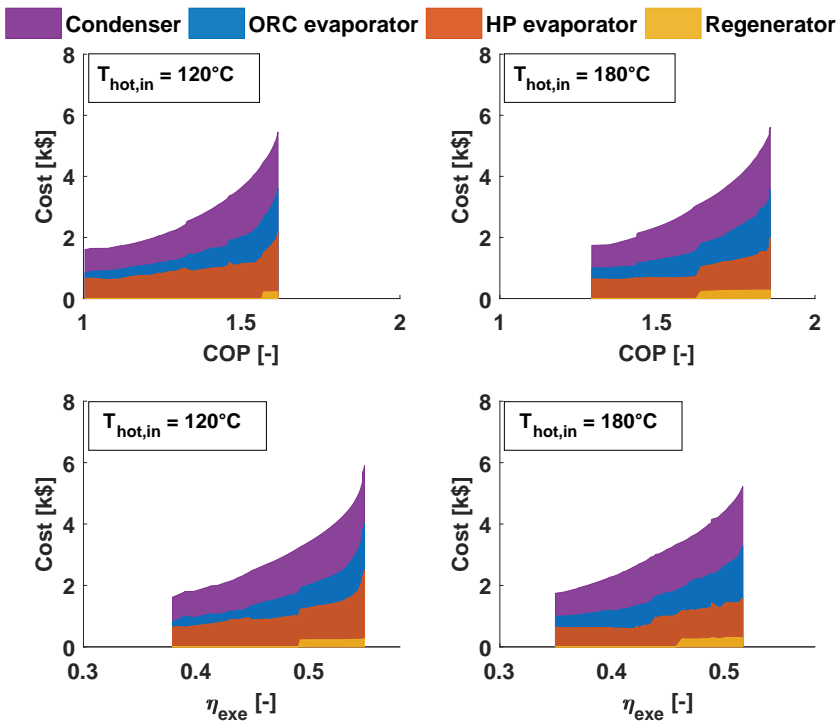


Figure 4.6 – HX cost repartition along the dominant Pareto fronts

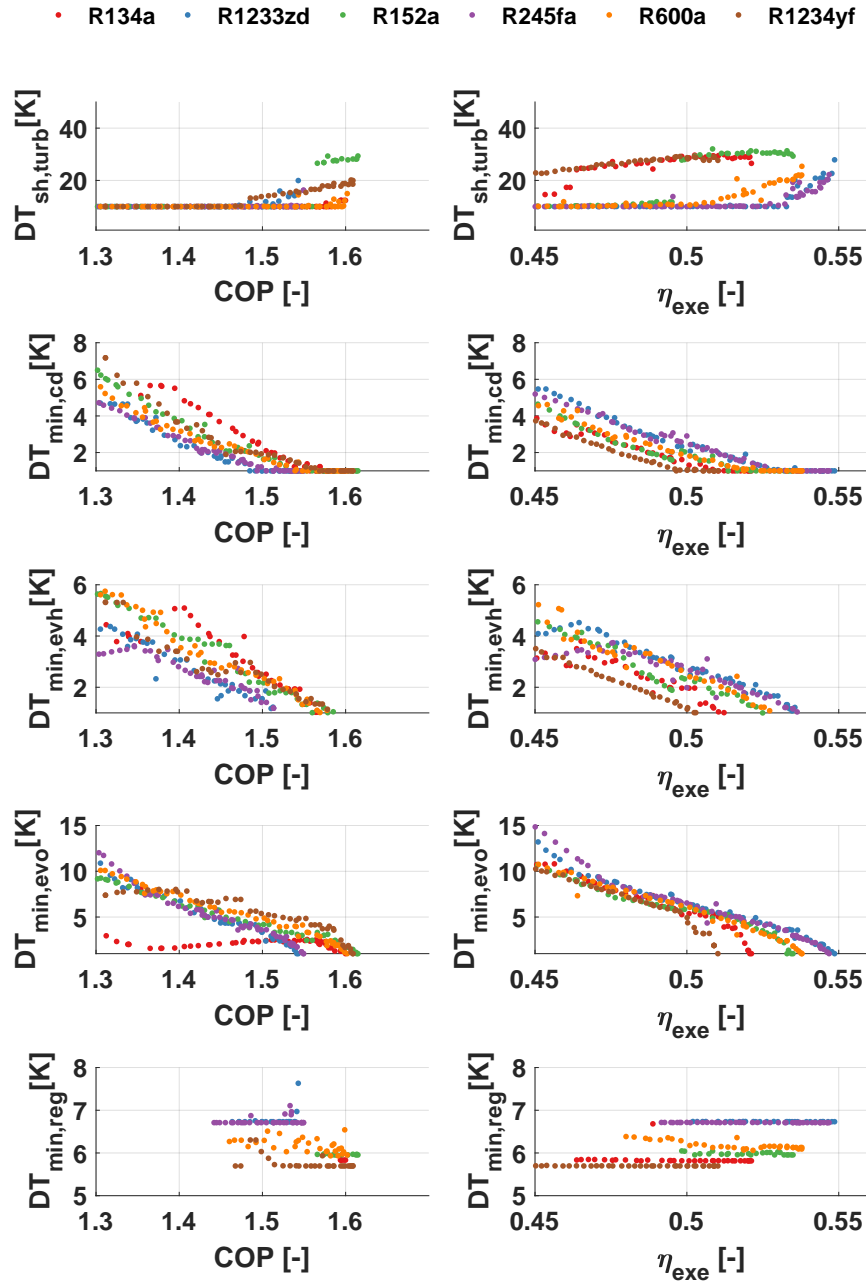


Figure 4.7 – Pareto optimum solutions of the selected working fluids for two performances objectives (COP and η_{exe}) at $T_{hot,in}=120^{\circ}\text{C}$

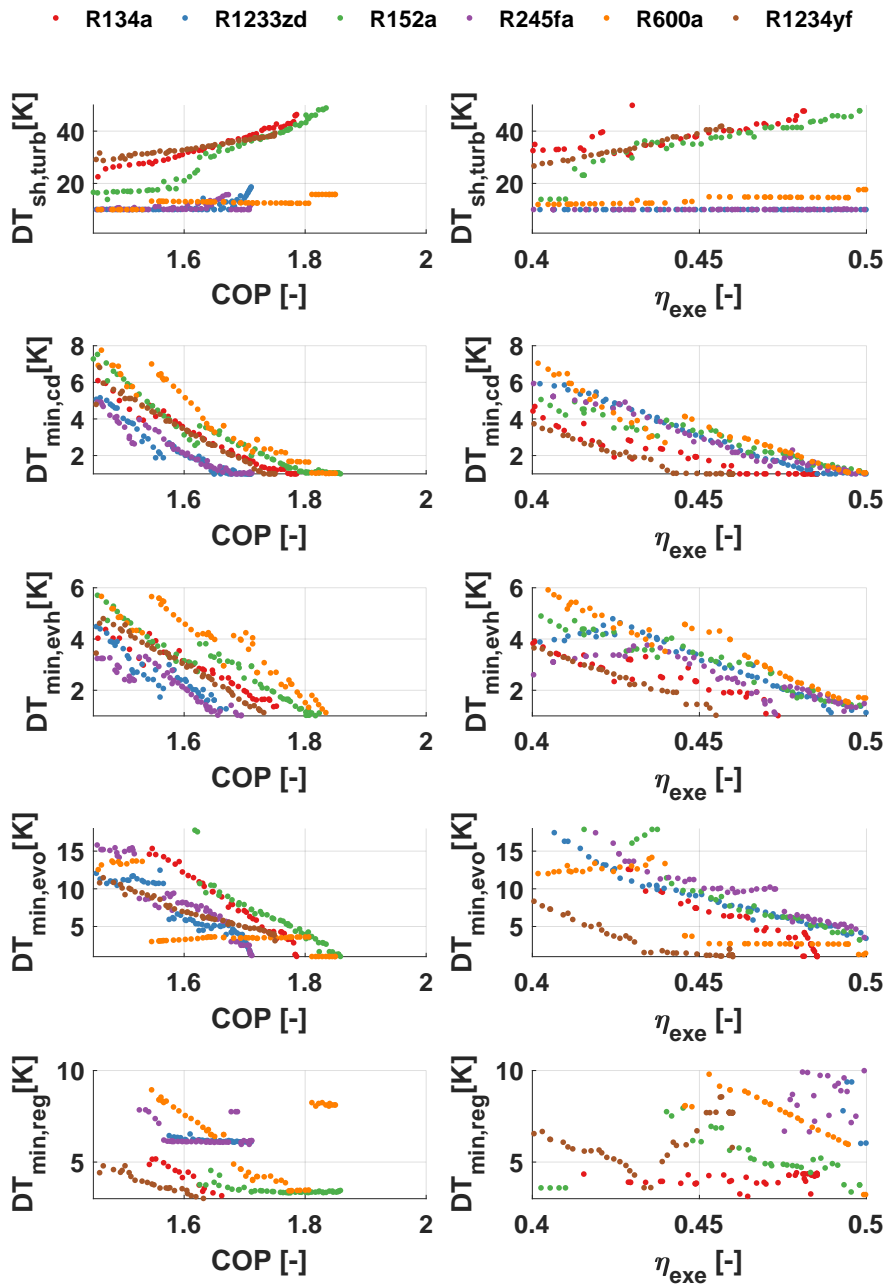


Figure 4.8 – Pareto optimum solutions of the selected working fluids for two performances objectives (COP and η_{exe}) at $T_{hot,in}=180^{\circ}\text{C}$

In order to understand the phenomena driving the Pareto-dominant working fluids, Tables 4.8 to 4.11 analyze the thermodynamic features corresponding to each case study, when targeting a fixed cost of \$5'000.

Considering a hot source at 120°C, Tables 4.8 and 4.9 explain why the working fluid selection changes from one performance objective to the other. Indeed, when maximizing the COP, the main driver to optimize the cycle is to decrease \dot{Q}_{hot} , which is the heating load needed at the ORC evaporator to achieve the 40 kW heating power at the condenser (equation 1.2). The electrical input required for the pump $\dot{W}_{el} = \dot{W}_{pump}$ does influence the performance but to a limited extent since its value is two orders of magnitude lower than \dot{Q}_{hot} . In Table 4.8, the optimum working fluid is, therefore, R134a, while R245fa and R1233zd are dominated. Indeed, the latter present high \dot{Q}_{hot} due to too high pressure ratios in the compressor PR_{comp} .

This trend, however, changes when maximizing the exergetic efficiency since the exergy load $\dot{E}x_{hot}$ is now only one order of magnitude higher than \dot{W}_{pump} . As a consequence, the electrical consumption of the pump has a higher weight on the trade-off mechanisms. Therefore, R245fa and R1233zd, while having still higher \dot{Q}_{hot} (and hence higher $\dot{E}x_{hot}$) due to the reasons explained earlier, achieve higher performance than the other working fluids due to their lower pump electrical power. R245fa and R1233zd present this characteristic since they operate further away from their critical point than the other working fluids (see Table 4.7).

Table 4.8 – Working fluids thermodynamic features at $C_{Tot}=\$5'000$ when maximizing the COP at $T_{hot,in}=120^\circ\text{C}$

Term	Unit	R134a	R1234yf	R152a	R600a	R245fa	R1233zd
COP	[-]	1.58	1.569	1.574	1.553	1.517	1.49
\dot{Q}_{hot}	[kW]	24.2	24.4	24.9	25.3	26.2	26.7
$\dot{E}x_{hot}$	[kW]	6.15	6.14	6.34	6.47	6.51	6.61
\dot{W}_{pump}	[kW]	0.62	0.63	0.28	0.22	0.11	0.09
PR_{turb}	[-]	4.75	3.82	3.18	3.12	3.98	3.65
PR_{comp}	[-]	2.96	2.85	3	3	3.96	3.86

Table 4.9 – Working fluids optimum thermodynamic features at $C_{Tot}=\$5'000$ when maximizing the η_{exe} at $T_{hot,in}=120^\circ\text{C}$

Term	Unit	R134a	R1234yf	R152a	R600a	R245fa	R1233zd
η_{exe}	[-]	0.51	0.497	0.523	0.522	0.535	0.529
\dot{Q}_{hot}	[kW]	25.3	25.5	25.1	25.4	26.2	26.7
$\dot{E}x_{hot}$	[kW]	6.38	6.43	6.38	6.49	6.52	6.62
\dot{W}_{pump}	[kW]	0.36	0.44	0.27	0.21	0.1	0.09
PR_{turb}	[-]	3.06	2.87	3.03	2.98	3.76	3.66
PR_{comp}	[-]	3.01	2.86	3.01	2.99	3.99	3.88

Chapter 4. Integrated design optimization of the HP-ORC cycle

The same conclusions apply at $T_{hot,in}=180^{\circ}\text{C}$, as shown in Tables 4.10 and 4.11. However, as highlighted in Table 4.10, R134a presents lower COPs than R600a since this working fluid is penalized by high \dot{W}_{pump} . Indeed, the higher the hot source temperature, the higher the ORC evaporation pressure for R134a, and hence the higher \dot{W}_{pump} .

Furthermore, in contrast to the results suggested by Table 4.9, Table 4.11 shows that R600a and R152a achieve slightly higher exergetic efficiencies than R245fa. Indeed R245fa, as well as R1233zd, is penalized by higher compressor pressure ratios and its lower pump power consumption \dot{W}_{pump} does not compensate this drawback anymore, hence giving a slight advantage to R600a and R152a.

Table 4.10 – Working fluids thermodynamic features at $C_{Tot}=\$5'000$ when maximizing the COP at $T_{hot,in}=180^{\circ}\text{C}$

Term	Unit	R134a	R1234yf	R152a	R600a	R245fa	R1233zd
COP	[-]	1.75	1.72	1.8	1.83	1.66	1.64
\dot{Q}_{hot}	[kW]	21.5	21.5	21.4	20.8	23.7	24
$\dot{E}x_{hot}$	[kW]	6.31	6.4	6.37	6.14	6.96	7.13
\dot{W}_{pump}	[kW]	0.74	0.94	0.46	0.58	0.17	0.15
PR_{turb}	[-]	6.16	5.87	5.24	8.2	6.19	6.1
PR_{comp}	[-]	3.07	2.85	3	2.98	3.94	3.93

Table 4.11 – Working fluids thermodynamic features at $C_{Tot}=\$5'000$ when maximizing the η_{exe} at $T_{hot,in}=180^{\circ}\text{C}$

Term	Unit	R134a	R1234yf	R152a	R600a	R245fa	R1233zd
η_{exe}	[-]	0.47	0.452	0.498	0.502	0.497	0.489
\dot{Q}_{hot}	[kW]	21.5	22	21.4	21.6	23.9	24.2
$\dot{E}x_{hot}$	[kW]	6.35	6.57	6.38	6.16	6.84	7
\dot{W}_{pump}	[kW]	0.73	0.75	0.45	0.54	0.21	0.18
PR_{turb}	[-]	6.13	4.98	5.27	7.27	7.53	8.19
PR_{comp}	[-]	3.04	2.85	3.01	3	4.01	3.79

Design selection: Turbomachinery and cycle featuresTable 4.12 – Turbomachinery and cycle features at $C_{Tot}=\$5'000$ when maximizing the η_{exe} at $T_{hot,in}=120^{\circ}\text{C}$

		R134a	R1234yf	R152a	R600a	R245fa	R1233zd
Turbomachinery							
N	[krpm]	162	134	210	189	102	101
D_{turb}	[mm]	15.7	17.2	15.1	18.1	26.1	27.3
D_{comp}	[mm]	22.2	24	21.5	25	35	37
$\eta_{is,turb}$	[-]	0.84	0.84	0.84	0.84	0.84	0.84
$\eta_{is,comp}$	[-]	0.77	0.78	0.77	0.78	0.77	0.77
Cycle							
P_{evo}	[bar]	29.5	27.9	26.4	15.1	9.2	7.4
P_{evh}	[bar]	3.2	3.4	2.9	1.7	0.6	0.5

Table 4.13 – Turbomachinery and cycle features at $C_{Tot}=\$5'000$ when maximizing the COP at $T_{hot,in}=180^{\circ}\text{C}$

		R134a	R1234yf	R152a	R600a	R245fa	R1233zd
Turbomachinery							
N	[krpm]	199	171	262	252	107	101
D_{turb}	[mm]	16.6	17.8	15.8	22.8	30.7	32.6
D_{comp}	[mm]	19.7	20.9	18.2	26	41.9	42.9
$\eta_{is,turb}$	[-]	0.82	0.83	0.83	0.79	0.83	0.84
$\eta_{is,comp}$	[-]	0.75	0.75	0.75	0.75	0.76	0.76
Cycle							
P_{evo}	[bar]	58.6	57.1	46.4	41.4	14.6	12.2
P_{evh}	[bar]	3.21	3.41	2.88	1.7	0.59	0.52

In order to gain more insights into the decision-making process, it is of great interest to look into alternative cycle design variables, which may impose additional operating constraints beyond cost and performance. Some of these variables are shown in Tables 4.12 and 4.13 for two design solutions: At 120°C when maximizing η_{exe} and at 180°C when maximizing COP, both for a heat exchanger cost target of $\$5'000$. The considered variables represent the turbomachinery design, the pressure levels in the cycle, and the constraints relative to the working fluid.

R245fa is very promising since it achieves the best investment cost/exergetic efficiency trade-off at 120°C while operating with the lowest rotational speeds and highest turbomachinery diameters. Nonetheless, R245fa presents sub-atmospheric HP evaporation pressures P_{evh} , which is a major operating constraint since there is a risk of cycle pollution with ambient air if the system is not fully hermetic. R152a is another good candidate since its thermo-economic trade-off is very close to the dominating working fluids shown in Figure 4.5. However, R152a presents the highest rotors speeds and lowest turbomachinery diameters, which is challenging regarding bearing design, manufacturing, and assembly.

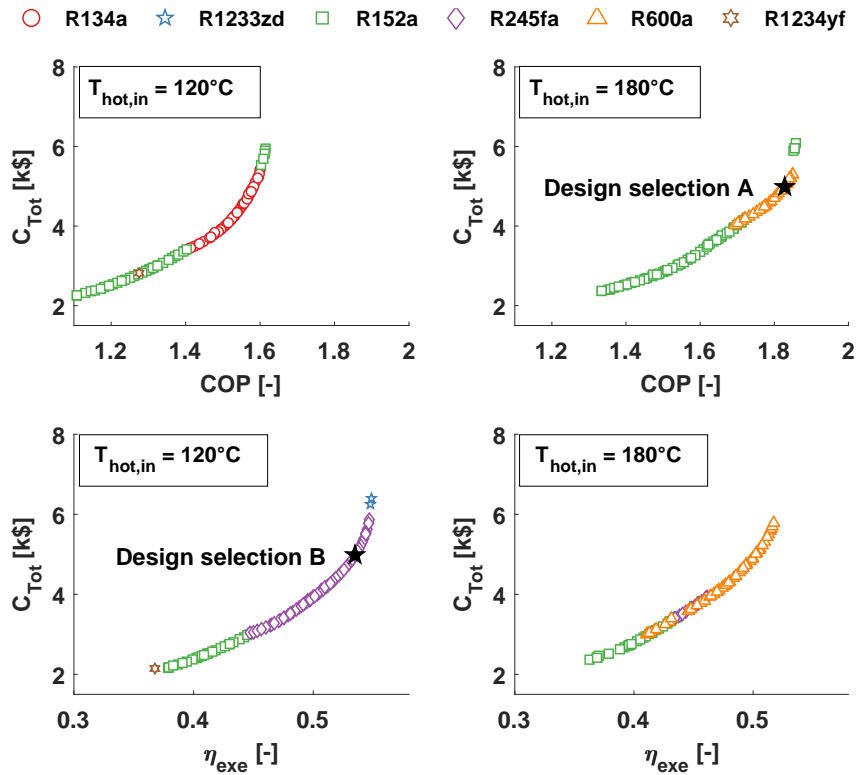


Figure 4.9 – Overall HP-ORC Pareto fronts for two performances objectives (COP and η_{exe}) and two hot source temperatures

On the other hand, R134a and R1234yf, which are alternative COP-optimum solutions at 120°C, are penalized by high pressures at the ORC evaporator P_{evo} . Finally, R600a, which optimizes both the COP and the exergetic efficiency at 180°C is highly flammable (ASHRAE standard 34 A2 - see Table 4.7). This discussion highlights the limitation of a multi-objective optimization limited to a pure thermo-economic consideration.

Finally, Figure 4.9 represents the overall Pareto fronts corresponding to each hot source temperature and performance objective. Thermo-economic optimum designs A and B are selected at 180°C when maximizing COP, and at 120°C when maximizing η_{exe} , both for a heat exchanger cost target of \$5'000.

4.6.3 Stage 2: Influence of the component costs

The optimization stage 1 highlighted the optimum working fluids and decision variables when considering the thermo-economic trade-off driven by the heat exchangers only. This second optimization stage aims at evaluating the influence of the other component costs.

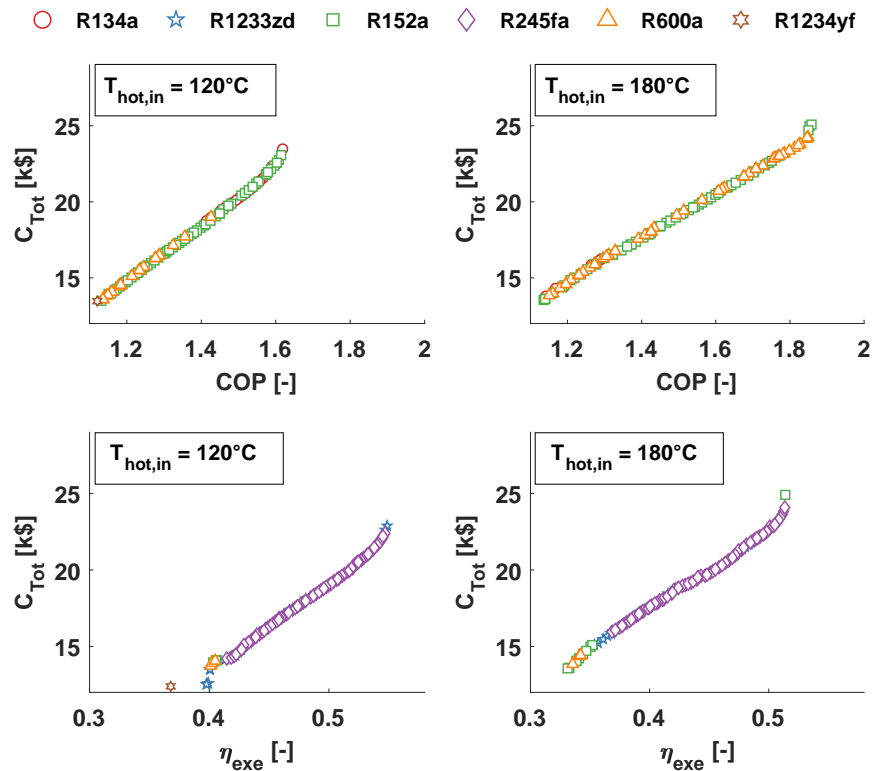


Figure 4.10 – Pareto-dominant curves for two performances objectives (COP and η_{exe}) and two hot source temperatures including the cost of the heat exchangers, boiler, CTU, and GHX

Figure 4.10 shows the new trade-off curves when including additional costs such as the CTU, the boiler, and the GHX into the thermo-economic optimization process. Only the Pareto-dominant working fluids are displayed. Figure 4.11 shows the cost repartition corresponding to each Pareto front. This figure highlights that at maximum performance, the total cost is composed of 22-25% by the HX, 35-40% by the GHX, 4% by the CTU, and 34-36% by the boiler.

The results suggest that the shape of the Pareto fronts is affected compared to the previous optimization stage. This is due to the effect of the GHX cost, which is higher than the HX cost and thus governs the thermo-economic trade-off. While the cost of the HX increases exponentially with the inverse of the pinch (equation 4.7), the cost of the GHX increases linearly with the HP evaporator heating power (equation 4.10). As a consequence, the new Pareto front approaches a straight line in which the investment cost linearly increases with the performance. In contrast, when considering the thermo-economic trade-off driven by the HX, one can identify a design solution beyond which increasing the cost would lead to marginal gains of efficiency, and hence not interesting thermo-economically.

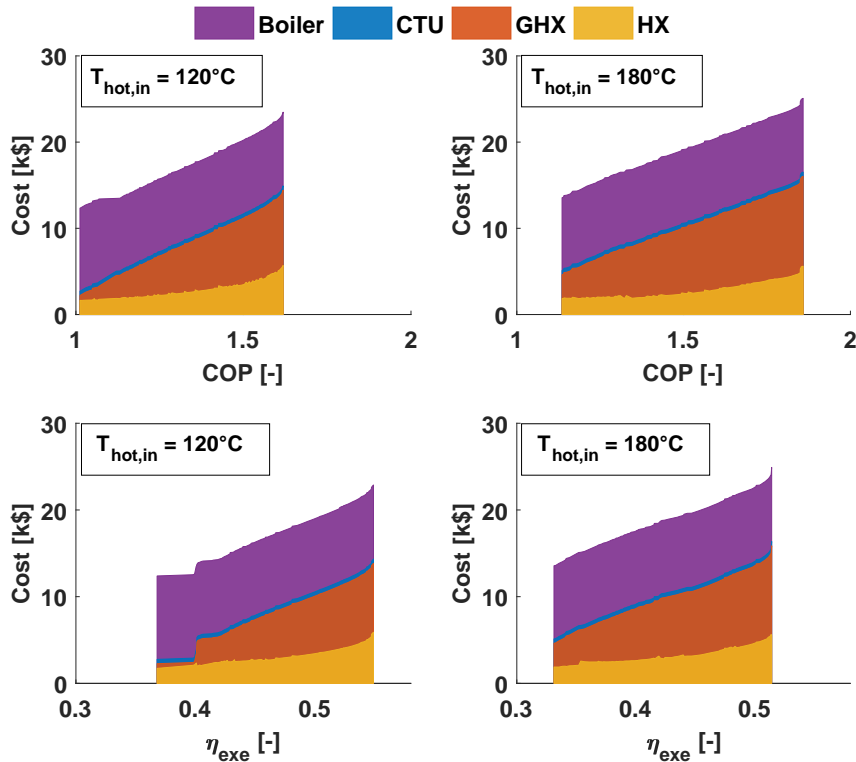


Figure 4.11 – Repartition of the component costs on the dominating Pareto fronts shown in Figure 4.10

When the COP is optimized, the Pareto-dominant working fluids remain similar, although the difference between them is less pronounced than in Figure 4.9. When the exergetic efficiency is optimized, the Pareto-dominant working fluids are also the same as before at 120°C , where R245fa outperforms the others. However, at 180°C , R245fa remains the dominant working fluid, while it was replaced by R600a when only HX costs were considered (Figure 4.9). As shown in Table 4.11, R245fa features higher \dot{Q}_{hot} than R600a since it presents higher compressor pressure ratios. Since the condenser heating power is fixed at 40 kW, higher \dot{Q}_{hot} lead to smaller \dot{Q}_{cold} , and hence decrease the GHX cost. Therefore, considering this component in the thermo-economic trade-off draws new conclusions when optimizing the exergetic efficiency at 180°C .

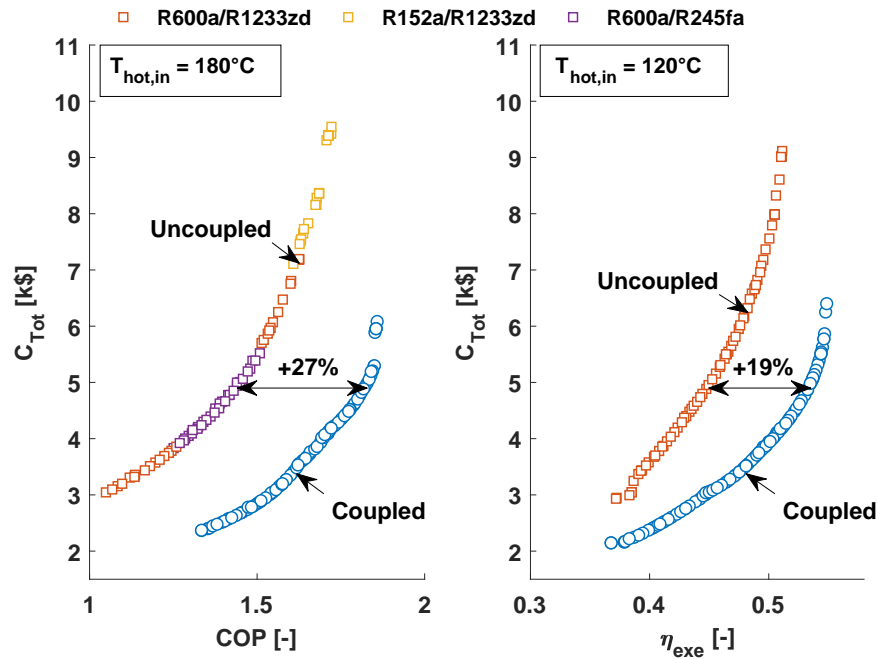


Figure 4.12 – Comparison of the HP-ORC Pareto-dominant fronts between the coupled and uncoupled configuration, based on the HX economic trade-off. The working fluid pair for the uncoupled HP-ORC is indicated as F_{HP}/F_{ORC} . For the coupled HP-ORC, only the Pareto-dominant front is displayed - see Figure 4.9

4.6.4 Stage 3: Influence of the HP-ORC configuration

The goal of this section is to compare two HP-ORC configurations, coupled and uncoupled, which are described in Figures 4.1a and 4.1b. Figure 4.12 shows the resulting Pareto curves of the uncoupled configuration, compared with the dominant Pareto fronts highlighted in Figure 4.9, i.e., when considering the cost of the HX only (stage 1). Figure 4.13 shows the Pareto fronts obtained when considering the overall cost of the system (stage 2). For both cost functions and case studies, the Pareto-dominant configuration is always the mechanically coupled one, suggesting that the coupled HP-ORC configuration always achieves more efficient and less expensive design solutions (12% to 27% efficiency gain). The underlying reasons why the uncoupled system underperforms are explained in this section.

Table 4.14 shows the optimum working fluids corresponding to the two case studies (A: COP maximization at 180°C and B: η_{exe} maximization at 120°C) for the two HP-ORC configurations. The optima are retrieved for the two cost functions, with cost targets set at \$5'000 for stage 1 and \$22'000 for stage 2. In the uncoupled configuration, the optimum working fluids in the HP loop are R600a and R152a, while R245fa and R1233zd prevail in the ORC loop.

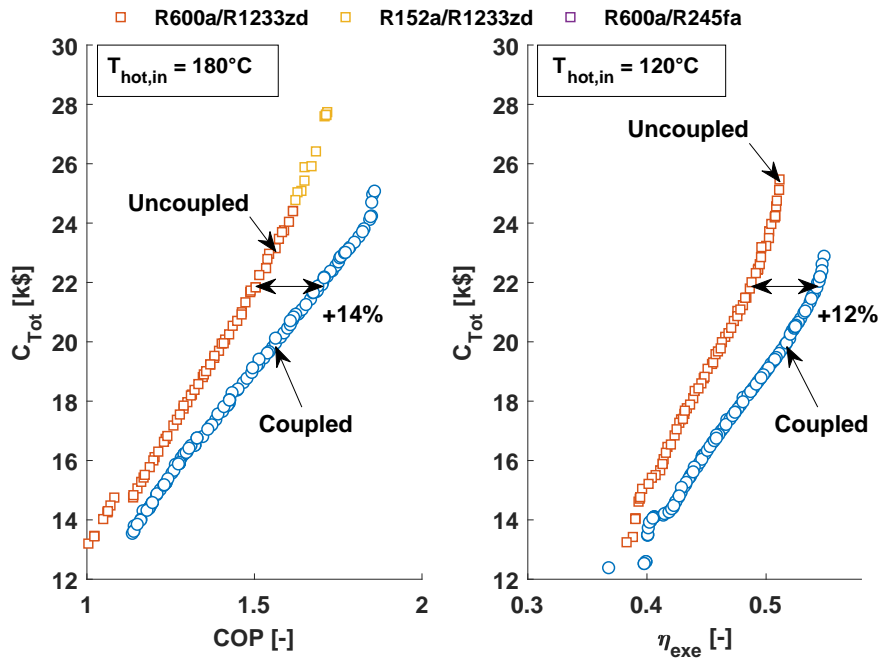


Figure 4.13 – Comparison of the HP-ORC Pareto-dominant fronts between the coupled and uncoupled configuration, based on the overall cycle economic trade-off (HX, GHX, CTU, and boiler). The working fluid pair for the uncoupled HP-ORC is indicated as F_{HP}/F_{ORC} . For the coupled HP-ORC, only the Pareto-dominant front is displayed - see Figure 4.10

Table 4.14 – Optimum working fluid selection for the two HP-ORC configurations

		stage 1: HX		stage 2: HX+GHX+Fixed Costs	
		Coupled	Uncoupled	Coupled	Uncoupled
$T_{hot,in} = 120^\circ\text{C}$ max(η_{exe})	F_{HP-ORC}	R245fa	-	R245fa	-
	F_{HP}	-	R600a	-	R600a
	F_{ORC}	-	R1233zd	-	R1233zd
$T_{hot,in} = 180^\circ\text{C}$ max(COP)	F_{HP-ORC}	R152a	-	R152a	-
	F_{HP}	-	R600a	-	R600a
	F_{ORC}	-	R245fa	-	R1233zd

Table 4.15 compares the cycle and CTU efficiencies of the coupled and uncoupled configurations. Only the results based on the overall cycle cost (HX, GHX, CTU, and boiler) when maximizing the COP at $T_{hot,in}=180^\circ\text{C}$ for a cost target of \$22'000 are shown (stage 2).

In the uncoupled configuration, the COP of the HP cycle is higher than for the coupled configuration (+1.1-pt), while the ORC efficiencies η_{ORC} are similar. This is a consequence of the optimizer being free to choose the working fluids that are best adapted to the ORC and HP cycles in the uncoupled HP-ORC. In addition, the turbomachinery isentropic efficiencies are higher for the uncoupled configuration than the coupled one (+4-pt for the compressor and +0.5-pt for the turbine) since a rotor speed trade-off is no longer needed.

In the coupled HP-ORC, the transmission efficiency $\eta_{trans} = \frac{\dot{E}_{turb}}{\dot{E}_{comp}}$ is governed by the shaft and bearing mechanical losses. Using the shaft and bearing loss models introduced in chapter 3, η_{trans} is estimated at 96% in the coupled HP-ORC. In the uncoupled HP-ORC, η_{trans} includes the shaft and bearing mechanical losses, the power generation unit mechanical losses (mechanical efficiency of 96%), and the frequency converter losses (conversion efficiency of 96%). As a consequence, the transmission efficiency η_{trans} of the uncoupled HP-ORC is 13-pt lower compared to the coupled system, which in spite of having higher turbomachinery isentropic efficiencies, leads to a 9-pt CTU efficiency drop ($\eta_{CTU} = \eta_{is,turb}\eta_{is,comp}\eta_{trans}$). This is illustrated in the Sankey diagram representing the CTU power flows in Figures 4.14a and 4.14b, for the coupled and uncoupled configuration, respectively.

Table 4.15 – Cycle and CTU parameters for the two HP-ORC configurations

Term	Unit	Coupled	Uncoupled
Cycle parameters			
$\eta_{ORC} = \frac{\dot{E}_{turb}}{\dot{Q}_{hot} + \frac{W_{pump}}{0.56}}$	[-]	0.13	0.13
$COP_{HP} = \frac{Q_{sink, hp}}{\dot{E}_{comp}}$	[-]	4.9	6
P_{evo}	[bar]	45	15.2
P_{evh}	[bar]	2.7	1.65
F_{ORC}	[-]	R152a	R1233zd
F_{HP}	[-]	R152a	R600a
CTU parameters			
η_{trans}	[-]	0.96	0.83
$\eta_{is,turb}$	[-]	0.84	0.845
$\eta_{is,comp}$	[-]	0.753	0.79
η_{CTU}	[-]	0.61	0.52
N_{comp}	[krpm]	262	178
N_{turb}	[krpm]	262	202
D_{comp}	[mm]	18	29
D_{turb}	[mm]	15.6	25

Furthermore, the overall cost of the uncoupled HP-ORC is penalized, as shown in Figure 4.15, where the HP-ORC costs are plotted as a function of the COP for the two configurations. While the cost of the GHX and the boiler are similar, the cost of the HX increases due to the addition of a heat exchanger (two condensers are required instead of a single one). Moreover, since the system must compensate the CTU efficiency loss, a higher total area is needed to achieve the same COP. Finally, since the uncoupled configuration is made of two distinct turbomachinery units instead of one for the coupled version, the total cost increases by \$500 (equation 4.11).

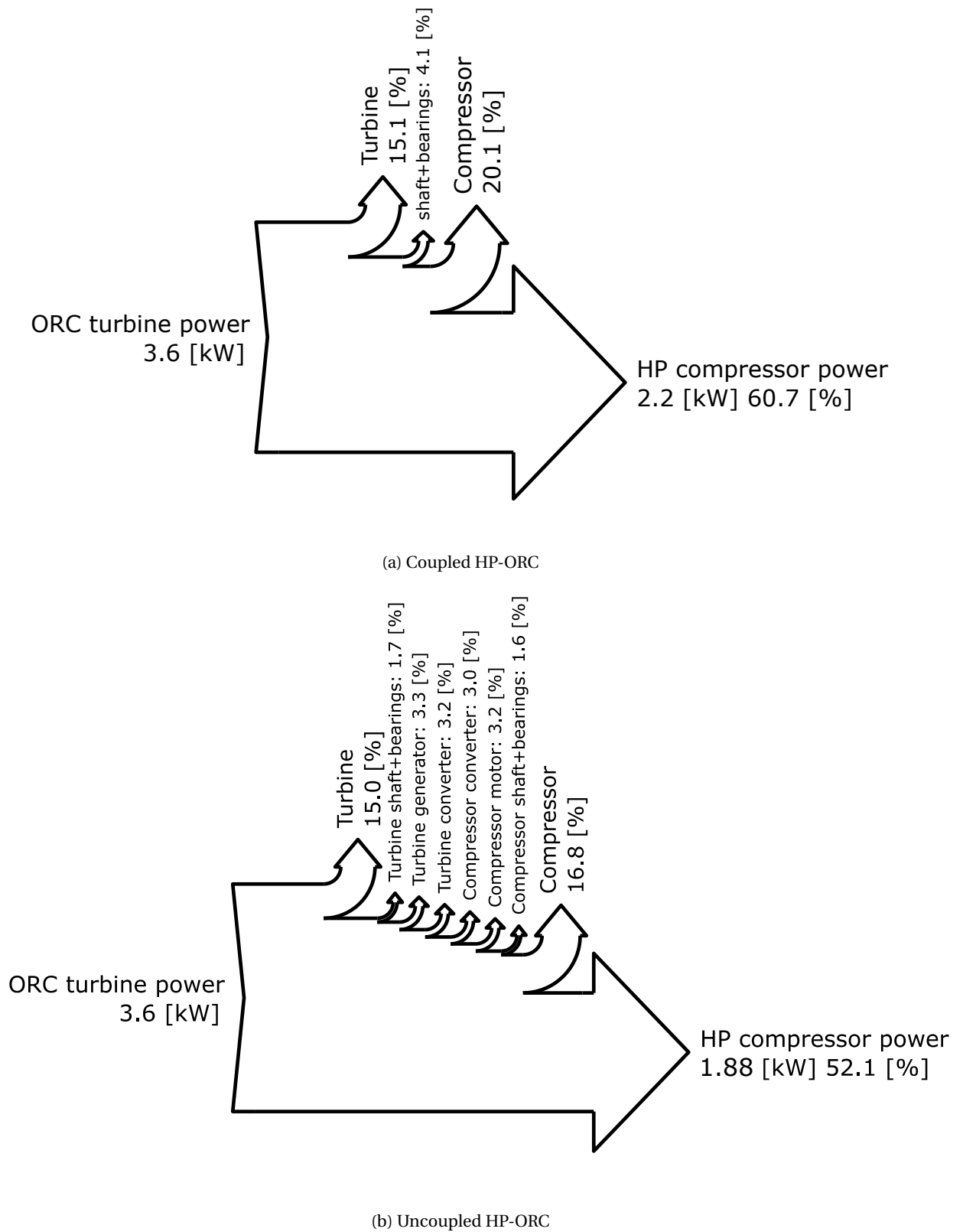


Figure 4.14 – Sankey diagram of the CTU power flows for the HP-ORC in its (a) coupled and (b) uncoupled configuration

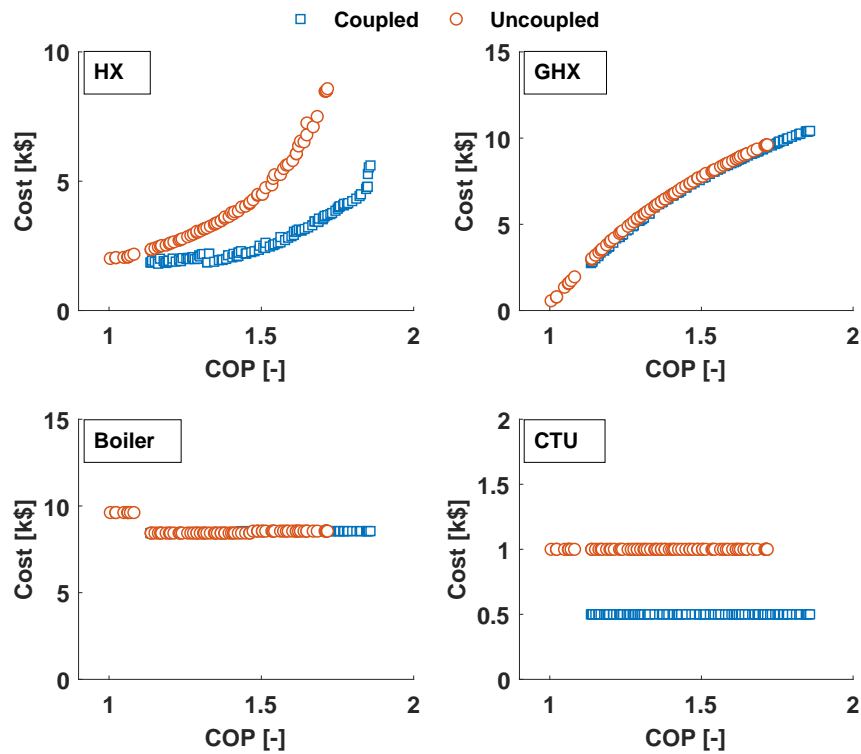


Figure 4.15 – Cost repartition comparison between the coupled and uncoupled HP-ORC configuration when maximizing the COP at $T_{hot,in}=180^{\circ}\text{C}$ (stage 2)

Therefore, the results suggest that the uncoupled HP-ORC is less thermo-economically interesting than the coupled one. Nonetheless, the uncoupled configuration might be of interest when the designer is asked to emphasize on other cycle constraints. Indeed, the pressure levels are better adapted in each loop due to the flexibility of selecting the most appropriate fluid for each cycle individually. In the uncoupled configuration, lower pressures are encountered in the ORC loop by using R1233zd working fluid as shown in Table 4.15 ($P_{evo}=15.2$ bar in the uncoupled HP-ORC, against 45 bar in the coupled one). Furthermore, since the optimum uncoupled HP-ORC operates with R600a in the HP loop, the pressure always remains above the ambient in the cycle. Finally, the investigation is restricted to the working fluids presented in Table 4.7, which have been selected for matching operating conditions of a coupled HP-ORC. In an uncoupled configuration, additional working fluids could be considered, especially in the ORC loop where higher temperatures can be targeted with Toluene and Siloxanes [36], or even steam. Finally, the uncoupled configuration may result in enhanced operational flexibility and easier control strategies since the absence of turbomachinery rotor speed matching mitigates the risk of encountering compressor surge or choke regions. Furthermore, since the two thermal loops are dissociated, there is no risk of working fluid migration from the ORC to the HP loop, which in the coupled configuration, may lead to a shortage of liquid working fluid at the pump inlet, hence stopping the system.

4.7 Comparison to a Single Effect Absorption Heat Pump (SEAHP)

Besides the HP-ORC technology, one of the most common thermally driven heat pump systems is the absorption heat pump, especially the Single Effect Absorption Heat Pump (SEAHP). This section compares the HP-ORC and SEAHP technologies regarding an investment cost/performance trade-off.

4.7.1 SEAHP description

The SEAHP cycle is represented in Figure 4.16 and is divided into two pressure levels: Low pressure (evaporator and absorber) and high pressure (generator, rectifier, and condenser). The solution coming from the absorber in a liquid state (1) is pumped up to the generator (3), where the heat input causes the boiling and evaporation of the volatile component (refrigerant) of the solution (7). The refrigerant is then purified (9) in the rectifier, condensed (10) and pre-cooled (11), before being expanded (11-12), evaporated (12-13), and preheated before flowing back to the absorber (14). The poor solution that leaves the generator (4) returns to the absorber through the Solution Heat Exchanger (SHX) (4-5) and the Solution Valve (SV) (5-6). \dot{Q}_{hot} and \dot{Q}_{cold} correspond to the heating powers delivered from the hot source to the SEAHP generator (or desorber) and from the cold source to the SEAHP evaporator, respectively. The sum of heating power rejected from the SEAHP condenser \dot{Q}_{sink1} , rectifier \dot{Q}_{sink2} , and the SEAHP absorber \dot{Q}_{sink3} corresponds to the heating power recovered from the cycle, and hence defined by $\dot{Q}_{sink} = \sum_j \dot{Q}_{sinkj} = 40$ kW (Table 4.1). The SEAHP operates with the NH₃-H₂O (ammonia-water) pair.

4.7.2 SEAHP modeling

The absorption cycle model is adapted from Herold et al. [125]. The thermo-physical and transport properties of the ammonia-water mixtures are obtained using REFPROP 9.1 [98]. For mixtures with more than 5% of water (molar), the models of Conde [126] and Kaern [127] are used for liquid and vapor phases, respectively. The cycle is first calculated with an initial guess of the mass flow rates, the saturated liquid temperatures in the SEAHP condenser and absorber (T_{10} and T_1 on Figure 4.16), and the vapor temperature at the SEAHP evaporator (T_{13} on Figure 4.16). Using a nonlinear solver routine from MATLAB [73], the procedure is iterated until satisfaction of (1) the total and ammonia mass balance over the cycle components, (2) the overall energy balance, and (3) of the targeted pinches.

The heat transfer areas of the SEAHP HXs are calculated using the same procedure and correlations introduced for the HP-ORC, except in the HXs where mass transfer is involved along with the heat transfer process. Plate Heat Exchangers (PHEs) are considered as well, except for the rectifier. A helical coil (HC) is selected for the SEAHP rectifier instead, which serves both as a distillation column and a heat exchanger [128]. More details about the helical coil geometry can be found in [56].

4.7. Comparison to a Single Effect Absorption Heat Pump (SEAHP)

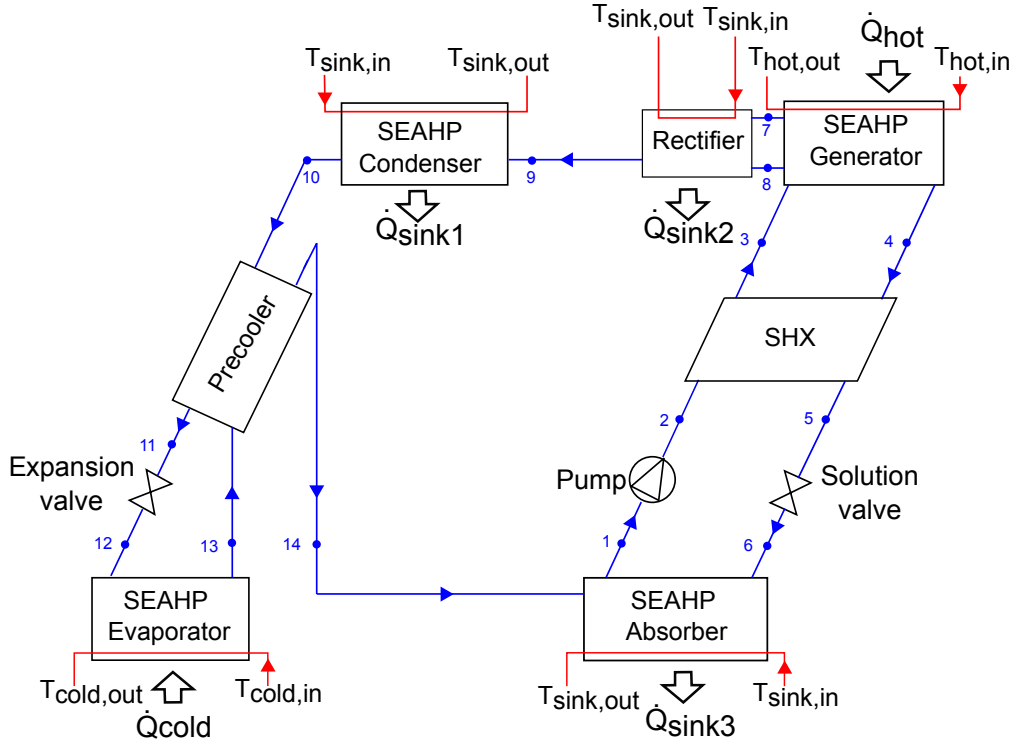


Figure 4.16 – Schematic layout of the Single Effect Absorption Heat Pump (SEAHP)

In the SEAHP heat transfer units involving mass transfer, the mass transfer area is predicted for a given section j as follows:

$$\dot{m}_{abs} = \gamma_j A_j LMCD_j \quad (4.13)$$

where \dot{m}_{abs} is the absorbed mass flow rate in the heat exchanger and γ_j the mass transfer coefficient. $LMCD_j$ is the logarithmic mean ammonia concentration difference in the liquid phase (the mass transfer in the vapor phase is assumed negligible compared to the liquid phase) and is given as follows [129]:

$$LMCD_j = \frac{[\rho_{in}^{sat} c_{in}^{sat} - \rho_{in} c_{in}] - [\rho_{out}^{sat} c_{out}^{sat} - \rho_{out} c_{out}]}{\log\left(\frac{\rho_{in}^{sat} c_{in}^{sat} - \rho_{in} c_{in}}{\rho_{out}^{sat} c_{out}^{sat} - \rho_{out} c_{out}}\right)} \quad (4.14)$$

The mass transfer coefficient γ_j described by equation 4.15 is calculated with the Sherwood number Sh as follows:

$$\gamma_j = Sh_j \frac{\alpha_j}{d_h} \quad (4.15)$$

where α_j is the fluid diffusivity and d_h the hydraulic diameter of the SEAHP heat exchangers. A summary of the correlations used for evaluating the Nusselt and Sherwood numbers in the SEAHP heat exchangers is given in Table 4.16, and detailed in Table C.2 (Appendix C).

Chapter 4. Integrated design optimization of the HP-ORC cycle

Table 4.16 – Heat and mass transfer correlations for the SEAHP heat exchangers

Absorber	Generator	Rectifier	Others ⁴
Lee et al. [129]	Taboàs et al. [130]	Qaswari [128]	Tables 4.3 and C.1

Since both the LMTD and LMCD methods yield a minimum area to satisfy both heat and mass transfer processes in a given heat exchanger section j , the more significant area of the two is selected for evaluating the cost.

To evaluate the SEAHP heat exchangers cost, the correlation of equation 4.9 valid for PHEs is used, except for the rectifier, which is of helical coil type. Unfortunately, not enough commercial data are available for estimating the investment cost of helical coils. However, catalog prices are available for shell and tubes heat exchangers, whose geometry and constraints are similar to the rectifier helical coils. Shell and tube heat exchanger prices collected from Henchoz et al. [122] have been used and a new correlation has been built as follows:

$$C_{HX,j} = 193 + 1161A_{HX,j} \text{ [\$]} \quad (4.16)$$

The cost of the boiler C_{Boiler} and GHX C_{GHX} are evaluated through the same correlations used to evaluate the investment cost of HP-ORCs (Table 4.4 and equation 4.10). The SEAHP total cost does not include the CTU though. However, SEAHPs operate with an additional component, the Solution Valve (SV), which has been estimated to $C_{SV}=\$500$ through a market investigation (Flow Regulator RW-15 AISI 316L ⁵). As a consequence, it is assumed in a first approximation that the considered fixed costs between the SEAHP and HP-ORC are equivalent.

The decision variables for optimizing the SEAHP cycle are presented in Table 4.17. In this case, only the heat exchanger pinches are optimized. No mechanical compression is present in SEAHP systems, hence constraints regarding vapor quality, pressure ratio, and turbomachinery dimensions are not relevant. However, similarly to the HP-ORC, the pressure in the generator is limited to 70 bar (see section 4.5).

Table 4.17 – Design variables of the SEAHP optimization

Component	Variable	Term	Range	Unit
G_{HX}	Generator pinch	$DT_{min,ahp,gen}$	[1-20]	[K]
	Absorber pinch	$DT_{min,ahp,abs}$	[1-20]	[K]
	Condenser pinch	$DT_{min,ahp,cond}$	[1-20]	[K]
	Evaporator pinch	$DT_{min,ahp,ev}$	[1-20]	[K]
	Precooler pinch	$DT_{min,ahp,precool}$	[1-20]	[K]
	SHX pinch	$DT_{min,ahp,shx}$	[1-20]	[K]
	Rectifier pinch	$DT_{min,ahp,rec}$	[1-20]	[K]
G_{Fluid}	Working fluid	F	NH ₃ -H ₂ O	[-]

⁴Condenser, evaporator, SHX, and precooler

⁵<http://www.palmstiermas.se/>

4.7. Comparison to a Single Effect Absorption Heat Pump (SEAHP)

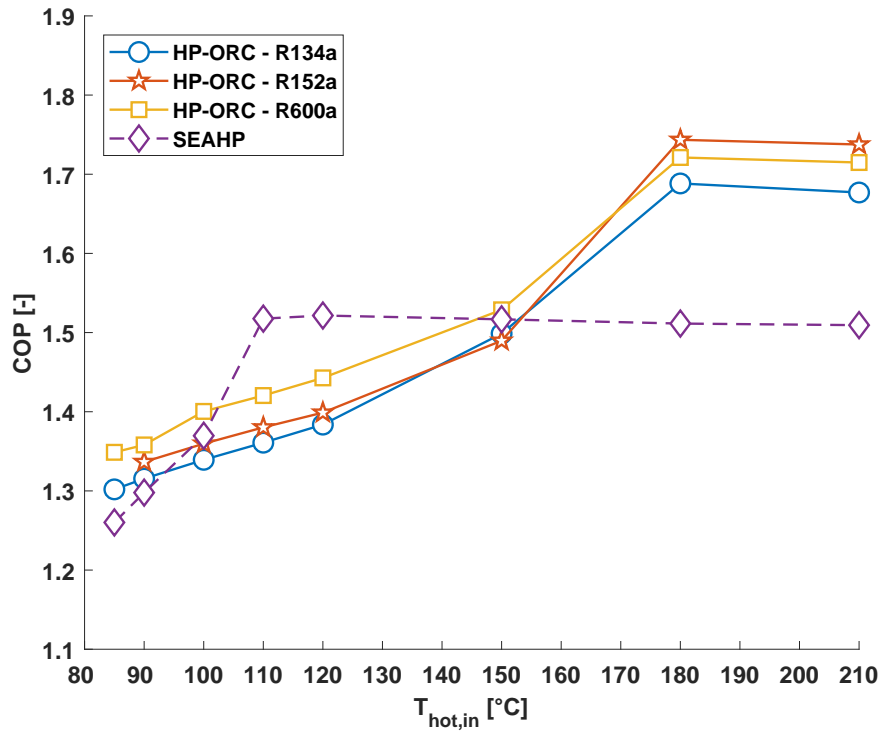


Figure 4.17 – COP versus the hot source temperature for the HP-ORC and the SEAHP

4.7.3 Results and discussion

Figure 4.17 shows the evolution of the COP with the hot source temperature of a SEAHP and a HP-ORC operating with the optimum working fluids R134a, R152a, and R600a (see Figures 4.9 and 4.10). The comparison is based purely on COP as a function of the hot source temperature and without considering the components sizing and cost. The HX pinches (DT_{min}) have been fixed at 10 K for the hot sources (ORC evaporator/SEAHP generator) and at 2 K for the cold sources (HP evaporator/SEAHP evaporator) and the sinks (HP-ORC condenser/SEAHP condenser/SEAHP Absorber/SEAHP rectifier). For the HP-ORC, the turbine super-heating $DT_{sh,turb}$ has been set to 45 K for R134a and R152a and at 10 K for R600a (see optimum design variables in Figures 4.7 and 4.8). The other thermodynamic variables are the same as presented in Table 4.1.

Regardless of the working fluid, the HP-ORC COP evolution with the hot source temperature presents a similar trend. A COP plateau is reached at 180°C, due to the limitation of the ORC evaporator pinch at 10 K. The SEAHP COP yields a fast increase from 85°C to 110°C, before reaching a COP threshold at 120°C, which has been highlighted by Balaras et al. [131]. Therefore, while the SEAHPs present the best COP between 105 and 140°C, HP-ORCs perform better at higher hot source temperatures. This is due to the limitation of the desorption process, which achieves its maximum potential at 120°C in a SEAHP.

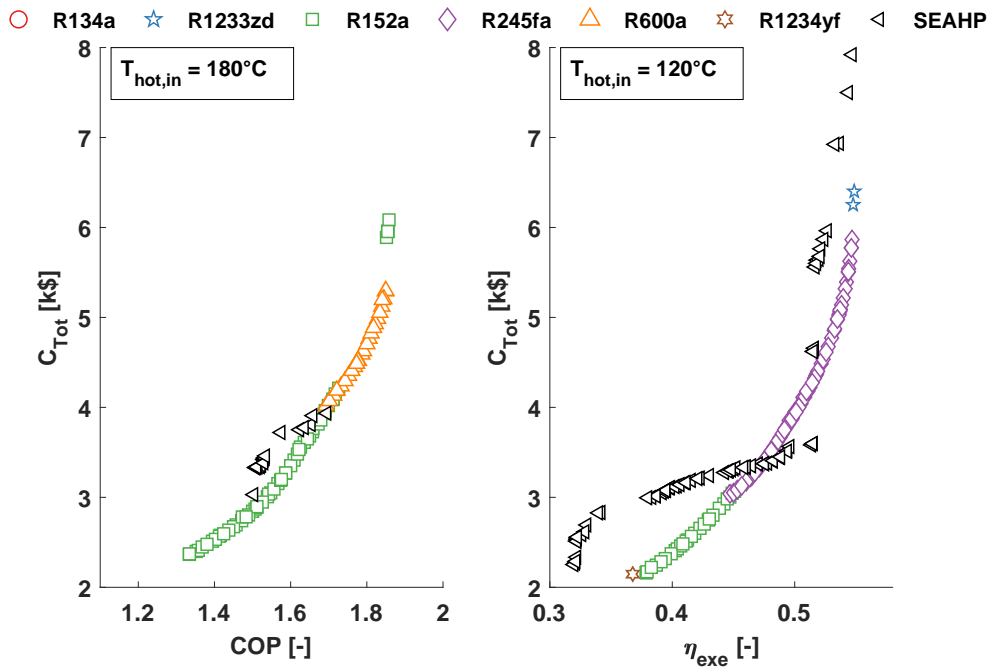
Chapter 4. Integrated design optimization of the HP-ORC cycle

Figure 4.18a shows the thermo-economic optimization results for the SEAHP cycle and compares them to the Pareto-dominant HP-ORC fluids for the hot source temperatures and performance objectives presented in Figure 4.9. Note that this graph only compares the thermo-economic trade-off driven by the heat exchangers. Figure 4.18b presents the comparison, integrating, however, the overall cost of the TDHPs (Boiler and GHX for both systems, CTU for the HP-ORC, and Solution Valve (SV) for the SEAHP).

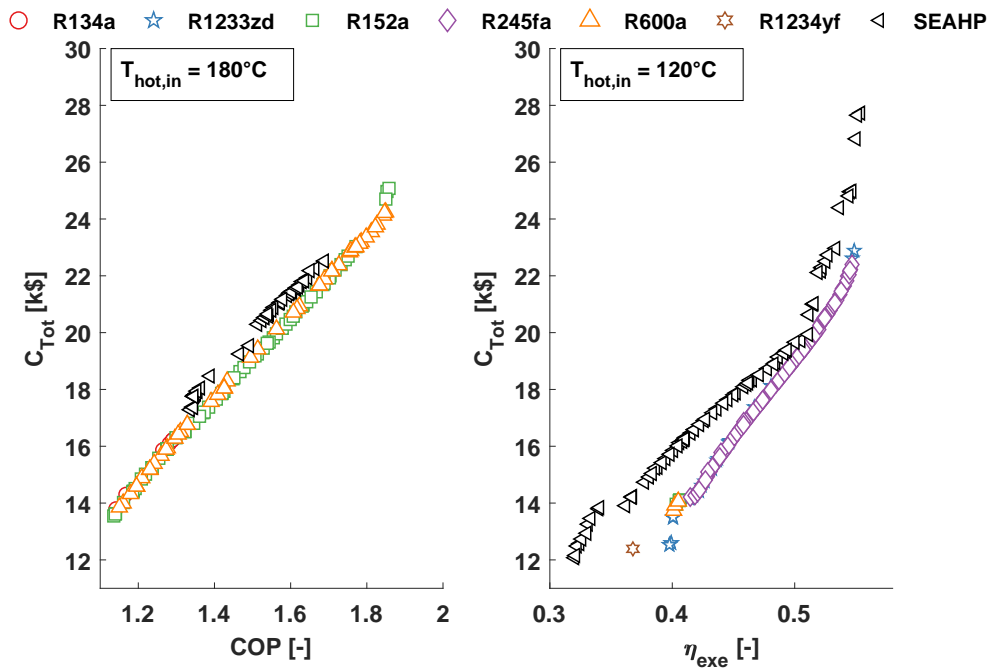
With the HX-based thermo-economic trade-off at 120°C, the Pareto front is defined by the HP-ORC technology, except for exergetic efficiencies between 45% and 52% where the SEAHP is dominating. In this region, the HX investment cost of the SEAHP can be lower than the HP-ORC, although the SEAHP requires more heat transfer units. This is due to the particularity of the AHPs where the heat transfer process occurs mostly in liquid/liquid regions, thus decreasing the required heat exchanger area. Furthermore, the HP-ORC and SEAHP yield similar values of highest performance achievable at $\eta_{exe}=55\%$. The two TDHP technologies are, therefore, highly competitive at 120°C.

At 180°C, the Pareto fronts are very similar, with the HP-ORC slightly dominating the SEAHP. However, the SEAHP technology yields a much smaller range of feasible solutions on the Pareto front, offering lower maximum performance (maximum SEAHP COP at 1.7 compared to 1.87 for the HP-ORC). As explained earlier, this is the consequence of considering only single effect AHPs, which are not made to operate at high hot source temperatures due to the limited potential of the desorption process in one single generator. In order to increase the feasibility domain of the SEAHP on the Pareto front, the pinches in the heat exchangers have to be raised further than 20 K, which results, however, only in solutions with lower COP and exergetic efficiencies. Note that the same trend is observed when the thermo-economic trade-off is based on additional costs (Figure 4.18b), at the difference that there are no regions where the SEAHP dominates the HP-ORC system.

4.7. Comparison to a Single Effect Absorption Heat Pump (SEAHP)



(a) Thermo-economic trade-off driven by the HXs



(b) Thermo-economic trade-off driven by the overall cycle components

Figure 4.18 – Thermo-economic comparison of the HP-ORC and the SEAHP cycles based on (a) HX cost only and (b) on all component costs

To conclude, the relatively simple HP-ORC system with single-stage expansion and compression offers higher efficiencies than the SEAHP while being more profitable regarding its thermo-economic potential. In particular, the SEAHP is outperformed at high hot source temperatures. In order to boost the SEAHP performance further and to profit from higher hot source temperatures, the number of effects (or generator units) has to be increased [4]. This is linked, however, to the penalty of an increased investment cost, due to the addition of three heat exchangers and one solution valve if a Double Effect Absorption Heat Pump (DEAHP) is considered. In order to highlight this, a DEAHP was simulated with the same design conditions as the one resulting in the highest efficiency point for the SEAHP optimized at 180°C. When applying the cost functions presented in this thesis, the COP increases by 8% and the investment cost by 12% compared to the single effect system, which is a solution that is still outperformed by the HP-ORC concept. As a consequence, it can be concluded that the HP-ORC concept outperforms absorption systems both in terms of efficiency and cost for hot source temperatures above 150°C. Furthermore, as shown by Mounier et al. [132], the HP-ORC has the advantage of performing on a wider operating range than SEAHPs while using working fluids which are less toxic and corrosive than ammonia.

4.8 Improvement of the prototype performance

In order to evaluate the performance improvement potential of the prototype, the measured data performed by Demierre et al. [30] are compared with the optimum Pareto curves described in this chapter. Table 4.18 shows a sample of the measured experimental data. Note that only one data point is presented here since it matches the boundary conditions chosen for the thermo-economic optimization of the HP-ORC. For these tests, the hot source temperature inlet was set at 193°C. The temperature at the ORC and HP condenser outlet is at 36°C. The HP evaporator inlet temperature is at 8.8°C. Two condensers have been implemented instead of a single one to have more operational flexibility between the ORC and HP loops. In this prototype, the ORC condenser, the HP condenser, and the HP evaporator are PHEs with heat transfer areas of 2.88 m², 1.13 m², and 2.88 m², respectively. The ORC evaporator is composed of three Double Tube Coils (DTC) in series with a heat transfer area of 0.23 m² each. The cost of the DTC has been assumed through the shell tube cost correlation (equation 4.16).

Table 4.18 – Experimental thermodynamic conditions of the HP-ORC proof of concept

N	$T_{cold,in}$	$T_{sink,out}$	$T_{hot,in}$	$P_{turb,in}$	$T_{turb,in}$	\dot{Q}_{sink}	\dot{Q}_{hot}
[krpm]	[°C]	[°C]	[°C]	[bar]	[°C]	[KW]	[kW]
206	8.8	36	193	50.5	123	42	30

Figure 4.19 shows the performance of the HP-ORC proof of concept compared with the optimum Pareto fronts based on the HX costs $C_{Tot} = C_{HX}$. The Pareto fronts corresponding to R134a, which is the working fluid of the prototype, and to R600a, which is the Pareto-optimum working fluid (Figure 4.9) are represented. At an equal C_{HX} , a potential COP gain of 0.27 (+20%) is possible with R134a, and 0.36 (+24%) with R600a.

4.8. Improvement of the prototype performance

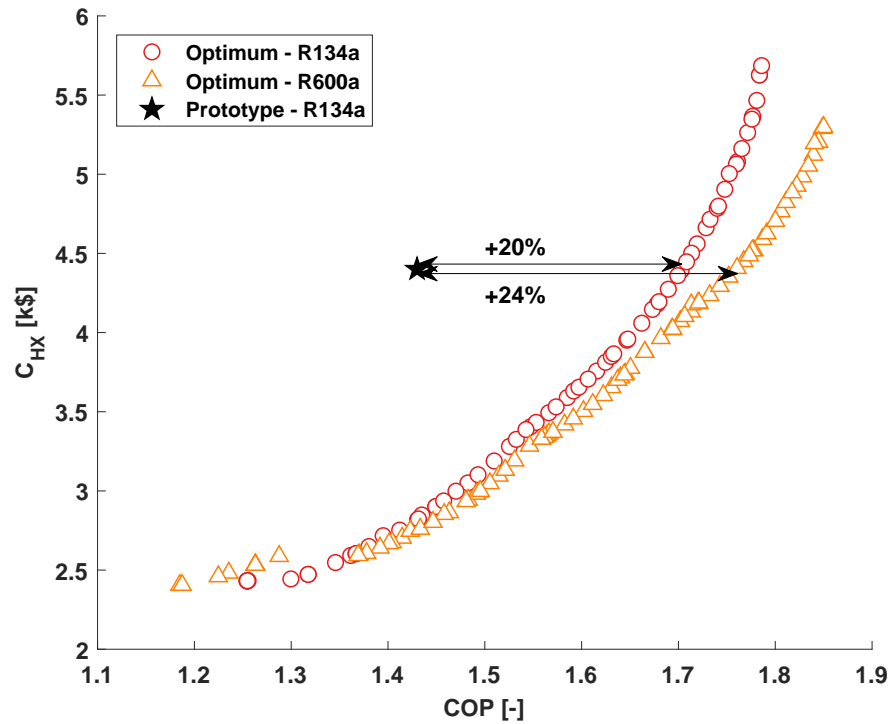


Figure 4.19 – Thermo-economic comparison of the HP-ORC prototype towards the optimum Pareto fronts shown in Figure 4.5

Table 4.19 presents the differences in design between the prototype, the optimum design 1 (R134a), and the optimum design 2 (R600a). Since the pinches were not known in the prototype, the heat exchange areas are compared instead. Note that the ORC evaporator is not of the same type between the prototype (DTCs) and the optimum designs (PHEs).

The area occupied by the two prototype condensers is higher than the one recommended by the optimizer, while the prototype HP and ORC evaporators seem to be undersized. In fact, the use of DTCs instead of PHEs for the ORC evaporator is suboptimal due to their low compactness. Indeed, it is observed that the temperatures at the refrigerant side of the ORC evaporator are much smaller than the hot source temperature (193°C at the thermal oil inlet versus 123°C at the turbine inlet). It follows that a very high pinch was encountered in the ORC evaporator, hence leading to a significant performance drop. Besides, in contrast to the optimum cycle designs, the prototype has no regenerator.

In addition, the investment cost of the prototype is penalized by having two condensers and three ORC evaporators instead of one. In the prototype, the total cost for the condenser is $C_{cond,tot} = C_{cond,orc} + C_{cond,hp} = 611 + 1015 = \1626 and for the ORC evaporator $C_{evo,tot} = 3 * C_{evo,DTC} = 3 * 496 = \1188 . If these heat exchangers were combined into one single unit, their cost decrease to $C_{cond,tot} = \$1460$ and $C_{evo,tot} = \$1021$, hence decreasing C_{HX} by 8%.

Chapter 4. Integrated design optimization of the HP-ORC cycle

Table 4.19 – Optimum design variables of the cycle optimization compared to the prototype

Component	Term	Prototype	Optimum 1	Optimum 2	Unit
	COP	1.43	1.7	1.76	[-]
Cycle	Fluid	R134a	R134a	R600a	[-]
	P_{evo}	50.5	57.9	42.5	[bar]
	$T_{turb,in}$	123	152	154	[°C]
	T_{cond}	35.5	37	38	[°C]
	T_{evh}	4	3	3	[°C]
	PR_{comp}	2.8	3	3.4	[-]
	PR_{turb}	4.4	6.1	8.2	[-]
Heat exchangers	$A_{evo,tot}$	0.69	2.45	2.47	[m ²]
	A_{evh}	1.13	2.15	2.64	[m ²]
	$A_{cond,tot}$	5.8	4.62	4.2	[m ²]
	Regenerator ?	No	Yes	Yes	[-]
CTU	N	206	199	251	[krpm]
	$\eta_{is,comp}$	0.66	0.75	0.75	[-]
	$\eta_{is,turb}$	0.69	0.82	0.79	[-]
	D_{comp}	20	19.5	25.3	[mm]
	D_{turb}	18	16.6	23.1	[mm]
	ϵ_{comp}	0.56	0.6	0.6	[-]
	ϵ_{turb}	0.7	0.5	0.5	[-]
	ζ_{comp}	0.12	0.15	0.23	[-]
	e_{turbo}	200	80	80	[μ m]
	C_{seal}	100	30	30	[μ m]

Furthermore, the measured turbomachinery isentropic efficiencies are lower than the optimal ones provided by the pre-design models. This efficiency drop is due firstly to a suboptimal CTU design, mainly turbomachinery dimensions and rotor speed (see Figure 3.17). Secondly, while the turbomachinery models used for the cycle optimization consider turbomachinery tip clearances equal to $e_{turbo} = \max(0.02b_4, 80\mu m)$, they were measured at 200 μ m in the prototype [35]. Nonetheless, as shown in the sensitivity analysis in chapter 3, increasing the tip clearances from 80 μ m to 200 μ m depreciates the turbomachinery isentropic efficiency by up to 7-pt. Finally, since labyrinth seals with clearances in the order of 100 μ m were implemented in the prototype, high leakage mass flows were encountered, estimated to 15% of the turbine mass flow rate [35]. In addition to depreciating the CTU efficiency by 3 to 7-pt (see chapter 3), the risk of having heat addition at the compressor inlet is high, which tends to decrease the compressor efficiency as well. Therefore, independently of the selection of the HP-ORC working fluid, the CTU must be optimized to deliver higher COPs. An updated design of the turbomachinery design as shown in Table 4.19 is required (tip clearances e_{turbo} , tip diameters D, blade height to tip radius ratios ζ , and shroud to tip radius ratios ϵ). In addition, the labyrinth seal should have a decreased clearance to mitigate the fluid leakage through the CTU. The ORC and HP evaporators should be replaced by PHEs since they seem to be currently

undersized. In order to reduce the investment cost, the condenser should not be split into two heat exchangers. While R134a is still the selected working fluid, the pressure should be increased at the turbine inlet. As a consequence, selecting this fluid may be challenging for safety issues and pump requirements. Although R600a is flammable, it presents lower pressure levels and a higher COP than R134a, and is thus a promising alternative.

4.9 Limitations of the integrated optimization procedure

- **Heat transfer model** For the computation of the heat exchanger areas, the models are based on empirical heat transfer correlations. The literature provides numerous references and validations for Plate Heat Exchangers (PHEs) in subcritical operation without mass transfer. However, since no satisfying correlations exist for PHEs in supercritical operation, the single-phase transfer correlation has been used instead, which may lead to discrepancies with reality. Similarly, for PHEs used in absorption heat pumps, only a few studies have been conducted leading to only small ranges of validated results.
- **Cost model** The investment cost evaluation is a challenge for domestic refrigeration applications, especially for the cost rating of small-scale turbomachinery and absorption heat exchangers, due to the scarcity of available products on the market.
- **Seasonal performance** The thermo-economic procedure has been applied considering the design at best conditions. Seasonal performances and how it would impact the thermodynamic cycle are not considered.
- **Limitations to Ground Source Heat Pumps** The target application is domestic heat pumping, considering Ground Source Heat Pumps (GSHPs). While the latter are more efficient since they provide a nearly constant temperature all over the year, they are also the most expensive systems. A thermo-economic comparison towards air source HP-ORCs could be of great interest. Note, however, that the heat pump compressor would require two compression stages.
- **Selection of the hot source** The thermo-economic investigation considers a low temperature thermal oil (<200°C) as the hot source of the HP-ORC, independently of the primary energy source selection (gas, oil, wood, solar thermal or waste heat). Nonetheless, in the economic evaluation, for the sake of simplification, a gas boiler is considered. The boiler has, however, a constant cost along the Pareto front (Figure 4.6), and hence does not affect the trade-off mechanisms. Nonetheless, comparing the investment cost of different primary energy sources would be of great interest for a better assessment of the potential of HP-ORCs, particularly when driven by low grade heat sources.
- **Comparison to other TDHPs** The HP-ORC technology has been thermo-economically compared to a SEAHP. Additional comparisons towards optimized sorption heat pumps (DEAHP and adsorption with other working fluids than NH₃-H₂O) and Gas Driven Heat Pumps (GEHPs), which are other competing technologies, would be of great interest.

4.10 Summary and conclusions

A thermo-economic optimization of the HP-ORC system based on small-scale gas bearing supported turbomachinery has been developed. It finds the optimum cycle design solutions that satisfy the best trade-off between the performance - either estimated with the COP or the exergetic efficiency - and the investment cost of the HP-ORC. For this purpose, thermodynamic and economic models of the HP-ORC system have been implemented. The heat exchangers have been modeled based on the LMTD (Logarithmic Mean Temperature Difference) method coupled with heat transfer and cost correlations valid for Plate Heat Exchangers (PHEs). The gas bearing supported Compressor Turbine Unit (CTU) has been implemented using the centrifugal compressor and radial inflow turbine pre-design models described in chapter 2, and the shaft and bearing loss models used in chapter 3. In chapter 3, the outcome of the CTU optimization suggests that the shaft and bearing design variables have limited effect on the system performance. As a consequence, the latter have not been included in the thermo-economic optimization. Since Ground Source Heat Pumps are considered, the cost of the Ground Heat Exchanger (GHX) has been introduced. The cost of the boiler and the CTU are based on market studies.

In a first step, the thermo-economic trade-off driven by the heat exchangers has been investigated. The analysis of the Pareto fronts of the HP-ORC system suggests that the best working fluid is primarily a function of the hot source temperature and of the considered performance indicator (COP or exergetic efficiency). For a cost target of \$5'000, R134a and R600a are the recommended working fluids to maximize the COP at 120°C and 180°C, respectively. On the other hand, R245fa and R600a prevail when maximum exergetic efficiency is to be reached. This discrepancy in the identification of the optimum working fluid is due mainly to the impact of the pump consumption. Furthermore, the observation of other thermodynamic states and turbomachinery design constraints (impeller diameters, rotor speeds, cycle pressure levels, and fluid hazards) gives more insights into the decision-making process for selecting the optimum HP-ORC working fluid.

In a second step, the thermo-economic trade-off driven by additional cycle components such as the GHX has been studied. The GHX cost is driven primarily by the heating power at the HP evaporator. While the trade-off mechanisms are not affected when optimizing the COP, they are modified when maximizing the exergetic efficiency with a hot source at 180°C. The GHX has, therefore, a significant impact on the optimum design selection of ground source HP-ORCs.

In a third step, two different HP-ORC configurations have been compared, where the HP and ORC loops are either coupled mechanically or electrically (i.e., uncoupled). Under the constraints and assumptions of the thermo-economic investigation, while the uncoupled HP-ORCs offer higher design flexibility and easier controllability, these systems are thermo-economically less profitable than the coupled HP-ORCs (14% less efficient and 16% more expensive on average). This is due mainly to the addition of the electrical conversion elements,

which decreases the CTU efficiency by 9-pt. Moreover, the uncoupled HP-ORC suffers from higher investment costs due to the presence of two condensers and two CTUs instead of one in the coupled HP-ORC.

The HP-ORC technology has been further compared with a Single Effect Absorption Heat Pump (SEAHP). After having introduced the modeling features of the SEAHP, the dominant HP-ORC Pareto fronts have been compared with those of the SEAHP. The SEAHP is highly competitive with HP-ORC systems at 120°C but is dominated at higher hot source temperatures (above 150°C).

Finally, the optimum HP-ORC solutions have been compared with the prototype measurements. Using an integrated design optimization procedure, including optimum CTU, heat exchanger design, and cycle configuration, COP gains up to 24% are predicted when selecting R600a as the HP-ORC working fluid.

5 Application examples

This chapter presents a general optimization to design the CTU and the cycle simultaneously altogether, ensuring best performance, lowest investment cost, and sufficient rotordynamic stability. The new optimization procedure is described first and then applied to the same domestic space heating application as presented in chapter 4. The methodology is further tested on two other applications: Greenhouse heating and helicopter cabin air-conditioning.

5.1 Introduction

The conclusions highlighted in chapter 3 suggest that the CTU efficiency is governed primarily by the turbomachinery design, while the shaft and bearing design affect the rotordynamic stability. In chapter 4, since the focus was set on the cost/performance optimization and since a fixed cost for the CTU was considered, the rotordynamic stability was not accounted for. As a consequence, it was assumed that for any selected design it would be possible to find a shaft and bearing design ensuring the rotordynamic stability with a marginal effect on the overall performance. However, an optimization procedure finding the design trade-offs between highest performance and minimum investment cost while ensuring that the CTU reaches sufficient rotordynamic stability would be of great interest. Furthermore, the previous optimizations were tailored for the target application of this thesis, which is domestic heating. However, many other applications exist in which TDHPs, and particularly HP-ORCs, may deploy their potential.

The goal is thus to develop a new optimization procedure, which outputs the optimum HP-ORC designs for various applications ensuring objectives of performance, investment cost, and feasibility. In a first step, the new optimization procedure is described. The selection of the optimization variables, component models, and boundary conditions is made using the conclusions drawn in the previous chapters. The optimization approach is further applied to three case studies: (1) 40 kW domestic heating, (2) 113 kW greenhouse heating, and (3) 9 kW air conditioning of a helicopter cabin.

5.2 Definition of the case studies

Three HP-ORC applications have been investigated, covering the residential, agricultural, and transport sectors. For the three case studies, the values of heating and cooling requirements, as well as the targeted temperatures of the sink, cold source, and hot source, are summarized in Table 5.1.

- **Case study A** focuses on residential floor heating. The heat source is a typical boiler, either powered by fossil fuel or by wood pellets.
- **Case study B** investigates the heating needs for agricultural greenhouses under Swiss climate.
- **Case study C** considers air conditioning in a helicopter cabin, where the heat source is provided by the engine exhaust gases.

Table 5.1 – Heating, cooling, and temperature requirements for the three considered case studies

Case study	Application	Sink	Cold source	Hot source	T_{sink}	T_{cold}	T_{hot}
	[-]	[-]	[-]	[-]	[°C]	[°C]	[°C]
A	Heating - 40 kW	Water	Ground	Boiler	35	7	180
B	Heating - 113 kW	Water	Ground	Boiler	20	7	180
C	Cooling - 9 kW	Air	Cabin	Engine	43	18	550

5.2.1 Modeling

CTU model

The CTU model comprises the gas bearings (axial and radial), the shaft, and the turbomachinery components (compressor and turbine). The bearing and shaft models described in chapter 3 have been implemented. The turbomachinery models correspond to the ones introduced in chapter 2, which have been applied for the cycle thermodynamic optimization in chapter 4 (equations 4.1 and 4.2).

Cycle model

In chapter 4, the effects of the performance objective, the component selection, and the cycle configuration on the optimum cycle design have been highlighted. Although uncoupled configurations offer higher design and operational flexibility, their overall performance is lower than the coupled HP-ORCs, and hence, only mechanically coupled solutions are considered. Furthermore, heat pumps for domestic heating applications in countries such as Switzerland,

where the seasonal temperature variations are high, present higher performance with water/water than with air/water configurations. In case studies A and B, the cost of the boiler and the GHX is included in the trade-off mechanism. In the case study C, since the HP-ORC heat source is the engine waste heat and both sink and cold sources exchange with air, only the costs for the Heat Exchangers (HX) and the CTU are considered. The assumptions made for the thermodynamic cycle calculation in chapter 4 remain valid (steady-state, adiabatic, and isobaric heat exchange). Table 5.2 shows the boundary conditions common to each case study.

Table 5.2 – Boundary conditions common to each case study

Term	Symbol	Value	Unit
Pump isentropic efficiency	$\eta_{is,pump}$	0.60	[-]
Compressor inlet super-heating	$DT_{sh,comp}$	2	[K]
Condenser sub-cooling	DT_{sc}	2	[K]

5.2.2 Case study A: Domestic space heating

The case study A considers a 40 kW domestic floor heating application (base case study investigated in the previous chapters). The boundary conditions of this case study are the same as shown earlier in chapter 4 and are summarized in Table 5.3.

Table 5.3 – Boundary conditions of the case study A

Term	Symbol	Value	Unit
Heating power	\dot{Q}_{sink}	40	[kW]
Heat sink inlet temperature	$T_{sink,in}$	30	[°C]
Heat sink outlet temperature	$T_{sink,out}$	35	[°C]
Hot source inlet temperature	$T_{hot,in}$	180	[°C]
Hot source outlet temperature	$T_{hot,out}$	80	[°C]
Cold source inlet temperature	$T_{cold,in}$	7	[°C]
Cold source outlet temperature	$T_{cold,out}$	4	[°C]

5.2.3 Case study B: Heating of agricultural greenhouses

Nowadays, more and more agricultural greenhouses are implemented under our latitudes to provide all year long a large variety of vegetables and fruits. As an example, the use of greenhouses enables Brittany, a region having an oceanic climate, to be one of the first producers of tomatoes in France, thus competing with southern European countries such as Spain. Agricultural greenhouses provide constant heating at 20°C, controlled CO₂ concentrations and relative humidity, depending on the vegetable or fruit to grow. The present case study considers the growth of lettuce in Switzerland, considering a surface of 750 m² and for constant heating at 20°C. The heating need corresponds to 150 W/m² on average when integrating the sun radiation and wall condensation [133], representing an energy consumption of 550

Chapter 5. Application examples

kWh/m² over a year. The heating capacity of the greenhouse is of 113 kW and the total energy consumption is 412 MWh/year. A HP-ORC powered by a gas/oil boiler and a ground source is implemented to provide the heating utility. The case study B is similar to the case study A yet with a different heating power (113 kW instead of 40 kW) and temperature target (20°C instead of 35°C). Table 5.4 summarizes the boundary conditions for this case study. [134, 135]. Table 5.5 summarizes the boundary conditions for this case study.

Table 5.4 – Boundary conditions of the case study B

Term	Symbol	Value	Unit
Heating power	\dot{Q}_{sink}	113	[kW]
Heat sink inlet temperature	$T_{sink,in}$	15	[°C]
Heat sink outlet temperature	$T_{sink,out}$	20	[°C]
Hot source inlet temperature	$T_{hot,in}$	180	[°C]
Hot source outlet temperature	$T_{hot,out}$	80	[°C]
Cold source inlet temperature	$T_{cold,in}$	7	[°C]
Cold source outlet temperature	$T_{cold,out}$	4	[°C]

5.2.4 Case study C: Cabin air conditioning in helicopters

The case study C focuses on environmental control systems for helicopters, which mostly require cooling needs for the cabin air conditioning and for the windshield defogging. HP-ORCs are well suited for such an application for their high power density and for the free heat source provided by the engine exhaust gases. The target temperature in the cabin is 20°C and a constant outside temperature of 40°C is considered. Temperature differences of 10 and 5 K are assumed at the cold source and heat sink, respectively. The exhaust gases temperatures of a helicopter engine are typically in the range of 550°C [136]. However, due to the risk of organic fluid decomposition at high temperature, the ORC turbine inlet temperature is limited to 200°C [137]. The minimum exhaust gas outlet temperature is set to 150°C. The heat transfer units typically exchange with air, and hence PHEs are not suitable. They have been considered in a first approximation though. The required cooling capacities for the cabin air conditioning are between 6 and 9 kW [134, 135]. Table 5.5 summarizes the boundary conditions for this case study.

Table 5.5 – Boundary conditions of the case study C

Term	Symbol	Value	Unit
Cooling power	\dot{Q}_{cold}	9	[kW]
Heat sink inlet temperature	$T_{sink,in}$	40	[°C]
Heat sink outlet temperature	$T_{sink,out}$	45	[°C]
Hot source inlet temperature	$T_{hot,in}$	550	[°C]
Hot source outlet temperature	$T_{hot,out}$	150	[°C]
Cold source inlet temperature	$T_{cold,in}$	30	[°C]
Cold source outlet temperature	$T_{cold,out}$	20	[°C]

5.3 Multi-objective optimization

The CTU optimization has been developed towards a rotordynamic stability/efficiency trade-off, whereas the cycle optimization looks at a thermo-economic objective (performance and investment cost). Ideally, the new optimization stage considers three objectives to find the optimum designs addressing constraints of cost, rotordynamic stability, and performance. However, the cost of the CTU is negligible compared to the other HP-ORC components, provided that it is produced at large-scale. It follows that the CTU design variables have no impact on the cost function. Furthermore, the results presented in chapter 3 have suggested that the shaft and bearing variables have a limited effect on the system performance.

Hence, instead of considering the rotordynamic stability as an additional objective, imposing a stability threshold τ as a constraint is proposed. The CTU and thermodynamic models are subject to the limitations described in chapters 3 and 4, respectively. The new optimization problem is described by equation 5.1 and the schematic layout of the modeling procedure is represented in Figure 5.1. For the sake of simplification, only the COP is investigated here, calculated in heating mode (equation 1.2) for case studies A and B, and in cooling mode for the case study C (equation 1.3).

$$[\max(COP), \min(C_{Tot})] = f_{FullOpt}(G_{CTU}, G_{Thermo}), \Gamma_{CTU} \geq \tau \quad (5.1)$$

G_{CTU} represent the CTU design variables, and G_{Thermo} the thermodynamic cycle variables. τ is the minimum required rotordynamic stability threshold, set to $\tau=0.7$. Table 5.6 presents the design variables that have considered for the evaluation of the case studies. In light of the conclusions drawn in chapters 3 and 4, some variables have been removed for the sake of simplification and set as constant. For the radial and axial bearings, since the optimizer always tends to converge towards $\alpha_{rad,ax}$ values of 0.6 and γ_{rad} values of 0.9 (Figures 3.13 and 3.14), the latter have been removed from the optimization. For the same reasons, $\frac{L_{ax-rad}}{D_{shaft}}$ and $\frac{L_{rad-turb}}{D_{shaft}}$ have been both fixed at 0.2 (Figure 3.15). Compared to the optimizations performed in chapter 3 (see Table 3.3), the remaining CTU design variables have been extended in order to cope with the wider power ranges tested, in particular the shaft and axial bearing diameter D_{shaft} and D_{ax} . The turbomachinery diameters D_{comp} and D_{turb} are retrieved such as to optimize the CTU efficiency at each condition. For the cycle design variables, since the regenerator pinch presents a negligible impact on the thermo-economic trade-off (Figures 4.7 and 4.8), the latter has been fixed to 5 K.

Chapter 5. Application examples

Table 5.6 – Design variables of the multi-objective optimization

Component	Term	Range	Unit
Thermodynamic cycle variables G_{Thermo}			
Working fluid G_{Fluid}	F	Table 4.7	[-]
Heat ex- changers G_{HX}	$DT_{sh,turb}$	[10-100]	[K]
	$DT_{min,cond}$	[1-20]	[K]
	$DT_{min,evh}$	[1-20]	[K]
	$DT_{min,evo}$	[1-20]	[K]
	Is_{reg}	Yes/No	[-]
CTU variables G_{CTU}			
Radial Bearing G_{rad}	$\frac{D_{rad}}{D_{shaft}}$	[1-3]	[-]
	C_{rad}	[3.5-20]	[μm]
	H_{rad}	[1.1-5]	[-]
	β_{rad}	[110-170]	[deg]
Axial Bearing G_{ax}	D_{ax}	[10-60]	[mm]
	C_{ax}	[5-20]	[μm]
	H_{ax}	[1.1-5]	[-]
	β_{ax}	[110-170]	[deg]
Shaft G_{shaft}	D_{shaft}	[8-30]	[mm]
	$\frac{L_{rad-rad}}{D_{shaft}}$	[1-3]	[-]

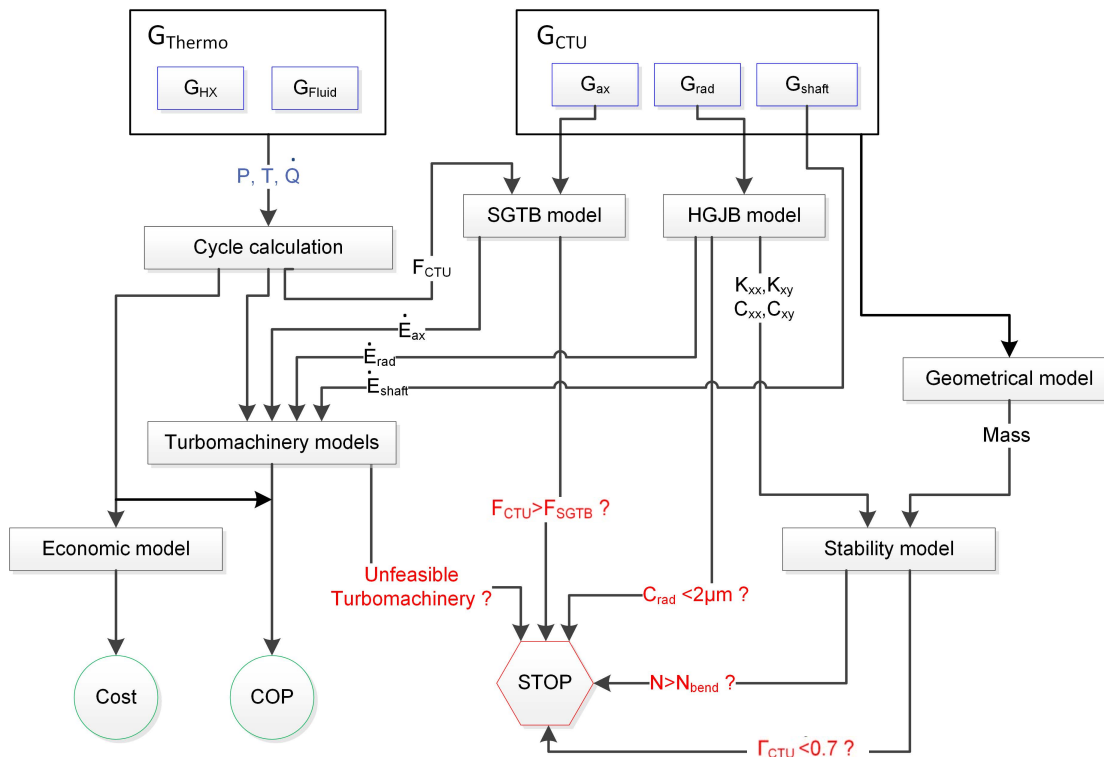


Figure 5.1 – Schematic layout of the optimization procedure

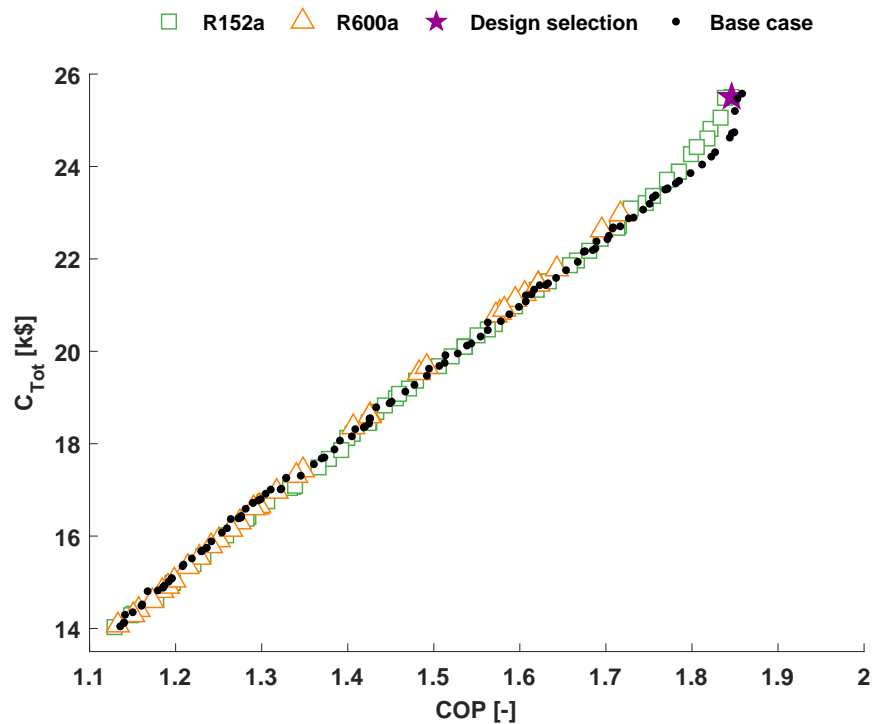


Figure 5.2 – Pareto curve of the case study A compared to the base case optimization shown in chapter 4 (Figure 4.10 - maximization of COP at $T_{hot,in}=180^{\circ}\text{C}$)

5.4 Results and discussion

5.4.1 Case study A

Figure 5.2 shows the Pareto front resulting from the full optimization procedure described above and applied to the case study A. It is compared with the purely thermo-economic based Pareto optimum presented in chapter 4 (annotated by "Base case"). The Pareto fronts are very similar, except at COPs above 1.76, where the base case Pareto front outperforms the present optimization case by 1%. Table 5.7 presents the optimum design variables of the full optimization (Full optim.) compared to the base case, for a COP of 1.85. Similarly to the results shown in chapter 4 (see Figure 4.10), R152a and R600a are the working fluids providing the best thermo-economic trade-off. For a COP of 1.85, the optimum CTU with the full optimization stage presents a rotordynamic stability of 0.81, rotates at 260 krpm and is composed of a 15.8 mm turbine and an 18.3 mm compressor. The optimum CTU design is very similar to the one of the baseline case presented in chapter 4. In light of these observations, the assumption made in chapter 4 claiming that the shaft and bearing variables can be neglected when considering a thermo-economic analysis, is thus justified. In other terms, this result shows that, under the assumptions and constraints of the proposed investigation, the thermo-economic and shaft optimizations can be performed separately.

Chapter 5. Application examples

Table 5.7 – Optimum design variables of the case study A for a COP target of 1.85

	Term	Full optim.	Base case	Unit
Performance indicators				
	COP	1.85	1.85	[-]
	C_{tot}	25.5	25.2	[k\$]
	Γ_{CTU}	0.81	-	[-]
Thermodynamic cycle variables G_{Thermo}				
Working fluid G_{Fluid}	F	R152a	R152a	[-]
Heat ex- changers G_{HX}	$DT_{sh,turb}$	55.7	42	[K]
	$DT_{min,cond}$	1	1	[K]
	$DT_{min,evh}$	1	1	[K]
	$DT_{min,evo}$	1.24	1	[K]
	Is_{reg}	Yes	Yes	[-]
CTU variables G_{CTU}				
Turbomachinery G_{turbo}	D_{turb}	15.8	15.8	[mm]
	D_{comp}	18.3	18.2	[mm]
	N	260	262	[krpm]
Radial Bearing G_{rad}	$\frac{D_{rad}}{D_{shaft}}$	1.23	-	[-]
	C_{rad}	3.53	-	[μm]
	H_{rad}	3.2	-	[-]
	β_{rad}	159	-	[deg]
Axial Bearing G_{ax}	D_{ax}	20.8	-	[mm]
	C_{ax}	9.7	-	[μm]
	H_{ax}	2.7	-	[-]
	β_{ax}	164.8	-	[deg]
Shaft G_{shaft}	D_{shaft}	8	-	[mm]
	$\frac{L_{rad-rad}}{D_{shaft}}$	1.36	-	[-]

As highlighted in the introduction (see Figure 1.1), a HP-ORC with a COP of 1.85 is a promising technology for domestic heating applications since it is highly competitive with conventional heating systems regarding operating cost and CO₂ emissions reductions (e.g., a HP-ORC using wood pellets as energy source reduces the CO₂ emissions by 96% compared to a conventional oil boiler).

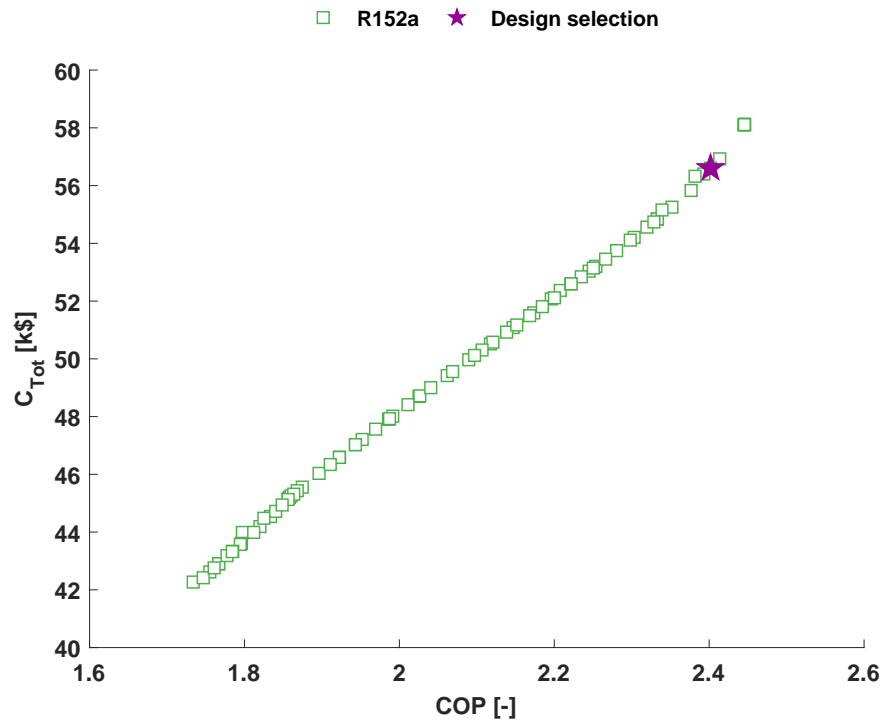


Figure 5.3 – Pareto curve of the case study B

5.4.2 Case study B

Figure 5.3 shows the Pareto front for the case study B. Similarly to the case study A, the optimizer found R152a to be the optimum working fluid. Note that due to the higher heating power considered, the total cost of the system corresponding to maximum COP is 2.3 times higher than for the case study A. Furthermore, since the target heating temperature is lower (20°C instead of 35°C for the case study A), the maximum COP is 1.3 times higher than for the case study A.

Table 5.8 presents the optimum design variables when a COP of 2.4 is targeted. Compared to the results of the case study A, a higher shaft diameter is found due to a larger compressor and turbine diameters. The CTU is also able to operate with a higher radial bearing clearance C_{rad} of 8.1 μm , due to a lower rotor speed. Finally, the axial bearing presents a higher diameter D_{ax} than the case study A. This is due to higher axial forces caused by higher turbomachinery diameters (D_{comp} and D_{turb}) and lower rotational speed N which decrease the SGTB axial load capacity.

Compared to gas and oil boilers, the CO₂ emissions and the fuel operating costs are reduced significantly with the HP-ORC. Figure 5.4 shows the cumulative fuel operating costs and the CO₂ emissions over 20 years of the greenhouse operation for different heating systems. Note that the case study considers a 750 m² greenhouse with a total energy consumption of 550

Chapter 5. Application examples

kWh/m²/year and a heating capacity of 113 kW. The CO₂ emissions and operating costs are compared based on oil, natural gas (NG), and wood pellets (WP) used as primary energy source and using the data given in Table 1.1. Boiler efficiencies are assumed at 0.95. The calculations do not consider the CO₂ injection in the greenhouse, which is estimated to 25 kg/m²/year to ensure a 20-25% growth enhancement¹. The results suggest that operating cost and CO₂ emissions reductions up to 60% can be achieved with a HP-ORC combined with conventional oil and gas boilers. In 2013, there are approximately 1'000 ha of agricultural greenhouses² in Switzerland, which are heated mostly by gas and oil boilers³. Retrofitting these boilers with a HP-ORC system would, therefore, represents a significant reduction of the CO₂ emissions inherent to the agricultural sector.

Table 5.8 – Optimum design variables of the case study B for a COP target of 2.4

	Term	Value	Unit
Performance indicators			
	COP	2.4	[-]
	C_{tot}	56.6	[k\$]
	Γ_{CTU}	0.75	[-]
Thermodynamic cycle variables G_{Thermo}			
Working fluid G_{Fluid}	F	R152a	[-]
Heat ex- changers G_{HX}	$DT_{sh,turb}$	30.6	[K]
	$DT_{min,cond}$	2.3	[K]
	$DT_{min,evh}$	1.21	[K]
	$DT_{min,evo}$	20.5	[K]
	Is_{reg}	Yes	[-]
CTU variables G_{CTU}			
Radial Bearing G_{rad}	$\frac{D_{rad}}{D_{shaft}}$	1.2	[-]
	C_{rad}	8.1	[μ m]
	H_{rad}	2.6	[-]
	β_{rad}	161.8	[deg]
Axial Bearing G_{ax}	D_{ax}	37.4	[mm]
	C_{ax}	17.6	[μ m]
	H_{ax}	2.6	[-]
	β_{ax}	161.5	[deg]
Shaft G_{shaft}	D_{shaft}	22	[mm]
	$\frac{L_{rad-rad}}{D_{shaft}}$	1	[-]
Turbomachinery G_{Turbo}	D_{turb}	27.4	[mm]
	D_{comp}	32.1	[mm]
	N	132	[krpm]

¹<http://www.crophouse.co.nz/>

²<http://www.gemuese.ch/>

³<https://www.news.admin.ch/newsd/message/attachments/38412.pdf>

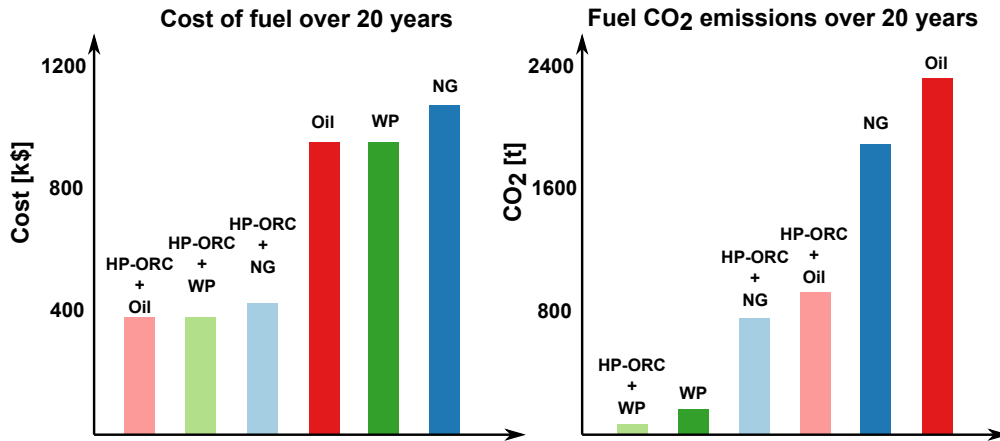


Figure 5.4 – Comparison of conventional heating systems with the HP-ORC technology for agricultural greenhouse heating

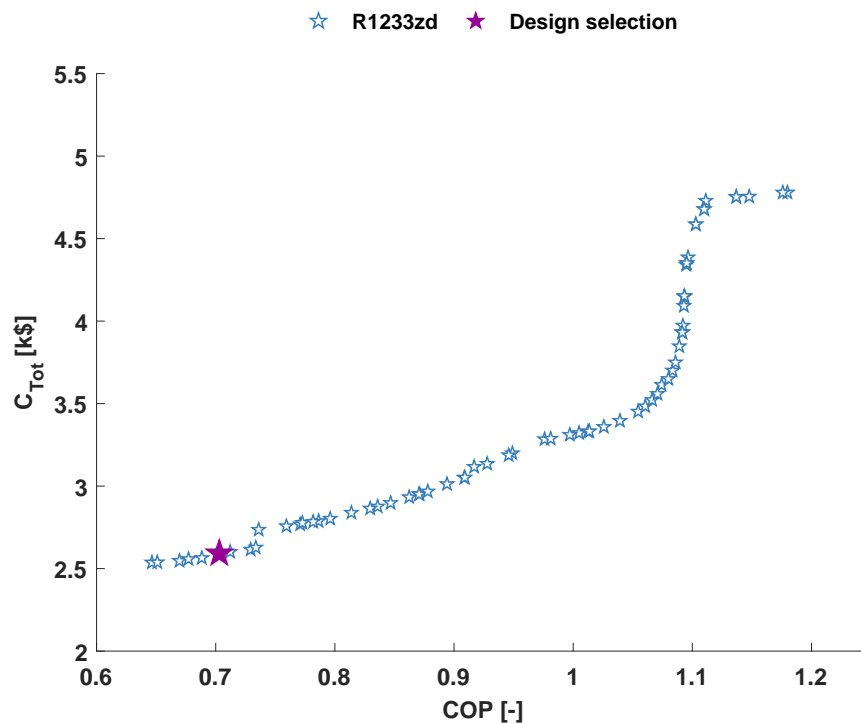


Figure 5.5 – Pareto curve of the case study C

5.4.3 Case study C

Figure 5.5 shows the Pareto front for the case study C. Note that the COP is calculated in cooling mode. Contrary to the case studies A and B, the optimum working fluid is R1233zd. Indeed, ORC-adapted working fluids, such as R1233zd and R245fa, are more suitable for the targeted application due to higher HP evaporator temperatures.

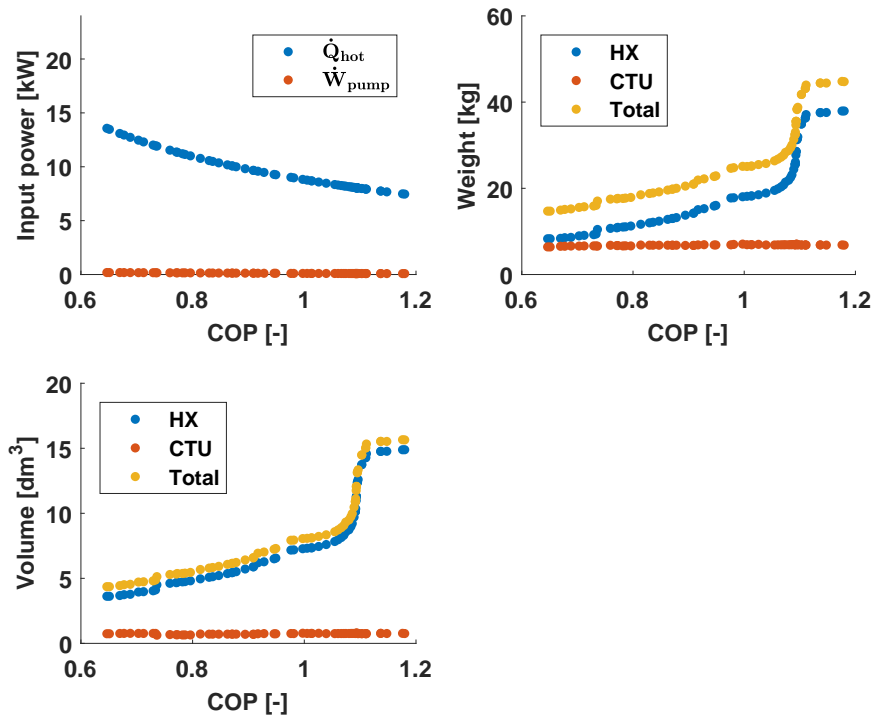


Figure 5.6 – HP-ORC power consumption, component weight, and component volume as a function of the COP

Figure 5.6 shows the required powers (electrical and thermal) to drive the HP-ORC and the HP-ORC components weight and volume as a function of the optimum COP. The heat exchanger weight and volume are calculated using their total heat transfer area, considering the geometry parameters shown in Table B.2 (Appendix B). For the estimation of the CTU volume, the following components are included: (1) The turbomachinery, (2) the shaft and bearings, (3) the shaft housing, and (4) the turbomachinery volutes. The turbomachinery, shaft and bearing volumes are retrieved from the Pareto optimum results - see Table 5.9. The shaft housing is assumed to be a cylinder with an outer diameter $D_{hous,o} = 4D_{shaft}$, an inner diameter $D_{hous,in} = D_{shaft}$, and a length $L_{hous} = L_{shaft}$. The turbomachinery volutes are approximated by cylinders with an outer diameter $D_{vol,o} = D_{hous}$, an inner diameter $D_{vol,in} = 0.5D_{turb,comp}$, and a length $L_{vol} = 4D_{turb,comp}$. The housing and volutes are made of stainless steel and the material of the other CTU components are described in Table 3.3.

The heating power \dot{Q}_{hot} ranges from 20 to 9 kW, while the pump electrical power consumption is ranging from 250 to 115 W. Considering that the helicopter engine has a nominal power between 700 and 1500 kW^{4 5} and an efficiency of 30% [138], it is assumed that the HP-ORC can operate on the whole range of COPs without affecting the engine performance.

⁴<https://www.safran-group.com/aviation/aircraft-engines-and-nacelles/helicopter-engines>

⁵<http://airbushelicoptersinc.com/products/overview.asp>

However, Figure 5.6 suggests that the system weight and volume, governed mainly by the heat exchangers, drastically increase with the system COP. It is thus recommended to select a design at a COP of 0.7, whose design variables are shown in Table 5.9.

Table 5.9 – Optimum design variables of the case study C for a COP target of 0.7

	Term	Value	Unit
Performance indicators			
	COP	0.7	[-]
	C_{tot}	2.6	[k\$]
	Γ_{CTU}	0.89	[-]
Thermodynamic cycle variables G_{Thermo}			
Working fluid G_{Fluid}	F	R1233zd	[-]
Heat ex- changers G_{HX}	$DT_{sh,turb}$	40.5	[K]
	$DT_{min,cond}$	8.8	[K]
	$DT_{min,evh}$	10.1	[K]
	$DT_{min,evo}$	50.1	[K]
	Is_{reg}	Yes	[-]
CTU variables G_{CTU}			
Radial Bearing G_{rad}	$\frac{D_{rad}}{D_{shaft}}$	1.5	[-]
	C_{rad}	3.5	[μm]
	H_{rad}	4.9	[-]
	β_{rad}	112.7	[deg]
Axial Bearing G_{ax}	D_{ax}	24	[mm]
	C_{ax}	7.9	[μm]
	H_{ax}	2.4	[-]
	β_{ax}	159.8	[deg]
Shaft G_{shaft}	D_{shaft}	14	[mm]
	$\frac{L_{rad-rad}}{D_{shaft}}$	1.8	[-]
Turbomachinery G_{Turbo}	D_{turb}	23.2	[mm]
	D_{comp}	32.6	[mm]
	N	95	[krpm]

At the selected design, the CTU weight and volume are of 6 kg and 0.75 dm³, respectively. To provide air conditioning to the helicopter cabin, the HP-ORC technology is of great interest compared to Electrically driven Heat Pumps (EDHPs). Indeed, compared to a EDHP with a COP of 3, the electrical power required to provide 9 kW air conditioning with a HP-ORC is decreased by 88%. Furthermore, since small-scale turbomachinery are more compact than scroll machines, a potential weight and volume reduction could be reached. Indeed, a conventional hermetic scroll compressor for 3 kW air conditioning, such as the ZR22K3E model for R134a from Emerson ⁶, presents a weight of 22 kg and a volume of 21.3 dm³. Based on the CTU scaling laws introduced above, the HP-ORC technology offers weight and size reductions in the order of 73% and 96%, respectively.

⁶<http://www.emersonclimate.com/europe/en-eu/Products/Compressors/>

5.4.4 Discussion

In this chapter, three different case studies have been investigated for the use of a HP-ORC based on gas bearing supported turbomachinery, showing promising results with regards to fuel consumption, CO₂ emissions, and weight/size reduction. In order to investigate more in-depth the potential of the considered case studies, additional analyses would be of great interest. The study of seasonal performances could be performed for the case studies A and B to find the best design that would match a full year of operation. Since weight and volume concerns are critical in the transportation sector, the case study C would gain in integrating these features as an objective as well. Furthermore, the case study C considers in a first approximation that the heat exchangers are PHEs, which is not best practice for exchanging with air and exhaust gases though. An appropriate design of a heat exchanger able to recover heat from the helicopter exhaust gases is here missing. Since finned-tube heat exchangers seem to be suitable candidates for recovering heat from car exhaust pipes [139, 140], they could replace the PHEs for such applications in future investigations. The cogeneration, which is one advantage of the HP-ORC technology, could be investigated as well and integrated into the optimization procedure.

Other applications of interest could also be studied. For instance, various industrial processes requiring both cooling and heating utilities could profit from such a technology. An interesting industrial case is the brewery process [141], which deals with available heat sources over 100°C, medium temperature requirements around 65 °C (e.g., mixing of malt with water) and cooling requirements below 6°C (e.g., fermentation). These processes are, however, usually performed by batch, which may not be suitable for HP-ORCs. Furthermore, most of these industrial applications operate at cooling and heating capacities above 300 kW, which is out of the scope of small-scale turbomachinery. Similarly, commercial buildings in which cooling and heating capacities are required are numerous, such as in shopping centers (e.g., floor heating and food cold chain) or ice skating rinks (e.g., heating of the locker rooms and ice maintenance). Additional case studies in the transportation sector could be investigated as well since HP-ORC based on small-scale turbomachinery are offering compact solutions. Air conditioning in cars and trucks using the power available at the exhaust gases could be explored. Refrigerated transports, such as trucks and fishing ships, are also applications of interest.

5.5 Summary and conclusions

A complete optimization method of the HP-ORC concept is proposed, which finds the designs offering the best thermo-economic trade-offs while guaranteeing sufficient rotordynamic stability. The methodology has been applied to three case studies: (A) 40 kW domestic heating at 35°C, (B) 113 kW agricultural greenhouse heating at 20°C, and (C) 9 kW cooling at 20°C in a helicopter cabin.

The case study A is the base case used throughout this thesis and the results show that the optimum COP/investment cost Pareto fronts are similar whether the rotordynamic stability is guaranteed or not. It follows that the assumption made in chapter 4, which did not include the shaft and bearing design for the HP-ORC thermo-economic optimization, is justified. For a heating COP of 1.85, the CTU presents a rotordynamic stability of 0.81, rotates at 260 krpm, and is composed of a 15.8 mm turbine and an 18.3 mm compressor. The optimum working fluid is R152a.

The results of the case study B show that a COP above 2.4 can be achieved for heating agricultural greenhouses, using R152a as the working fluid, and with a rotordynamic stability guaranteed at 0.75. Knowing that most of the agricultural greenhouses across Europe are heated by oil and gas boilers, the retrofitting into HP-ORCs would, therefore, represent a significant yearly reduction in fuel consumption and CO₂ emissions.

COPs in cooling mode over 1.2 are obtained for the case study C, which investigates a helicopter cabin AC system using the exhaust gases as the HP-ORC heat source. A design presenting relatively low efficiency (COP in cooling mode of 0.7) is recommended since (1) enough heat is available at the exhaust gases without affecting the engine performance, and (2) the weight and volume of the heat exchangers are reduced by 70% compared to the best COP solution. Furthermore, embedding HP-ORCs for helicopter cabin AC has an advantage over electrically driven heat pumps operating with conventional volumetric machines. Indeed, the electricity consumption can be decreased by 88% and the compressor weight and volume are expected to be reduced by 73% and 96% when compared to a conventional hermetic scroll compressor from the market.

6 Conclusions and future work

Concluding remarks

Electrically Driven Heat Pumps (EDHPs) play a significant role in reducing energy consumption in the domestic space heating sector. Nonetheless, since EDHPs rely entirely on electrical power, issues related to network overload at peak-time, high operating costs, and high electricity carbon intensity are encountered. A promising alternative to address these shortcomings is the use of Thermally Driven Heat Pumps (TDHPs), which are powered by a heat source instead of electricity. TDHPs offer the possibility of running with numerous types of heat sources and temperatures. Among TDHPs, literature usually refers to sorption heat pumps, ejectors, and Gas Engine driven Heat Pumps (GEHP). An alternative technology consists in the combination of an Organic Rankine Cycle (ORC) and a vapor compression Heat Pump (HP) cycle, in which the ORC turbine drives directly the HP compressor. This technology is of great interest since it provides high flexibility in the heat source selection, which can be low grade and renewable (in contrast to GEHPs) while offering the possibility of performing trigeneration (unlike sorption and ejectors systems). Domestic ORC expanders and HP compressors are nowadays dominated by volumetric machines for their high robustness and low cost. Nonetheless, dynamic machines are gaining interest, especially radial turbines and centrifugal compressors, since they offer higher power density and efficiency than volumetric machines. Furthermore, combining dynamic radial turbomachinery with self-acting gas bearings allows oil-free operation, reduced maintenance costs, and higher heat transfer efficiency. As a consequence of both the operational flexibility of ORC driven HPs and of the high potential of reduced scale turbomachinery, a HP-ORC based on gas bearing supported turbomachinery is investigated in this thesis, with the goal of exploring its potential and challenges.

Since HP-ORCs are complex thermodynamic and mechanical systems, a dedicated optimization procedure is implemented. It aims at providing the best-integrated system design while satisfying competitive objectives such as performance, investment cost, and feasibility.

Chapter 6. Conclusions and future work

In a first step, since quick and reliable turbomachinery pre-design tools are missing for small-scale refrigeration applications, updated reduced order models for radial turbines and centrifugal compressors are developed. From experimentally validated 1D models of a radial turbine and a centrifugal compressor, new polynomial pre-design models predicting the isentropic efficiency are performed, with goodness of fit presenting R^2 over 0.985 and RMSEs below 0.016. These models provide an alternative to the ones found in literature, by offering a higher level of design detail while being valid for small-scale ORC and refrigeration applications. By analyzing the aerodynamic phenomena and losses in radial turbines and centrifugal compressors, the reason why their isentropic efficiency contours have their characteristic shape is now more apprehended. In particular, the key turbomachinery dimensions that impact their performance have been identified, and hence, updated design guidelines for small-scale turbomachinery are provided. Finally, when compared to the use of the 1D code, it has been observed that the evaluation time is 1500 times faster with the updated pre-design models, while the variation between the two models stays below 2 and 4% for the turbine and compressor, respectively. Using the new reduced order models is, therefore, of great interest, in particular when embodied in complex integrated design optimization, which in practice require more than 100'000 evaluations for achieving a satisfactory convergence.

Using the turbomachinery models developed previously, the integrated design optimization of the Compressor Turbine Unit (CTU) has been performed in a second step. The design trade-offs between maximum efficiency and rotordynamic stability were investigated. The radial (Herringbone Grooved Journal Bearing HGJB) and axial (Spiral Grooved Thrust Bearings SGTB) gas bearing models used for the optimization were developed by Schiffmann [47]. New models for predicting the axial load of the CTU and the fluid leakage in a labyrinth seal are introduced. In order to assess the effect of the model complexity on the integrated design approach, the optimization procedure was divided into different levels of complexity and applied to the measured data performed by Demierre et al. [35] on a 40 kW ORC driven Heat Pump. Using the integrated design procedure, CTU efficiencies in excess of 60% have been achieved, representing a 20-pt efficiency gain compared to the proof of concept. The performance trade-off is governed mainly by the turbomachinery components, in particular the turbine and compressor shroud to tip radius ratios, while the rotordynamic stability is governed by the radial bearing and shaft design. Furthermore, it was shown that optimizations based on the 1D turbomachinery models offer only a 1-pt efficiency rise, at the penalty of obtaining the results within weeks instead of days compared to the optimizations based on the 0D turbomachinery models. Finally, the robustness of the optimum CTU design has been investigated. While the off-design effects on the CTU performance and stability are marginal, the tip and seal clearances have a significant impact on the CTU efficiency and need to be as small as possible. On the other hand, manufacturing errors related to the bearing design have a dramatic impact on the rotordynamic stability since discrepancies of few microns lead to systems that are unstable or unable to sustain the axial loads.

In a third step, the integrated design optimization of the HP-ORC thermodynamic cycle, which aims at finding the optimum thermo-economic trade-offs, has been performed. The best cycle

design variables are retrieved (working fluid and heat exchanger), yielding HP-ORC exergetic efficiencies in excess of 50% and COPs above 1.8. The results suggest that the selection of the best working fluid is primarily a function of the hot source temperature and of the performance indicator to optimize (R134a and R600a are the recommended working fluids to maximize the COP, while R245fa and R600a prevail when optimum exergetic efficiency is to be reached). In a second step, two configurations have been compared, where the ORC and HP loops are either coupled mechanically or electrically (two individual spindles with an electric machine each). While the electrically coupled HP-ORCs offer higher design and operational flexibility, these systems are thermo-economically less profitable than the mechanically coupled solution (14% less efficient and 16% more expensive on average). This is due to the addition of the electrical conversion elements, which decreases the CTU efficiency by 9-pt on the one hand, and to the higher investment costs caused by having two condensers and two high-speed spindles instead of one in the mechanically coupled HP-ORC. In addition, the HP-ORC has been compared to conventional absorption heat pumps. While Single Effect Absorption Heat Pumps (SEAHPs) are highly competitive at low temperature hot sources (<120°C), HP-ORCs outperform when the hot source temperature exceeds 150°C. Finally, the optimum HP-ORC solutions have been compared with prototype measurements. Using an integrated design optimization procedure, including optimum CTU, heat exchanger design, and cycle configuration, COP gains up to 24% are predicted when selecting a R600a based system and optimum CTU design.

In a final step, the optimization tools developed in this thesis have been applied to three case studies: Domestic heating, greenhouse heating, and air conditioning in helicopters. In this final optimization problem, the design of the CTU shaft and bearings is implemented as well, hence retrieving small-scale turbomachinery based HP-ORC designs which satisfy maximum performance and minimum cost while guaranteeing sufficient rotordynamic stability. Heating COPs in excess of 1.8 and 2.4 are found for domestic and greenhouse heating, hence offering a significant reduction in CO₂ emissions when retrofitting conventional gas/oil boilers with the HP-ORC technology. Cooling COPs above 1.2 are obtained for an AC system in a helicopter cabin using the exhaust gases as the heat source. However, a design presenting a cooling COP of 0.7 is recommended instead since more than enough heat rate is available at the exhaust gases without incurring significant engine losses while the weight and volumes of the heat exchangers are reduced by 70% compared to the best COP solution.

For domestic heating applications, two business models can be considered. The first solution consists in combining the HP-ORC with a conventional gas boiler, promoting a more environmentally friendly fuel heating system. This business model is already applied by the absorption heat pump manufacturer Robur¹. The second solution consists in driving the HP-ORC with the waste heat from a domestic cogeneration unit or fuel cell. Although it involves higher investment costs, such a system provides the electricity, heating, and cooling needs of a residential building with a more rational use of energy.

¹<http://www.robur.com/>

Future work

Small-scale gas bearing supported turbomachinery

In a first step, the reduced order models for small-scale gas bearing supported turbomachinery could gain in being investigated further. The presented pre-design models are based on 1D mean-line models, which consider enthalpy loss correlations that have not been extensively validated in the small-scale domain so far. Therefore, more experimental data on a broader range of compressor and turbine geometries, working fluids, and operating conditions are required. Furthermore, in order to improve the level of design detail and the accuracy of the turbomachinery pre-design models, other surrogate modeling techniques and procedures could be applied. For example, using a new set of predictors other than specific speeds and diameters that could capture the behavior of small-scale radial turbomachinery even better would be of great interest. Moreover, dedicated classification methods could be used to not only estimate the turbomachinery efficiency but also determine whether they are operating in unfeasible regions, such as choke, surge, and two-phase flows.

In a second step, investigations on heat transfer considerations in small-scale gas bearing supported turbomachinery could be performed. It would enable to gain more insights into the efficiency drop caused by the high temperature gradients between the compressor and the turbine. Ultimately, the heat transfer feature could even be part of the integrated design procedure. For this, however, reduced order models are required, which could be based either on thermal resistances or 2D finite element methods.

Another key element of gas bearing supported turbomachinery is the axial thrust bearing. However, an accurate estimation of the CTU axial load remains a challenge. In this thesis, a simple model based on strong assumptions is implemented. A more in-depth investigation is needed, for instance by performing streamline curvature and CFD analysis, which could lead to more accurate axial load models. In addition, dedicated experimental tests capturing the behavior of the axial thrust bearing when subject to a known axial load would be of great interest since it would allow predicting the CTU axial load during operation.

Finally, the integrated optimization procedure could be enhanced with additional features (heat transfer, fluid leakage, updated axial load model, different seal and bearing technologies) and new objectives. As shown in this thesis, although self-acting gas bearings are of great interest, they have limited robustness, especially when manufacturing errors occur. A new optimization procedure could include the robustness as an objective, and hence retrieve designs in which the tolerance ranges can be increased. It could be further linked to the manufacturing costs of gas bearing supported turbomachinery and thus being part of the thermo-economic optimization of the cycle.

HP-ORC modeling approach and applications

With the presented thermo-economic approach, further applications for HP-ORCs could be investigated. Since these systems operate with low grade heat sources, solar cooling applications could be considered, accounting for the seasonal performance throughout the year. Based on the same approach, a thermo-economic comparison between air source and ground source HP-ORCs could be made to select the technology that presents the best performance/cost trade-off. For this purpose, two-stage compression in the HP loop should be investigated as well. Also, since it is one of the advantages of HP-ORCs, the generation of electricity could be included in the thermo-economic trade-off.

The modeling of the HP-ORC could also be further improved by integrating the pressure drops in the pipes and the heat exchanger. The optimum plate heat exchanger geometry could be, therefore, incorporated into the optimization procedure.

Finally, other applications could be explored for the technology in which cooling, heating, and possibly electrical powers are required. In particular, the transport sector (refrigeration in trucks and ships), industrial processes (beer and metal processing), and commercial buildings (shopping centers, ice skating rinks,..) are of great interest. For these applications, different TDHP concepts (absorption, adsorption, and gas engine driven heat pumps) could be compared.

A Turbomachinery pre-design models

Radial turbine

The following 6th degree $\eta_{is} = f(Ns, Ds, PR)$ polynomial model is obtained for characterizing the turbine. Ns is the turbine specific speed (equation 2.1), Ds the specific diameter (equation 2.1), and PR the Pressure Ratio. This model is valid for a shroud to tip radius ratio $\epsilon = \frac{r_{6s}}{r_4} = 0.7$, for $Ns \in [0.2 - 1.2]$, $Ds \in [2.2 - 8.2]$, and $PR \in [1.5 - 8.5]$. The other models presented in this thesis can be found in Ref. [92].

$$\begin{aligned} \eta_{is} = & 9.183PR - 2.279PR^2 + 0.288PR^3 - 0.0266PR^4 + 0.002PR^5 + 9.12Ds - 2.507DsPR + 0.55DsPR^2 - \\ & 0.0422DsPR^3 + 0.00168DsPR^4 - 3.2 \cdot 10^{-7}DsPR^5 - 2.033Ds^2 + 0.153Ds^2PR - 0.0484Ds^2PR^2 + \\ & 0.0029Ds^2PR^3 - 0.00012Ds^2PR^4 + 0.269Ds^3 + 0.0119Ds^3PR + 0.0013Ds^3PR^2 + 6.3 \cdot 10^{-10}Ds^3PR^3 - \\ & 0.0216Ds^4 - 0.0014Ds^4PR - 1.4 \cdot 10^{-5}Ds^4PR^2 + 0.001Ds^5 + 3.4 \cdot 10^{-5}Ds^5PR + 133.66Ns - 44.83NsPR + \\ & 7.57NsPR^2 - 0.428NsPR^3 + 0.0113NsPR^4 + 1.8 \cdot 10^{-5}NsPR^5 - 76.394NsDs + 12.967NsDsPR - \\ & 1.871NsDsPR^2 + 0.0661NsDsPR^3 - 0.0017NsDsPR^4 + 18.11NsDs^2 + -0.973NsDs^2PR + 0.133NsDs^2PR^2 - \\ & 0.0004NsDs^2PR^3 - 2.124NsDs^3 + 0.0038NsDs^3PR - 0.00462NsDs^3PR^2 + 0.117NsDs^4 + 0.00198NsDs^4PR - \\ & 0.0024NsDs^5 - 360.1Ns^2 + 88.27Ns^2PR - 12.35Ns^2PR^2 + 0.462Ns^2PR^3 - 0.006Ns^2PR^4 + 217.2Ns^2Ds - \\ & 23.086Ns^2DsPR + 2.423Ns^2DsPR^2 - 0.0379Ns^2DsPR^3 - 47.256Ns^2Ds^2 + 1.47Ns^2Ds^2PR - \\ & 0.103Ns^2Ds^2PR^2 + 4.365Ns^2Ds^3 - 0.015Ns^2Ds^3PR - 0.143Ns^2Ds^4 + 367.45Ns^3 - 65.13514Ns^3PR + \\ & 7.637Ns^3PR^2 + -0.151Ns^3PR^3 - 227.3Ns^3Ds + 13.8174Ns^3DsPR - 0.925Ns^3DsPR^2 + 40.117Ns^3Ds^2 - \\ & 0.533Ns^3Ds^2PR - 2.13Ns^3Ds^3 - 112.98Ns^4 + 12.11Ns^4PR - 1.363Ns^4PR^2 + 90.92Ns^4Ds - \\ & 1.73Ns^4DsPR - 10.709Ns^4Ds^2 - 27.474Ns^5 + 1.83Ns^5PR + -8.603Ns^5Ds - 18.46 + 12.954Ns^6 - \\ & 1.8 \cdot 10^{-5}Ds^6 - 5.22 \cdot 10^{-5}PR^6 \end{aligned}$$

Centrifugal compressor

The following 5th degree $\eta_{is} = f(Ns, PR, \zeta, CR)$ polynomial model is obtained for characterizing a centrifugal compressor, where $\zeta = \frac{b_4}{r_4}$ is the blade height to tip radius ratio and $CR = \frac{e_{tp}}{b_4}$ the clearance ratio. This model is valid for a shroud to tip radius ratio $\epsilon = \frac{r_{2s}}{r_4} = 0.56$, for $Ns \in [0.2 - 1.5]$, $PR \in [1.5 - 5]$, $\zeta \in [0.015 - 0.3]$, and $CR \in [0.02 - 0.3]$. The other models presented in this thesis can be found in Ref. [93].

$$\begin{aligned} \eta_{is} = & 16.024CR - 41.566CR^2 - 293.18CR^3 + 1496.16CR^4 + 5.844\zeta - 153.02\zeta CR + 918.416442\zeta CR^2 - \\ & 2343.77\zeta CR^3 + 5172.68\zeta CR^4 - 38.883\zeta^2 + 454.86\zeta^2 CR - 5876.29\zeta^2 CR^2 - 1490.59\zeta^2 CR^3 + 152.09\zeta^3 - \\ & 677.48\zeta^3 CR + 12844.96\zeta^3 CR^2 - 393.47\zeta^4 - 544.57\zeta^4 CR + 0.416PR - 9.184PRCR + 46.9323PRCR^2 - \\ & 56.771PRCR^3 - 67.17PRCR^4 - 11.062PR\zeta + 67.821PR\zeta CR - 231.65PR\zeta CR^2 - 10.43PR\zeta CR^3 + \\ & 35.698PR\zeta^2 - 225.51PR\zeta^2 CR + 638.25PR\zeta^2 CR^2 - 129.69PR\zeta^3 + 388.96PR\zeta^3 CR + 166.07PR\zeta^4 - \\ & 0.128PR^2 + 1.744PR^2 CR - 6.811PR^2 CR^2 + 6.724PR^2 CR^3 + 2.733PR^2\zeta - 19.956PR^2\zeta CR + 42.63PR^2\zeta CR^2 - \\ & 13.443PR^2\zeta^2 + 62.976PR^2\zeta^2 CR + 21.832PR^2\zeta^3 + 0.0237PR^3 - 0.186PR^3 CR + 0.407PR^3 CR^2 - \\ & 0.319PR^3\zeta + 1.411PR^3\zeta CR + 0.723PR^3\zeta^2 - 0.0022PR^4 + 0.007PR^4 CR + 0.0105PR^4\zeta + 6.689Ns - \\ & 68.313NsCR + 239.8NsCR^2 + 43.39NsCR^3 - 1478.7NsCR^4 - 4.514Ns\zeta + 450.67Ns\zeta CR - 652.31Ns\zeta CR^2 - \\ & 683.016Ns\zeta CR^3 - 25.86Ns\zeta^2 - 476.93Ns\zeta^2 CR - 130.44Ns\zeta^2 CR^2 + 281.33Ns\zeta^3 + 29.913Ns\zeta^3 CR - \\ & 246.81Ns\zeta^4 + 0.456NsPR + 17.99NsPRCR - 108.68NsPRCR^2 + 201.35NsPRCR^3 + 12.94NsPR\zeta - \\ & 35.316NsPR\zeta CR + 215.73NsPR\zeta CR^2 + 59.124NsPR\zeta^2 - 205.04NsPR\zeta^2 CR - 105.04NsPR\zeta^3 - \\ & 0.31NsPR^2 + 0.821NsPR^2 CR - 0.326NsPR^2 CR^2 + 2.067NsPR^2\zeta - 13.947NsPR^2\zeta CR - 5.874NsPR^2\zeta^2 + \\ & 0.0406NsPR^3 - 0.131NsPR^3 CR - 0.0977NsPR^3\zeta - 0.00133NsPR^4 - 14.424Ns^2 + 69.17Ns^2 CR - \\ & 198.45Ns^2 CR^2 + 281.64Ns^2 CR^3 + 14.227Ns^2\zeta - 450.7Ns^2\zeta CR + 644.53Ns^2\zeta CR^2 - 134.92Ns^2\zeta^2 + \\ & 595.16Ns^2\zeta^2 CR + 69.42Ns^2\zeta^3 - 1.512Ns^2 PR - 11.19Ns^2 PRCR + 22.82Ns^2 PRCR^2 - 32.146Ns^2 PR\zeta + \\ & 78.44Ns^2 PR\zeta CR + 18.9Ns^2 PR\zeta^2 - 0.0104Ns^2 PR^2 + 1.144Ns^2 PR^2 CR + 0.772Ns^2 PR^2\zeta - 0.0023Ns^2 PR^3 + \\ & 15.14Ns^3 - 26.81Ns^3 CR + 23.12Ns^3 CR^2 + 24.24Ns^3\zeta + 38.96Ns^3\zeta CR + 19.46Ns^3\zeta^2 + 3.44Ns^3 PR - \\ & 3.63Ns^3 PRCR + 7.43Ns^3 PR\zeta - 0.073Ns^3 PR^2 - 10.75Ns^4 + 10.79Ns^4 CR - 10.8Ns^4\zeta - 1.254Ns^4 PR - \\ & 0.509 + 3.105Ns^5 + 8.15 \cdot 10^{-5} PR^5 + 319.75\zeta^5 - 1345.12CR^5 \end{aligned}$$

B Plate Heat Exchanger design

PHE geometry parameters

In a first approximation, typical geometry parameters of PHEs have been set to each transfer unit according to the literature [115, 116]. They are summarized in Table B.1.

Table B.1 – Geometry parameters of the Plate Heat Exchangers common to each transfer unit

Term	Symbol	Value	Unit
Channel spacing	b	1	[mm]
Plate thickness	δ	0.5	[mm]
Chevron angle	β	30	[deg]
Wavelength of surface corrugation	Λ	4	[mm]
Plate thermal conductivity	k_{PHE}	15	[W.m ⁻¹ .K ⁻¹]
Material	Stainless Steel		

Table B.2 – Geometry parameters of the Plate Heat Exchangers specific to each transfer unit as designed by SWEPI¹

Term	Symbol	Unit	Cond.	ORC evap.	HP evap.	Regen.
Plate width	W	[mm]	243	119.5	119.5	117.5
Plate length	L	[mm]	393	377	526	287
Number of channels	N_{ch}	[-]	50	20	30	9
Inlet temperature (hot)	$T_{in,hs}$	[°C]	61.35	160	5	92
Outlet temperature (hot)	$T_{out,hs}$	[°C]	32.15	125	2	50
Inlet temperature (cold)	$T_{in,cs}$	[°C]	61.35	30	-0.9	34
Outlet temperature (cold)	$T_{out,cs}$	[°C]	35	148.9	2.13	62
Cond./evap. temperature	$T_{cond,evap}$	[°C]	35.36	100	-0.9	-
Mass flow rate	\dot{m}	[g.s ⁻¹]	200	92	91	92
Working fluid	F	[-]	R134a			

Appendix B. Plate Heat Exchanger design

Table B.2 shows the PHE overall dimensions used to estimate the PHE heat transfer areas in chapter 4. These dimensions are based on calculations made by SWEP¹ for the ORC evaporator (ORC evap.)², HP-ORC condenser (Cond.)³, HP evaporator (HP evap.)⁴, and regenerator (Regen.)⁵. The thermodynamic conditions at which these PHEs have been designed are also indicated.

These calculations are only valid for a coupled HP-ORC configuration. In the uncoupled configuration, since the condenser is divided into two distinct units, the plate width has been decreased to 121.5 mm. Similarly, the SEAHP absorber and condenser have been simulated with a width of 121.5 mm. For the case studies A and C of chapter 5, the geometry parameters of Table B.2 have been applied since similar power scales are simulated. In the case study B, where 113 kW heating is targeted, every heat transfer unit width has been multiplied by a factor 2.83 to account for the increased power scale.

Pressure drops

The optimization methodology of chapter 4 considers that the pressure drops in the heat exchanger units are negligible. To verify this statement, the pressure drops have been estimated in each heat transfer unit for the optimum Pareto designs defined by the dominant working fluids R152a and R600a (maximum COP at $T_{hot,in}=180^{\circ}\text{C}$ - see Figure 4.9). The pressure drop correlation proposed by Amalfi et al. [142] has been used for the two-phase flow regime since it fitted at best the pressure drops estimated by SWEP. The correlation of Martin has been used for evaluating the pressure drops in single-phase regimes [118]. Figure B.1 shows the computed pressure drops along the optimum Pareto curves. The maximum pressure drops occur in the HP evaporator and in the regenerator but always stay below 13 kPa. Figure B.2 shows the influence of the pressure drops on the cycle performance along the Pareto curves for R152a and R600a. The results suggest that the estimated pressure drops have only a negligible effect (below 1.5%) on the system performance. Assuming isobaric heat exchanges is, therefore, justified.

¹<https://www.swep.net/products/>

²SWEP reference: B18Hx41/1P-SC-U

³SWEP reference: B35TH0x101/1P-SC-M

⁴SWEP reference: F80ASHx61/1P-SC-M

⁵SWEP reference: B12Hx20/1P-SC-S

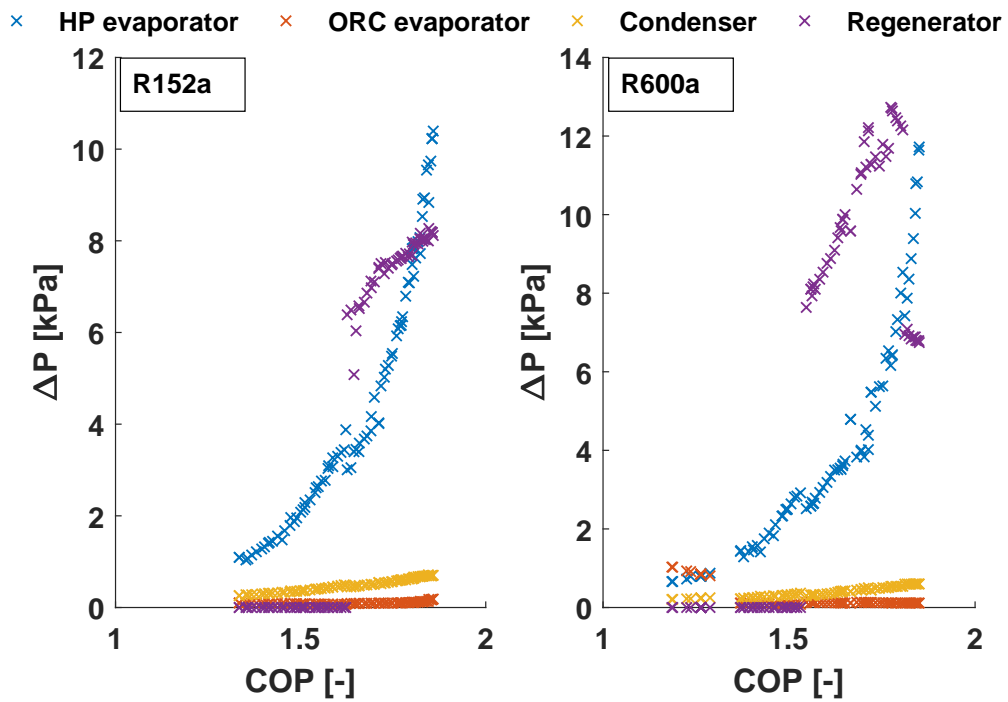


Figure B.1 – Pressure drops occurring in the HP-ORC heat transfer units

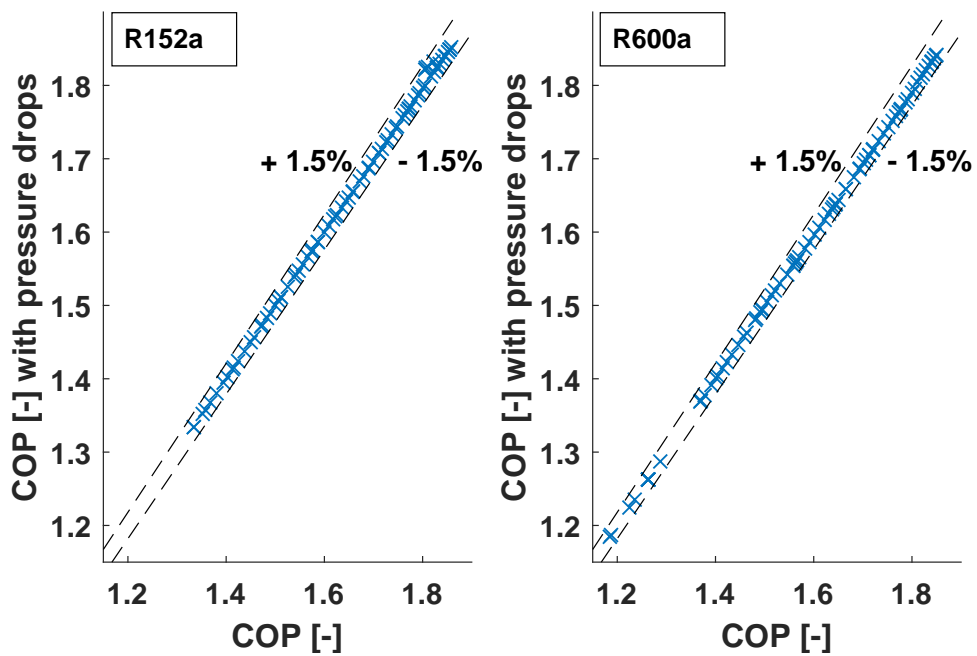


Figure B.2 – Influence of the pressure drop on the HP-ORC performance when the COP is maximized at 180°C

C Heat and mass transfer correlations

Table C.1 – Nusselt number correlations used for the different flow regimes/heat transfer processes occurring in the HP-ORC

Flow condition	Correlation	Reference
Single-phase	$Nu = \frac{Nuh}{\phi}$ $Nuh = 0.122Pr^{0.333} \left(\frac{\mu_b}{\mu_w} \right)^{0.167} (fRe^2 \sin 2\beta)^{0.374}$	Martin [118]
Condensation	$Nu = 4.118Re^{0.4} Pr^{0.333}$ $Re = \frac{G_{eq}d_h}{\mu_l}$ $G_{eq} = G \left(1 - x_m + x_m \sqrt{\frac{\rho_l}{\rho_v}} \right) \quad G = \frac{\dot{m}}{N_{ch}bW}$	Yan et al. [120]
Evaporation	$0.025 < Re_s \leq 0.25 \quad Nu = 3Re_v^{0.3} Bd^{0.33}$ $0.25 < Re_s < 2.5 \quad Nu = 4.2Re_v^{0.3} Bd^{0.33} Re_s^{0.2}$ $Bd = \frac{g\rho_l d_h^2}{\sigma}$ $Re_s = \frac{q'' d_h}{\Delta h_{lat} \mu_l}$ $Re_v = \frac{Gx d_h}{\mu_v}$	Danilova et al. [121]

Appendix C. Heat and mass transfer correlations

Table C.2 – Nusselt and Sherwood number correlations used for the different flow regimes/heat and mass transfer processes occurring in the SEAHP

Flow condition	Correlation	Reference
Absorber	$Nu = 3.133 Re_s^{0.2519} Re_v^{0.2995} \left(\frac{\Delta c}{c_s}\right)^{0.08636} \left(\frac{\Delta T}{T_s}\right)^{0.06851}$ $Sh = 43.57 Re_s^{0.0403} Re_v^{0.2865} \left(\frac{\Delta c}{c_s}\right)^{0.0462}$	Lee et al. [129]
Generator	$u_{ref} = -111.88 u_l + 11.848$ $u_v = \frac{Gx}{\rho_v} \qquad u_l = \frac{G(1-x)}{\rho_l}$ $Bo = \frac{q''}{\Delta h_{lat} G} \qquad X_{tt} = \frac{u_l}{u_v \left(\frac{\rho_v}{\rho_l}\right)^{0.5}}$ $Nu = \frac{5Bo h_l d_h}{k_l} \qquad u_v \leq u_{ref}$ $Nu = \left(1 + \frac{3}{X_{tt}} + \frac{1}{X_{tt}^2}\right)^2 \frac{h_l d_h}{k_l} \qquad u_v > u_{ref}$	Tàboas et al. [130]
Rectifier	$Nu = 0.951 \left(\frac{\rho_l (\rho_l - \rho_v) g q'' L}{\mu_l \Delta h_{lat}}\right)^{0.333} d_h$	Qaswari et al. [128]

Bibliography

- [1] IEA, “Key World Energy 2014 Statistics,” tech. rep., 2014.
- [2] J. Demierre, *Theoretical and Experimental Study of Thermally Driven Heat Pump Based on a Double Organic Rankine Cycle*. Ph.d. thesis, Ecole Polytechnique Fédérale de Lausanne, 2012.
- [3] L. Borel and D. Favrat, *Thermodynamique et énergétique*. No. 1, Presses Polytechniques et Universitaires Romandes, 2005.
- [4] J. Labus, C. Bruno, and A. Coronas, “Review on absorption technology with emphasis on small capacity absorption machines,” *Thermal Science*, vol. 17, no. 3, pp. 739–762, 2013.
- [5] Y. Chen, W. Han, and H. Jin, “Proposal and analysis of a novel heat-driven absorption–compression refrigeration system at low temperatures,” *Applied Energy*, vol. 185, no. 2, pp. 2106–2116, 2015.
- [6] W. Wu, B. Wang, W. Shi, and X. Li, “Absorption heating technologies: A review and perspective,” *Applied Energy*, vol. 130, pp. 51–71, 2014.
- [7] S. Wu and I. Eames, “Innovations in vapour-absorption cycles,” *Applied Energy*, vol. 66, no. 3, pp. 251–266, 2000.
- [8] P. Schossig, “Thermally driven heat pumps (Foreword),” *IEA Heat Pump Center Newsletter*, vol. 29, no. 1, pp. 18–22, 2011.
- [9] A. Fangmeier, A. Hadwiger-Fangmeier, L. Van der Eerden, and H.-J. Jäger, “Effects of atmospheric ammonia on vegetation : a review,” *Environmental Pollution*, vol. 86, pp. 43–82, 1994.
- [10] W. J. Visek, “Ammonia: its effects on biological systems, metabolic hormones, and reproduction.,” *Journal of Dairy Science*, vol. 67, no. 3, pp. 481–98, 1984.
- [11] S. Dasarathy, R. P. Mookerjee, V. Rackayova, V. R. Thrane, B. Vairappan, P. Ott, and C. F. Rose, “Ammonia toxicity: From head to toe?,” *Metabolic brain disease*, vol. 32, no. 2, pp. 529–538, 2017.

Bibliography

- [12] M. Khamooshi, K. Parham, and U. Atikol, "Overview of ionic liquids used as working fluids in absorption cycles," *Advances in Mechanical Engineering*, vol. 5, p. 620592, 2013.
- [13] K. Annett and F. Ziegler, *Thermally Driven Heat Pumps for Heating and Cooling*. Universitätsverlag der TU Berlin, 2013.
- [14] A. Selvaraju and A. Mani, "Experimental investigation on R134a vapour ejector refrigeration system," *International Journal of Refrigeration*, vol. 29, no. 7, pp. 1160–1166, 2006.
- [15] G. K. Alexis, "Estimation of ejector's main cross sections in steam-ejector refrigeration system," *Applied Thermal Engineering*, vol. 24, no. 17-18, pp. 2657–2663, 2004.
- [16] X. Chen, S. Omer, M. Worall, and S. Riffat, "Recent developments in ejector refrigeration technologies," *Renewable and Sustainable Energy Reviews*, vol. 19, pp. 629–651, 2013.
- [17] J. Yu, H. Chen, Y. Ren, and Y. Li, "A new ejector refrigeration system with an additional jet pump," *Applied Thermal Engineering*, vol. 26, no. 2-3, pp. 312–319, 2006.
- [18] L. Kairouani, M. Elakhdar, E. Nehdi, and N. Bouaziz, "Use of ejectors in a multi-evaporator refrigeration system for performance enhancement," *International Journal of Refrigeration*, vol. 32, no. 6, pp. 1173–1185, 2009.
- [19] A. Sözen, M. Özalp, and E. Arcaklıoğlu, "Prospects for utilisation of solar driven ejector-absorption cooling system in Turkey," *Applied Thermal Engineering*, vol. 24, no. 7, pp. 1019–1035, 2004.
- [20] M. Sokolov and D. Hershgal, "Solar-powered compression enhanced ejector air conditioner," *Solar Energy*, vol. 51, no. 3, pp. 183–194, 1993.
- [21] Y. Zhu, W. Cai, C. Wen, and Y. Li, "Simplified ejector model for control and optimization," *Energy Conversion and Management*, vol. 49, no. 6, pp. 1424–1432, 2008.
- [22] A. Hepbasli, Z. Erbay, F. Icier, N. Colak, and E. Hancioglu, "A review of gas engine driven heat pumps (GEHPs) for residential and industrial applications," *Renewable and Sustainable Energy Reviews*, vol. 13, no. 1, pp. 85–99, 2009.
- [23] J. Brenn, P. Soltic, and C. Bach, "Comparison of natural gas driven heat pumps and electrically driven heat pumps with conventional systems for building heating purposes," *Energy and Buildings*, vol. 42, no. 6, pp. 904–908, 2010.
- [24] D. Strong, *Development of a Directly Fired Domestic Heat Pump*. Ph.d thesis, University of Oxford, UK, 1980.
- [25] F. Biancardi, J. Sitler, and G. Melikian, "Development and test of solar heating and cooling systems," *International Journal of Refrigeration*, vol. 5, no. 6, pp. 351–360, 1982.

- [26] S. Kaushik, A. Dubey, and M. Singh, "Steam Rankine Cycle Cooling system: Analysis and Possible Refinements," *Energy Conversion and Management*, vol. 35, no. 10, pp. 871–886, 1994.
- [27] J. Jeong and Y. T. Kang, "Analysis of a refrigeration cycle driven by refrigerant steam turbine," *International Journal of Refrigeration*, vol. 27, no. 1, pp. 33–41, 2004.
- [28] S. Aphornratana and T. Sriveerakul, "Analysis of a combined Rankine–vapour–compression refrigeration cycle," *Energy Conversion and Management*, vol. 51, no. 12, pp. 2557–2564, 2010.
- [29] H. Li, X. Bu, L. Wang, Z. Long, and Y. Lian, "Hydrocarbon working fluids for a Rankine cycle powered vapor compression refrigeration system using low-grade thermal energy," *Energy and Buildings*, vol. 65, pp. 167–172, 2013.
- [30] J. Demierre, D. Favrat, J. Schiffmann, and J. Wegele, "Experimental investigation of a Thermally Driven Heat Pump based on a double Organic Rankine Cycle and an oil-free Compressor-Turbine Unit," *International Journal of Refrigeration*, vol. 44, pp. 91–100, 2014.
- [31] D. Prigmore and R. Barber, "Cooling with the sun's heat: Design considerations and test data for a Rankine Cycle prototype," *Solar Energy*, vol. 17, no. 3, pp. 185–192, 1975.
- [32] H. Wang, R. Peterson, and T. Herron, "Design study of configurations on system COP for a combined ORC (organic Rankine cycle) and VCC (vapor compression cycle)," *Energy*, vol. 36, no. 8, pp. 4809–4820, 2011.
- [33] R. L. Amalfi, F. Vakili-Farahani, and J. R. Thome, "Flow boiling and frictional pressure gradients in plate heat exchangers: part 1, review and experimental database," *International Journal of Refrigeration*, vol. 61, pp. 166–184, 2015.
- [34] S. Kakaç, H. Liu, and A. Pramuanjaroenkij, *Heat Exchangers: Selection, Rating, and Thermal Design*. Boca Raton, FL: CRC Press, second ed., 2002.
- [35] J. Demierre, A. Rubino, and J. Schiffmann, "Modeling and Experimental Investigation of an Oil-Free Microcompressor-Turbine Unit for an Organic Rankine Cycle Driven Heat Pump," *Journal of Engineering for Gas Turbines and Power*, vol. 137, no. 3, p. 032602, 2015.
- [36] P. Colonna, E. Casati, C. Trapp, T. Mathijssen, J. Larjola, T. Turunen-Saaresti, and A. Uusitalo, "Organic Rankine Cycle Power Systems: From the Concept to Current Technology, Applications, and an Outlook to the Future," *Journal of Engineering for Gas Turbines and Power*, vol. 137, no. 10, p. 100801, 2015.
- [37] R. Zanelli and D. Favrat, "Experimental Investigation of a Hermetic Scroll Expander Generator," in *12th International Compressor Engineering Conference*, (Purdue University, USA), pp. 459–464, 1994.

Bibliography

- [38] M. Zehnder, *Efficient air-water heat pumps for high temperature lift residential heating, including oil migration aspects*. PhD thesis, Ecole Polytechnique Fédérale de Lausanne, 2004.
- [39] E. Bandarra-Filho, L. Chen, and J. Thome, “Flow boiling characteristics and flow pattern visualization of refrigerants/lubricant oil mixture,” *International Journal of Refrigeration*, vol. 32, no. 2, pp. 185–202, 2009.
- [40] K. Spindler and E. Hahne, “The influence of oil on nucleate pool boiling heat transfer,” *Heat and Mass Transfer*, vol. 45, pp. 979–990, 2009.
- [41] S. Quoilin, M. V. D. Broek, S. Declaye, P. Dewallef, and V. Lemort, “Techno-economic survey of organic rankine cycle (ORC) systems,” *Renewable and Sustainable Energy Reviews*, vol. 22, pp. 168–186, 2013.
- [42] J. Schiffmann, “Enhanced Groove Geometry for Herringbone Grooved Journal Bearings,” *Journal of Engineering for Gas Turbines and Power*, vol. 135, no. 10, p. 102501, 2013.
- [43] J. Schiffmann and D. Favrat, “Integrated Design and Optimization of Gas Bearing Supported Rotors,” *Journal of Mechanical Design*, vol. 132, no. 5, p. 051007, 2010.
- [44] D. Fuller, “A Review of the State-of-the-Art for the Design of Self-Acting Gas-Lubricated Bearings,” *Journal of Lubrication Technology*, vol. 91, no. 1, pp. 1–16, 1969.
- [45] S. Malanoski, “Experiments on an Ultra-Stable Gas Journal Bearing,” *Journal of Lubrication Technology*, pp. 433–438, 1965.
- [46] J. Schiffmann and D. Favrat, “Design, experimental investigation and multi-objective optimization of a small-scale radial compressor for heat pump applications,” *Energy*, vol. 35, no. 1, pp. 436–450, 2010.
- [47] J. Schiffmann, *Integrated Design, Optimization and Experimental Investigation of a Direct Driven Turbocompressor for Domestic Heat Pumps*. PhD thesis, Ecole Polytechnique Fédérale de Lausanne, 2008.
- [48] G. Leyland, *Multi-Objective optimization applied to industrial energy problems*. PhD thesis, Ecole Polytechnique Fédérale de Lausanne, 2002.
- [49] A. Molyneaux, G. Leyland, and D. Favrat, “Environomic multi-objective optimisation of a district heating network considering centralized and decentralized heat pumps,” *Energy*, vol. 35, no. 2, pp. 751–758, 2010.
- [50] J. Bao and L. Zhao, “A review of working fluid and expander selections for organic Rankine cycle,” *Renewable and Sustainable Energy Reviews*, vol. 24, pp. 325–342, 2013.
- [51] F. Heberle and D. Brüggemann, “Exergy based fluid selection for a geothermal Organic Rankine Cycle for combined heat and power generation,” *Applied Thermal Engineering*, vol. 30, no. 11-12, pp. 1326–1332, 2010.

- [52] T. Hung, T. Shai, and S. Wang, "A review of organic Rankine cycles (ORCs) for the recovery of low-grade waste heat," *Energy*, vol. 22, no. 2, pp. 661–667, 1997.
- [53] B. Saleh, G. Koglbauer, M. Wendland, and J. Fischer, "Working fluids for low-temperature organic Rankine cycles," *Energy*, vol. 32, no. 7, pp. 1210–1221, 2007.
- [54] B. F. Tchanche, G. Papadakis, G. Lambrinos, and A. Frangoudakis, "Fluid selection for a low-temperature solar organic Rankine cycle," *Applied Thermal Engineering*, vol. 29, no. 11-12, pp. 2468–2476, 2009.
- [55] P. A. Domanski, J. Steven Brown, J. Heo, J. Wojtusiak, and M. O. McLinden, "A thermodynamic analysis of refrigerants: Performance limits of the vapor compression cycle," *International Journal of Refrigeration*, vol. 38, pp. 71–79, 2014.
- [56] V. Mounier, L. C. Mendoza, and J. Schiffmann, "Thermo-economic optimization of an ORC driven heat pump based on small scale turbomachinery and comparison with absorption heat pumps," *International Journal of Refrigeration*, vol. 81, pp. 96–110, 2017.
- [57] O. Balje, *Turbomachines : a guide to design, selection and theory*. John Wiley & Sons, 1981.
- [58] O. Cordier, *Ähnlichkeitsbedingungen für Strömungsmaschinen*. VDI Bericht 3, 1955.
- [59] M. Casey, C. Zwissig, and C. Robinson, "The Cordier line For Mixed Flow Compressors," in *ASME Turbo Expo 2010: Power for Land, Sea and Air*, vol. 7, pp. 1859–1869, 2010.
- [60] L. Bommers, J. Fricke, and R. Grundmann, *Ventilatoren*. Essen, Germany: Vulkan-Verlag, 2002.
- [61] J. Gülich, *Centrifugal Pumps*. Berlin, Germany: Springer, 2008.
- [62] M. V. Casey and F. Marty, "Centrifugal Compressors – performance at design and off-design," in *Proceedings of the Institute of Refrigeration*, (London), 1985.
- [63] R. Capata and E. Sciubba, "Experimental fitting of the re-scaled Balje maps for low-reynolds radial turbomachinery," *Energies*, vol. 8, no. 8, pp. 7986–8000, 2015.
- [64] Y. Gong, B. Sirakov, A. Epstein, and C. Tan, "Aerothermodynamics of Micro-Turbomachinery," in *ASME Turbo Expo 2004, Power for Land, Sea and Air*, pp. 95–102, 2004.
- [65] B. Sirakov, *Characterization and Design of a Non-Adiabatic Micro-Compressor Impeller and Preliminary Design of Self Sustained Micro Engine System*. Ph.d thesis, Massachusetts Institute of Technology, 2005.
- [66] K. Rahbar, S. Mahmoud, R. K. Al-Dadah, and N. Moazami, "Parametric analysis and optimization of a small-scale radial turbine for Organic Rankine Cycle," *Energy*, vol. 83, pp. 696–711, 2015.

Bibliography

- [67] L. Da Lio, G. Manente, and A. Lazzaretto, "New efficiency charts for the optimum design of axial flow turbines for organic Rankine cycles," *Energy*, vol. 77, pp. 447–459, 2014.
- [68] L. Da Lio, G. Manente, and A. Lazzaretto, "Predicting the optimum design of single stage axial expanders in ORC systems: Is there a single efficiency map for different working fluids?," *Applied Energy*, vol. 167, pp. 44–58, 2016.
- [69] A. Forrester, A. Sobester, and A. Keane, *Engineering Design via Surrogate Modelling: A Practical Guide*. John Wiley & Sons, 2008.
- [70] M. Schmidt and H. Lipson, "Distilling Free-Form Natural Laws from Experimental Data," *Science*, vol. 324, no. 5923, pp. 81–85, 2009.
- [71] K. Bamberger and T. Carolus, "A novel optimization based design method for centrifugal fans," *12th European Conference on Turbomachinery Fluid Dynamics and Thermodynamics, ETC 2017*, pp. 1–12, 2017.
- [72] E. Macchi and A. Perdichizzi, "Efficiency Prediction for Axial-Flow Turbines Operating with Nonconventional Fluids," *ASME. J. Eng. Power.*, vol. 103, no. 4, pp. 718–724, 1981.
- [73] *MATLAB*. The MathWorks, Natick, MA, USA, 2013.
- [74] H. Moustapha, M. Zelesky, N. Baines, and D. Japikse, *Axial and radial turbines*. USA: White River Junction, 2003.
- [75] J. Baets, O. Bernard, T. Gamp, and M. Zehnder, "Design and performance of ABB turbocharger TPS57 with variable turbine geometry," *Turbocharging and Air Management Systems I Mech E*, pp. 315–325, 1998.
- [76] C. Wasserbauer and A. Glassman, "FORTRAN program for predicting the off-design performance of radial inflow turbines Tech. Rep TN-8063," tech. rep., NASA, 1975.
- [77] H. Rohlik, *Radial Inflow Turbines*. NASA SP 290, 1975.
- [78] S. Futral and C. Wasserbauer, "Off-design performance prediction with experimental verification of a radial inflow turbine. Tech. Rep TN D-2621," tech. rep., NASA, 1965.
- [79] R. Benson, "A review of methods for assessing loss coefficients in radial gas turbines," *International Journal of Mechanical Sciences*, vol. 12, no. 10, pp. 905–932, 1970.
- [80] K. Rosset, V. Mounier, E. Guenat, O. Pajot, and J. Schiffmann, "Potential of Small-Scale Turbomachinery for Waste Heat Recovery on Automotive Internal Combustion Engines," in *3rd International Seminar on ORC Power Systems*, (Brussels), pp. 1–10, 2015.
- [81] M. Galvas, "Fortran program for predicting off design performance of centrifugal compressors, Tech.Rep TN D-7487," tech. rep., NASA, 1973.
- [82] N. Baines, *Fundamentals of Turbocharging*. Concepts NREC, 2005.

- [83] W. Jansen, "A method for calculating the flow in centrifugal compressor impeller when entropy gradients are present," in *Royal Society conference on internal aerodynamics (turbomachinery)*, 1967.
- [84] J. Coppage, F. Dallenbach, H. Eichenberger, G. Hlavaka, E. Knoernschild, and N. Le, "Study of supersonic radial compressors for refrigeration and pressurization systems, Tech.Rep TR 55-257," tech. rep., WADC, 1956.
- [85] J. Brasz, "Investigation into the effect of tip clearance on centrifugal compressor performance," *ASME Paper 88-GT-190*, 1988.
- [86] C. Rodgers, "Impeller stalling as influenced by diffusion limitations," *Journal of Fluids Engineering*, pp. 84–97, 1977.
- [87] C. Rodgers, "A diffusion factor correlation for centrifugal impeller stalling," *Journal of Engineering for Power*, vol. 100, pp. 592–603, 1978.
- [88] J. Daily and R. Nece, "Chamber dimension effects on induced flow and frictional resistance of enclosed rotating disks," *Trans ASME J.Basic Eng*, vol. 82, no. 1, pp. 217–232, 1960.
- [89] Y. Senoo and Y. Kinoshita, "Influence of Inlet Flow Conditions and Geometries of Centrifugal Vaneless Diffusers on Critical Flow Angle for Reverse Flow," *Journal of Fluids Engineering*, vol. 99, no. 1, pp. 98–102, 1977.
- [90] C. Rodgers, "Mainline Performance Prediction for Radial Inflow Turbine," *Small High Pressure Ratio Turbines, VKI Lecture Series*, 1987.
- [91] M. Schmidt and H. Lipson, "Eureqa (Version 0.98 beta) [Software]," 2014.
- [92] V. Mounier, "Small-scale radial turbine pre-design model for ORCs," *Mendeley Data, v1*, <http://dx.doi.org/10.17632/yw4s626xxw.1>, 2018.
- [93] V. Mounier, "Small-scale centrifugal compressor pre-design model for domestic refrigeration," *Mendeley Data, v1*, <http://dx.doi.org/10.17632/sxbhxzh9t4.1>, 2018.
- [94] J. Schiffmann and D. Favrat, "Experimental investigation of a direct driven radial compressor for domestic heat pumps," *International Journal of Refrigeration*, vol. 32, no. 8, pp. 1918–1928, 2009.
- [95] J. Schiffmann, "Integrated Design and Multi-Objective Optimization of a Single Stage Heat-Pump Turbo-compressor," *Journal of Turbomachinery*, vol. 137, no. 7, p. 071002, 2015.
- [96] J. Zhang and H. Sun, "Fault diagnosis and failure prediction by thrust load analysis for a turbocharger thrust bearing," in *ASME Turbo Expo 2010: Power for Land, Sea and Air*, pp. 491–498, 2010.

Bibliography

- [97] S. L. Dixon, *Fluid Mechanics, Thermodynamics of Turbomachinery*. Elsevier Butterworth-Heinemann, 1998.
- [98] E. Lemmon, M. Huber, and M. McLinden, "NIST Standard Reference Database 23: Reference Fluid Thermodynamic and Transport Properties-REFPROP, Version 9.1," 2013.
- [99] P. Garrison, D. Harvey, and I. Catton, "Laminar Compressible Flow Between Rotating Disks," *Journal of Fluids Engineering*, vol. 98, pp. 382–389, 1976.
- [100] M. V. Casey and T. M. Fesich, "The Efficiency of Turbocharger Compressors With Diabatic Flows," *Journal of Engineering for Gas Turbines and Power*, vol. 132, no. 7, p. 072302, 2010.
- [101] R. A. Van Den Braembussche, "Micro Gas Turbines – A Short Survey of Design Problems," *AVT/VKI Lecture Series on "Micro-Gas Turbines", Paper No. RTO-EN-AVT-131*, pp. 1–18, 2004.
- [102] D. Verstraete and C. Bowkett, "Impact of heat transfer on the performance of micro gas turbines," *Applied Energy*, vol. 138, pp. 445–449, 2015.
- [103] S. Lecompte, H. Huisseune, M. van den Broek, S. De Schampheleire, and M. De Paepe, "Part load based thermo-economic optimization of the Organic Rankine Cycle (ORC) applied to a combined heat and power (CHP) system," *Applied Energy*, vol. 111, pp. 871–881, 2013.
- [104] H. Madhawa Hettiarachchi, M. Golubovic, W. M. Worek, and Y. Ikegami, "Optimum design criteria for an Organic Rankine Cycle using low-temperature geothermal heat sources," *Energy*, vol. 32, no. 9, pp. 1698–1706, 2007.
- [105] S. Quoilin, S. Declaye, B. F. Tchanche, and V. Lemort, "Thermo-economic optimization of waste heat recovery Organic Rankine Cycles," *Applied Thermal Engineering*, vol. 31, no. 14-15, pp. 2885–2893, 2011.
- [106] A. Schuster, S. Karellas, E. Kakaras, and H. Spliethoff, "Energetic and economic investigation of Organic Rankine Cycle applications," *Applied Thermal Engineering*, vol. 29, no. 8-9, pp. 1809–1817, 2009.
- [107] Z. Shengjun, W. Huaixin, and G. Tao, "Performance comparison and parametric optimization of subcritical Organic Rankine Cycle (ORC) and transcritical power cycle system for low-temperature geothermal power generation," *Applied Energy*, vol. 88, no. 8, pp. 2740–2754, 2011.
- [108] M. H. Yang and R. H. Yeh, "Thermodynamic and economic performances optimization of an organic Rankine cycle system utilizing exhaust gas of a large marine diesel engine," *Applied Energy*, vol. 149, pp. 1–12, 2015.

- [109] J. Wang, Z. Yan, M. Wang, M. Li, and Y. Dai, "Multi-objective optimization of an organic Rankine cycle (ORC) for low grade waste heat recovery using evolutionary algorithm," *Energy Conversion and Management*, vol. 71, pp. 146–158, 2013.
- [110] M. Astolfi, M. C. Romano, P. Bombarda, and E. Macchi, "Binary ORC (Organic Rankine Cycles) power plants for the exploitation of medium-low temperature geothermal sources - Part B: Techno-economic optimization," *Energy*, vol. 66, pp. 435–446, 2014.
- [111] EHPA, "EHPA Testing Regulation Testing of Water / Water and Brine / Water Heat Pumps," tech. rep., European heat Pump Association (EHPA), 2014.
- [112] S. Quoilin, S. Declaye, B. F. Tchanche, and V. Lemort, "Thermo-economic optimization of waste heat recovery Organic Rankine Cycles," *Applied Thermal Engineering*, vol. 31, no. 14-15, pp. 2885–2893, 2011.
- [113] I. H. Bell, J. Wronski, S. Quoilin, and V. Lemort, "Pure and pseudo-pure fluid thermophysical property evaluation and the open-source thermophysical property library coolprop," *Industrial and Engineering Chemistry Research*, vol. 53, no. 6, pp. 2498–2508, 2014.
- [114] R. Turton, R. Bailie, W. Whiting, J. Shaieiwitz, and D. Bhattacharyya, *Analysis, Synthesis, and Design of Chemical Processes*. Prentice Hall, fourth ed., 2012.
- [115] B. Sundèn and R. M. Manglik, *Plate heat exchangers : design, application and performance*. Wit Press, 11 ed., 2007.
- [116] R. L. Amalfi, *Two-Phase Heat Transfer Mechanisms within Plate Heat Exchangers Experiments, Modeling and Simulations*. Ph.d. thesis, Ecole Polytechnique Fédérale de Lausanne, 2016.
- [117] F. P. Incropera, D. P. DeWitt, T. L. Bergman, and A. S. Lavine, *Fundamentals of Heat and Mass Transfer*, vol. 6th of *Dekker Mechanical Engineering*. John Wiley & Sons, 2007.
- [118] H. Martin, "A theoretical approach to predict the performance of chevron-type plate heat exchangers," *Chemical Engineering and Processing: Process Intensification*, vol. 35, pp. 301–310, 1996.
- [119] J. García-Cascales, F. Vera-García, J. Corberán-Salvador, J. González-Maciá, and D. Fuentes-Díaz, "Assessment of boiling heat transfer correlations in the modelling of fin and tube heat exchangers," *International Journal of Refrigeration*, vol. 30, no. 6, pp. 1004–1017, 2007.
- [120] Y. Yan, H. Lio, and T. Lin, "Condensation heat transfer and pressure drop of refrigerant R134a in a plate heat exchanger," *International Journal of Heat and Mass Transfer*, vol. 42, no. 6, pp. 993–1006, 1999.

Bibliography

- [121] G. Danilova, V. Azarrskov, and B. Zemskov, "Teploobmen v plastinchatihispariteljan razichnole geometri (Heat transfer in plate evaporators of different geometry)," *Kholod. Tek.*, vol. 4, pp. 25–31, 1981.
- [122] S. Henchoz, C. Weber, F. Maréchal, and D. Favrat, "Performance and profitability perspectives of a CO₂ based district energy network in Geneva's City Centre," *Energy*, vol. 85, pp. 221–235, 2015.
- [123] M. A. Bernier, "Closed-Loop Heat Pump Systems," *ASHRAE journal*, pp. 13–19, 2006.
- [124] The U.S. Department of Energy, "Ground-Source Heat Pumps Applied to Federal Facilities – Second Edition," tech. rep., 2001.
- [125] K. E. Herold, R. Radermacher, and S. A. Klein, *Absorption Chillers and Heat Pumps*. Taylor & Francis, 1996.
- [126] M. Conde, "Thermophysical Properties of {NH₃ + H₂O} Mixtures for the Industrial Design of Absorption Refrigeration Equipment," tech. rep., Zurich, Switzerland, 2006.
- [127] M. R. Kærn, A. Modi, J. K. Jensen, and F. Haglind, "An Assessment of Transport Property Estimation Methods for Ammonia–Water Mixtures and Their Influence on Heat Exchanger Size," *International Journal of Thermophysics*, vol. 36, no. 7, pp. 1468–1497, 2015.
- [128] A. Qaswari, R. Treece, and R. Blakeley, *The Design and Development of an Absorption Cycle Heat Pump Optimised for the Achievement of Maximum Coefficient of Performance*. COMMISSION OF THE EUROPEAN COMMUNITIES, 1972.
- [129] K. B. Lee, B. H. Chun, J. C. Lee, C. H. Lee, and S. H. Kim, "Experimental analysis of bubble mode in a plate-type absorber," *Chemical Engineering Science*, vol. 57, no. 11, pp. 1923–1929, 2002.
- [130] F. Táboas, M. Vallès, M. Bourouis, and A. Coronas, "Assessment of boiling heat transfer and pressure drop correlations of ammonia/water mixture in a plate heat exchanger," *International Journal of Refrigeration*, vol. 35, no. 3, pp. 633–644, 2012.
- [131] C. A. Balaras, G. Grossman, H.-M. Henning, C. A. Infante Ferreira, E. Podesser, L. Wang, and E. Wiemken, "Solar air conditioning in Europe—an overview," *Renewable and Sustainable Energy Reviews*, vol. 11, no. 2, pp. 299–314, 2007.
- [132] V. Mounier, L. C. Mendoza, and J. Schiffmann, "Performance Assessment and comparison of Thermally Driven Heat Pump Systems," in *International Congress of Refrigeration 2015*, (Yokohama, Japan), 2015.
- [133] N. Douet, L. E. Olmedo, and P. Grandgeorge, *Thermodynamic Modeling and Thermo-Economic Analysis with Optimization of Energy Utility Systems for High-Tech Greenhouses in Europe*. Semester project, EPFL, 2013.

- [134] B. Rebbechi, "A Vapour Cycle Cabin Cooling System For the Sea King MK.50 Helicopter," tech. rep., DEPARTMENT OF DEFENCE, DEFENCE SCIENCE AND TECHNOLOGY ORGANISATION AERONAUTICAL RESEARCH LABORATORIES, MELBOURNE, VICTORIA, 1980.
- [135] F. Cougnenc and M. Lescaudron, "Air Conditioning Systems For Helicopters," in *TWELFTH EUROPEAN ROTORCRAFT FORUM*, (Garmisch-Partenkirchen), 1986.
- [136] C. X. Pan, J. Z. Zhang, L. F. Ren, and Y. Shan, "Effects of rotor downwash on exhaust plume flow and helicopter infrared signature," *Applied Thermal Engineering*, vol. 65, no. 1-2, pp. 135–149, 2014.
- [137] J. R. Juhasz and L. D. Simoni, "A review of potential working fluids for low temperature organic Rankine cycles in waste heat recovery," in *3rd International Seminar on ORC Power Systems*, (Brussels), 2015.
- [138] G. Alberto and E. Benini, "Performance of a Turboshift Engine for Helicopter Applications," *Proceedings of the ASME 2012 Gas Turbine India Conference*, pp. 1–15, 2012.
- [139] T. A. Horst, H. S. Rottengruber, M. Seifert, and J. Ringler, "Dynamic heat exchanger model for performance prediction and control system design of automotive waste heat recovery systems," *Applied Energy*, vol. 105, pp. 293–303, 2013.
- [140] H. G. Zhang, E. H. Wang, and B. Y. Fan, "Heat transfer analysis of a finned-tube evaporator for engine exhaust heat recovery," *Energy Conversion and Management*, vol. 65, pp. 438–447, 2013.
- [141] F. Marechal, A. Sachan, and L. Salguiero, "Application of Process Integration Methodologies in the Brewing Industry," in *Handbook of Process Integration : Minimisation of energy and water use, waste and emissions*, ch. 27, pp. 820–862, Woodhead Publishing Limited, 2013.
- [142] R. L. Amalfi, F. Vakili-Farahani, and J. R. Thome, "Flow boiling and frictional pressure gradients in plate heat exchangers: part 2, Comparison of literature methods to database and new prediction methods," *International Journal of Refrigeration*, vol. 61, pp. 185–203, 2015.

Violette Mounier

violette.mounier@gmail.com

French

12.04.1991

Skills

Software

Microsoft Office, Inkscape, Matlab, Git, CAD (CATIA, SW), Latex

Mechanical engineering

Design, Turbomachinery, Heat transfer, Thermodynamics, Rotordynamics, Optimization

Energy engineering

Energy recovery, Renewable energy, Energy optimization, Heating systems

Personal

Creative, Problem solver, Curious
Open-minded

Languages

French	Native
English	C1/C2 (Business)
German	B1/B2 (Conversation)
Italian	A1 (Basics)

Interests

Toastmaster
Geopolitics
Trivia quizz
Travels
Science fiction literature and movies
Learning new skills

Sports

Bouldering
Swimming
Yoga
Dancing

References

Prof. Dr. Jürg Schiffmann
Assistant Professor, EPFL
jurg.schiffmann@epfl.ch

Dr. Bruno Agostini
Principal Scientist, ABB
bruno.agostini@ch.abb.com

Education & Certifications

Ph.D. – Doctoral school of Energy 2014-2018
EPFL – Lausanne, Switzerland

PRINCE2 Foundation certificate 2017
Certificate in project management

MSc in Energy / Mechanical engineering 2010-2013
Ecole Centrale Lyon – Lyon, France

Preparatory courses for French engineering schools 2008-2010
Lycée du Parc – Lyon, France

Experience

Doctoral Assistant (Ph.D.) 02.2014 – Present
EPFL – Lausanne, Switzerland

Development of an innovative thermally driven heat pump

- Design, optimization, and tests of mechanical / thermodynamic systems
- Teaching (Bachelor) and student coaching (Term and Master projects)
- Journal and conference papers:
 - *Thermo-economic optimization of an ORC driven heat pump based on small scale turbomachinery and comparison with absorption heat pumps*, 2017, Int. J. Ref doi:10.1016/j.ijrefrig.2017.05.021
 - *Small scale radial inflow turbine performance and pre-design maps for Organic Rankine Cycles*, 2017, Energy doi:10.1016/j.energy.2017.11.0021
 - *Performance assessment and comparison of thermally driven heat pumps systems*, 2015, 24th IIR International Congress of Refrigeration, doi : 10.18462/iir.icr.2015.0316
 - *Data-driven Updated Pre-design Tool for Small Scale Centrifugal Compressors In Refrigeration*. Turbo Expo: Power for Land, Sea, and Air, Oslo, 2018

Research Engineer 04.2013 – 12.2013
ABB – Baden, Switzerland

Study of an advanced power electronic cooling device

- Knowledge on power electronic cooling applications and challenges
- Communication to ABBs Business Units
- Conference papers:
 - *Characterization of an Open Loop Pulsating Heat Pipe Cooler*, ASME 12th International Conference on Nanochannels, Microchannels, and Minichannels, 2014
 - *Characterization of a Novel Pulsating Heat Pipe Cooler for Power Electronics at Extreme Ambient Temperatures*, ASME 13th International Conference on Nanochannels, Microchannels, and Minichannels, 2015

Research Intern 05.2012 – 08.2012
CEA – Grenoble, France

Study of an innovative chemical sensor for food processing analysis

- Implementation and test of chemical sensors (surface plasmon resonance)
- Data analysis and benchmarking (PCA)
- Journal paper:
 - *SPR imaging based electronic tongue via landscape images for complex mixture analysis*, 2014, Talanta

Student projects 2011 – 2013
SEB – Lyon, France

Domestic water cleaning and remineralization
Ecole Centrale Lyon - Lyon, France

Event organizer for an association helping unprivileged high school students